CDF-741

CENTRAL PRODUCTION OF CHARGED PARTICLES AT CDF

A Thesis
Submitted to the Faculty

of

Purdue University

by

Aesook Byon

In Partial Fulfillment of the
Requirements for the Degree

of

Doctor of Philosophy

December 1989

ACKNOWLEDGMENTS

I wish to thank my parents for their support. I also want to thank my advisor Professor Virgil E. Barnes. I thank the Central Tracking Chamber group - Dr. J. P. Berge, Dr. R. W. Kadel, Dr. A. Mukherjee, Dr. A. Para, and Dr. R. L. Wagner - for their immearsureable support and good advise. I wish to thank the members of the minimum bias analysis working group for all of their supporting works. This work was supported in part by the United States Department of Energy under contract DE-AC02-76ER01428.

TABLE OF CONTENTS

LIST OF TABLES

Table Page

LIST OF FIGURES

Figure Page

Figure Page

ABSTRACT

Byon, Aesook. Ph.D., Purdue University, December 1989. Central Production of Charged Particles at CDF. Major Professor: Virgil E. Barnes.

Particles produced in soft proton antiproton interactions at the Fermilab Tevatron collider are studied at center of mass energies ($\sqrt{s}$) of 630 and 1800 GeV. The data were taken using a minimum bias trigger during the 1987 run of the Collider Detector at Fermilab (CDF). The event structure of proton antiproton interactions has been studied. Analyses of inclusive charged particle transverse momenta, multipicity distribution and correlations of charged particles are presented. Particle clusters in minimum bias triggers are studied to verify whether the hard interaction QCD models are applicable in the low E_T region.

CHAPTER 1 – INTRODUCTION

All particles can be divided into two groups: hadrons which can undergo strong interactions and leptons that do not. Since leptons have shown no sign of substructure, they can be viewed as elementary particles. Hadrons appear to have substructure. According to the Quark Parton Model, hadrons consist of quarks and gluons and interactions among hadrons are analysed in terms of their constituents. The interactions of the quarks and gluons, collectively referred to as partons, are described by a non-abelian renormalizable gauge theory called Quantum Chromodynamics (QCD). Asymptotic freedom suggests that QCD very successfully describes high momentum transfer processes (hard interactions), where the fundamental constituents of hadrons are probed and the strong coupling constant is small enough for applying the methods of perturbative field theory. The majority of events in hadron-hadron interactions, however, result from low momentum transfer, non-perturbative QCD mechanisms (soft processes) that are poorly understood at the fundamental parton level. This chapter describes some of the considerable efforts that have been made to better understand the processes of soft hadronic interactions.

1.1 Structure of Hadrons

Hadron is the generic name for strongly interacting particles like baryons and mesons which can be formed from quark bound states. According to the Quark Parton Model [1,2], hadrons consist of quarks and gluons which are bound by forces that have some similarities to the well known electromagnetic force, but which also exhibit some important differences. The process which the colored quark or gluon undergoes in order to reach the observable final state consisting of color singlet hadrons is called a "hadronization" or "fragmentation".

Quarks are pointlike, spin $\frac{1}{2}$ fermions having color charge as the analogue of electric charge in the electromagnetic interactions and fractional electric charge ($\pm\frac{1}{3}$ or $\pm\frac{2}{3}$). The quarks include the valence quarks and sea quarks. The valence quarks determine the quantum numbers of the hadrons such as the mass, spin, charge, isospin and strangeness. All the observed mesons can be accounted for as quark-antiquark pairs and all the baryons (antibaryons) as composites of three quarks (antiquarks). The sea quarks are virtual quark-antiquark pairs which can be spontaneously created from the vacuum, or from the dissociation of gluons.

Gluons are the force carriers of the strong interaction. They are massless spin 1 bosons, possessing color charge and having no electric charge. On the average, gluons carry ~ 50 % of the momentum of all the constituents inside a hadron [3]. The interaction between two quarks can be described as the exchange of virtual gluons.

QCD is a field theory analogous to the field theory of electromagnetism, Quantum Electrodynamics (QED). In QCD, there is a massless boson (gluon) which intermediates the strong interaction just as in QED the photon intermediates the electromagnetic interaction. Therefore, if QCD is a valid theory, some evidence should be observed for the existence of the gluon. No quark or gluon has ever been seen directly. Instead, only hadrons are observed in detectors. This observation is accounted for by the hypothesis of color confinement which suggests that only those composites of quarks and gluons that have no net color charge can exist in a free state.

When two high energy hadrons collide, the bulk of the cross section consists of events in which a large number of particles are produced with small transverse momenta with respect to the collision axis. Since QCD is generally accepted as the theory of strong interactions, it would be advantageous to compute these "soft" multiparticle production processes directly from the QCD Lagrangian. However only a tiny fraction of the hadron-hadron cross section can be fully described by QCD computations, because the running coupling constant of soft processes is too large for ordinary perturbation theory to be sensible and the understanding of non-perturbative QCD is limited.

1.2 Recent Developments in Soft Hadronic Interactions

In hadron colliders with center of mass energy ($\sqrt{s}$) above $\sim$ 100 GeV, the interaction between two incoming hadrons typically results in the production of 10 - 100 outgoing particles produced in mostly low momentum transfer processes. Some studies of hadron-hadron interactions have focussed on the properties of the typical ("Minimum Bias") event. These properties include the cross sections, particle multiplicities, distributions of transverse momenta, ratios of particle types and correlations between particles. The dependences of these average quantities on $\sqrt{s}$ have been extensively studied using measurements from the Tevatron collider ($\sqrt{s} = 1800$ and 630 GeV), the S$\bar{\text{P}}$PS collider ($\sqrt{s} = 200\sim900$ GeV), the ISR collider ($\sqrt{s} = 23\sim63$ GeV), and FNAL fixed target experiments using bubble chambers or electronic counters ($\sqrt{s} = 1.5\sim30$ GeV). In particular, some very interesting changes in the properties of minimum bias events occur between ISR and higher energy data.

Multiplicity Distributions

For collider interactions with $\sqrt{s} > 10$ GeV, the multiplicity distribution can be divided into two regions of rapidity, y,

$$y = \frac{1}{2}\, ln(\frac{E + p_z}{E - p_z})$$

where E is the energy of the produced particle and p_z is it's component of momentum parallel to the beam direction. In the beam fragmentation region, the particles have rapidities close to that of the beam particles. The production of particles in this region results from the fragmentation of the beam particles. The central region, where particle production is independent of beam fragmentation, is dominated by charged and neutral pions. Theorists predict a plateau in the rapidity distribution for the central region [4]. This plateau is barely visible at $\sqrt{s} < 63$ GeV [5,6], but is clearly seen at $\sqrt{s} = 546$ GeV [7] and the width and height of the plateau increase with $\sqrt{s}$ [8,9]. Particle multiplicities have recently been measured up to $\sqrt{s} = 1.8$ TeV. There is no significant change in shape from $\sqrt{s} = 546$ GeV, but there is a steady rise in the height of the central rapidity plateau that seems to be increasing faster than $\log(s)$. This rise was quantified over a wide energy range with different fits of the type $\mathrm{A} + \mathrm{B}\log(s) + \mathrm{C}\log^2(s)$ or $\alpha + \beta s^{\mathrm{n}}$ [10].

KNO scaling

Scaling laws and other regularities have been used to study the properties of the multiplicity distribution. The scaling principle proposed by Koba, Nielsen and Olesen (KNO scaling) [11] suggests that a probability function Ψ becomes independent of the center of mass energy when the multiplicity distribution of charged hadrons is parametrized as a function Ψ by normalizations of the topological cross section σ_n and the multiplicity of charged particles n to the total inelastic cross section $\sigma_{\mathrm{inel}}(s)$ and the average multiplicity $<n>$:

$$<n> \frac{\sigma_n(s)}{\sigma_{\mathrm{inel}}(s)} = \Psi\left(\frac{n}{<n>}\right).$$

KNO scaling was shown to be valid for pp interactions up to $\sqrt{s} = 63$ GeV [6]. However for $\sqrt{s} > 100$ GeV, KNO scaling is violated in that the multiplicity distribution shows larger fluctuations around the mean value than previously observed at lower energies [7-9].

Transverse momentum distributions

The rapidly falling spectrum in transverse momentum, p_{T}, of the produced particles is one of the most striking characteristics of hadronic collisions, and is considered to be directly related to the underlying scattering processes [12]. It has been shown that the transverse momentum distributions of particle production strongly depend on the scale of the interacting constituents [13]. The scale for soft $\bar{\mathrm{p}}\mathrm{p}$ interactions is the proton radius and for hard interactions, the parton size. At $\sqrt{s} < 63$ GeV, it was observed that this kinematic limitation gives an exponential form to the single particle transverse momentum distribution [14-17]. However, at SPS collider energies, the distribution is enhanced at high p_{T} relative to a simple exponential extrapolation from low p_{T} [18,19]. This was interpreted as a signature of increasing contribution from the hard scattering component to the total cross section as $\sqrt{s}$ increases. An increase in the value of the average transverse momentum, $< p_{\mathrm{T}} >$, with $\sqrt{s}$ is also apparent above ISR energies [16,17]. It is still in question whether this indicates some threshold between ISR energies and $\sqrt{s} > 100$ GeV for new phenomena.

Dependence of $< p_{\mathrm{T}} >$ on multiplicity

The behavior of the p_{T} distributions in relation to the event multiplicity has been one of the important subjects in minimum bias physics. At lower center of mass energies, a decrease of $< p_{\mathrm{T}} >$ with increasing event multiplicity had been observed [17,20]. This decrease was mainly visible at the high multiplicity tail of the distribution and has been generally interpreted as a phase space effect [21]. However, an increase of $< p_{\mathrm{T}} >$ with increasing charged particle density has been observed by the UA1 [18,22] and C0 [23] collaborations. Due to large systematic errors coming from calculation of $< p_{\mathrm{T}} >$ and statistical errors of true multiplicities of the high density events, the shape of the dependence is not really clear. Even though many interpretations have been proposed in terms of large p_{T} effects (semi-hard effects) in the central region [24], possible evidence for hadronic phase transition [21], or small impact parameter scattering in a geometrical model [25], the correct explanation is still an open question.

Feynman Scaling

Unlike transverse distributions, the limits on the longitudinal distributions of particles in soft hadronic interactions seem to depend strongly on $\sqrt{s}$ [14-17]. A general scaling principle applicable to all regions of longitudinal phase space was proposed by Feynman [1]. Arguing on the basis of the parton model, Feynman suggested that there might be some way to see how the cross sections might behave so that significant quantities can be extracted from data taken at different energies. For this purpose, a normalization of p_z was proposed to give the scaling variable x_F:

$$x_F = \frac{p_z}{p_{\max}} \sim 2\frac{p_z}{\sqrt{s}}$$

where $p_{\max}$ is the maximum momentum of the particle in the center of mass system. For inclusive studies of particles in the final state of collision, if the beams are unpolarized, the invariant cross section depends only on s, p_z and p_{T}; as $s \to \infty$, the single particle spectrum obeys the scaling principle

$$\mathrm{E}\frac{d^3\sigma}{d^3p}(p_{\mathrm{T}}, p_z, s) = \mathrm{E}\frac{d^3\sigma}{d^3p}(p_{\mathrm{T}}, x_F).$$

This implies that for large s, and for fixed p_{T} and p_z, the momentum spectra of particles are independent of s. Feynman scaling is a good approximation to experimental data up to $\sqrt{s} = 63$ GeV [26]. For higher energies, experimental data deviate from Feynman scaling [27].

Correlations between charged particles

With the presence of a high p_{T} particle, strong correlations in both azimuthal angle and rapidity between charged particles have been observed [28]. This is consistent with the framework of parton scattering and subsequent fragmentation of the partons into hadrons [29] and has been interpreted as a signature of low E_{T} jets (mini-jets) in the minimum bias events [30]. However, other studies show that the transition from soft to hard events occurs at much larger values of jet E_T than 5 GeV [31] and observed "mini-jet" events are due to statistical effects resulting from the experimental cuts [32]. More measurements and studies have to be done to understand what these events really are.

Other interesting results

Other interesting topics concerning the production mechanisms and non-scaling behavior of soft interactions are: the measurement of the total cross section, which appears to grow like $\log^2(s)$ [33]; the increase in the ratio of the elastic to total cross section as energy increases [33,34]; and changes in particle composition, such as the rise of the ratio K/π with $\sqrt{s}$ and p_T [19,35].

Summary of the recent developments

In soft interactions, many changes in event characteristics have been observed as $\sqrt{s}$ increases. There are strong indications of an increase in the hard interaction component as the center of mass energy increases. However, the distinction between soft and hard collisions is not well defined and how soft and hard interactions can be joined is not well understood. Whether particular observed effects are due to an increase in the hard interaction component or to an increase in heavy particle production as $\sqrt{s}$ increases is still in question. Several theoretical models for soft and semi-hard hadron production have been built to describe the changes which have been observed.

1.3 Particle Production Models for Soft Hadronic Interactions

QCD is well established for hard scattering processes, but the mechanism for the majority of quark and gluon interactions via soft scattering processes is not well understood. Since the average transverse momenta of particles in minimum bias events are small ($< p_T > \sim$ 400 MeV/c), most particles are produced in soft processes for which QCD does not provide a perturbative theory, so the final states of interactions have been described by simplified models using phenomenological techniques.

In most of models, particle production is assumed to have two components. The hard interaction component is described by a parton scattering shower where the basic mechanism comes from perturbative QCD theory. As in perturbative QCD theory, this gives a divergent result for the splitting of a low mass gluon, coming from a soft scattering process, into two parallel gluons. The soft interaction component, the basic mechanism for hadron production, is usually described as a separation of color charges resulting in the production of strings of gluons. or cluster chains. At higher energies, many of the changes in the event characteristics can be understood as an increased gluon activity in the central region, and this is usually described by bent strings or by adding more strings (cluster chains).

Three of these models will be introduced in order to give some insights into their basic assumptions, how they picture the process of interactions, and their predictive powers. References 37 through 38 have good summaries of these and other models.

Lund String Model

In contrast to the Lund Pythia Model [39], which is essentially a one component model that uses perturbative QCD as far as possible (low p_T cut off $\sim$ 1.6 GeV/c), the Lund Fritiof Model [40] assumes that when two hadrons collide they exchange gluons (gluon exchange or color exchange), and in particular, soft collisions are dominated by longitudinal color neutral momentum exchange. According to the model, a collision in a $\bar{p}p$ hadronic interactions can be pictured as reactions between two bags containing quarks. Within this bag, a confined color field exists and the energy is stronger approaching the center of the field. When an interaction occurs, these color fields overlap and the field lines act like massless relativistic strings. For a hard scattering, the two bags come so close together that their centers interact (gluon exchange),

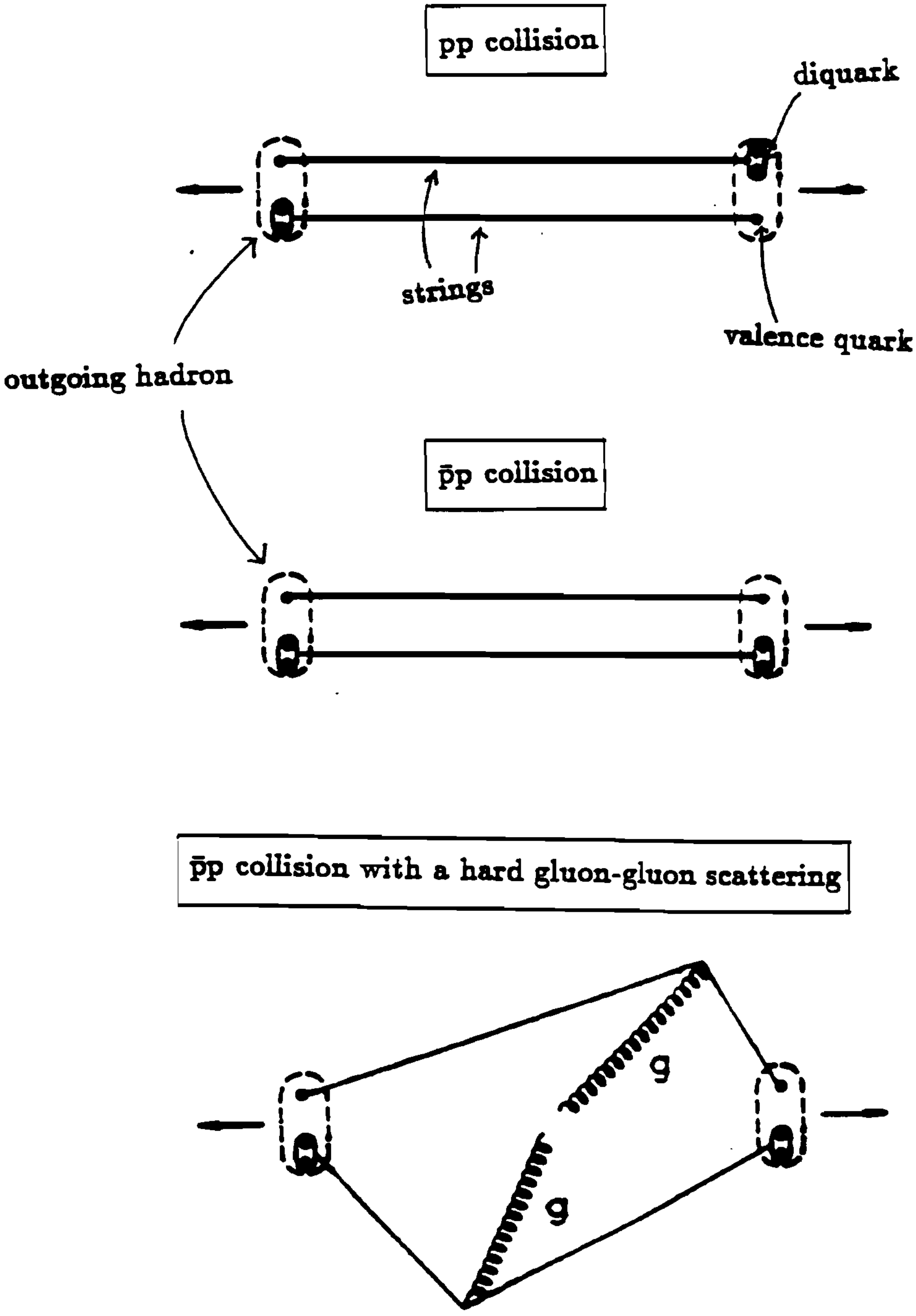

Figure 1.1 Schematic view of interaction in Lund String Model.

resulting in breaking and recoupling the strings. In a soft scattering, the centers of the field do not overlap (large impact parameter) and only the fields interact with an additional exchange of extra soft gluons which neutralize the color exchange (color neutral momentum exchange). Since the momentum is transfered mainly in the beam direction, the string will stretch along the longitudinal direction and fragment. When the color charges at the ends of the strings separate, they can emit gluon bremsstrahlung. The strings will thus not be straight but will bend and produce more particles and more transverse momentum. With increasing center of mass energy, more bremsstrhlung will occur and this produces more particles and more p_T in a correlated way.

Dual Parton Model

The Dual Parton Model (DPM) [41] is a multiple scattering model which incorporates the quark-gluon structure of hadrons and non-perturbative QCD. The DPM uses the interaction string theory which will be suitable to express the effective degrees of freedom for QCD at the soft hadronic scale regardless of confinement. In this model, a soft $\bar{p}p$ interactions can be pictured in the following way. In the interaction, the valence quarks from each incoming proton or antiproton are separated into a quark and a diquark pair. Valence quarks and diquarks from opposite directions are linked with two chains (Figure 1.2), each chain being a color singlet. As these two chains are stretched, fragmentations occur which produce final hadrons, giving the leading order term (soft interaction term) of the DPM. The non-leading terms contain extra chains involving sea quarks coming mainly from gluon-gluon interactions (Figure 1.2). As $\sqrt{s}$ increases, this sea quark contribution becomes important as a semi-hard scattering component. In all the processes, each chain is assumed to be independent of other chains and the hadronic spectra of each chain are obtained from a convolution of momentum distribution functions and fragmentation functions. The other assumptions are:

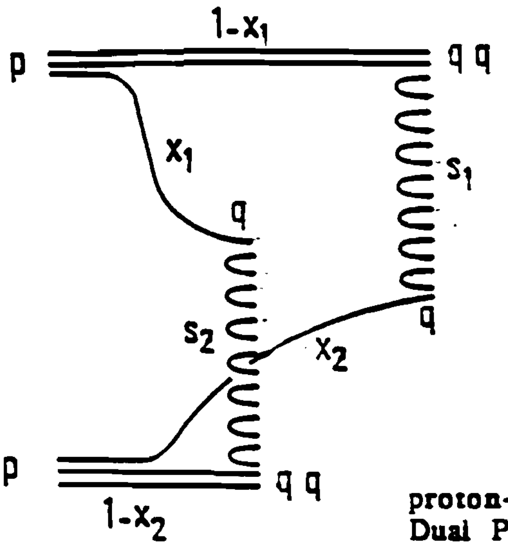

Two chain diagram for proton-proton interactions in the Dual Parton Model.

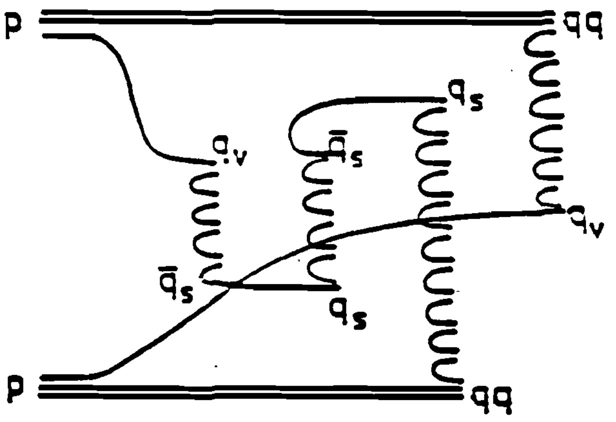

Four chain diagram for proton-proton interactions in the Dual Parton Model.

Figure 1.2 Diagrams of interaction in Dual Parton Model.

(1) By knowing the momentum distribution functions of quarks and gluons, the quantum number flow of the incoming hadrons can be tracked and the sharing of available energy among the various inelastic collisions can be calculated.
(2) The fragmentation function does not depend on the momentum transfer of the process.
(3) The total multichain contribution is controlled by unitarity [42].

These assumptions allow no free parameters, resulting in more predictive power for the DPM. The increasing number of chains at higher energies gives a rising central plateau and increased forward-backward correlations. The main properties of mini-jet production can be understood by the introduction of semi-hard scattering in the DPM. This has the obvious consequence of higher average particle multiplicity for jet events than for the no-jet sample.

Both the DPM and Lund String model assume that hard parton collisions above a cut-off give extra chains (strings) and both also assume certain impact parameter distributions. A major difference between these two models is that DPM recognizes the color (N=3) of interacting quarks and goes through a 1/N expansion, while the Lund model uses color singlet gluons only.

QCD Motivated Model

One of the interpretations proposed for the change in characteristics of minimum bias events as $\sqrt{s}$ increases, is that an increasing fraction of the inelastic non-diffractive cross section (σ_{ND}) contains QCD jets [43]:

$$\sigma_{\mathrm{ND}} = \sigma_{\mathrm{Nojet}} + \sigma_{\mathrm{Jet}}.$$

The first term σ_{Nojet} arises from multiple parton-parton collisions and its magnitude is independent of $\sqrt{s}$. This σ_{Nojet} is supposed to be the dominant contribution to the non-diffractive cross section up to ISR energies and to have many of the characteristics of low energy data (< 20 GeV), such as an exponential p_T spectrum and multiplicities that can be described by KNO scaling.

The second term, σ_{Jet}, is the result of hard collisions of low Bjorken-x partons in the incident hadrons. These are dominantly hard gluon-gluon scatterings at high energy, for which the differential scattering cross section is the Rutherford type of

$$\frac{d\sigma_{\mathrm{Jet}}}{(dx_1 dx_2 d\theta)} \sim \frac{g(x_1)g(x_2)}{sin^4(\theta/2)}$$

where

$g(x)$ = gluon structure function and

θ = scattering angle of the two partons in their rest frame [44].

In this model , the broadening of the charged particle p_{T} distribution for higher $\sqrt{s}$ can be explained by an increased contribution from the jet component. Also, the existence of two components to the inclusive cross section with different energy dependences can lead to a breakdown of KNO scaling. Also, since the underlying events in hard parton scatterings are known to have dramatically different properties from soft collisions (their $< p_{\mathrm{T}} >$ is large and increases with $\sqrt{s}$, and they are characterized by higher multiplicity due to enhanced gluon radition), the introduction of the σ_{Jet} component can explain the correlation between $< p_{\mathrm{T}} >$ and multiplicity. Furthermore, some calculations [45] indicate that hard QCD scatterings are capable of contributing to the total cross section to a large degree, rising from a few mb at 50 GeV to the order of 30 mb at 1800 GeV.

1.4 Minimum Bias Physics at CDF

Many changes and new developments have been observed as the center of mass energy increased above the ISR region. Models for soft hadronic interactions have been tested by experimental p_{T} distributions, multiplicity distributions, and possible low E_{T} jet phenomena. More information is needed to determine the dynamics of hadron production. The study of inclusive charged particle production in $\bar{\mathrm{p}}\mathrm{p}$ interactions at CDF further tests the various parton models of soft and semihard interactions by extending measurements to $\sqrt{s} =$ 1800 GeV. Analyses of minimum bias data from the 1987 run will be presented with emphasis on measurements by the Central Tracking Chamber and central calorimetry.

CHAPTER 2 – THE CDF EXPERIMENT

The Collider Detector at Fermilab (CDF) [46] is a general purpose detector built to study proton antiproton interactions at the Tevatron collider. It includes electromagnetic and hadronic calorimetry and charged particle tracking coverage over $2° < \theta < 178°$ and 2π in ϕ. (See pp. 20 - 22 for a definition of variables and coordinates.) Muon coverage exists over a portion of this solid angle. The detector is approximately cylindrically symmetric and has calorimeters uniformly segmented in pseudorapidity(η) and azimuth(ϕ) so that it can provide fairly complete information about the interaction.

2.1 Overview of the CDF Detector

The basic goal of CDF is to measure the energy, momentum and where possible, the identity of particles produced at the Tevatron collider [47] over a large fraction of the solid angle in order to study a large number of different physics processes. To accomplish this, many layers of different detector components surround interaction region (Figure 2.1). Starting from the interaction point, particles enter in sequence a thin wall beryllium vacuum pipe, charged particle tracking chambers, the cryostat and coil of a superconducting solenoid magnet in the central detector, sampling calorimeters, and muon detectors. In addition there are trigger counters and small angle silicon strip detectors. An isometric view of the CDF detector is shown in Figure 2.2. The regions of pseudorapidity covered by the tracking chambers calorimetry and muon chambers are listed in Tables 2.1-2.3.

The interaction region is covered by a beryllium vacuum chamber which is about 7.6 cm in diameter, 1.45 m in length and 0.64 mm thick. The pipe was

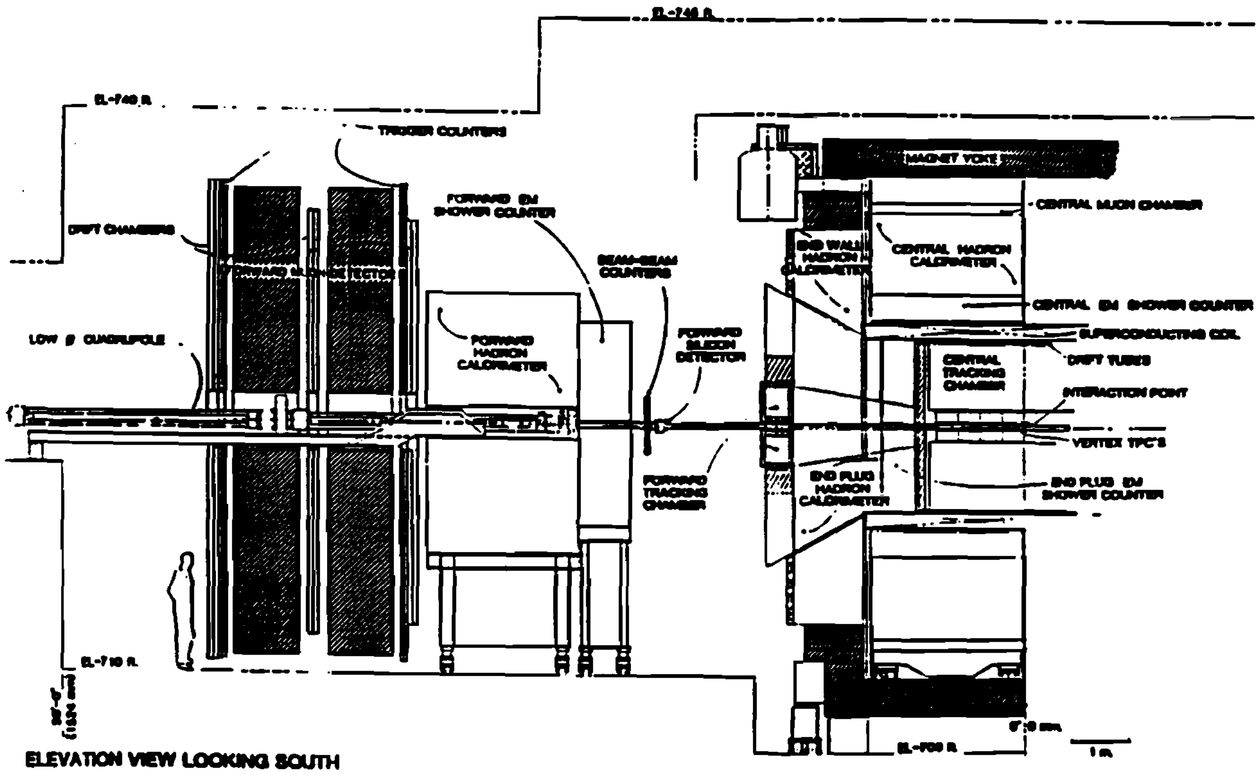

Figure 2.1 A vertical cut through 1/2 of the CDF detector.

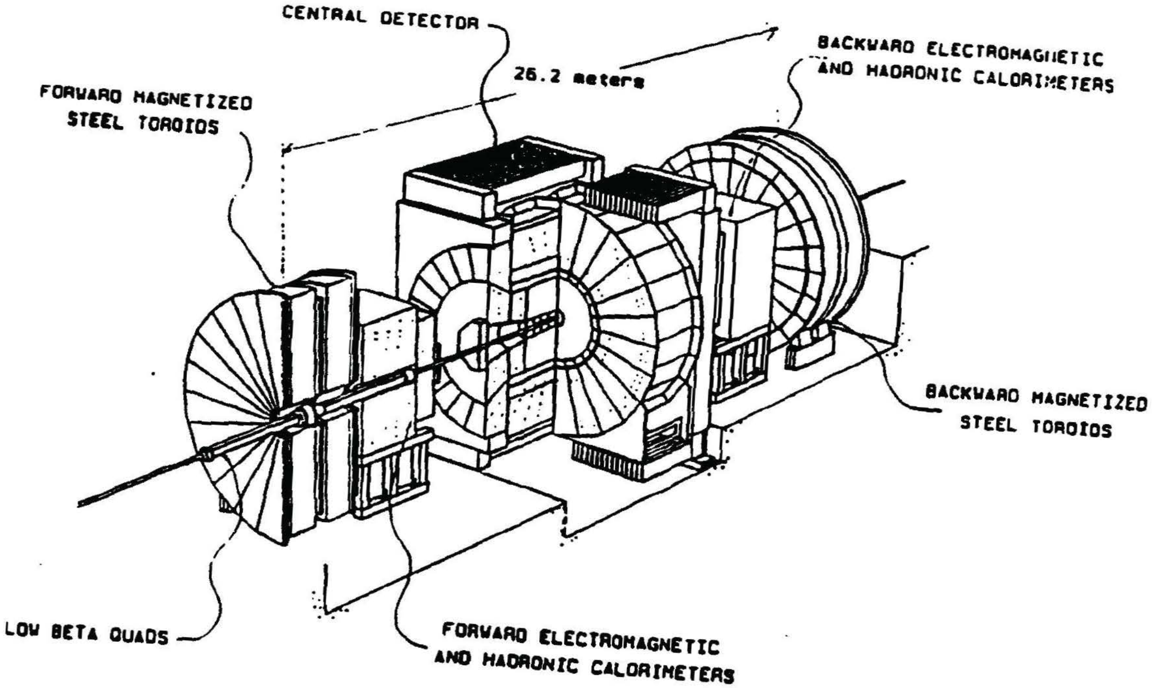

Figure 2.2 An isometric view of the CDF detector.

Table 2.1 Angular coverage of tracking chambers.

tracking system	$\|\eta\|$ coverage (inner layer)	(outer layer)	number of sense wires	spatial resolution per hit
VTPC	0.0 - 3.5	0.0 - 2.6	3072	$< 200\mu m$ ($\theta = 90°$) $< 500\mu m$ ($\theta = 150°$)
CTC	0.0 - 2.0	0.0 - 1.0	6156	$< 200\mu m$ (R-ϕ) < 6 mm (z)
CDT	0.0 - 1.0	0.0 - 1.0	2016	$< 200\mu m$ (R-ϕ) < 2.5 mm (z)
FTC	2.4 - 4.0	2.4 - 4.0	3024	$< 150\mu m$ (R-ϕ)

Table 2.2 Angular coverage of calorimetry.

calorimetry	$\|\eta\|$ coverage	tower size $\Delta\eta \times \Delta\phi$	energy resolution*
Central Electromagnetic	0.0 - 1.1	0.1 × 15°	2%
Central Hadron	0.0 - 0.9	0.1 × 15°	11%
Wall Hadron	0.7 - 1.3	0.1 × 15°	14%
Plug Electromagnetic	1.1 - 2.4	0.09 × 5°	4%
Plug Hadron	1.3 - 2.4	0.09 × 5°	20%
Forward Electromagnetic	2.2 - 4.2	0.1 × 5°	4%
Forward Hadron	2.3 - 4.2	0.1 × 5°	20%

(* σ/E at E=50 GeV)

Table 2.3 Angular coverage of muon chambers.

muon chamber	$\|\eta\|$ coverage	spatial precision/hit	
CMU	0.0 - 0.63	$< 250\mu m$ (ϕ),	< 1.2 mm (z)
FMU	2.0 - 3.64	$< 5°$(ϕ),	$< 200\mu m$ (R)

designed to minimize the number of absorption lengths and radiation lengths in the wall and thereby minimize secondary interactions and photon conversions. Outside of the beam pipe, a nearly 4π solid angle tracking of charged particles is provided by the Vertex Time Projection Chamber, the Central Tracking Chamber, the Central Drift Tubes, the Forward Tracking Chamber and the forward silicon strip detectors. These tracking systems provide the momenta of charged particles, the charged particle multiplicity, the position of the event vertex, the identification of multiple interactions and calibration data for the calorimeter response. The Vertex Time Projection Chamber and the Central Tracking Chamber are described in section 2.4 and 2.5. At the outer radius of the Central Tracking Chamber, there are three layers of axial drift tubes which are instrumented for charge division in order to determine a three-dimensional space point. These Central Drift Tubes (CDT) [48] are 3 m long and have a z measurement resolution (σ) of 6 mm. The Forward Tracking Chamber (FTC) [49] is a radial drift chamber which contains a total of 3024 sense wires in the forward and backward direction. A fraction of these sense wires are instrumented for charge division, so that a three-dimensional measurement can be made for each track. The designed spatial resolutions of the FTC are listed in Table 2.1.

The superconducting solenoidal magnet [50] is located outside of the CDT. The magnet, 3 meters in diameter and 5 meters long, produces a 1.5 Tesla field parallel to the beam direction with a current of 5 kA. The iron in the endplug and endwall calorimetry along with the yoke form the return path for the magnetic field. Only a small part of the flux is returned through the central calorimetry iron. In combination with the central tracking chamber, an accurate momentum measurement for charged particles in the central region is achieved.

The CDF detector also has almost full coverage in electromagnetic (EM) and hadron (HA) calorimetry with fine granularity and good energy resolution.

It provides the basic information in the detection of quark/gluon jets, gives a good measurement of the energy of electrons and an indirect measurement of neutrino momentum. There are seven calorimeter systems in the detector (see Table 2.2) [51-53]. The central calorimetry has scintillator as the sampling medium in order to optimize energy resolution. In the plug and forward direction, gas proportional tubes were used for sampling in order to minimize the effects of radiation damage and allow very small segmentation. The central calorimeter systems are segmented into about 500 projective solid angle elements called "towers" and the plug and forward calorimeters have about $\sim$ 4800 towers. Each tower has an electromagnetic shower counter in front of a corresponding hadron calorimeter, so that a comparison of electromagnetic to hadronic energy can be made on a tower by tower basis.

The muon detection system [54] covers the central and forward rapidity regions (Table 2.3). The Central section (CMU) includes drift chambers outside the central hadron calorimetrers and measures the momentum of muons using the magnetic field of the solenoid. The Forward spectrometer (FUM) has magnetized iron toroids with chambers for identifying muons and measuring their momenta.

2.2 Geometric and Kinematic Detector Variables

Figure 2.3 shows a 1/4 side view of the central part of CDF, along with relavant geometrical and kinematic variables. The 'z-axis' is defined as being along the proton beam direction and 'R' is the radial distance from the beam. The right-handed coordinate system's y-axis is in the vertical (up) direction, and the polar angle 'θ' is defined as the angle of the particle with respect to the proton beam direction.

The "natural" kinematic variables for hadron collisions are rapidity, transverse momentum, and azimuthal angle [55]. The azimuthal angle, ϕ, is defined

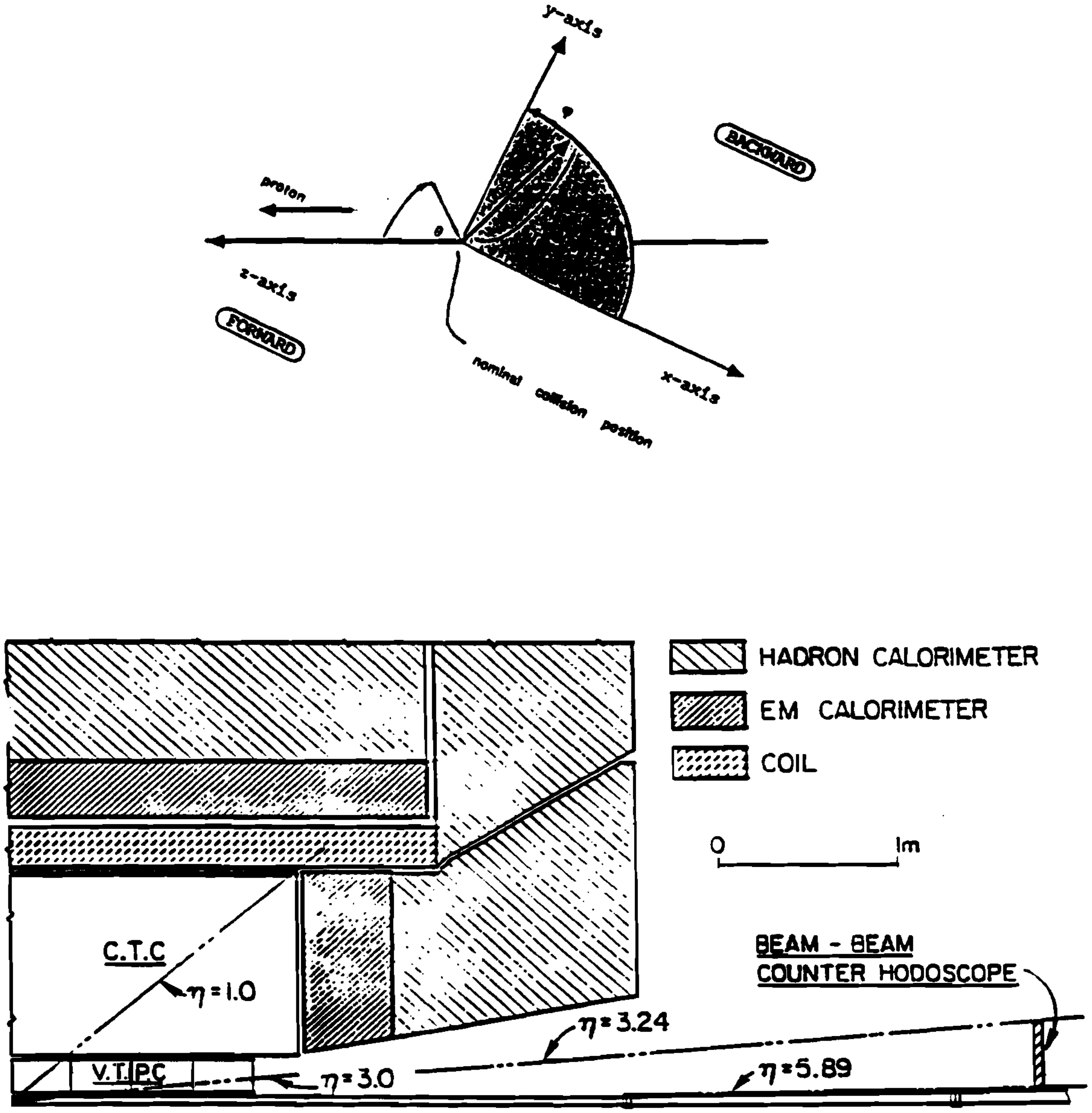

Figure 2.3 A side view of the CDF detector.

as

$$\phi = tan^{-1}(\frac{p_{\rm y}}{p_{\rm x}}),$$

and the transverse momentum, $p_{\rm T}$, is defined as

$$p_{\rm T} = \sqrt{p_{\rm x}^2 + p_{\rm y}^2}.$$

The transverse momentum and azimuthal angle are invariant to Lorentz transformations along the z-axis. The rapidity y is given by

$$y = \frac{1}{2}\ ln(\frac{{\rm E} + p_z}{{\rm E} - p_z}).$$

All three variables (ϕ , y and $p_{\rm T}$) have a simple Lorentz transformation. Hence the shapes of their distributions are invariant under Lorentz transformation.

In experiments where the produced particles are not identified and only the production angles of particles are measured, the variable pseudorapidity η is used instead of rapidity, where η is given by

$$\eta = \frac{1}{2} ln(\frac{p + p_z}{p - p_z}) = -ln(tan(\frac{\theta}{2})).$$

Pseudorapidity reduces to rapidity when the particle's momentum is much greater than the mass of the particle ($p \gg m$).

2.3 Beam-Beam Counters

The Beam-Beam Counters (BBC) [56] are two sets of scintillation counters which were used for triggering and as a luminosity monitor. They are located at ±5.82 m in the z-direction from the nominal interaction point, directly in front of the forward electromagnetic calorimeters. The BBC surround the beam pipe and cover the pseudorapidity range $3.24 < |\eta| < 5.89$ (Figure 2.4).

Each set has 16 counters, arranged in 4 rings of 4 counters each. The radii of the rings range from 3.3 to 47.0 cm. The counters have a measured time resolution of 200 psec, which enables them to determine the event vertex and event time with good precision.

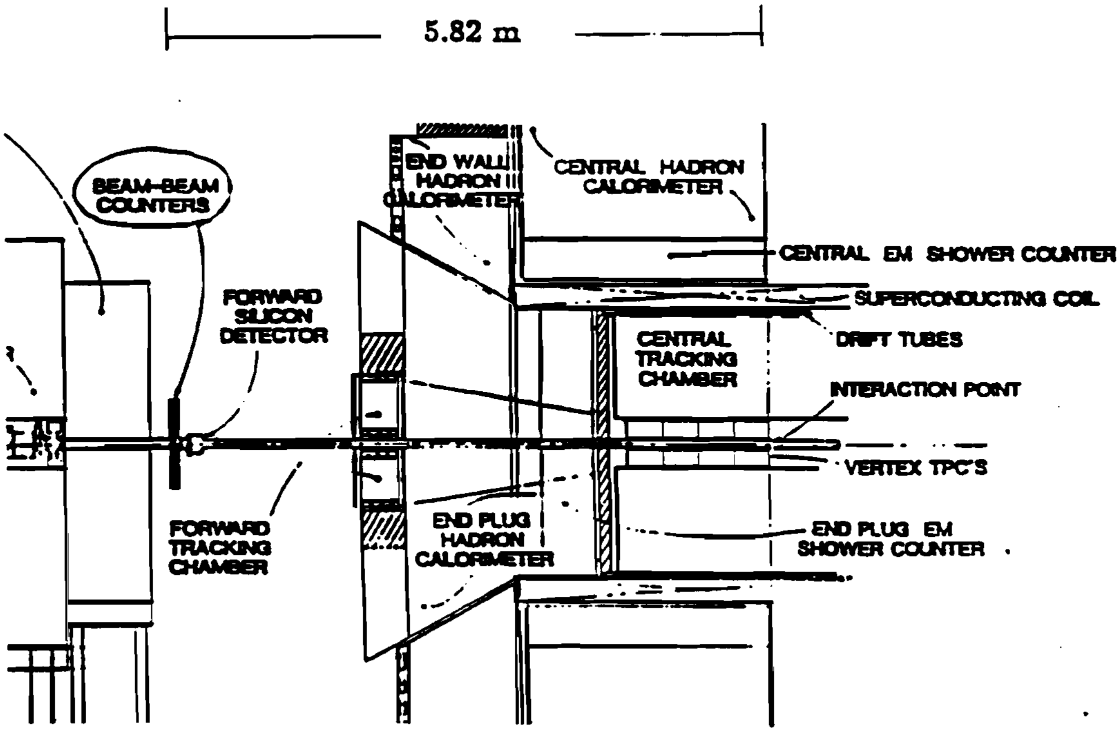

Figure 2.4 Location of the Beam-Beam Counters.

The requirement that at least one charged particle traverse each set of BBC in coincidence with the beam crossing, called the minimum bias trigger, is used in the trigger system to select beam-beam collisions and reject beam-gas interactions. The Beam-Beam Counters are also used as a luminosity monitor by assigning an estimated cross section of 44 mb at $\sqrt{s} = 1800$ GeV and 34.8 mb at 630 GeV for triggered minimum bias events.

2.4 Vertex Time Projection Chamber

The innermost tracking system, the Vertex Time Projection Chamber (VTPC) [57], is a set of eight time projection chamber modules which measure charged particle trajectories primarily in the R-z plane. It was used to determine the vertex position, the presence of multiple beam-beam interactions and the overall event topology. The VTPC modules are arranged along the beam pipe and centered around the collision point. Figure 2.5 is a schematic drawing of two octagonal VTPC modules. Each module has two 15 cm long drift regions separated by a center high voltage grid. The active area of the chamber extends from 6.8 cm to 21.4 cm in radius and the length in z of one module is approximately 35 cm. The VTPC contains a total of 3072 sense wires for the measurement of track coordinates in the R-z plane using Time-to-Digital Converters (TDC's), and 3072 pads for the measurement of coordinates in the R-ϕ plane using Flash Analogue-to-Digital Converters (FADC's). The total length of the chamber is 2.8 m which can assure adequate coverage of the event vertices which had a Gaussian distribution with a typical width (σ_z) of ≈ 40 cm.

All particles from $\bar{p}p$ interactions that are detected by the calorimeters and other tracking chambers first pass through the VTPC, so there was a considerable effort to minimize the mass of the VTPC to prevent problems such as a decrease in tracking accuracy due to multiple scattering and an increase in the conversion of photons from π^0 decay.

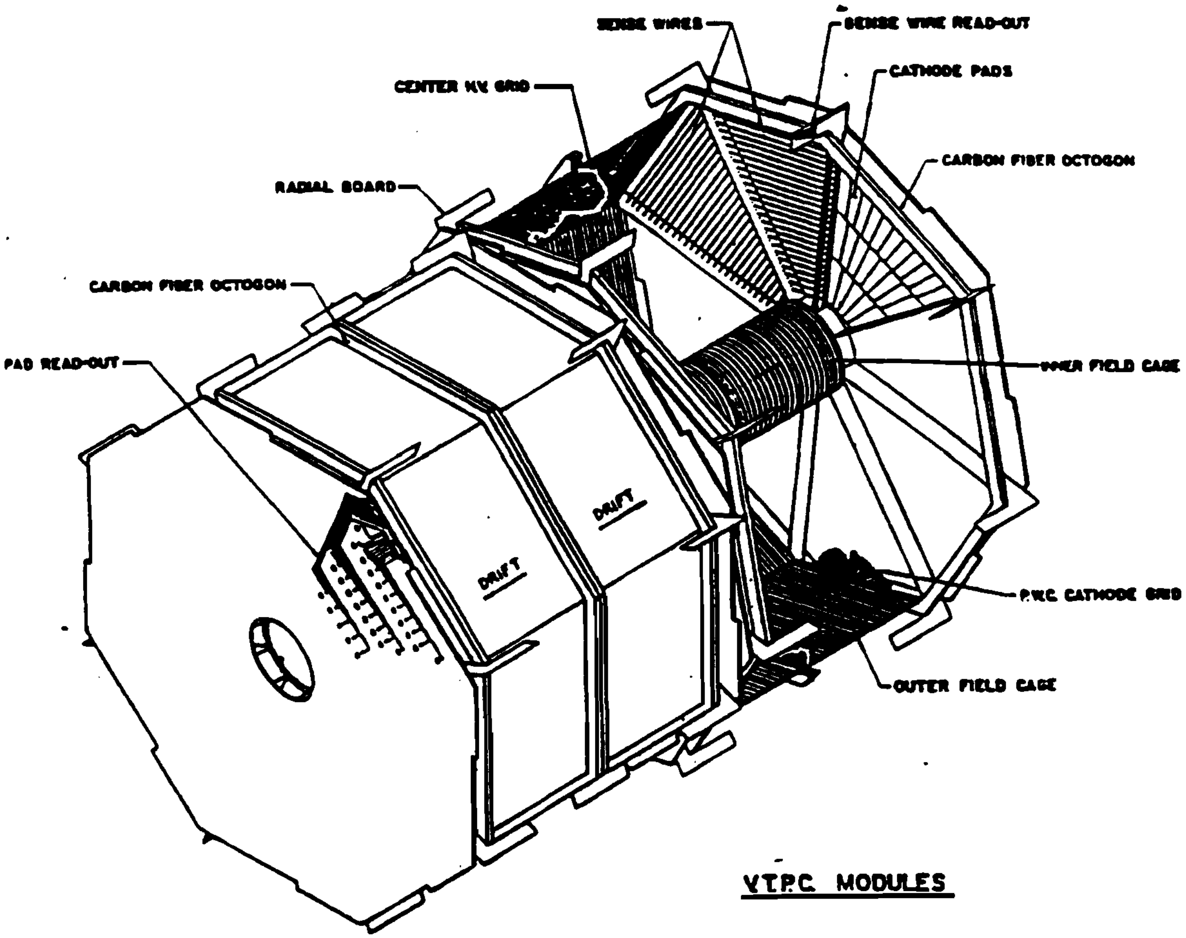

Figure 2.5 A schematic drawing of two VTPC modules.

R-z resolution varies depending on drift distance and track angle but can be characterized as being the order of $\sigma \sim 200$ μm (minimum drift) to 500 μm (15 cm drift) for tracks at $\theta = 90°$. The two hit separation in the R-z plane was about 6 mm and R-ϕ resolution was $\sigma \sim 300$ μm/cm of track length depending on the drift distance. The acceptance of the VTPC depends on the position of the interaction but typically extended to $|\eta| = 3.5$.

2.5 Central Tracking Chamber

The Central Tracking Chamber (CTC) [58] is a wire drift chamber used to measure the transverse momentum and determine the sign of charged particles in the central region ($30° < \theta < 150°$). Other functions of the CTC include
(1) intermediate angle ($10° < \theta < 30°,\ 150° < \theta < 170°$) tracking,
(2) the study of calorimeter response as a function of momentum, and the identification of energy directed at cracks in the calorimetry for events with large missing $\not{E}_{\mathrm{T}}$,
(3) measuring secondary vertices from the decays of long-lived particles, and
(4) identifying electrons and muons by combining its accurate momentum measurement with information from the calorimetry and muon chambers.

The CTC was constructed to operate efficiently at the original design luminosity of $10^{30}\mathrm{cm}^{-2}\mathrm{sec}^{-1}$, which is equivalent to an interaction rate of 50,000 events per second. In addition, the maximum drift time of a particle was required to be less than the beam crossing time for 6 bunches of 3.5 μsec. Since the CTC is completely enclosed by other detector components, reliability, redundancy, low power consumption, and remote calibration had to be considered.

The CTC is located in a 1.5 Tesla magnetic field provided by a superconducting solenoid aligned with the beam axis (Figure 2.3). It has 6156 sense wires spaced by 7 mm in the radial direction as a maximum drift distance of 35 mm. The length of the wires is 3.2 m and the innermost and outermost sense wire layers are located 30.9 cm and 132.0 cm from the beam axis, respectively. The 84 radially increasing sense wire layers are grouped into 5 axial "superlayers" and 4 stereo superlayers which alternate with the axial superlayers (Figure 2.6). Each axial superlayer contains 12 sense wire layers in parallel to the beam direction, and each stereo superlayer contains 6 sense wire layers at $\pm 3^\circ$ to the beam direction. Both axial and stereo superlayers are divided into cells (Figure. 2.7) so that the maximum drift distance is less than 40 mm, corresponding to about 800 nsec of drift time. In order to reduce dead space and linearize the time-to-distance relationship at the end of the cells caused by a large Lorentz angle, the cells (and thus the drift electric field) are tilted by $\approx 45^\circ$ with respect to the radial direction, so that in the presence of a magnetic field, the drift trajectories are approximately azimuthal.

The design goal for the position measurement accuracy is $\sigma < 200\mu\text{m}$ per wire, for the transverse momentum resolution is $\sigma p_\mathrm{T}/p_\mathrm{T}^2 \sim 0.001(\mathrm{GeV/c})^{-1}$, and for the average two hit resolution is 3.5 mm. The double track resolution is expected to be less than 5 mm (≈ 100 nsec). At the time of this analysis, the position measurement accuracy was $\sim 300\mu\text{m}$, dominated by uncertainties in the drift constants (Figure 2.8). Including multiple scattering effects, the resulting transverse momentum resolution was $\sigma p_\mathrm{T}/p_\mathrm{T}^2 < 0.003\ (\mathrm{GeV/c})^{-1}$ for $p_\mathrm{T} > 1$ GeV/c for primary tracks that pass through all superlayers.

Figure 2.9 is a block diagram of the CTC Data Acquisition (DAQ) electronics for a single sense wire. Each sense wire is connected to a preamplifier mounted directly on the endplate of the chamber. The function of the preamplifier card is to provide fast, low noise amplification of the signals from the sense wires and to eliminate wire to wire cross talk caused by slow motion of positive ions. The output signal for a minimum ionizing particle at $\theta = 90^\circ$ has a rise time of about 8 nsec, an amplitude of about 40 mV and a RC decay time constant of approximately 40 nsec (Figure 2.10). The baseline to baseline width of a typical signal is 250 nsec. This analog signal is transmitted through miniature 56 Ω coaxial cables to an intermediate circuit known as the Amplifier-Shaper-Discriminator (ASD) which shapes the pulse, amplifies it and produces a time over threshold logic signal. This circuit is mounted on the magnet yoke, and provides an auxiliary analog output for each sense wire. The input signal to the ASD is filtered and amplified by a factor of 20. The net voltage gain after the filter and amplification is typically a factor of 5. Then a high speed comparator used as a discriminator produces a differential ECL pulse whose width, typically < 90 nsec, is equal to the time over threshold of the input signal. These ASD discriminated signals are fed to multiple hit FASTBUS Time-to-Digital-Converters (TDC's). In order not to affect the resolution of the chamber, the TDC must have a time resolution of better than 1 nsec, a range of about 1 μsec, and be capable of recording at least 8 hits per wire per event. To meet this specification, Lecroy 1879 FASTBUS TDC's were used. The TDC's are connected to the ASD's on the magnet yoke via 70 m of flat ribbon cable. The TDC's in each FASTBUS crate are read out by a modified version of the SLAC Scanner Processor (SSP) [59]. In addition, the SSP sorts the TDC data by wire number and time, and associates leading and trailing edge hits. The reformatted data from the SSP's is then read by the host VAX. In a typical $\bar{p}p$ event, about 5500 words (1 word per hit) are read from the TDC's.

Calibration of the CTC

The total time delays coming from the interconnections between the CDF master clock system and the TDC system must be known in order to calibrate individual channels. To measure these time delays, the calibration system has a calibration card, a gate generator, a LeCroy 1810 Calibration-And-Timing (CAT) FASTBUS module, and a LeCroy 4222 programmable delay time generator. The general layout of the Data Acquisition system and the calibration system for the CTC are shown in Figure 2.11.

Table 2.4 The CTC design specification.

Number of Layers:	84
Number of Superlayers:	9
Number of Super Cells/Layer:	30, 42, 48, 60, 72, 84, 96, 108, 120
Total Number of Wires:	36,504
Wire Length:	3214.0 mm
Stereo Angle:	$\pm 3^\circ$
Radius at Intermost Sense Wire:	309 mm
Radius at Outermost Sense Wire:	1320 mm
Sense Wire Spacing:	10 mm in plane of wires
Maximum Drift Distance:	40 mm
Maximum Hits Per Wire:	> 7
Gas:	Argon-Ethane-Alcohol (49.6:49.6:0.8)%
Drift Field (E_o):	~1350 V/cm
Drift Field Uniformity:	dE_o/E_o ~1.5% (rms)
Gain:	3×10^4 (250 nsec gate)
Efficiency:	> 0.98 per point
Resolution:	$< 200\mu m$ per wire
Z Resolution:	$< 0.200 mm/(\sin 3^\circ) = 4$ mm
Double Track Resolution:	< 5 mm or 100 nsec
Momentum Resolution:	$\sigma p_T/p_T^2 < 0.001$ GeV/c at $\theta = 90^\circ$

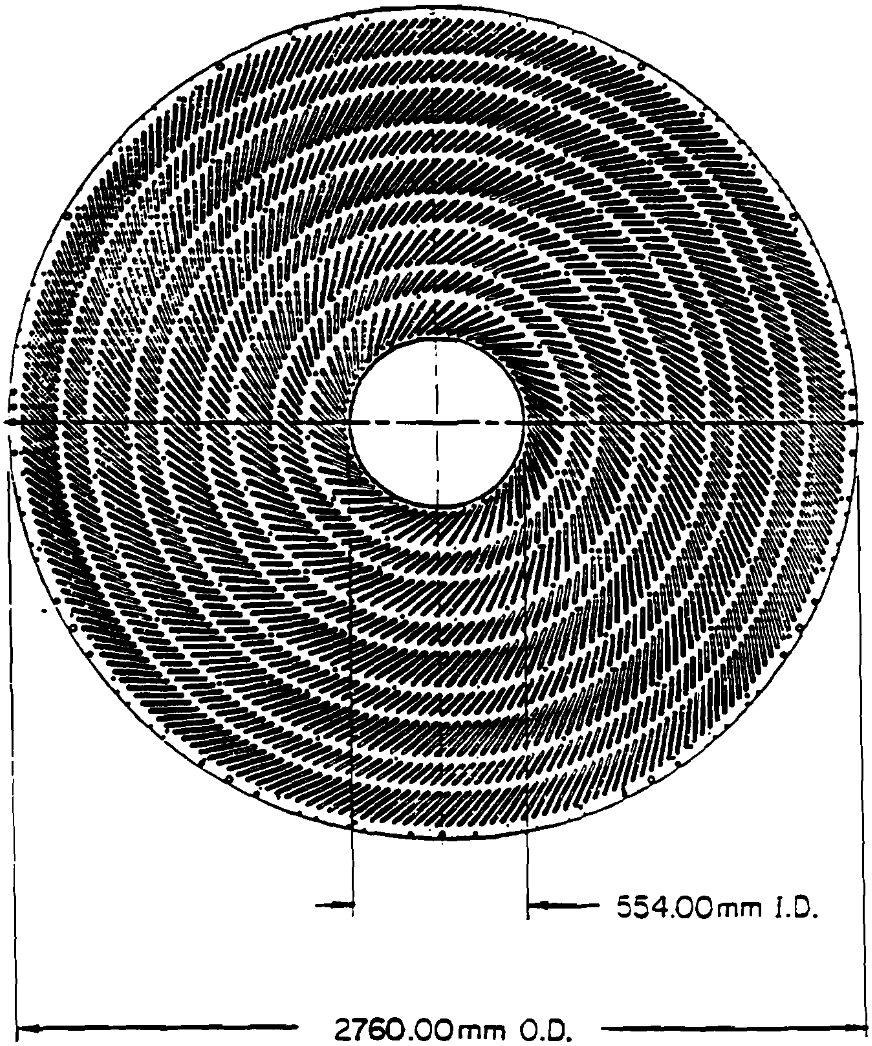

Figure 2.6 A schematic drawing of the CTC's end plate.

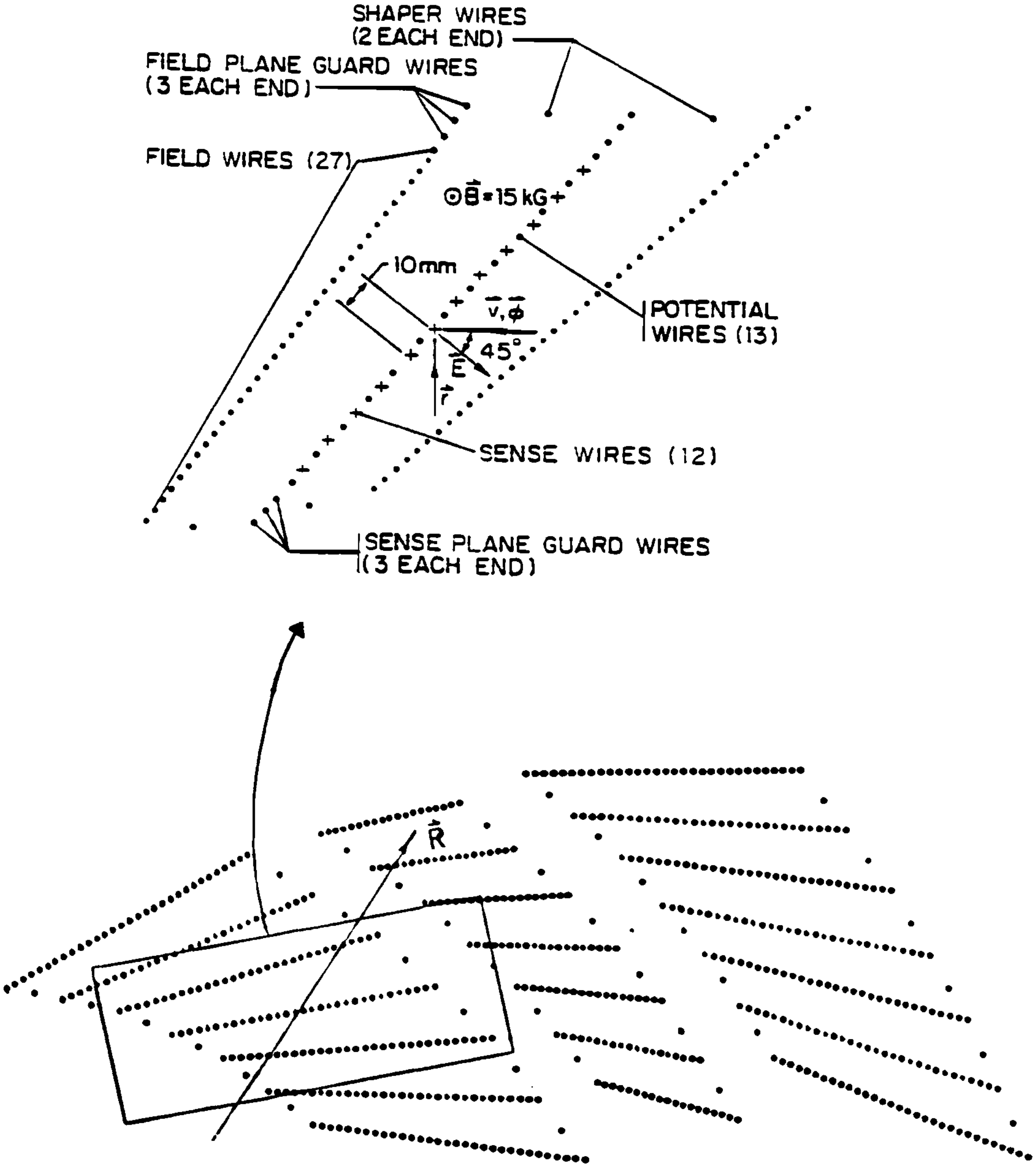

Figure 2.7 Wire geometry for a super cell in the CTC.

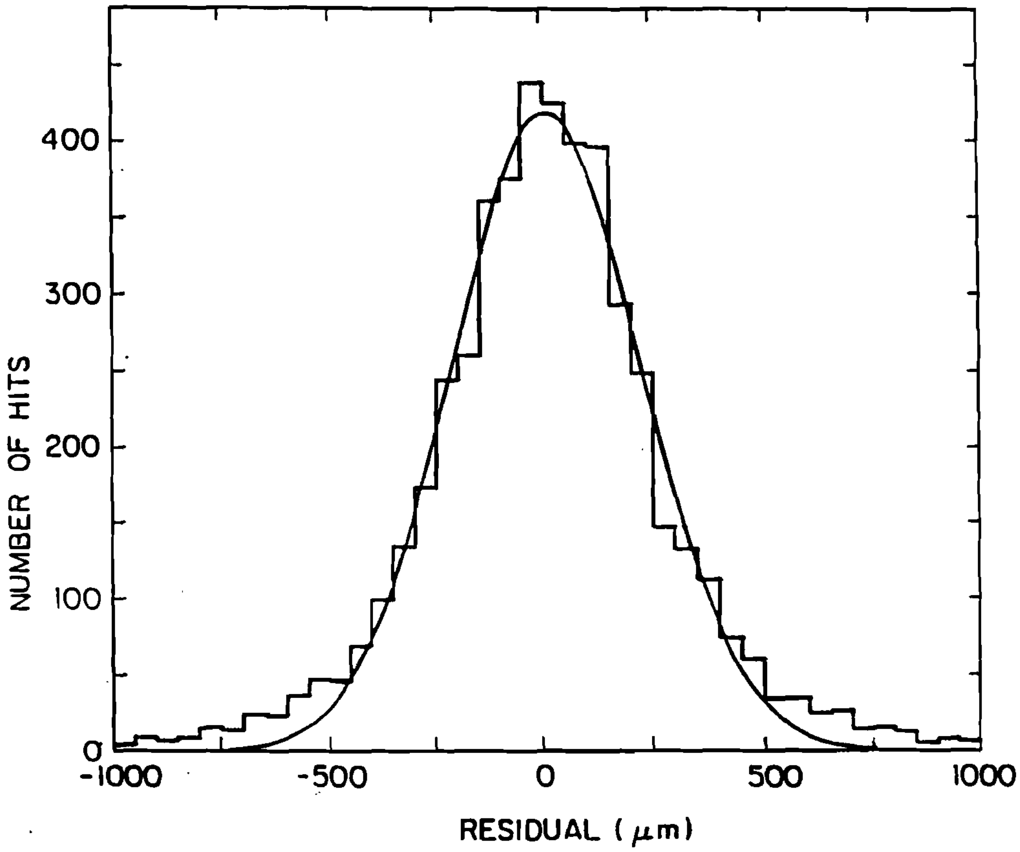

Figure 2.8 Position resolution of the CTC.

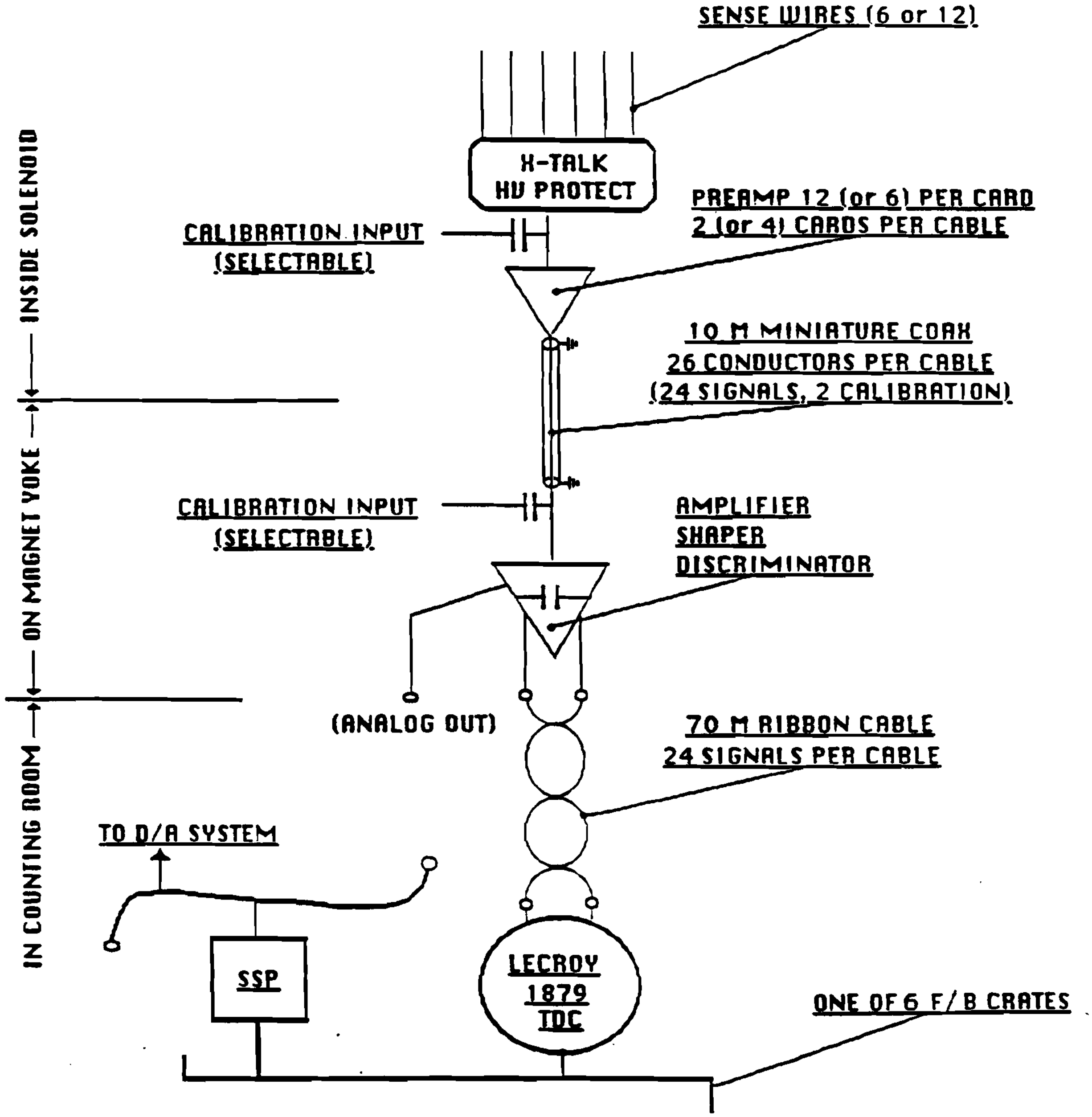

Figure 2.9 DAQ system for a single wire in the CTC.

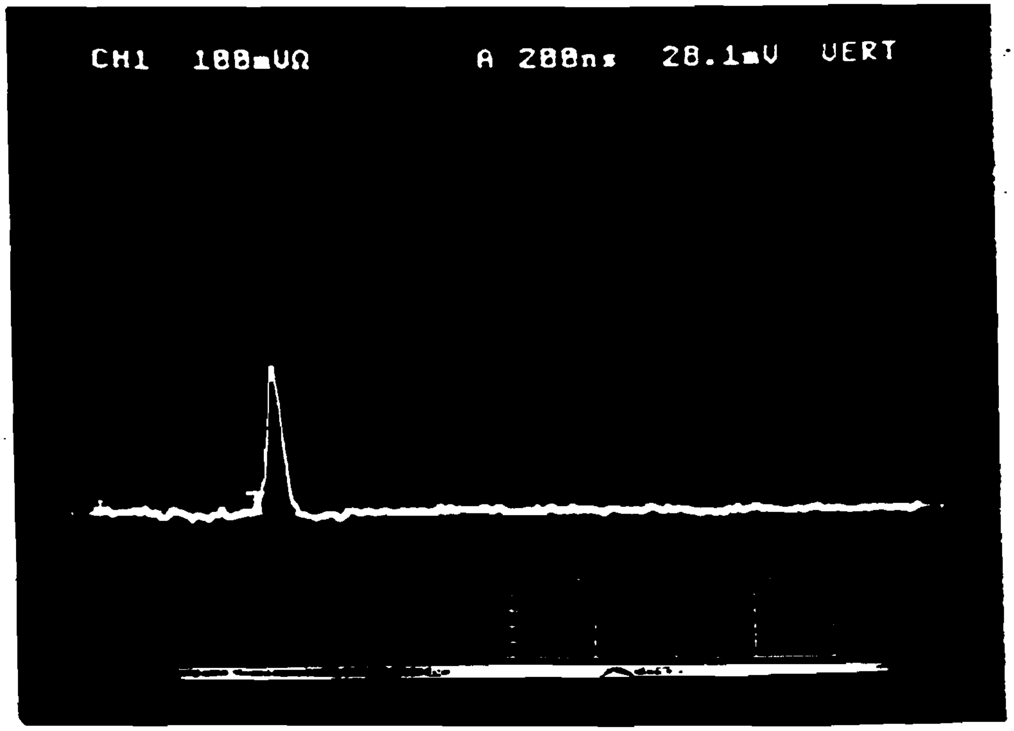

Figure 2.10 A typical output pulse from the Pre-Amp.

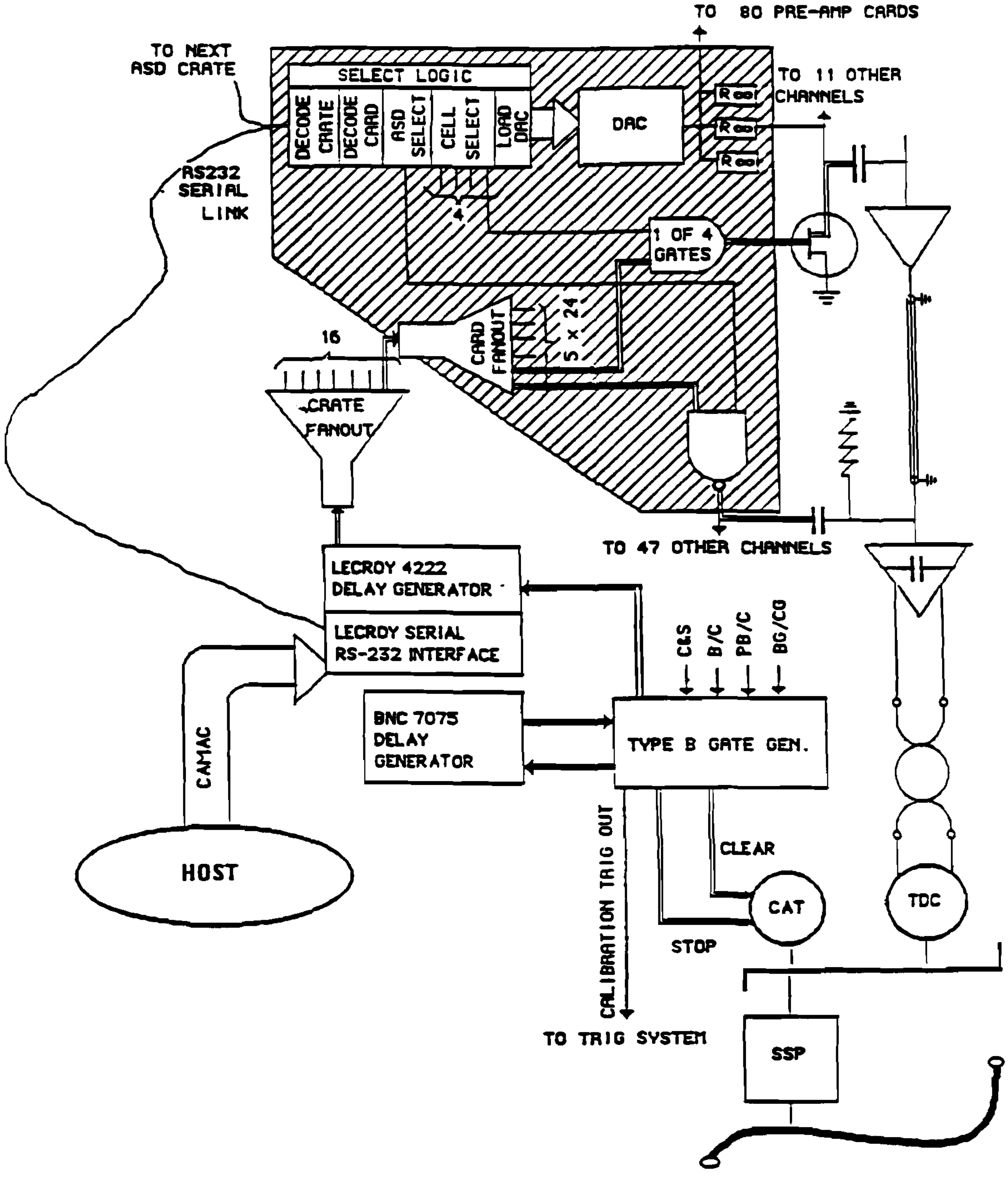

Figure 2.11 DAQ and calibration system of the CTC.

Timing signals [60] from the master clock system are processed in the custom built gate generator to produce the clear and stop pulses needed by the TDC. They are fanned out to the individual TDC cards in a crate by a CAT module, which drives these signals onto the FASTBUS backplane. The calibration signals at the preamplifier or ASD inputs are generated by a programmable delay time generator, controlled via CAMAC. The calibration card decodes the information down-loaded from the DAQ system and fans-out the calibration signals to the selected ASD cards or Pre-Amplifiers.

Calibration of the chamber is initiated by a process in the host VAX. For selected channels, the particular calibration test pulse (CAT, ASD or Pre-Amplifier), and the amplitude of the pulse to be input to the Pre-Amplifier were chosen. The host VAX downloads the first delay time into the programmable delay generator and the channel and pulse height information into the calibration modules. A number of events, typically 50, are taken. For these events, the SSP accumulates summary information including the average leading edge time and associated variance, the average pulse width, the number of TDC hits per event, and the fraction of events with data. This summary data is read from the SSP by the host VAX, and the process is repeated for a number of different delay settings. When data from all delay settings has been read, a linear fit is made to the average observed TDC time versus delay setting for each channel, giving a slope and an offset time. These are compared to an expected range of values, and bad channels flagged. This information is recorded in a database and the offset information is then used by the offline reconstruction program to correct the raw TDC data prior to pattern recognition.

2.6 Central Calorimetry

The central calorimeter consists of 48 wedged-shapes modules. Because of the importance of jets in high energy $\bar{p}p$ collisions, a projective tower geometry was chosen with the tower being 0.1 units in η and 15° in ϕ. Each tower has an electromagmetic shower counter in front of a corresponding hadron calorimeter to make a comparison of electromagnetic to hadronic energy on a tower by tower basis.

Central Electromagnetic Calorimeter

The Central Electromagnetic Calorimeters (CEM) [51] are a combination of shower counters and strip chambers to measure energy and shower position of electrons and photons. The CEM cover the angular region $|\eta| < 1.1$ and 2π in ϕ with the strip chambers located at shower maximum. Each wedge contains 10 towers as shown in Figure 2.12 with the shower counter and the strip chamber.

The shower counters use 30, 3.2 cm thick, layers of lead sheets as absorbers interspersed with 5 mm thick plastic scintillators as the active detector medium. This corresponds to a total of 20 radiation lengths and 1.1 absorption lengths at $\eta = 0$. Each tower is read out at each extreme end in ϕ. The light from the scintillator is shifted in wavelength and taken to two phototubes by light guides. This collected light is converted to electrons at the photomultiplier tubes with a gain of about 10^6. The difference in signal pulse height from the two phototubes allows the ϕ-position to be determined to an accuracy (σ) of $5°$. The energy resolution of the CEM was measured to be $14/\sqrt{E}$ %, with E in GeV.

The strip chambers are proportional chambers located at a depth of 6 radiation lengths in the shower counters. They measure an accurate shower position for the separation of photons from π^0 decays. The strip chambers have 128 strips and 64 wires and a position resolution of 2 mm in R-ϕ.

Central and Endwall Hadron Calorimeters

In order to measure the energy of charged and neutral hadrons (mainly charged pions, kaons and protons along with the long lived neutral hadrons) in the central region, two hadron calorimeter systems were used. The Central

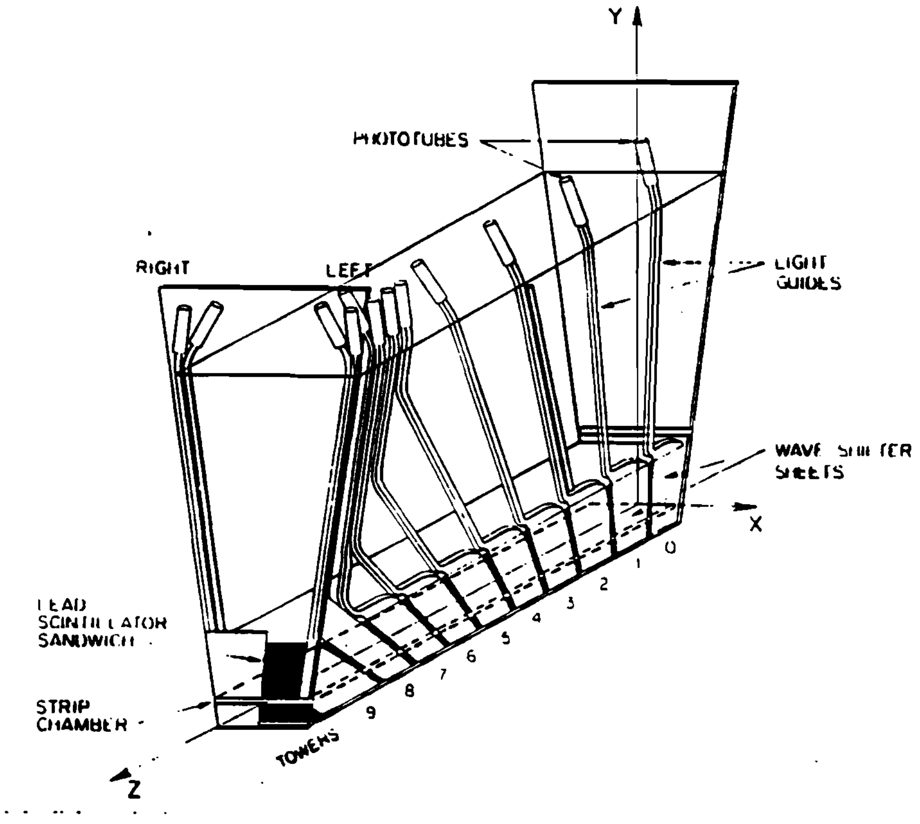

Figure 2.12 A wedge of the central calorimeter.

(A) CEM & CHA
(B) WHA
(C) PEM & PHA

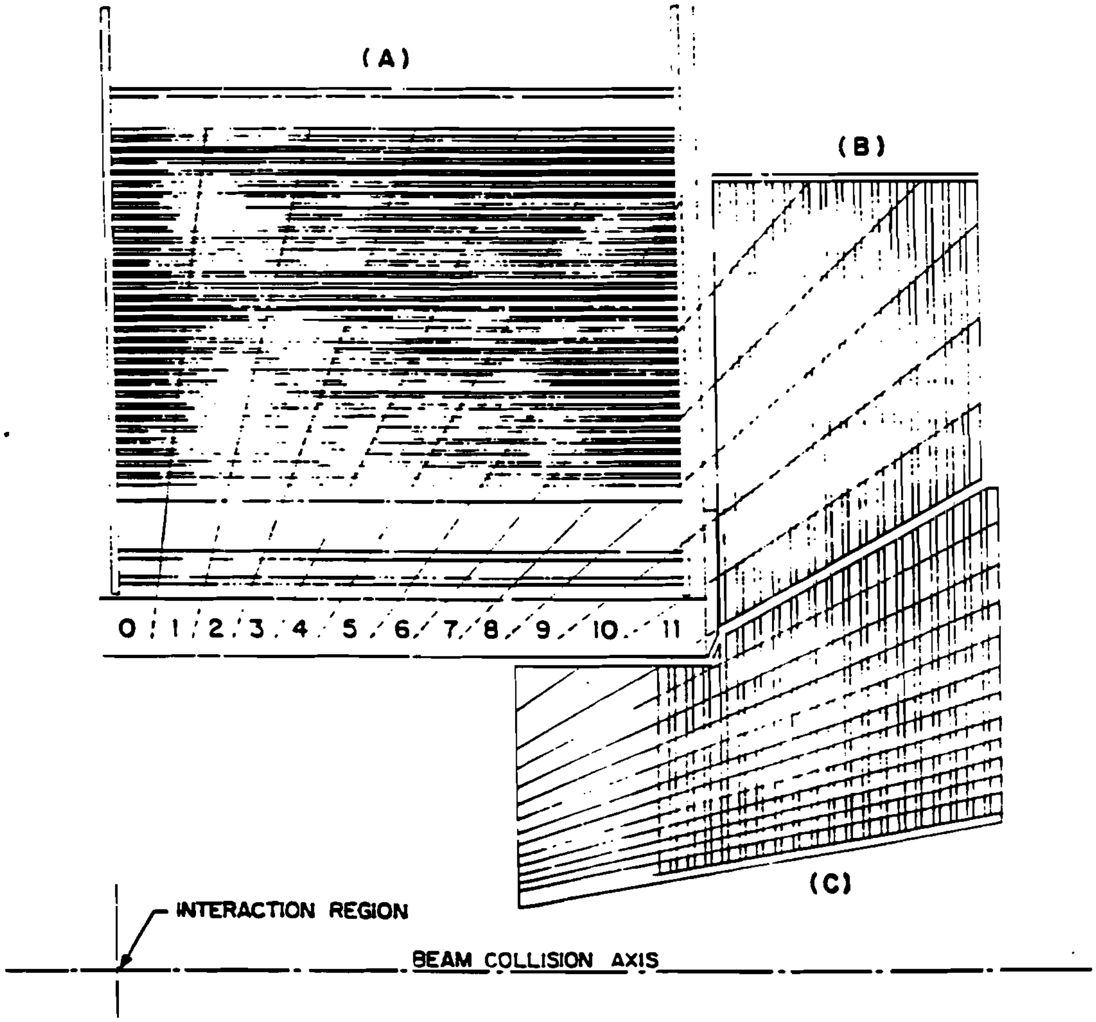

Figure 2.13 The position of the central and endwall calorimeters.

Hadron Calorimeters (CHA) [52] cover 2π in ϕ and $|\eta| < 0.9$, and the Endwall Hadron Calorimeters (WHA) [52] overlap the CHA slightly and cover $0.7 < |\eta| < 1.3$ and 2π in ϕ. Figure 2.13 shows the position of the central and endwall hadron calorimeters.

The CHA contains 32 layers of 2.5 cm thick steel plates alternated with 1 cm thick plastic scintillator sheets, giving altogether 4 absorption lengths. A wedge has 8 towers and the light from each tower is collected at both ϕ boundries and routed to phototubes.

Hadrons shower in the steel produce charged particles, and these charged particles produce blue light in the scintillator. This light is shifted in wavelength and trapped in wavelength shifting fingers and then carried to photomultiplier tubes by light guides. If the primary interaction occurs in the hadron calorimeter, the energy resolution is $70/\sqrt{\mathrm{E}}$ % up to $\mathrm{E} = 50$ GeV, and becomes constant at 10 % for 50 GeV $< \mathrm{E} <$ 150 GeV. If the primary interaction occurs in the EM shower counters, the resolution is $65/\sqrt{\mathrm{E}}$ % up to $\mathrm{E} = 80$ GeV, and becomes constant at 8 % for 80 GeV $< \mathrm{E} <$ 150 GeV.

The WHA are constructed in a similar manners to the CHA, but with reduced sampling. The endwalls have 15 steel plates, each 5.1 cm thick, and a 1 cm scintillator sheet between each pair of plates. The resolution of the WHA was measured to be 14 % at $\mathrm{E} = 50$ GeV.

Calibration of CEM, CHA and WHA

The calibration of each central calorimeter wedge was determined using cosmic ray muons [62] and with test beams of various energy electrons and pions [61]. As a monitor for long term gain variations, the response to a Cs(137) gamma source [63] is recorded periodically during data taking. The source is driven along one layer of scintillator, and the peak current is measured for each tower.

Short term phototube gain changes are also monitored by light flasher systems [63]. The CEM phototube gains are monitored by a xenon flasher and a Light-Emitting-Diode (LED) flasher system, and for the CHA, a nitrogen laser is pulsed electrically and the light is carried to the phototubes by quartz fibers.

CHAPTER 3 - MINIMUM BIAS DATA

This analysis used minimum bias data at $\sqrt{s} = 1800$ GeV and 630 GeV from the first physics run of CDF, which occured between January and May of 1987. The raw data were carefully checked for hardware problems and the criteria for selecting events and the efficiency to reject beam-gas interactions have been studied. Since there are no direct measurements of absolute cross sections at $\sqrt{s} = 1800$ and 630 GeV, they were estimated from cross section measurements at $\sqrt{s} = 200$, 546 and 900 GeV by the UA4 experiment [33,34]. Monte Carlo studies of the acceptance efficiencies of the BBC trigger and event selection were then used to estimate the effective cross sections (σ_{eff}) of the selected events at $\sqrt{s} = 1800$ and 630 GeV.

3.1 Raw Data

The name "Minimum Bias physics" comes from the characteristics of the event trigger used at the collider to obtain the data. Depending on the configuration of the interaction process, the total cross section can be broken into Non-Diffractive (ND), Single-Diffractive (SD), Double-Diffractive (DD) and elastic components [64] (see Figure 3.1). In order to have a high probability to record an event each time an inelastice, non-diffractive interaction takes place, the trigger must have very little bias so that the data recorded represents most of the inelastice, non-diffractive cross section.

Acceptance efficiency of the minimum bias trigger

In CDF, the minimum bias data were collected with a trigger (minimum bias trigger) which required that at least one charged particle traverse each set

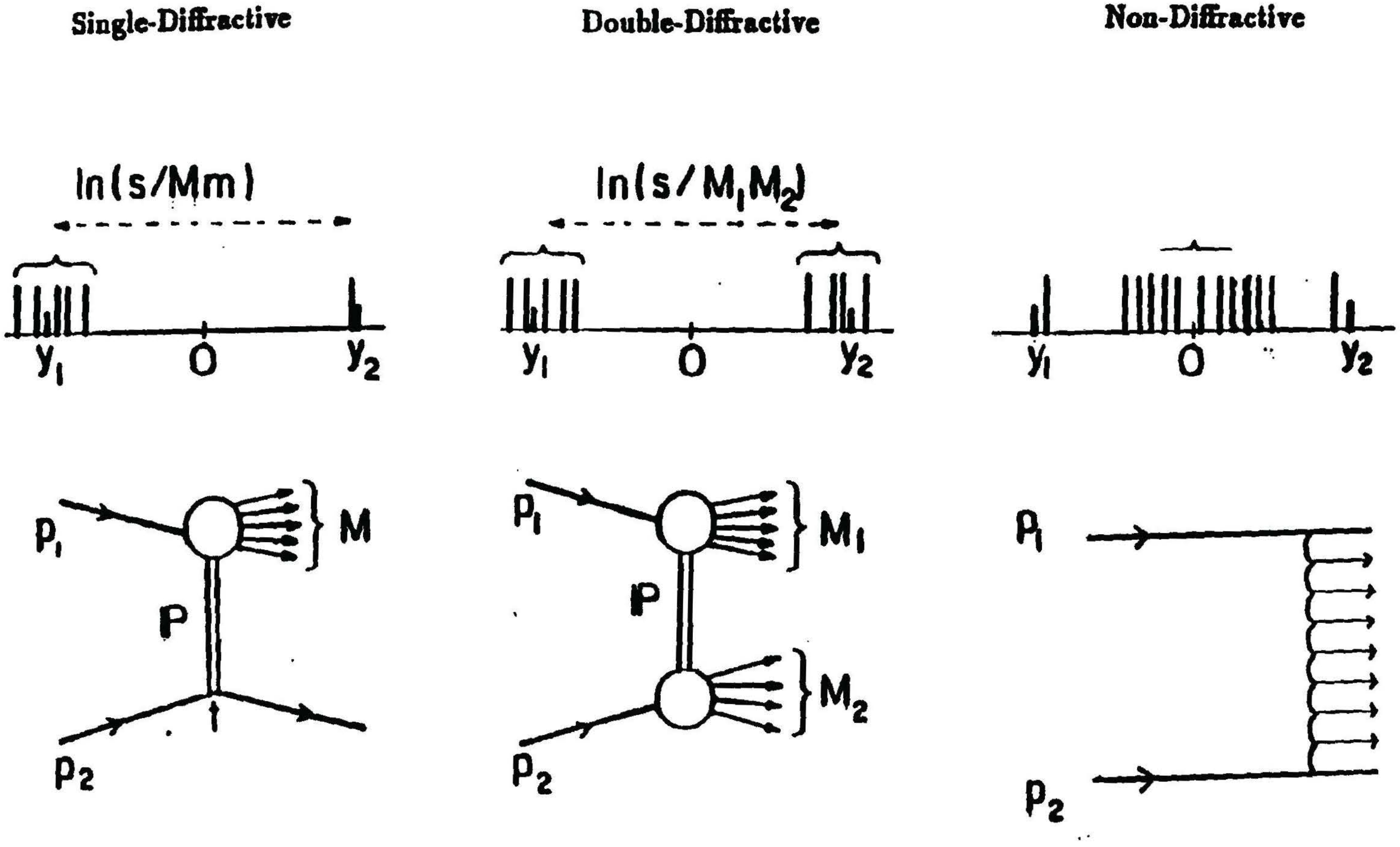

Single-Diffractive

Double-Diffractive

Non-Diffractive

Figure 3.1 Different event types for inelastic collisions.

of the BBC in coincidence with the beam crossing. With this trigger requirement, each set of the BBC had an average of 13 hits (charged particles) per event. The collected event sample is a mixture of ND, SD and DD interactions from beam-beam collision, along with a small contamination from beam-gas interactions (Figure 3.2).

The average acceptance of the minimum bias trigger for each type of beam-beam interaction was determined by a Monte Carlo simulation. Two thousand events of each type were generated using the Rockfeller minimum bias generator, and detector and trigger simulations were performed. For $\sqrt{s}$ = 1800 GeV, 96.2 % of ND, 16.6 % of SD and 70.9 % of DD events triggered the BBC (Table 3.1). The trigger efficiencies at 630 GeV are summarized in Table 3.2.

Estimation of BBC cross section

Since there is no direct measurement of the absolute beam-beam collision cross sections at $\sqrt{s}$ = 1800 and 630 GeV, the effective cross sections corresponding to the events which pass the minimum bias trigger ($\sigma_{\rm BBC}$) were estimated using cross section measurements from the UA4 experiment [33] in combination with the acceptance efficiencies of the trigger. By interpolation of the measured cross sections at $\sqrt{s}$ = 200, 546 and 900 GeV, cross sections for ND, SD, DD interactions and the total cross section at $\sqrt{s}$ = 630 GeV were estimated (Table 3.1). Using predicted values for the total cross section at 1800 GeV [65] and extrapolating the measured cross sections, cross sections for each type of interaction were derived and are listed in Table 3.2. The $\sigma_{\rm BBC}$ are 44±6 mb at 1800 GeV and 34.8±3.5 mb at 630 GeV.

The data analysed here are based on a sample of 55,700 minimum bias triggers at 1800 GeV and 9,400 minimum bias triggers at 630 GeV. The instantaneous luminosity ranged from 2×10^{27} to $4 \times 10^{28} \mathrm{cm}^{-2}\mathrm{s}^{-1}$ at 1800 GeV and was $\sim 7 \times 10^{26} \mathrm{cm}^{-2}\mathrm{s}^{-1}$ during the single 630 GeV run.

Table 3.1 The minimum bias trigger acceptance at $\sqrt{s} = 1800$ GeV.

type of interaction	estimated σ (mb)	trigger acceptance efficiency	trigger σ (mb)
total (σ_{total})	77±6		
elastic (σ_{el})	17.6±1.6		
ND (σ_{ND})	40.2±6.9	0.962	38.7±6.6
SD (σ_{SD})	15.0±5.0	0.166	2.5±0.8
DD (σ_{DD})	4.2±1.0	0.709	3.0±0.7
σ_{BBC}			44±6

Table 3.2 The minimum bias trigger acceptance at $\sqrt{s} = 630$ GeV.

type of interaction	estimated σ (mb)	trigger acceptance efficiency	trigger σ (mb)
total (σ_{total})	59.1±1.5		
elastic (σ_{el})	12.7±1.1		
ND (σ_{ND})	33.9±3.7	0.938	31.76±3.47
SD (σ_{SD})	10.0±0.7	0.116	1.16±0.08
DD (σ_{DD})	2.5±0.6	0.750	1.88±0.45
σ_{BBC}			34.8±3.5

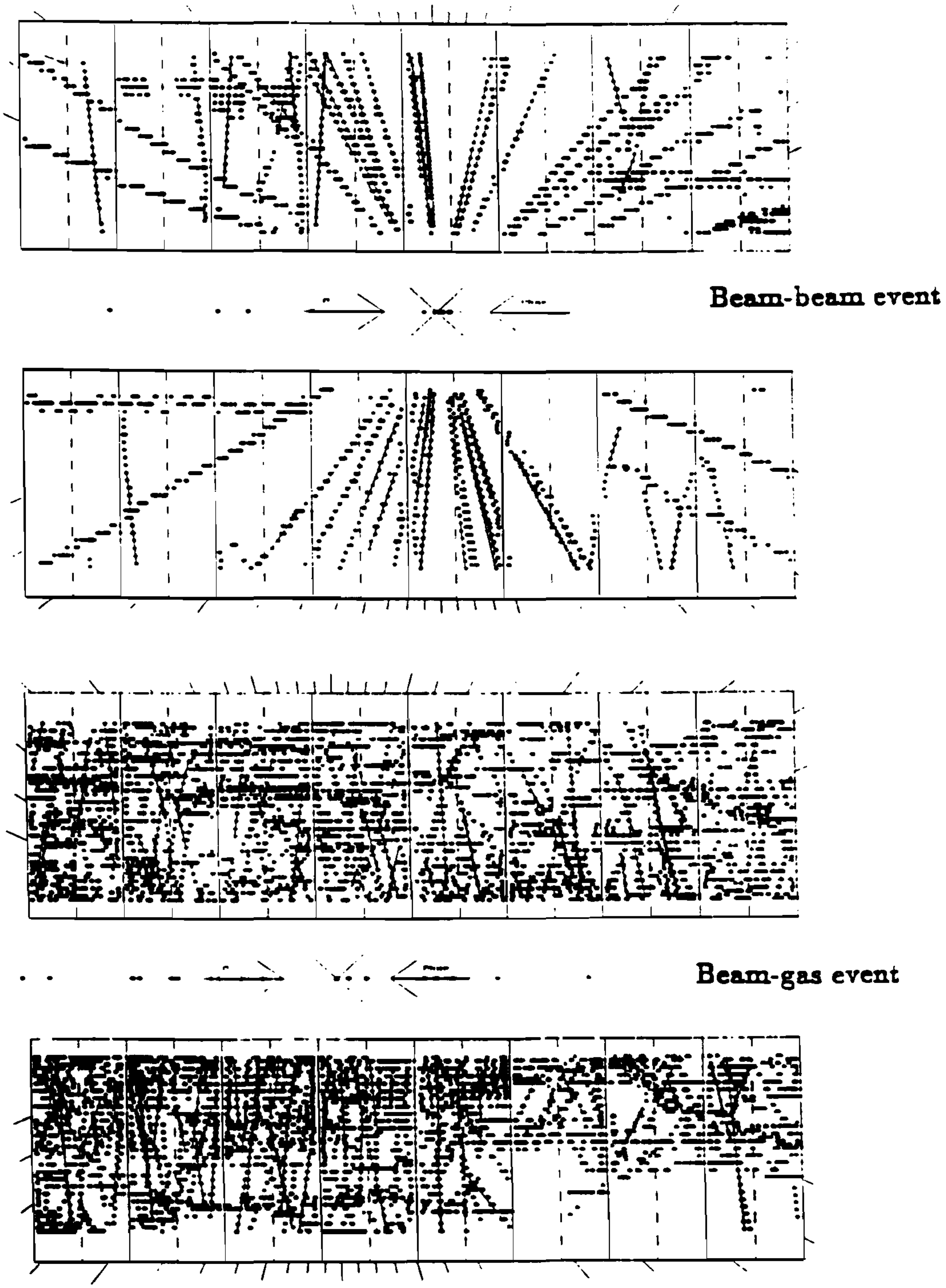

Figure 3.2 Typical beam-beam and beam-gas event in the VTPC.

3.2 Event Selection

The main goal of the event selection was to remove the contamination of beam-gas (and/or "beam-wall") interactions. Also, since the beam-beam data set is a mixture of the ND, SD and DD interactions, which have different event configurations, the selection criteria were optimized to remove the diffractive interactions and maximize the fraction of ND interactions for the study of central production. In addition, due to the $\sim$ 1 m long interaction region in the z-coordinate, the geometrical acceptance of the central detector varied depending on the event vertex position (z_{VTX}). Therefore, the event selection was a function of z_{VTX}, as reconstructed by the BBC and the VTPC.

Calculation of the event vertex

The event vertex was calculated by the VTPC or the BBC. In the VTPC, segments of tracks were found in each octant by reqiring at least 3 consecutive TDC hits. Then the straight lines were extended from each track segment to form a interaction point of the collision on the z-axis. If no VTPC segments were found, BBC time of flight information was used to calculate the event vertex position. The distribution of collision vertices along the beam axis was Gaussian with a typical σ of 40 cm (Figure 3.3). An event vertex calculated by the BBC agreed within measurement errors with the much more accurate VTPC reconstruction (see Figure 3.3).

Track selection in the VTPC

Charged particles with $p_T \geq 50$ MeV/c were measured in the VTPC with high efficiency for $|\eta| \leq 3$ [66]. For this analysis, VTPC tracks were required to traverse more than 11 wires out of 24 and have impact parameters within 5σ of the event vertex in order to reject non primary particles. The

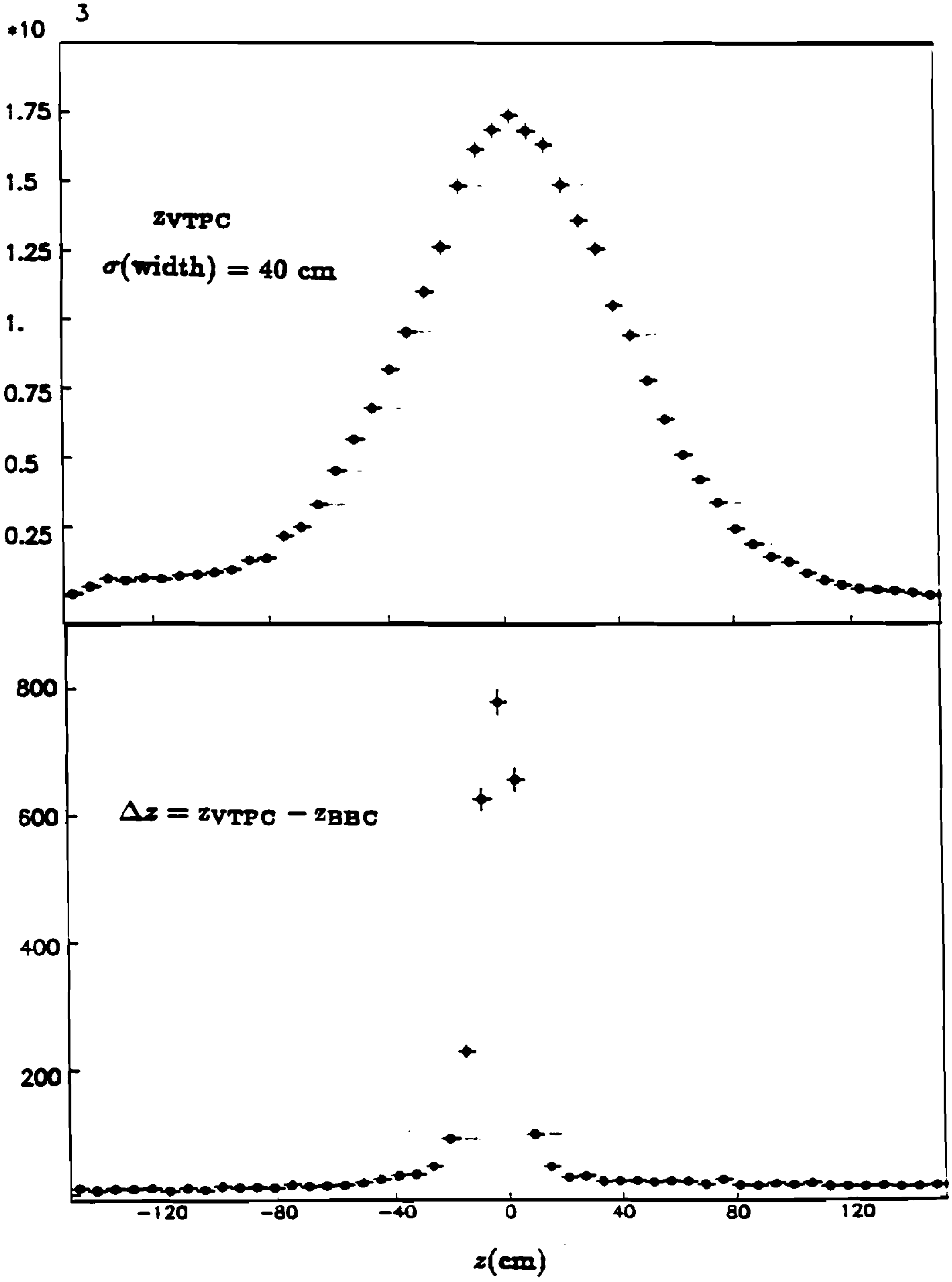

Figure 3.3 Distributions of z_{VTPC} and $z_{VTPC} - z_{BBC}$.

effects of reconstruction efficiency, decays of strange particles, γ conversions, and secondary hadronic interactions are still under study. The preliminary results show that the total corrections to the number of primary tracks will be between 5 and 10 %.

Event selection criteria

Based on the analysed data from VTPC and BBC, as discussed above, the following selection criteria were established.

(1) To reject beam-gas interactions, the position of the interaction derived from the VTPC was required to agree with that determined from the BBC timing information within 16 cm.

(2) To remove beam-gas and diffractive interactions, events with no charged particle in one of the ranges $-3 < \eta < 0$ or $0 < \eta < 3$ were rejected.

(3) To remove diffractive interactions, only events with at least 4 charged particles in the range $0 < |\eta| < 3$ were used.

(4) To ensure full acceptance of the VTPC down to $|\eta| = 3$, events originating at $|z| > 65$ cm were rejected.

About 44,300 out of 55,700 triggers at $\sqrt{s} = 1800$ GeV passed these selection criteria. For the data sample at 630 GeV, due to low luminosity and one empty antiproton bunch (see the next section for more discussion), 5,600 triggers were rejected from the total of 9,400. Figure 3.4 - Figure 3.6 shows the vertex distributions, number of hits in each set of the BBC and number of tracks seen by the VTPC in $|\eta| < 3.0$ for the selected and rejected events at $\sqrt{s} = 1800$ GeV.

3.3 Efficiency of Event Selection

During the 1987 run, the Tevatron was operated with 3 bunches of protons and antiprotons. On the average, there were 5×10^{10} protons and 1×10^{10} antiprotons in each bunch with a typical beam size of $\sigma = 0.75$ mm at the

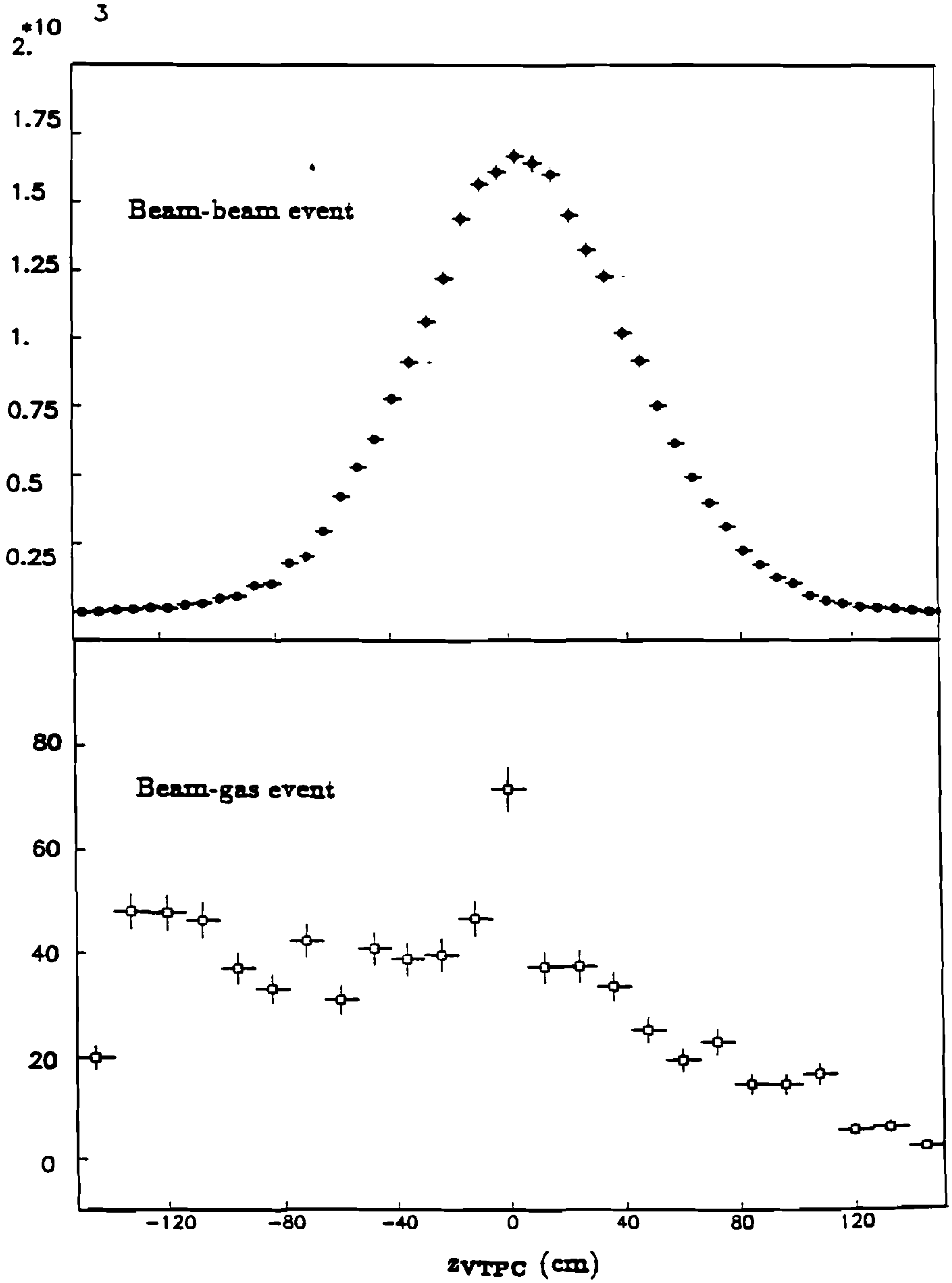

Figure 3.4 The vertex distributions from the VTPC.

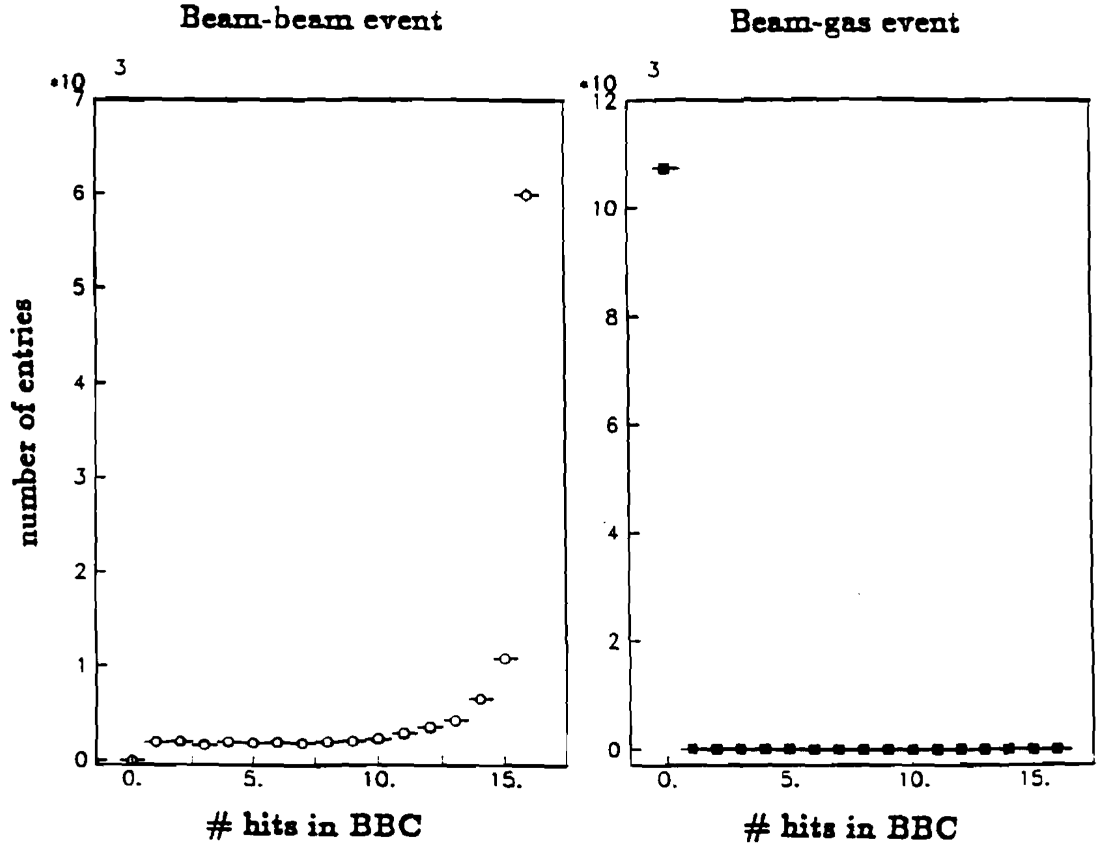

Figure 3.5 The number of hits in the BBC.

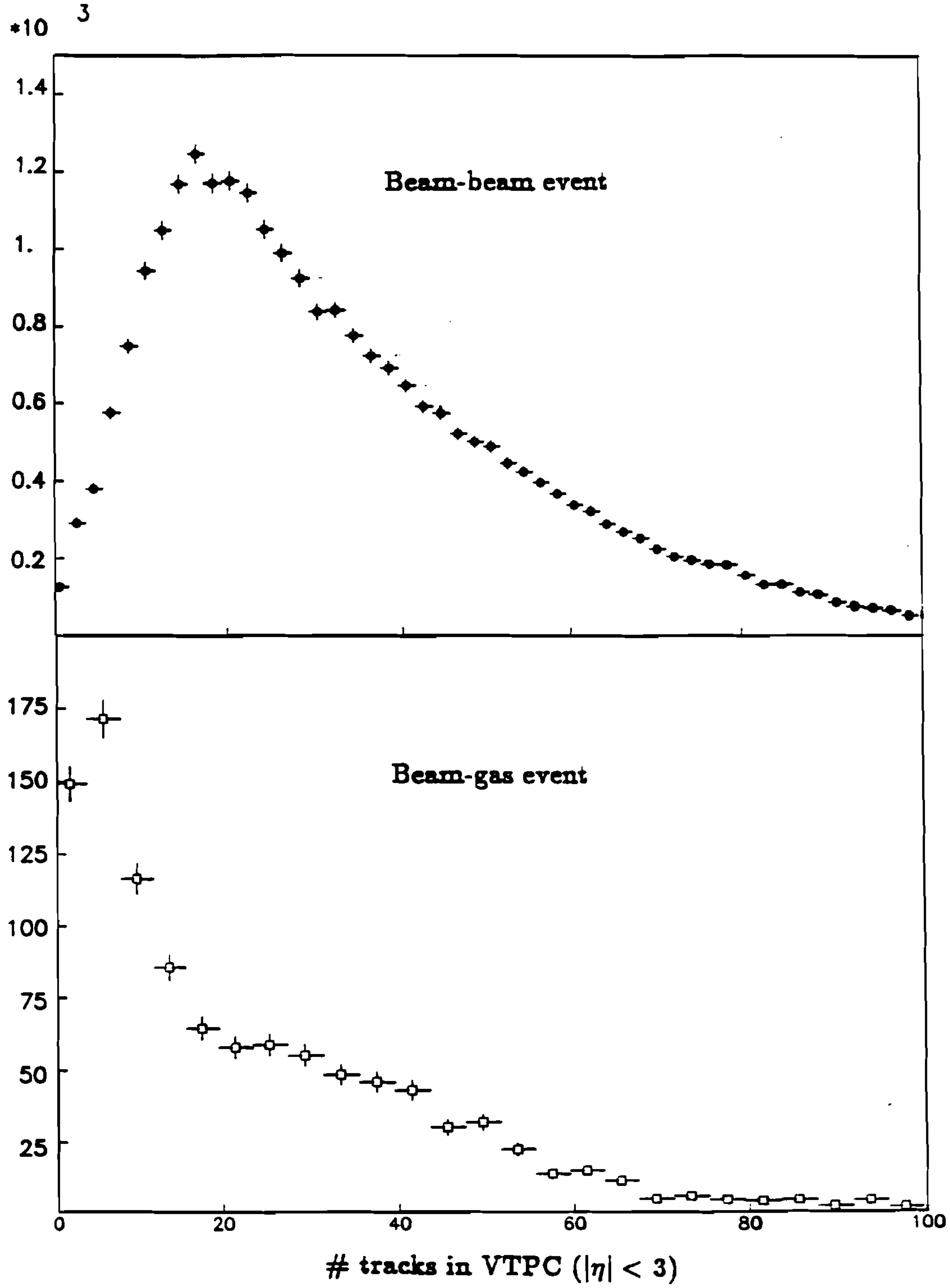

Figure 3.6 The number of tracks in the VTPC.

interaction point. Each of p and $\bar{p}$ bunches was tagged and the bunch numbers resulting in the collisions were kept with other trigger informations. About 15 % of the data set for $\sqrt{s}$ = 1800 GeV and all of the data at $\sqrt{s}$ = 630 GeV were taken with one empty antiproton bunch. The rejection efficiencies for the beam-gas interactions were studied with these empty bunch triggers. The contamination of misidentified beam-gas interactions to the data sample was estimated to be less than 0.5 % at 1800 GeV and less that 2.5 % at 630 GeV. At $\sqrt{s}$ = 1800 GeV, the fraction of triggers due to beam-gas interactions ranged from $\sim$ 4 % at the instantaneous luminosity of $4\times10^{28}\text{cm}^{-2}\text{s}^{-1}$ to about 20 % for the data set taken with an empty antiproton bunch. The beam-gas interaction was about 50 % of all triggers at $\sqrt{s}$ = 630 GeV.

The acceptance efficiency after the event selection for each type of interactions was estimated by the Monte Carlo method as described in Section 3.1.1. Approximately 25 % of DD and 4 % of SD interactions were removed from the raw data by the event selection, but the loss of ND interactions was only 0.1 %. The results are listed in Table 3.3 and 3.4. Using the estimated cross sections at $\sqrt{s}$ = 1800 (630) GeV, the effective cross section for the final data sample, σ_{eff}, is 43±6 mb (34±3 mb). The fraction of non-diffractive interactions in the sample is 89 % (93 %) at 1800 (630) GeV. The uncertainty in the estimate of the effective cross section is the principle error on the overall normalization of the cross sections which will be presented in Chapter 5.

Table 3.3 The selected trigger acceptance at $\sqrt{s} = 1800$ GeV.

type of interaction	estimated σ (mb)	trigger acceptance efficiency	trigger σ (mb)
ND (σ_{ND})	40.2±6.9	0.961	38.6±6.6
SD (σ_{SD})	15.0±5.0	0.160	2.4±0.8
DD (σ_{DD})	4.2±1.0	0.573	3.4±0.6
σ_{eff}			43±6

Table 3.4 The selected trigger acceptance at $\sqrt{s} = 630$ GeV.

type of interaction	estimated σ (mb)	trigger acceptance efficiency	trigger σ (mb)
ND (σ_{ND})	33.9±3.7	0.931	31.6±3.4
SD (σ_{SD})	10.0±0.7	0.111	1.1±0.1
DD (σ_{DD})	2.5±0.6	0.572	1.4±0.3
σ_{eff}			34±3

CHAPTER 4 – ANALYSIS AND CORRECTIONS FOR CTC DATA

Minimum bias events which were reconstructed using standard CTC tracking code have been studied to determine the selection cuts, track finding efficiency and other effects which are needed to distinguish true primary tracks from secondary tracks and false tracks. The structures of the track finding algorithm and track selection are described along with the rejection power of the track selection and the possible loss of good tracks.

4.1 Track Finding Algorithm

From the raw data, the TDC information was corrected for channel to channel variations, checked for internal consistency and reformatted to superlayer and cell oriented output. These reformatted hits were 'marked' at their 'usage flags' if they were used as part of a track.

Track finding in the CTC was started by looking for a track segment ('seed') in an outer axial superlayer. When a seed was found, it was extended to inner axial superlayers. After the process of finding R-ϕ tracks was completed, stereo reconstruction was performed (see Figure 4.1).

Find a seed for a R-ϕ track

The track finding began with the search for a straight line segment (seed) which would cross the sense wire plane (Figure 2.7) in a cell of an axial superlayer. To form a candidate seed in a cell required unmarked hits with pulse widths $\geq$ 36 nsec on at least 5 wires. The cut on pulse width was made to reject hits from after-pulsing and cross talk between wires. The straight line segment was found in two steps. First, lines through all two-hit combinations

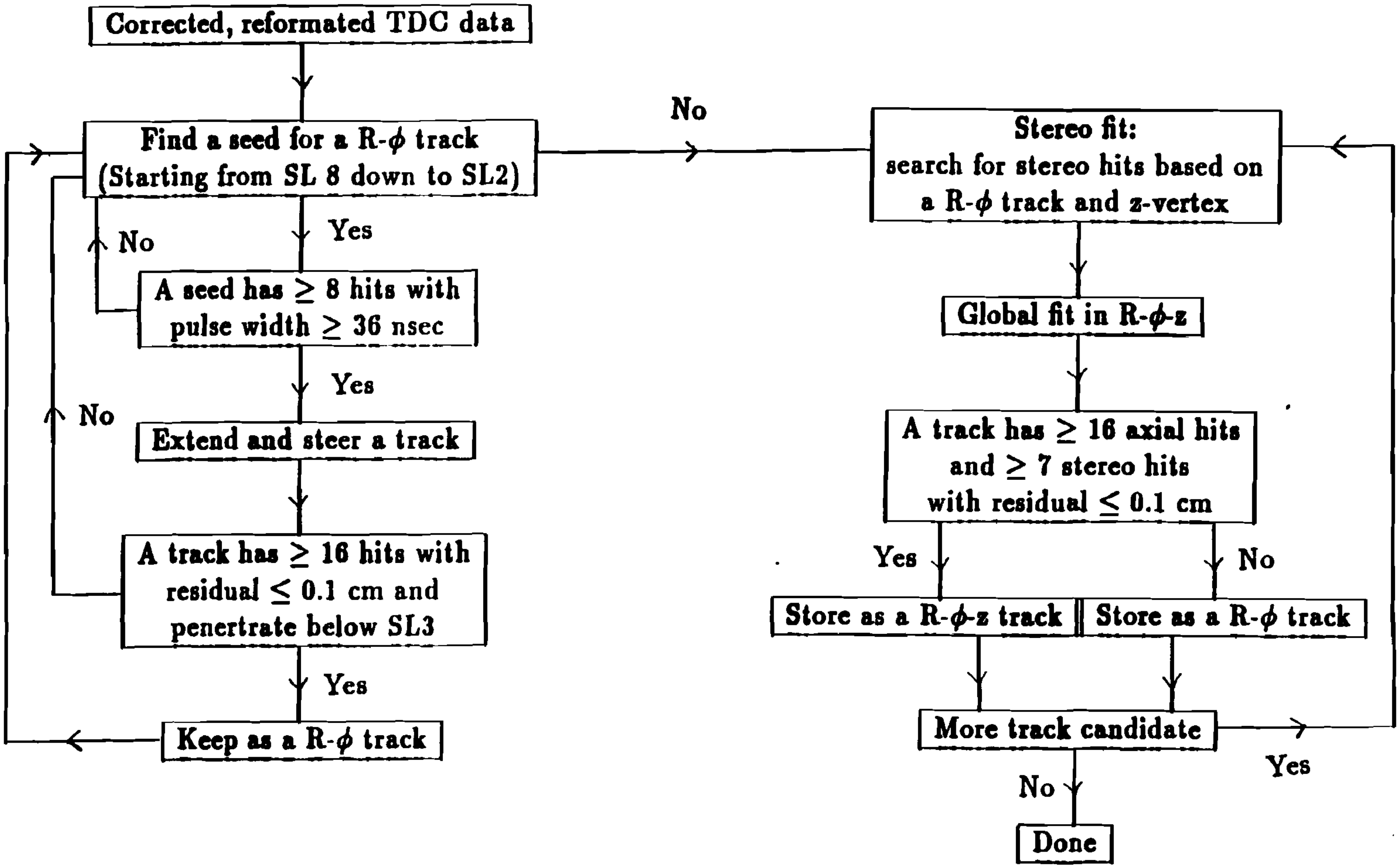

Figure 4.1 Flow diagram of track reconstruction.

were drawn to find the best candidate. For those pairs which were consistent with a sense wire crossing, the angles of the hits at a point where the track should cross the sense wire plane were used to resolve sign ambiguities. In this way, a straight line segment was found in one cell only, but in general, the track could also pass through neighbouring cells in the same superlayer. By extrapolating the straight line segment from the seed cell into the two neighboring cells in the same superlayer, predicted hits were searched for and added to the seed if they were unmarked and had pulse widths ≥ 36 nsec. The resulting line segment candidate within the superlayer was required to have at least 8 hits in order to be accepted and extended as a track candidate.

Extend a track

The qualified straight line segment at a certain radius was extended to be a track candidate by the beam constraint method. This method of track extension biased against the reconstruction of tracks from secondary vertices. By assuming that the track was coming from the main vertex, the track parameters could be estimated by performing an arc fit to hits in the seed and the position of the beam, $(x_{\mathrm{beam}}, y_{\mathrm{beam}})$. For the 1987 run data, it was $(x_{\mathrm{beam}}, y_{\mathrm{beam}}) = (-0.055, -0.013)$ cm. Having a first approximation of track parameters, a circle path was drawn to define a road and hits close to the predictions were collected from other axial superlayers.

Steer a track

To be included in a track candidate, hits were required to have residuals less than 0.25 cm. If a hit had a residual ≤ 0.25 cm but also had a too narrow (< 36 nsec) or too broad (> 160 nsec) pulse width or was marked by the usage flag, the weight of the hit in the fit was reduced. Since the predicted position was only approximate, a hit with residual > 0.25 cm was also included in the fit with reduced weight if the pulse width was between 36 nsec and 160 nsec.

In the process of searching for and collecting predicted hits, 'missing' and 'bad' hits were counted in order to set a cut for the termination of the track extrapolation. Missing hits were defined as the number of wires without any signal. A wire which had hits but was not included in the collecting procedure was defined as a bad hit except if the distance from the trailing edge of the hit to the prediction point was less than 30 nsec. A hit that had a residual greater than 0.25 cm and had a too narrow or broad (as defined above) pulse width was not counted as a bad or missing hit.

After the searching and weighting of all hits, if there were more than 3 layers (not superlayers) with consecutive missing hits or 4 layers with consecutive bad hits or if the number of collected hits was less than 18 then the track extrapolation was stopped and a search for a new seed was initiated. For the track candidate satisfying the above cuts, the collected hits were fitted and the weighted mean residual was calculated. If the residual was greater than 0.1 cm the hit was rejected. The weighted mean residual was recalculated and the rejection process was cycled once more. The final R-ϕ track was required to have at least 16 hits and to penetrate into superlayer 3 to eliminate some of the secondary tracks and spiralling tracks not passing near the primary vertex.

Stereo fit

The cycle of Finding seed, Extending, and Steering was started in superlayer 8 and continued until all seeds were examined down to and including superlayer 2. Based on the z-vertex position of the interaction measured by the VTPC, the z-coordinate of an R-ϕ track was estimated using the stereo superlayers.

First, a stereo track segment was searched for and reconstructed between the two outermost axial superlayers of the R-ϕ track. The sense wire crossing was not required for this stereo track segment. From this stereo track segment in conjunction with z-vertex position, a first approximation of the track parameters in R-ϕ-z space was made. Within a defined road, hits close to the prediction were collected from other stereo superlayers. After all hits were found, they were included in a global fit with a 0.1 cm residual cut. The final R-ϕ-z track was required to have at least 7 hits from stereo layers and 16 hits from axial layers.

The R-ϕ tracks which failed to be converted into R-ϕ-z space were examined using an interactive fitting program. Out of 1,000 R-ϕ tracks which were not converted, 40 % had $\eta > 1$, 40 % were low p_T tracks which spiraled in the chamber (average p_T of < 250 MeV/c), 12 % were fake tracks, and 8 % were coming from a secondary vertex as decay particles. For the study of central primary charged particles, those tracks constructed only in R-ϕ space were ignored and only R-ϕ-z tracks were used.

4.2 Track Selection

Since the track finding algorithm had very loose requirements, further quality controls with tighter cuts were needed to remove false tracks. Also, in order to distinguish primary particles from secondaries originating from decays and interactions, tracks were required to pass through the interaction vertex within the accuracy given by the measurement error and multiple scattering: 5 cm along the beam direction and $\sqrt{0.5^2 + 0.17p_T^2}$ cm in the transverse plane. The loss of good tracks due to the track selection was negligible.

Quality control

By estimating the radius at which the particle would exit the CTC from the fitted parameters of tracks, the fraction of possible hits that were used for a given track was calculated. To eleminate falsely reconstructed tracks, tracks were required to use more than half of the possible hits. From event scanning, it was found that false tracks consisting of one good superlayer fit (usually from part of a spiral) and a few random hits from other superlayers could pass the above cut. Defining "good" segments as

(1) more than 7 hits used out of 12 possible for axial superlayers and

(2) more than 3 hits used out of 6 possible for stereo superlayers,

a track was required to have at least 2 good axial segments and at least 1 good stereo segment.

Removing secondaries

The non-primary particles resulting from decays or secondary interactions would likely have large impact parameters (d) with respect to the nominal beam axis or not be associated with the z-position of the interaction vertex.

Since the best value of drift constants were not available at the time of this analysis, the average residual was of the order of 300 μm (Figure 2.8) rather than designed value of 200 μm. Also, the CTC was displaced with respect to the beam axis by about 500 μm in the R-z plane. The resulting resolution of the impact parameter (δd) should be worse accordingly. In addition to the component coming from intrinsic resolution (Δd_{res}) δd would have a contribution from multiple scattering (Δd_{sca}) which should be a function of p_{T}, as indicated in Figure 4.2.

From the width of the impact parameter distribution as a function of p_{T} (Figure 4.3), the upper limit of the intrinsic resolution was estimated to be < 0.1 cm. The multiple scattering of tracks in the CTC would occur mostly near $R \approx 30$ cm where the CTC inner wall and the VTPC cables were located. The number of radiation lengths, x/x_0, between the beam axis and $R = 30$ cm averaged $\sim$ 2.5 % and had a maximum value of $\sim$ 4 % where the VTPC read-out boards were located. Since the measurement error due to multiple scattering at radius R can be written as

$$\Delta d_{\mathrm{sca}} = \frac{0.014}{p_{\mathrm{T}}} R \sqrt{\frac{x}{x_0}},$$

the expected contribution to the impact parameter due to multiple scattering was estimated as $\Delta d_{\mathrm{sca}} = \sqrt{0.0068/p_{\mathrm{T}}^2}$, using the maximum value of x/x_0.

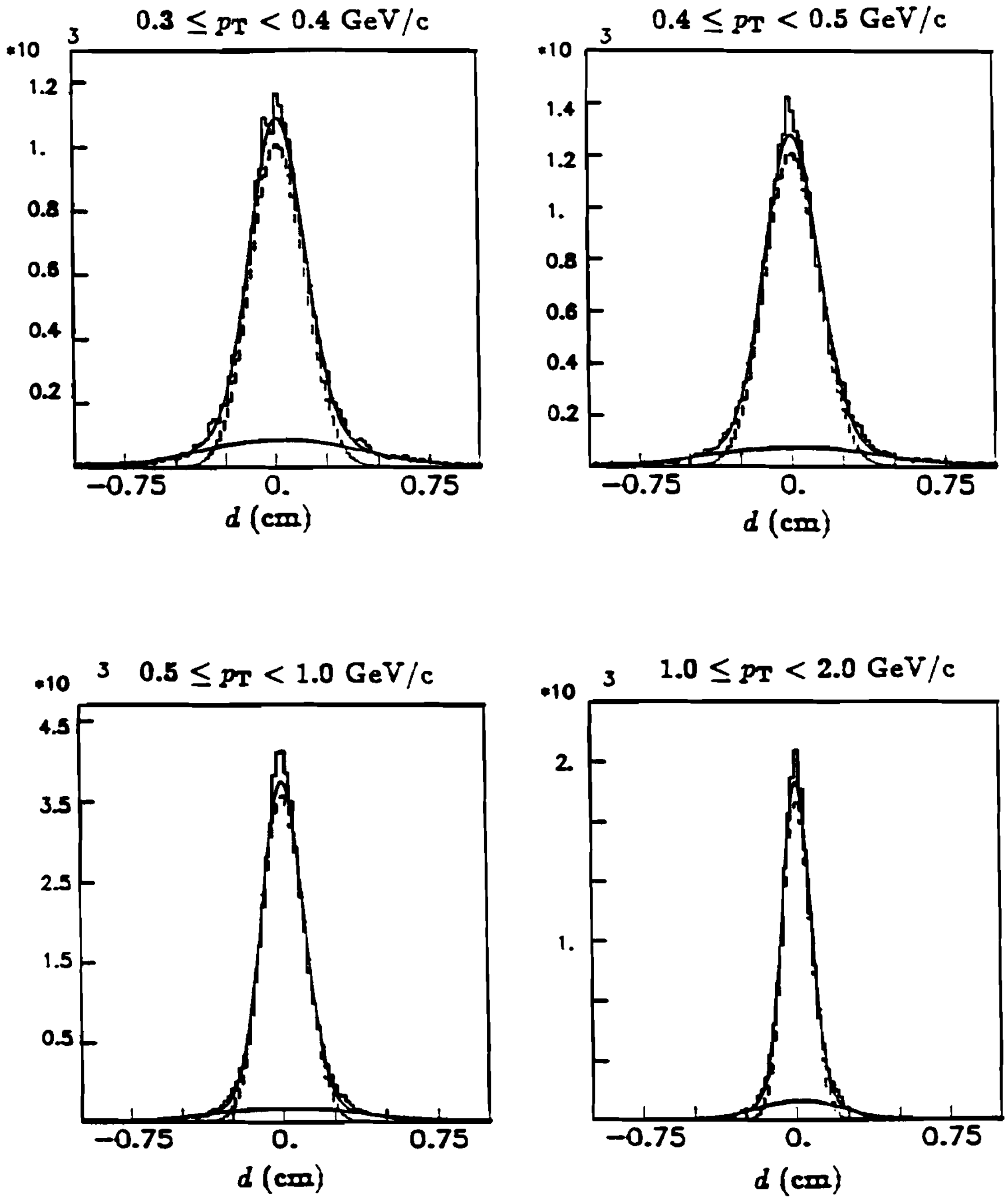

Figure 4.2 Impact parameter distributions as a function of p_T.

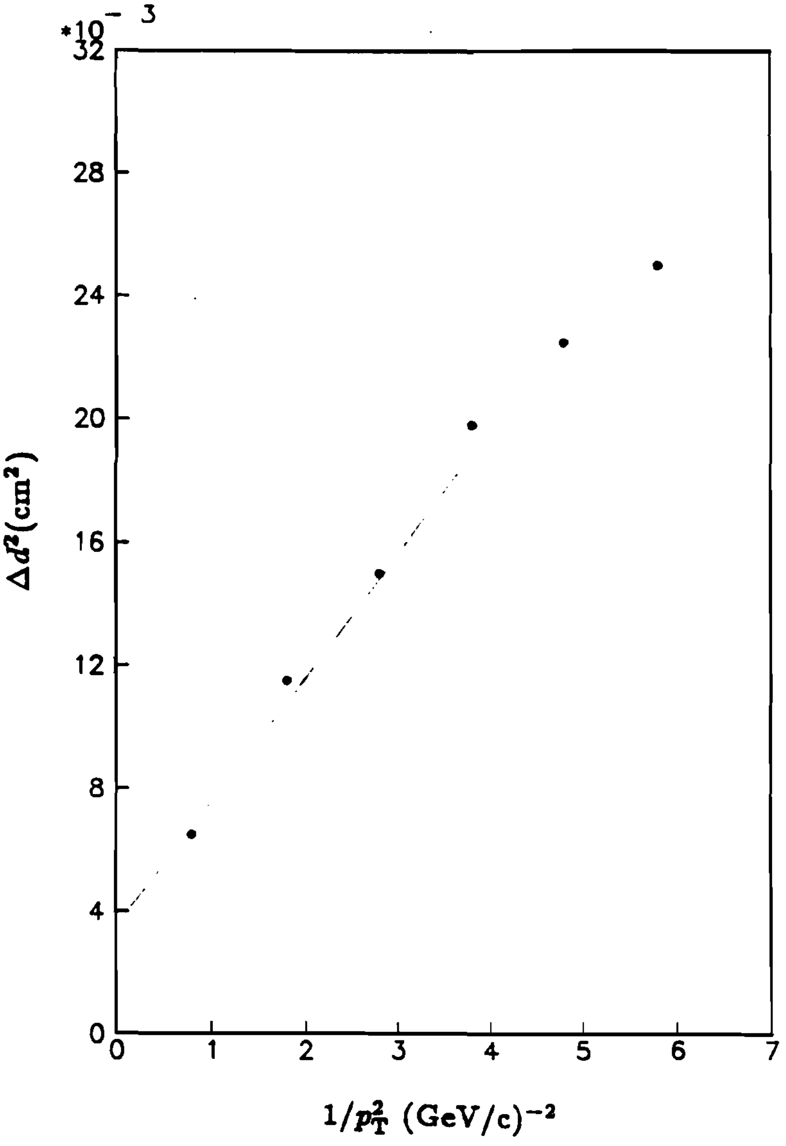

Figure 4.3 Δd^2 as a function of $1/p_T^2$.

The resulting width of the impact parameter distribution was

$$\delta d = \sqrt{\Delta d_{\rm res}^2 + \Delta d_{\rm sca}^2} = \sqrt{0.1^2 + 0.0068/p_{\rm T}^2}\ ({\rm cm}).$$

Tracks with impact parameter $> (5 \times \delta d)$ were rejected as secondaries.

The distribution of the distance between the event z-vertex to the closest approach to the beam of the track (Δz) had a width of < 1 cm. To remove tracks which were not associated with the primary vertex, Δz was required to be less than 5 cm.

Possible loss of tracks due to selection

Even though the selection cuts were purely geometrical, a higher rejection rate in the high $p_{\rm T}$ range (> 3 GeV/c) was observed. A possible deficiency or excess of high $p_{\rm T}$ tracks was studied by scanning and by comparison of the energy deposited in the calorimeters for tracks with $p_{\rm T} > 3$ GeV/c and in $|\eta| < 1$. The scanning of high $p_{\rm T}$ track candidates in 15,000 events (~ 35 % of total data sample) showed that the track selection was 100 ± 1 % efficient (neither over efficient nor under efficient) for high $p_{\rm T}$ tracks in the central region. The comparison of calorimetry energy to the $p_{\rm T}$ of the track set an upper limit to the track counting error when track selection was used of 0.028 ± 0.02 %.

The possible stereo misreconstruction could result in incorrect prediction of Δz. Tracks rejected by the Δz cut in 5,500 events were scanned, and the loss of primary tracks was estimated to be less than 0.2 %.

The overall ratio of the transverse momentum spectrum of positive particles to that of negative particles was consistent with 1 within errors and independent of $p_{\rm T}$ (Figure 4.4). The track selection was very effective in removing non-primary particles.

4.3 Reconstruction Efficiency

The reconstruction efficiency of primary tracks in the central region ($|\eta| < 1$) was studied by two independent methods. First, the CTC information for

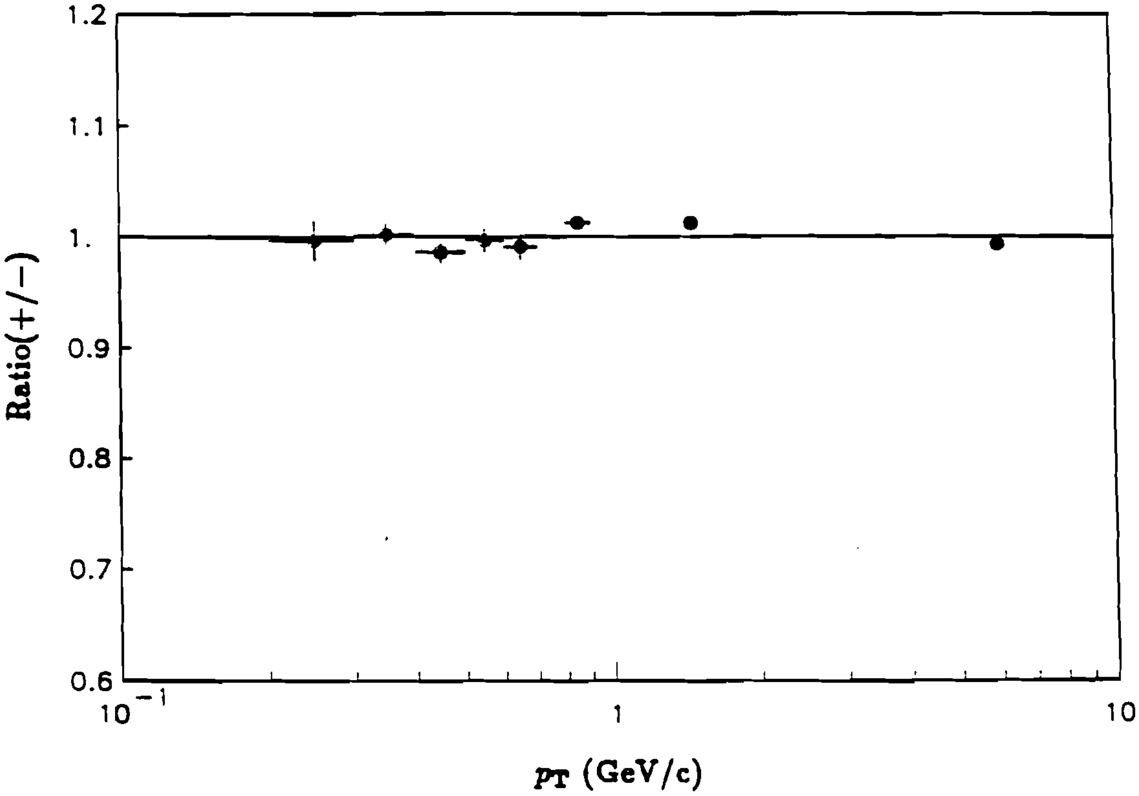

Figure 4.4 Ratio of positive and negative charged particles.

500 reconstructed events were scanned and, using an interactive fitting program, mistakes made by the standard reconstruction program were corrected. Second, simulated tracks of varying momenta were superimposed on real events and reconstructed using the standard reconstruction program. Both methods gave consistent estimates of the reconstruction efficiency as a function of p_T (Figure 4.5). Since charged particles with p_T less than 0.33 GeV/c spiral inside the solenoid and the track finding criteria were optimized for high p_T tracks to avoid misreconstructions largely due to these spirals, the reconstruction efficiency dropped rapidly for p_T below 0.4 GeV/c.

The scanning using the interactive fitting program also showed that the reconstruction efficiency was close to 1 within errors and independent of η for the tracks with $p_T > 400$ MeV/c, in $|\eta| < 1.0$ (Figure 4.6). The reconstruction efficiency for high multiplicity minimum bias events was determined using the interactive fitting program and the results were consistent with those from average minimum bias events.

For tracks with p_T above 0.4 GeV/c and with $|\eta| < 1$, the average reconstruction efficiency was 99.2 ± 1.0 %, independent of the polar angle and event multiplicity.

4.4 Acceptance in the CTC

During the 1987 run, there were 4 dead cells in axial superlayer 4. The corresponding ϕ angles for these regions are indicated in Figure 4.7. The ϕ distribution at the inner radius of superlayer 4 showed an inefficiency in finding tracks which passed through these regions. For the inclusive invariant cross sections, particles passing through these regions were excluded.

The p_T distributions from 8 separate regions in ϕ, excluding the inefficient area, showed very similar shapes and the same mean values. Excluding the inefficient regions due to the dead cells in superlayer 4, the ϕ-acceptance in the CTC was uniform in p_T.

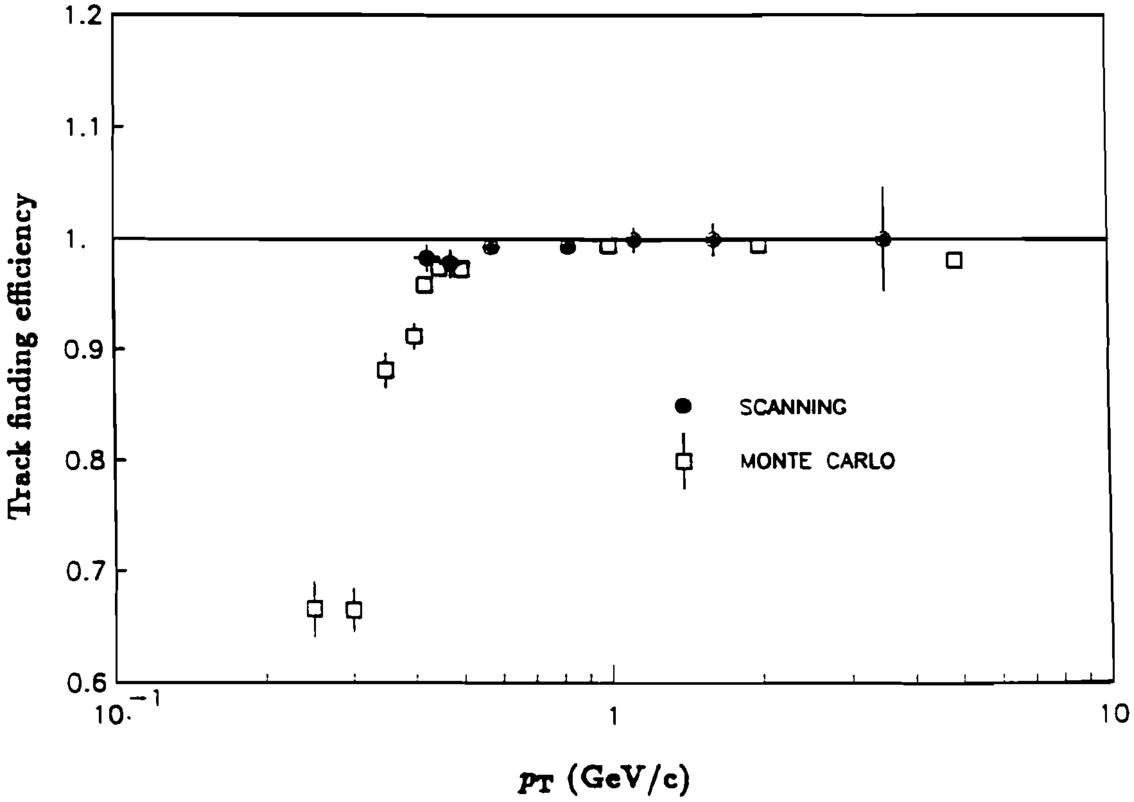

Figure 4.5 Reconstruction efficiency as a function of p_T.

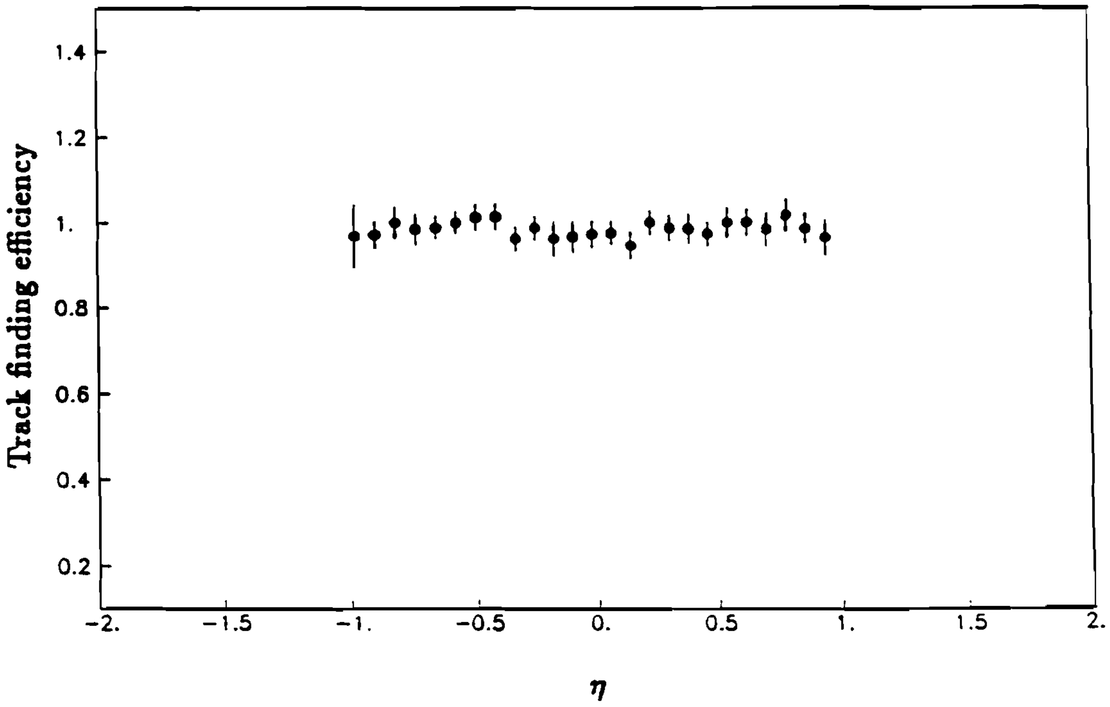

Figure 4.6 Reconstruction efficiency as a function of η.

Since the distribution of the event z-vertex had a width $\sigma \approx 40$ cm, the z-acceptance of the CTC was checked in the following way. The ratio of η distributions for the tracks in sets of events with different z-vertex positions should be flat until the acceptance starts to drop. From the value of the polar angle, θ, at the point where the ratio started to change, the full acceptance range in z at the outer radius of the chamber was calculated. The results showed nearly full acceptance up to the geometric range (within $|z| < 155$ cm) of the CTC. The z-acceptance was also symmetric about the center. For the inclusive invariant cross sections, tracks were required to traverse all layers of the CTC which corresponds to an approximate cut $|\eta| < 1$, depending on the vertex position.

The p_T spectra for 4 bins in $|\eta| < 1.0$ had very similar shapes and the same mean values. From the ratios of these 4 distributions to the overall p_T distribution, factorization of the p_T distribution in η (or y) was seen. Therefore the inclusive invariant cross section also factors into

$$\mathrm{E}\frac{d^3\sigma}{d^3p} = f_1(p_T)\; f_2(\phi)\; f_3(y)$$

in $|\eta| < 1.0$.

4.5 Systematic Errors and Corrections

In addition to the reconstruction efficiency, the overall normalization and the shape of the observed transverse momentum distribution were influenced by: photon conversions, secondary interactions, decays in flight of charged pions and kaons, misreconstructed trajectories of decaying charged kaons, decays of neutral strange particles, and finite momentum resolution. The contributions from these effects were estimated for $p_T > 400$ MeV/c and $|\eta| < 1.0$, and the overall correction was found to be small and nearly independent of p_T for $p_T > 450$ MeV/c, as shown in Figure 4.8.

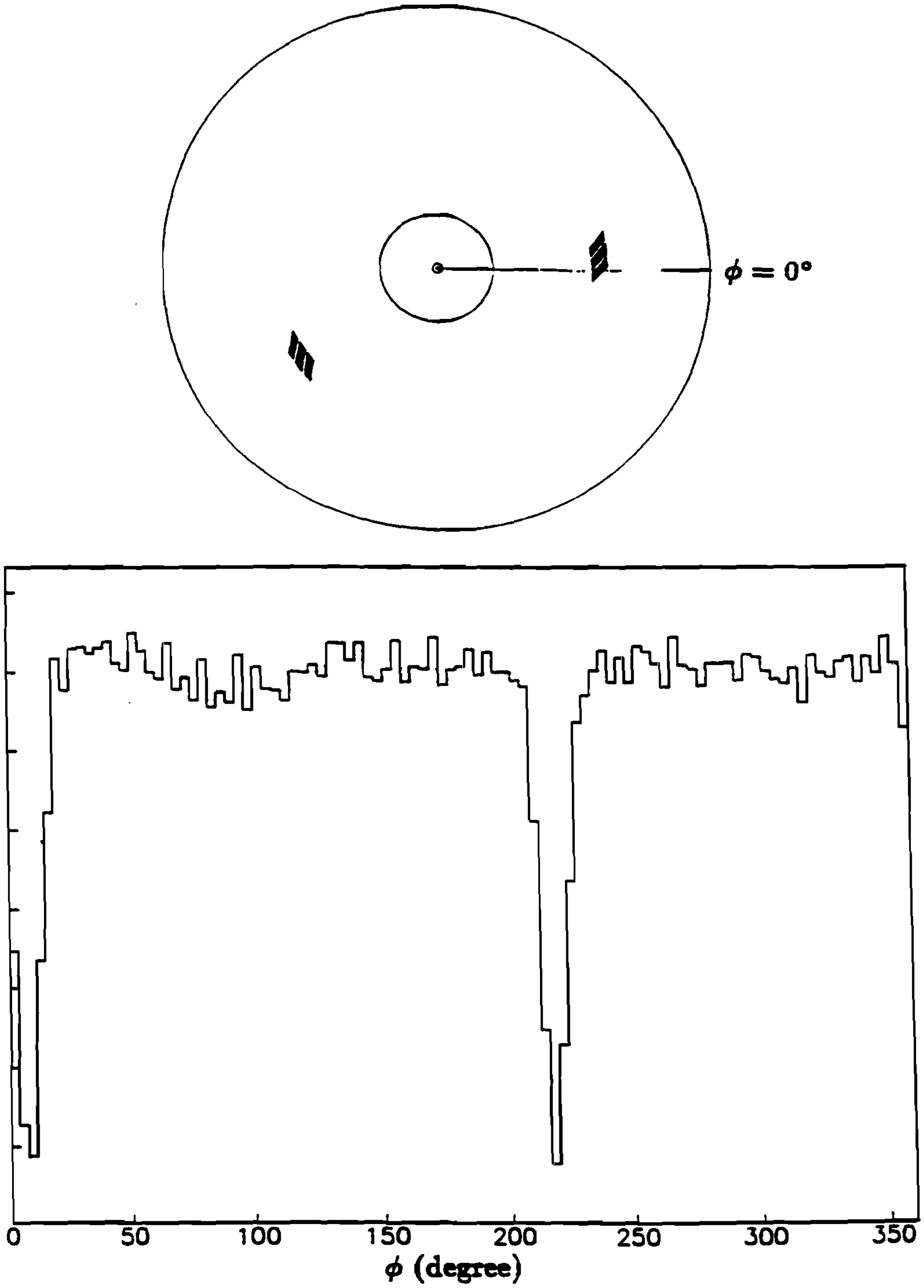

Figure 4.7 ϕ distribution in CTC at superlayer 4.

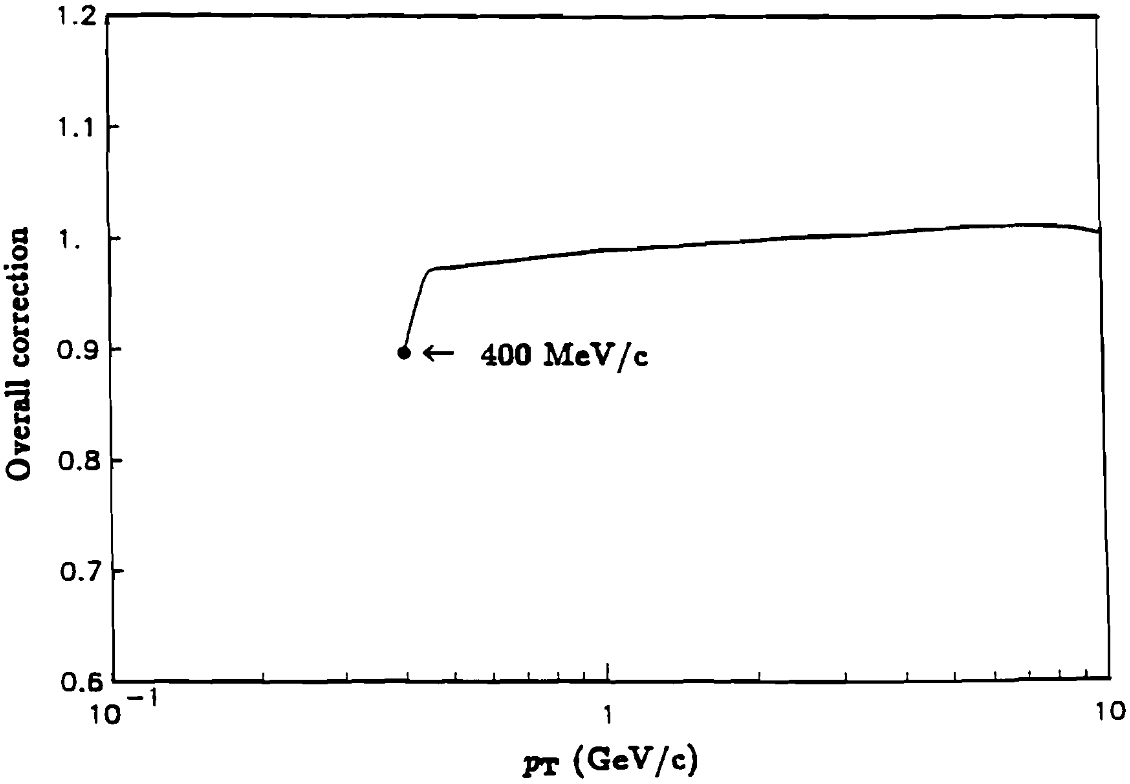

Figure 4.8 Overall correction as a function of p_T.

Photon conversions

The total number of photons produced at the vertex, mostly from decay products of π°'s, should be approximately equal to the total number of charged particles, but with a much softer p_T spectrum. The conversion of these photons would occur mostly near the beam pipe and the inner radius of the CTC chamber where the VTPC read-out boards, cables and the CTC inner wall were located.

Using the same p_T spectrum for π°'s as that of charged particles [19], a flat probability distributions for π° decays, and a 0.25 % photon conversion probability in the wall of the beam pipe, the contribution of conversions in the beam pipe to the p_T distribution of the charged particles was calculated to be of 0.3 % at $p_T = 0.35$ GeV and 0.1 % at $p_T = 1$ GeV.

Due to the magnetic field, particles coming from the photon conversions near the CTC inner wall would have an apparent impact parameter, d, of

$$d = \frac{2\mathrm{e}\,\mathrm{B}R^2}{p_T} = \frac{R^2}{444 \times p_T}\ (\mathrm{cm}),$$

with $R \approx 30$ cm. The resulting contribution of these conversions was negligible for all p_T because of the track selection cut on the impact parameter. Therefore, the overall contribution from photon conversions to the charged particle p_T distribution is $0.1 \sim 0.3$ % which is in agreement with the average value of ~ 0.12 % from the Monte Carlo simulation.

Secondary interactions

The secondary interactions of charged and neutral hadrons with the material in the detector occured predominantly near the inner radius of the CTC where there is approximately 0.25 to 0.4 % of an interaction length. Secondaries produced in the interactions would have typical transverse momenta of 300 MeV/c with respect to the parent particle direction, and were usually excluded by the impact parameter cuts. From the Monte Carlo simulation, the net correction due to secondary interactions was estimated to be a loss of about 0.5 % of the primary charged particles.

Decays in flight of charged particles

Decays of charged particles (mostly pions and kaons) would remove tracks from the sample, thus resulting in a loss of primary charged particles. Considering the structure of track reconstruction and selection, particles decaying at large radii (about $R > 1$ m) would have a large probability of their trajectories being properly reconstructed. For pions and kaons decaying with $R <$ 1 m, possible losses were estimated using Monte Carlo generated sampes of $\pi, K \rightarrow \mu\nu$ decays.

The probability of charged pions decaying below $R = 1$ m was calculated as a function of p_T (Figure 4.9). From the reconstruction of simulated π decays, it was observed that about 50 % of the secondaries were reconstructed as charged muons with momentum close to the parent momentum and passed all selection criteria. No significant number of secondaries were reconstructed with higher p_T values than the parent momentum. The loss of primary charged particles due to the decays of charged pions was, therefore, 50 % of the decay probability.

Using the K/π ratio measured by UA2 [19] and UA5 [35,36] and the probability of charged pions decaying below $R = 1$ m, the loss of primary charged particles due to the decays of charged kaons was estimated (also shown in Figure 4.9). Since only a small fraction (< 2 %) of secondaries were reconstructed, and most of those are reconstructed with p_T close to that of the parent particle, the contribution to the overall correction was the same as the decay probability.

Due to the steeply falling p_T spectrum, misreconstructed trajectories of decaying charged kaons could conceivably contaminate the high p_T region. From reconstructing a sample of simulated K decays, an upper limit of 0.3 %

contamination was established for $p_T \leq 10$ GeV/c. Compared to the statistical errors in this region, this correction was negligible and therefore was not applied.

Decays of neutral strange particles

The contamination from the decay products of neutral stange particles, K°'s and Λ°'s, should be subtracted. K°_{S} production at $\sqrt{s} = 1800$ GeV was studied by reconstructing the decay channel into π^{+} and π^{-}. Each pair of oppositely charged particles with impact parameter greater than 2 mm and $p_T \geq 0.25$ GeV/c was fit to a common vertex point. Assuming the pion mass for the daughters, the invariant mass of the parent particle was calculated and a clear mass peak is seen near 500 MeV [67].

Normalizing the K°_{S}/π ratio to agree with the UA2 measurement [19] and taking into account the 68 % branching ratio, the fraction of secondaries coming from K°_{S} decays to the total number of charged particles was estimated. Using the impact parameter distribution of pions coming from K°_{S} decays, the correction to the observed spectrum was estimated to be $\sim$ 2.4 %. The correction estimated by the Monte Carlo simulation was $\sim$ 1.4 %, and the difference comes from the K/π ratio used in the CDF minimum bias event generator. The upper limit of correction was set to be 2.4 %.

Since the ratio of $K^{\circ}/\Lambda^{\circ}$ is known to be > 1, the contribution from Λ° decay should be smaller and was neglected by assigning a ± 1 % error to the K° correction.

p_T smearing

The momentum resolution of the CTC has a contribution from multiple scattering of $\sigma p_T/p_T \sim 0.003$ and a contribution from the average per hit resolution of the chamber of $\sigma p_T/p_T \sim 0.002\ p_T$. Since tracks were required to pass through superlayer 8, the same p_T resolution is valid for all tracks. The correction for p_T smearing to the invariant cross section was estimated by parameterizing the p_T dependence of the data as $E\frac{d^3\sigma}{d^3p} = A[p_0/(p_o + p_T)]^n$ and using the measured Gaussian resolution,

$$\frac{dN}{dp_T}_{True} = \frac{dN}{dp_T}_{Meas} \times Ratio$$

where

$$Ratio = \frac{N(p_T)}{\int_0^\infty dp_T{}' N(p_T{}') \frac{1}{\sigma(p_T{}')\sqrt{2\pi}} \exp -\frac{1}{2}(\frac{p_T - p_T{}'}{\sigma(p_T{}')})^2}.$$

The resulting correction to the measured p_T spectra at $\sqrt{s} = 1800$ and 630 GeV was less than 1 % at all values of momentum. For p_T values below 1.0 GeV/c, where multiple scattering dominates the momentum resolution, the effect of smearing was extremely small (< 0.1 %) and even at $p_T = 8.0$ GeV/c, the correction was still less than 1 %. The smearing correction could still be neglected even if the momentum resolution was degraded by a factor of 2 at high momentum.

Overall correction

The observed p_T spectrum was corrected for reconstruction efficiency and for the effects described in this section and summarized below:

(1) Photon conversions, secondary interactions and decays of neutral strange particles. These effects were calculated as increasing the number of tracks by 3.0 ± 1.0 %, nearly independent of p_T.

(2) Decays in flight of charged pions and kaons caused a depletion of the observed distribution ranging from 5 % at $p_T = 0.4$ GeV/c to 2 % at $p_T = 2$ GeV/c.

The overall correction applied was small and nearly independent of p_T for > 0.45 GeV/c (Figure 4.8). The distortion of the spectrum due to misreconstructed trajectories of decaying charged kaons and finite momentum resolution was negligible compared to the statistical errors.

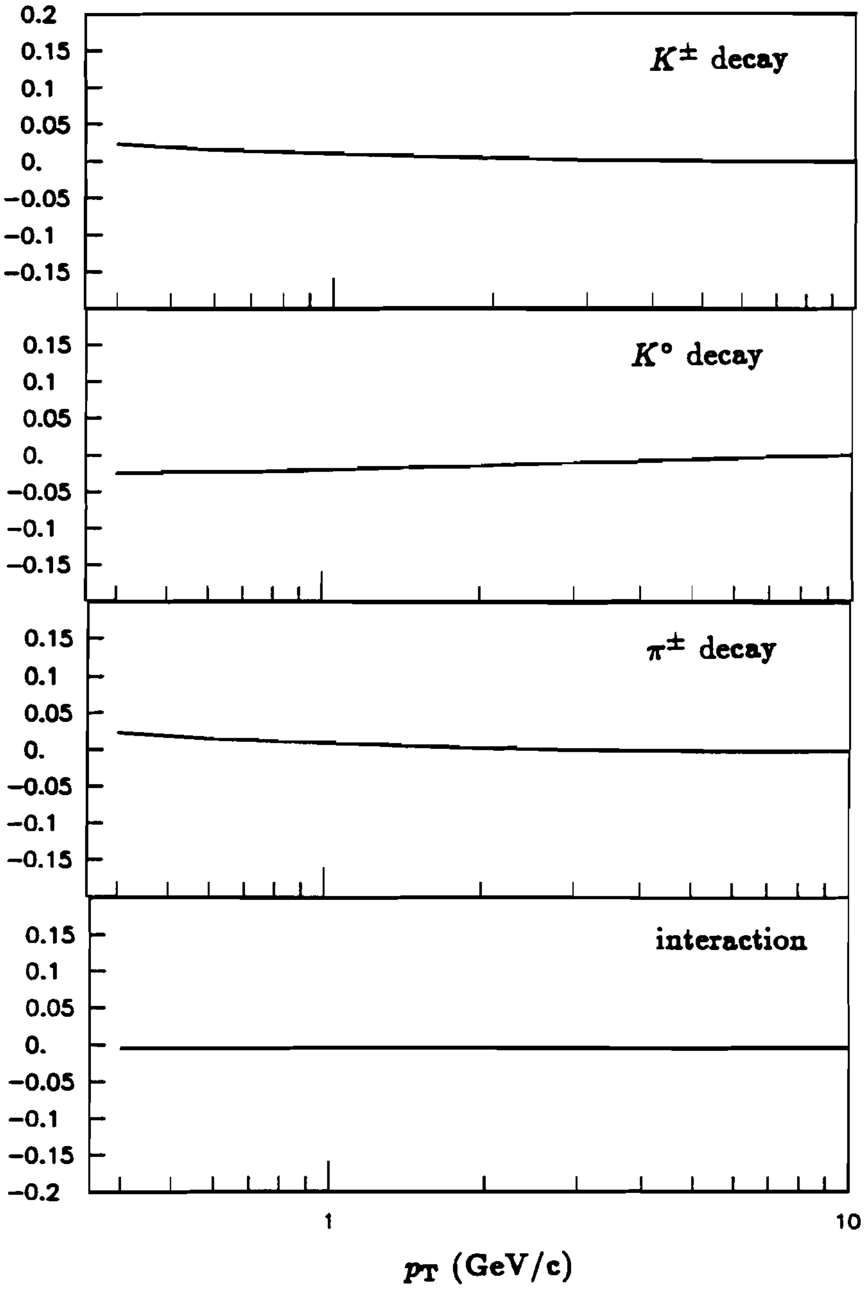

Figure 4.9 Systematic errors as a function of p_T.

CHAPTER 5 – INCLUSIVE INVARIANT CROSS SECTION

The transverse momentum spectra of charged particles and their mean values were measured at a $\sqrt{s}$ of 630 and 1800 GeV. Results are presented for pseudorapidity $|\eta| \leq 1$ and compared with lower energy data in the range of $\sqrt{s}$ from 23 to 900 GeV and with a parton model calculation. The mean value of the transverse momentum showed a strong dependence on $\sqrt{s}$ and event multiplicity.

5.1 Normalization of p_T Spectrum

The Lorentz invariant single particle phase space (the behavior of a single particle in the absence of any dynamics and any exterior energy and momentum constraints) is given as

$$d^4p\ \delta(p^2 - m^2) = \frac{d^3p}{2\mathrm{E}} = \frac{p_T\, dp_T\, d\phi\, dp_z}{\mathrm{E}} \tag{1}$$

where m is the mass, E is the energy of the particle and δ is the Dirac delta function expressing the condition that the particle is on the mass shell. It shows that all 4-momenta are equally probable as long as the particle is on the mass shell. The above quantity is called the invariant phase space element, dτ. Using the equivalence dy = dp_z/E, dτ can be rewritten as $d\tau = p_T\, dp_T\, dy\, d\phi$ and the contribution of the cross section in unit phase space element then becomes

$$\frac{d\sigma}{d\tau} = \mathrm{E}\frac{d^3\sigma}{d^3p} = \frac{d^3\sigma}{p_T\, dp_T\, dy\, d\phi}. \tag{2}$$

Since this quantity is defined in a Lorentz invariant way, it is called the Lorentz invariant inclusive cross section for single particles. The corrected inclusive p_T

spectrum of charged particles in the CTC was converted to the invariant cross section in the following way.

The number of charged particles ($\mathrm{N_{ch}}$) produced for a time integrated luminosity ($\mathcal{L}$) can be written as $\mathrm{N_{ch}} = \mathcal{L} \times \sigma$, where σ is the single particle inclusive cross section. In a given interval $\Delta p_{\mathrm{T}} = (p_{\mathrm{T1}}, p_{\mathrm{T2}})$, the total number of particles can be expressed as

$$\mathrm{N_{ch}}(\Delta p_{\mathrm{T}}) = \mathcal{L} \times \sigma \,\Big|_{p_{\mathrm{T1}}}^{p_{\mathrm{T2}}} = \mathcal{L}\, \Delta p_{\mathrm{T}} \, \left(\frac{d\sigma}{dp_{\mathrm{T}}}\right). \tag{3}$$

As was shown in section 4.4, the p_{T} distribution in y (or η) and ϕ factorizes, and the invariant cross section can be written as

$$\int dy \ \mathrm{E}\frac{d^3\sigma}{d^3p} = \int dy \ \left(\frac{d^3\sigma}{p_{\mathrm{T}}\, dp_{\mathrm{T}}\, dy\, d\phi}\right) = \left(\frac{d^3\sigma}{p_{\mathrm{T}}\, dp_{\mathrm{T}}\, dy\, d\phi}\right) \Delta y \tag{4}$$

and therefore,

$$\begin{aligned} \frac{d\sigma}{dp_{\mathrm{T}}} &= \int d\phi \ \left(\frac{d^2\sigma}{dp_{\mathrm{T}}\, d\phi}\right) = \int d\phi \ p_{\mathrm{T}} \ \left(\frac{d^2\sigma}{d^2 p_{\mathrm{T}}}\right) \\ &= \int d\phi \int dy \ p_{\mathrm{T}} \ \mathrm{E}\frac{d^3\sigma}{d^3p} = \Delta\phi \ \Delta y \ p_{\mathrm{T}} \ \mathrm{E}\frac{d^3\sigma}{d^3p}. \end{aligned} \tag{5}$$

From equation (3) and (5), it can be deduced

$$\mathrm{E}\frac{d^3\sigma}{d^3p} = \frac{\mathrm{N_{ch}}(\Delta p_{\mathrm{T}})}{\mathcal{L}\ p_{\mathrm{T}}\ \Delta p_{\mathrm{T}}\ \Delta\phi\ \Delta y}. \tag{6}$$

Since the effective cross section for a given event is

$$\sigma_{\mathrm{eff}} = \frac{\mathrm{N_{event}}}{\mathcal{L}}, \tag{7}$$

by finding the $\Delta\phi$ and Δy acceptance for each event, the invariant cross section can be obtained from the p_{T} distrbution and the estimated value of σ_{eff} to be

$$\mathrm{E}\frac{d^3\sigma}{d^3p} = \frac{\sigma_{\mathrm{eff}}}{\mathrm{N_{event}}} \frac{(\mathrm{N_{ch+}} + \mathrm{N_{ch-}})/2}{p_{\mathrm{T}} \Delta p_{\mathrm{T}} \Delta\phi \Delta y} \tag{8}$$

where

$N_{ch\pm}$ = number of positive/negative tracks in the p_T bin,

N_{event} = total number of accepted events,

σ_{eff} = effective cross section for the accepted event sample,

Δp_T = bin width in p_T, and

Δy and $\Delta\phi$ are the accepted regions in phase space.

The results of the inclusive cross sections are presented as the average of the spectra of particles with both signs of charge.

Calculation of $\Delta\phi$

Since the CTC is symmetric in ϕ, the normalization factor $\Delta\phi$ should be 2π if the ϕ distribution of the CTC is uniform. Due to 4 disconnected cells in superlayer 4, there were some regions which were excluded and

$$\Delta\phi = 2\pi \times \frac{322^\circ}{360^\circ}. \tag{9}$$

Calculation of Δy

The acceptance in rapidity (y) was calculated on a track by track basis assuming all particles to be pions. Due to the limited acceptance in y (or η) of the CTC and the change in z-vertex position for each event, the following technique was used to calculate Δy.

For events that occured in a given range of Δz, the local invariant cross section was expressed as

$$E\frac{d^3\sigma}{d^3p}\,|_{\Delta z} = \frac{N_{ch}(\Delta z, \Delta p_T)}{\mathcal{L}\ p_T\ \Delta p_T\ \Delta\phi\ \Delta y\,|_{\Delta z}\ \frac{N_{event}(\Delta z)}{N_{event}}} \tag{10}$$

where

N_{event} is the total number of events in the data sample, and

$N_{event}(\Delta z)$ is the number of events with z-vertex within Δz.

The total inclusive cross section for all the values of z-vertex is then

$$\begin{aligned} E\frac{d^3\sigma}{d^3p} &= \frac{1}{N_{event}}\sum_{\Delta z}[E\frac{d^3\sigma}{d^3p}\,|_{\Delta z} \times N_{event}(\Delta z)] \\ &= \frac{1}{\mathcal{L}\ p_T\ \Delta p_T\ \Delta\phi} \times \sum_{\Delta z}\frac{N_{ch}(\Delta z, \Delta p_T)}{\Delta y\,|_{\Delta z}}. \end{aligned} \tag{11}$$

For a given event with known z-vertex position, the maximum η range ($\eta_{\min}$ and $\eta_{\max}$) for full acceptance in the CTC was calculated:

$$\begin{aligned} \theta_{max} &= tan^{-1}(\frac{R_{CTC}}{z_{max0} - z_{VTX}}) \rightarrow \eta_{max} = -ln\{tan(\frac{\theta_{max}}{2})\} \\ \theta_{min} &= tan^{-1}(\frac{R_{CTC}}{z_{max0} + z_{VTX}}) \rightarrow \eta_{min} = ln\{tan(\frac{\theta_{min}}{2})\} \end{aligned} \tag{12}$$

where

R_{CTC} = outer radius of the CTC boundary,

z_{max0} = half length of CTC acceptance in z, and

z_{VTX} = z coordinate of the event vertex found by the VTPC.

By using $sinh(y) = \beta_T\ sinh(\eta)$ where

$$\beta_T = \frac{p_T}{\sqrt{m^2 + p_T^2}}, \tag{13}$$

the accepted region in the phase space for Δy was calculated from η_{min} and η_{max} for each charged particle, assuming the pion mass.

5.2 Inclusive Invariant Cross Section

The inclusive invariant cross sections of single charged particles at $\sqrt{s}$ = 630 and 1800 GeV are shown in Figure 5.1 (Table 5.1 and 5.2). At p_T = 2 GeV/c the cross section increases by about a factor of 3 from 630 GeV to 1800 GeV. The cross sections are compared with data from other experiments and with predictions of a parton model at high p_T.

Comparison with other experiments

In Figure 5.2, the invariant cross section at 630 GeV was compared with the measurements of UA1 [18] and UA2 [19] at 546 GeV. Since non-diffractive

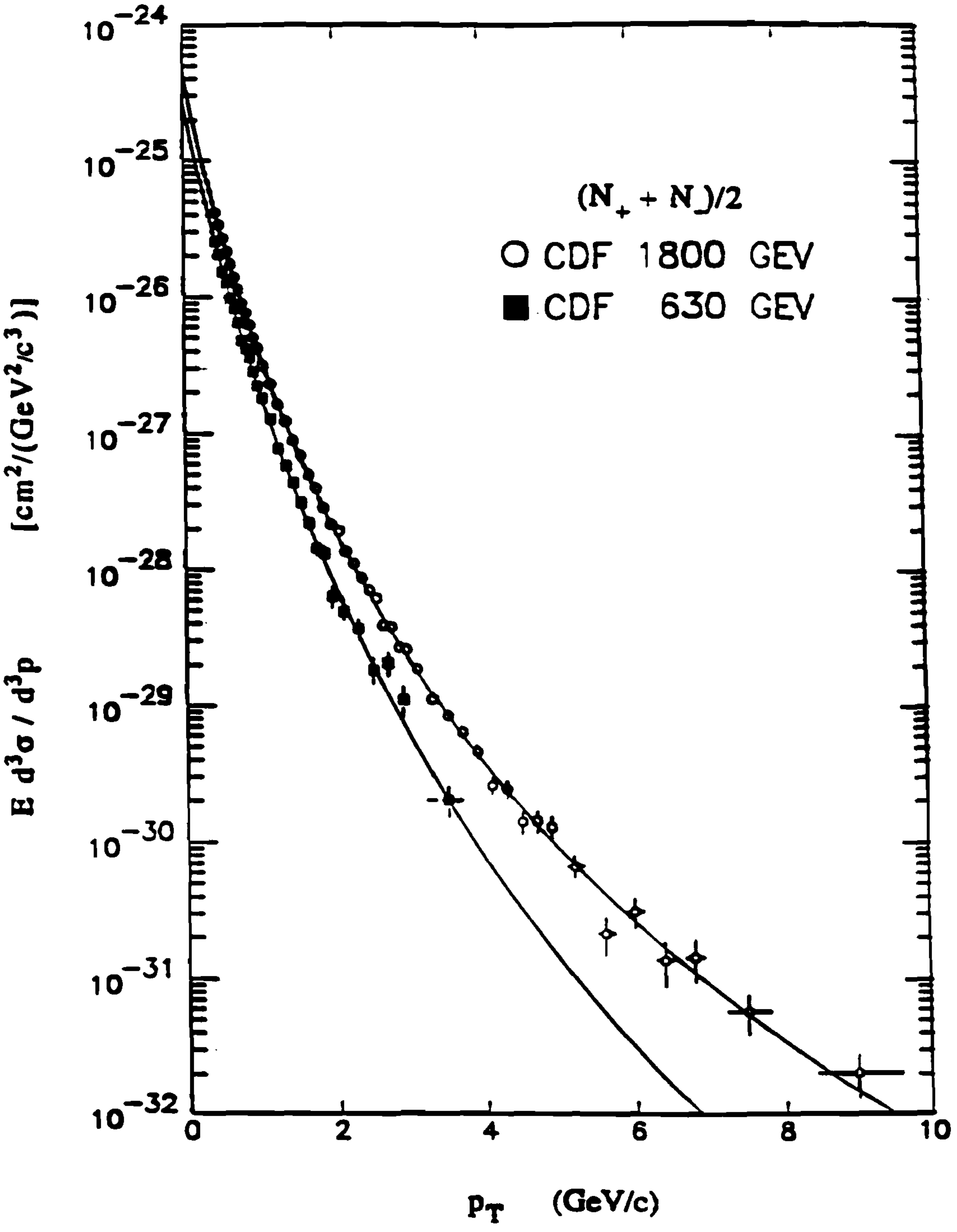

Figure 5.1 The inclusive invariant cross sections.

Table 5.1 The invariant cross section at $\sqrt{s} = 1800$ GeV.

p_T (GeV/c)	$Ed^3\sigma/d^3p$ (10^{-27}cm^2/(GeV^2/c^3))	p_T (GeV/c)	$Ed^3\sigma/d^3p$ (10^{-27}cm^2/(GeV^2/c^3))
0.40-0.45	41.83±0.32	2.30-2.40	$(8.86\pm0.41)\times10^{-2}$
0.45-0.50	34.16±0.26	2.40-2.50	$(7.20\pm0.37)\times10^{-2}$
0.50-0.55	27.13±0.22	2.50-2.60	$(6.23\pm0.33)\times10^{-2}$
0.55-0.60	21.69±0.19	2.60-2.70	$(3.99\pm0.26)\times10^{-2}$
0.60-0.65	17.59±0.16	2.70-2.80	$(3.86\pm0.25)\times10^{-2}$
0.65-0.70	13.95±0.14	2.80-2.90	$(2.77\pm0.21)\times10^{-2}$
0.70-0.75	11.44±0.12	2.90-3.00	$(2.63\pm0.20)\times10^{-2}$
0.75-0.80	9.03±0.10	3.00-3.20	$(1.89\pm0.12)\times10^{-2}$
0.80-0.85	7.65±0.09	3.20-3.40	$(1.14\pm0.09)\times10^{-2}$
0.85-0.90	6.27±0.08	3.40-3.60	$(8.60\pm0.75)\times10^{-3}$
0.90-0.95	5.13±0.07	3.60-3.80	$(6.47\pm0.63)\times10^{-3}$
0.95-1.00	4.30±0.06	3.80-4.00	$(4.65\pm0.52)\times10^{-3}$
1.00-1.10	3.20±0.04	4.00-4.20	$(2.64\pm0.38)\times10^{-3}$
1.10-1.20	2.35±0.03	4.20-4.40	$(2.46\pm0.36)\times10^{-3}$
1.20-1.30	1.65±0.02	4.40-4.60	$(1.42\pm0.27)\times10^{-3}$
1.30-1.40	1.23±0.02	4.60-4.80	$(1.45\pm0.26)\times10^{-3}$
1.40-1.50	$(9.05\pm0.17)\times10^{-1}$	4.80-5.00	$(1.31\pm0.25)\times10^{-3}$
1.50-1.60	$(6.98\pm0.14)\times10^{-1}$	5.00-5.40	$(6.76\pm1.21)\times10^{-4}$
1.60-1.70	$(5.05\pm0.12)\times10^{-1}$	5.40-5.80	$(2.16\pm0.66)\times10^{-4}$
1.70-1.80	$(3.99\pm0.10)\times10^{-1}$	5.80-6.20	$(3.13\pm0.77)\times10^{-4}$
1.80-1.90	$(2.88\pm0.08)\times10^{-1}$	6.20-6.60	$(1.38\pm0.49)\times10^{-4}$
1.90-2.00	$(2.20\pm0.07)\times10^{-1}$	6.60-7.00	$(1.46\pm0.49)\times10^{-4}$
2.00-2.10	$(1.96\pm0.06)\times10^{-1}$	7.00-8.00	$(5.89\pm1.88)\times10^{-5}$
2.10-2.20	$(1.39\pm0.06)\times10^{-1}$	8.00-10.00	$(1.95\pm0.70)\times10^{-5}$
2.20-2.30	$(1.13\pm0.05)\times10^{-1}$		

Averaged over the bin size.
Statistical errors only.

Table 5.2 The invariant cross section at $\sqrt{s}$ = 630 GeV.

p_T (GeV/c)	$Ed^3\sigma/d^3p$ ($10^{-27}\text{cm}^2/(\text{GeV}^2/\text{c}^3)$)	p_T (GeV/c)	$Ed^3\sigma/d^3p$ ($10^{-27}\text{cm}^2/(\text{GeV}^2/\text{c}^3)$)
0.40-0.45	25.56±0.75	1.30-1.40	$(5.83\pm0.43)\times 10^{-1}$
0.45-0.50	20.55±0.61	1.40-1.50	$(4.41\pm0.36)\times 10^{-1}$
0.50-0.55	15.35±0.50	1.50-1.60	$(3.15\pm0.29)\times 10^{-1}$
0.55-0.60	12.82±0.44	1.60-1.70	$(2.23\pm0.24)\times 10^{-1}$
0.60-0.65	9.91±0.37	1.70-1.80	$(1.47\pm0.19)\times 10^{-1}$
0.65-0.70	8.29±0.32	1.80-1.90	$(1.33\pm0.17)\times 10^{-1}$
0.70-0.75	6.52±0.28	1.90-2.00	$(6.49\pm1.18)\times 10^{-2}$
0.75-0.80	4.78±0.23	2.00-2.20	$(4.96\pm0.70)\times 10^{-2}$
0.80-0.85	4.19±0.21	2.20-2.40	$(3.71\pm0.58)\times 10^{-2}$
0.85-0.90	3.64±0.19	2.40-2.60	$(1.87\pm0.39)\times 10^{-2}$
0.90-0.95	2.86±0.16	2.60-2.80	$(2.10\pm0.40)\times 10^{-2}$
0.95-1.00	2.26±0.14	2.80-3.00	$(1.12\pm0.28)\times 10^{-2}$
1.00-1.10	1.84±0.09	3.00-4.00	$(1.97\pm0.48)\times 10^{-3}$
1.10-1.20	1.30±0.07	4.00-10.00	$(1.05\pm0.32)\times 10^{-4}$
1.20-1.30	$(7.89\pm0.52)\times 10^{-1}$		

Averaged over the bin size.
Statistical errors only.

inelastic interactions dominate each of the event samples, the UA1 and UA2 cross sections were scaled to reflect our current estimation of σ_{eff}. The shapes of the p_T distributions agree well. Figure 5.3 shows a comparison of the measurements of the invariant cross sections from the Chicago-Princeton [15] ($\sqrt{s}$ = 27 GeV), British-Scandinavian [17] (53 GeV), UA1 [18] (546 GeV) and CDF (1800 GeV) collaborations. The previously observed flattening in the shape of the p_T distribution with energy continues up to 1800 GeV.

Comparison with a parton model calculation

A naive extrapolation down to low p_T of the QCD prediction [68] of the invariant cross section was made for the $\sqrt{s}$ range from 27 to 1800 GeV. Figure 5.4 compares the measured charged particle cross sections with predictions of a parton model calculation [69]. In the parton model [1,2], the inclusive single particle distribution can be expressed as a convolution of structure functions, F_n, (parton densities) with the parton-parton scattering cross section (σ) and the fragmentation function (D_m):

$$\begin{aligned} \mathrm{E}\frac{d^3\sigma}{d^3p} = \sum_{ijk} \int\int\int\int dx_1 dx_2 \frac{dz}{z^2} d\hat{t}\; F_i(x_1, Q^2)\; F_j(x_2, Q^2)\; \hat{\sigma}^k_{ij}(\hat{s}, \hat{t}, \hat{u}) \\ D_k(z, Q^2)\delta(\hat{s} + \hat{t} + \hat{u}) \end{aligned} \quad (14)$$

where

(1) The longitudinal momentum distributions of initial partons inside the incoming hadrons (pp or $\bar{\mathrm{p}}$p) are taken according to the Duke-Owens structure functions [70] based on measurements from deep inelastic scattering experiments [71].

(2) The initial partons scatter according to the lowest order QCD scattering cross sections.

(3) The final partons fragment into hadrons according to the fragmentation functions from reference [72].

(4) From 27 GeV to 1800 GeV, the majority of partons contributing to the cross section changed from valence quarks with $x > 0.5$ to gluons with $x < 0.01$.

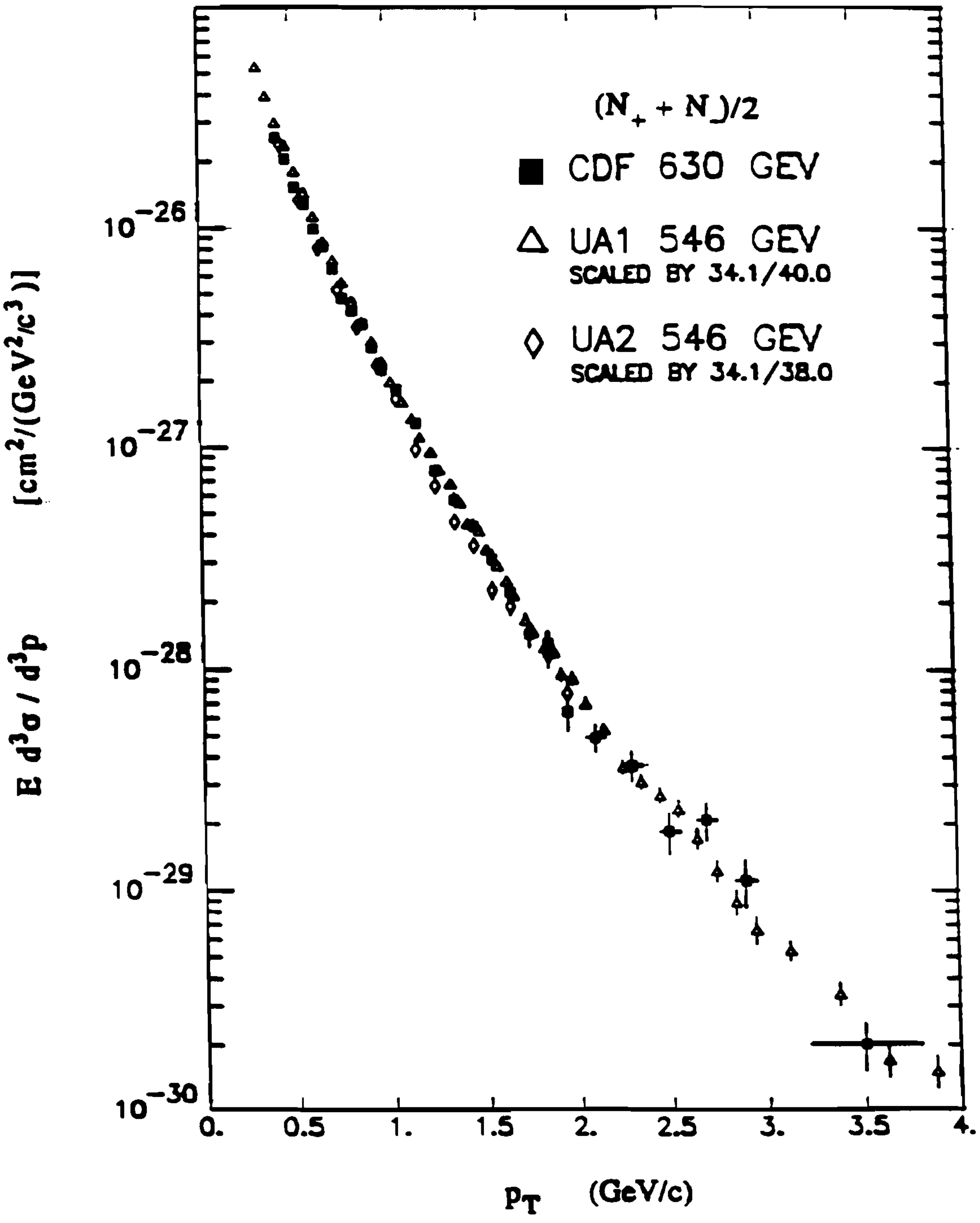

Figure 5.2 A comparison of $E\frac{d^3\sigma}{d^3p}$ between CDF, UA1 and UA2.

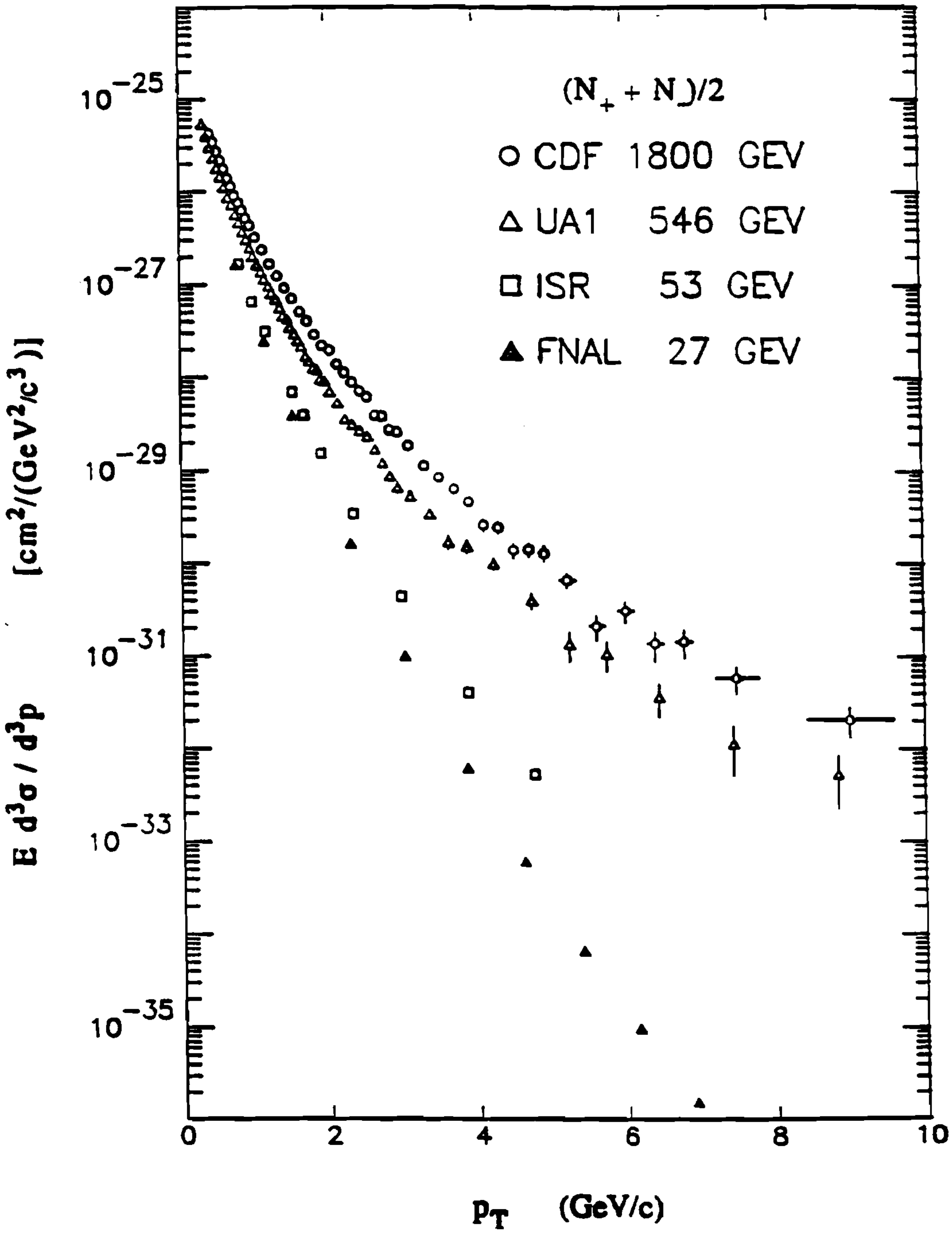

Figure 5.3 $E\frac{d^3\sigma}{d^3p}$ at various center of mass energies.

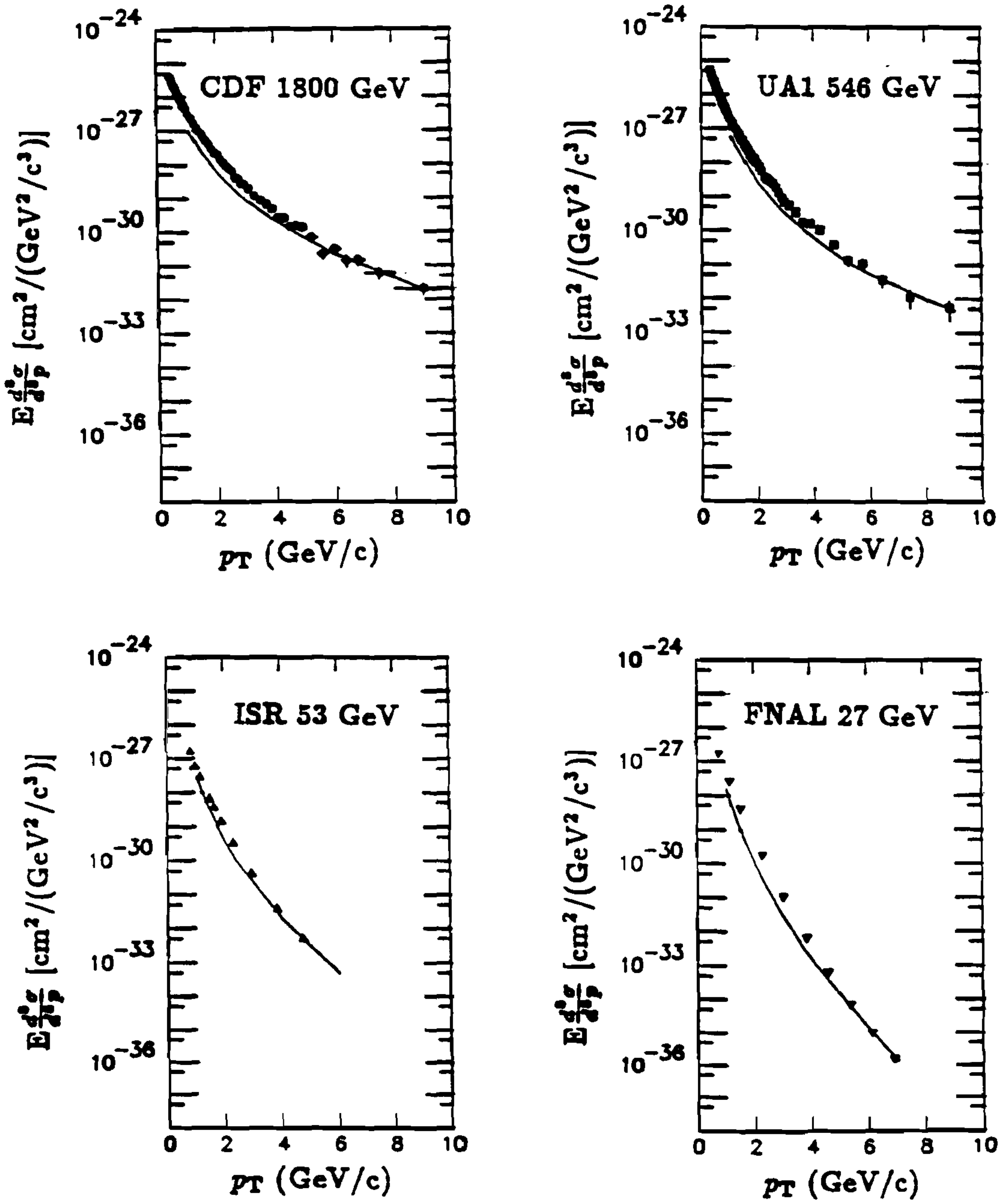

Figure 5.4 A comparison of $E\frac{d^3\sigma}{d^3p}$ with the parton model calculation.

(5) The average value of z decreased as $\sqrt{s}$ increased, hence an increase in the average value of the fragmentation function.

(6) The elementary cross section increased due to a decrease of the average scattering angle.

Given the intrinsic uncertainties of the model, such as applicability of the perturbative calculations, structure functions at very low x, higher order corrections, and Q^2-scale definition, the agreement between the experimental and calculated cross sections is surprisingly good over the p_T range 2 GeV/c to 10 GeV/c, for a range of 10 orders of magnitude in the measured cross section and over a range of $\sqrt{s}$ increasing by a factor of 60.

5.3 Fit Results to the Functional Forms

If the p_T distribution for soft $\bar{p}p$ interactions were kinematically limited and almost independent of the center of mass energy, the inclusive invariant cross section for charged particles should change slowly with $\sqrt{s}$ and have an exponential dependence on p_T [13-17,73]:

$$E\frac{d^3\sigma}{d^3p} \propto e^{-ap_T},$$

where a is related to the proton radius. However, at the Tevatron collider, the available energy is so high that the accessible high p_T region should be unaffected by kinematic limitations and the spectrum should reflect the distribution of constituents in the proton, their hard scattering cross section and their subsequent fragmentation [12]. In the previous measurements [16-19] at $\sqrt{s} > 100$ GeV, the cross section has been observed to depend more strongly on $\sqrt{s}$ and to exhibit a power law dependence in p_T

$$E\frac{d^3\sigma}{d^3p} \propto p_T^n, \qquad (15)$$

as in Rutherford scattering [44].

The invariant cross sections at 630 GeV and 1800 GeV were fitted with the functional form

$$\mathrm{E}\frac{d^3\sigma}{d^3p} = \mathrm{A}(\frac{p_o}{p_o + p_\mathrm{T}})^n. \tag{16}$$

The fits describe the data well in the entire p_T range (see Figure 5.1) and were stable against changes of the p_T range used in the fit. The fit parameters and their statistical errors are given in Table 5.3 and 5.4. As a consequence of a very strong correlation between p_o and n (correlation coefficient = 0.98), their errors are relatively large. To see the power law dependence on p_T as a function of $\sqrt{s}$, the data was fitted with p_o fixed at 1.3 GeV/c. The power n decreases by 0.6 with the increase of $\sqrt{s}$ from 630 GeV to 1800 GeV, reflecting the hardening of the p_T spectrum with increasing $\sqrt{s}$. The result at 630 GeV: $n = 8.89 \pm 0.06$ is in reasonable agreement with a slightly harder spectrum than the UA1 result at 546 GeV: $n = 9.14 \pm 0.02$ [18].

5.4 The Mean Value of Transverse Momentum

The definition of the mean value of transverse momentum, $< p_\mathrm{T} >$, is

$$< p_\mathrm{T} > = \frac{\int_0^\infty \frac{d\sigma}{dp_\mathrm{T}} p_\mathrm{T} dp_\mathrm{T}}{\int_0^\infty \frac{d\sigma}{dp_\mathrm{T}} dp_\mathrm{T}} \tag{17}$$

where the determination of the mean value of transverse momentum relies on the extrapolation of the observed spectrum ($p_\mathrm{T} \geq 400$ MeV/c) to $p_\mathrm{T} = 0$. The error in $< p_\mathrm{T} >$ due to uncertainty in the shape of the spectrum at low p_T can be reduced by using constraints from the measurement of dN/dη.

Calculation of $< p_\mathrm{T} >$

Since the p_T spectrum is factorized in η and ϕ space, the multiplicity distribution in η (dN/dη) can be written in terms of the invariant cross section ($\mathrm{E}\frac{d^3\sigma}{d^3p}$):

$$\frac{dN}{d\eta} = \frac{2\,\Delta\phi}{\sigma_{\mathrm{eff}}\,\Delta\eta}\int_0^\infty \mathrm{E}\frac{d^3\sigma}{d^3p}\, p_\mathrm{T}\, dp_\mathrm{T} \int_{\eta\ \mathrm{min}}^{\eta\ \mathrm{max}} J_{y\rightarrow\eta} d\eta, \tag{18}$$

Table 5.3 Fit parameters for $E\frac{d^3\sigma}{d^3p}$ at $\sqrt{s} = 1800$ GeV.

Fit interval (GeV/c)	A (10^{-24}cm^2/(GeV^2/c^3))	p_o (GeV/c)	n	χ^2	DOF
0.4-10.0	0.45 ± 0.01	1.29 ± 0.02	8.26 ± 0.08	102	64
0.5-10.0	0.45 ± 0.01	1.30 ± 0.02	8.26 ± 0.07	90	62
0.6-10.0	0.46 ± 0.01	1.27 ± 0.02	8.18 ± 0.06	87	60
0.7-10.0	0.43 ± 0.01	1.32 ± 0.02	8.31 ± 0.07	80	58
0.4- 5.0	0.44 ± 0.01	1.30 ± 0.01	8.29 ± 0.06	101	61
0.5- 5.0	0.47 ± 0.01	1.25 ± 0.01	8.12 ± 0.05	86	59
0.6- 5.0	0.46 ± 0.01	1.27 ± 0.01	8.17 ± 0.05	85	57
0.7- 5.0	0.43 ± 0.01	1.31 ± 0.01	8.29 ± 0.05	79	55
0.4- 3.0	0.46 ± 0.01	1.26 ± 0.01	8.11 ± 0.08	92	49
0.5- 3.0	0.50 ± 0.01	1.16 ± 0.01	7.82 ± 0.05	72	47
0.6- 3.0	0.50 ± 0.01	1.16 ± 0.01	7.79 ± 0.05	72	45
0.4-10.0	0.45 ± 0.01	1.30 fixed	8.28 ± 0.02	103	65
0.5-10.0	0.45 ± 0.01	1.30 fixed	8.29 ± 0.02	90	63
0.6-10.0	0.44 ± 0.01	1.30 fixed	8.28 ± 0.02	88	61
0.7-10.0	0.44 ± 0.01	1.30 fixed	8.25 ± 0.02	80	59

Statistical errors only.

to the functional form

$$E\frac{d^3\sigma}{d^3p} = A\frac{p_o^n}{(p_T + p_o)^n}.$$

Table 5.4 Fit parameters for $E\frac{d^3\sigma}{d^3p}$ at $\sqrt{s} = 630$ GeV.

Fit interval (GeV/c)	A (10^{-24}cm^2/(GeV^2/c^3))	p_o (GeV/c)	n	χ^2	DOF
0.4-10.0	0.27 ± 0.01	1.63 ± 0.13	10.2 ± 0.56	32	33
0.4-5.0	0.27 ± 0.01	1.67 ± 0.06	10.3 ± 0.11	30	31
0.5-5.0	0.26 ± 0.01	1.70 ± 0.14	10.4 ± 0.26	30	29
0.6-5.0	0.28 ± 0.01	1.61 ± 0.12	10.1 ± 0.25	28	27
0.7-5.0	0.27 ± 0.01	1.62 ± 0.05	10.2 ± 0.11	27	25
0.4-3.0	0.26 ± 0.01	1.79 ± 0.05	10.8 ± 0.08	29	30
0.5-3.0	0.24 ± 0.01	1.92 ± 0.09	10.8 ± 0.18	28	28
0.6-3.0	0.24 ± 0.01	1.87 ± 0.13	11.1 ± 0.27	27	26
0.4-10.0	0.33 ± 0.01	1.30 fixed	8.89 ± 0.06	39	34
0.4-5.0	0.33 ± 0.01	1.30 fixed	8.90 ± 0.05	36	32
0.5-5.0	0.33 ± 0.01	1.30 fixed	8.93 ± 0.07	34	30
0.6-5.0	0.35 ± 0.01	1.30 fixed	9.00 ± 0.08	30	28
0.7-5.0	0.36 ± 0.01	1.30 fixed	9.03 ± 0.08	29	26
UA1 data 0.3-2.0	0.46 ± 0.01	1.30 fixed	9.14 ± 0.02	29	32

Statistical errors only.

to the functional form

$$E\frac{d^3\sigma}{d^3p} = A\frac{p_o^n}{(p_T + p_o)^n}.$$

where

$$J_{y\rightarrow\eta} = \frac{dy}{d\eta} = \frac{cosh(\eta)}{\sqrt{1 + \frac{m^2}{p_T^2} + sinh^2(\eta)}}. \tag{19}$$

If the value of dN/dη at $\sqrt{s}$ = 1800 or 630 GeV can be either measured or estimated in the whole p_T range (0,∞), then the shape of the invariant cross section at the region of p_T below 400 MeV/c can be determined. Using the data points from the measured invariant cross section for $p_T \geq$ 400 MeV/c and the constraining condition;

$$\begin{aligned} \frac{dN}{d\eta}_{(0,p_T^*)} &= \frac{dN}{d\eta}_{(0,\infty)} - \frac{dN}{d\eta}_{(p_T^*,\infty)} \\ &= \frac{2\,\Delta\phi}{\sigma_{eff}\,\Delta\eta}\int_0^{p_T^*} \mathrm{E}\frac{d^3\sigma}{d^3p}_{(0,p_T^*)} p_T\, dp_T \int J_{y\rightarrow\eta} d\eta \end{aligned} \tag{20}$$

with p_T^* = 400 MeV/c, the shape of the invariant cross section in the range (0,p_T^*) was fitted to various functions. The corrected $< p_T >$ for all p_T was calculated from

$$< p_T >= \frac{\int_0^{p_T^*} \frac{d\sigma}{dp_T} dp_T}{\int_0^{\infty} \frac{d\sigma}{dp_T} dp_T}\int_0^{p_T^*} \frac{d\sigma}{dp_T} p_T dp_T + \frac{\int_{p_T^*}^{\infty} \frac{d\sigma}{dp_T} dp_T}{\int_0^{\infty} \frac{d\sigma}{dp_T} dp_T}\int_{p_T^*}^{\infty} \frac{d\sigma}{dp_T} p_T dp_T \tag{21}$$

using the fit result for the shape of p_T distribution below 400 MeV/c.

Interpolation of dN/dη measurements in the range 200 to 900 GeV [9] gives dN/dη = 3.30±0.15 at 630 GeV, in agreement with the preliminary result from the VTPC data of dN/dη = 3.3±0.2 [10]. Using the ratio of dN/dη at 1800 GeV to that at 630 GeV from the analysis of the VTPC data, 1.27±0.04, the value of dN/dη at 1800 GeV was estimated to be 4.2±0.2. Using these values, the constrained fit gives $< p_T >=$ 432±4 MeV/c at 630 GeV and $< p_T >=$ 495±14 MeV/c at 1800 GeV. The errors were estimated by including uncertainties due to the extrapolation to low p_T as well as in the ratio of dN/dη. By varying the functional form of the p_T spectrum for $p_T <$ 400 MeV/c with fixed dN/dη (see Figure 5.5), the systematic error on $< p_T >$ due to the choice of functional form was estimated to be 3 MeV/c. In addition, the 5 % uncertainty in the

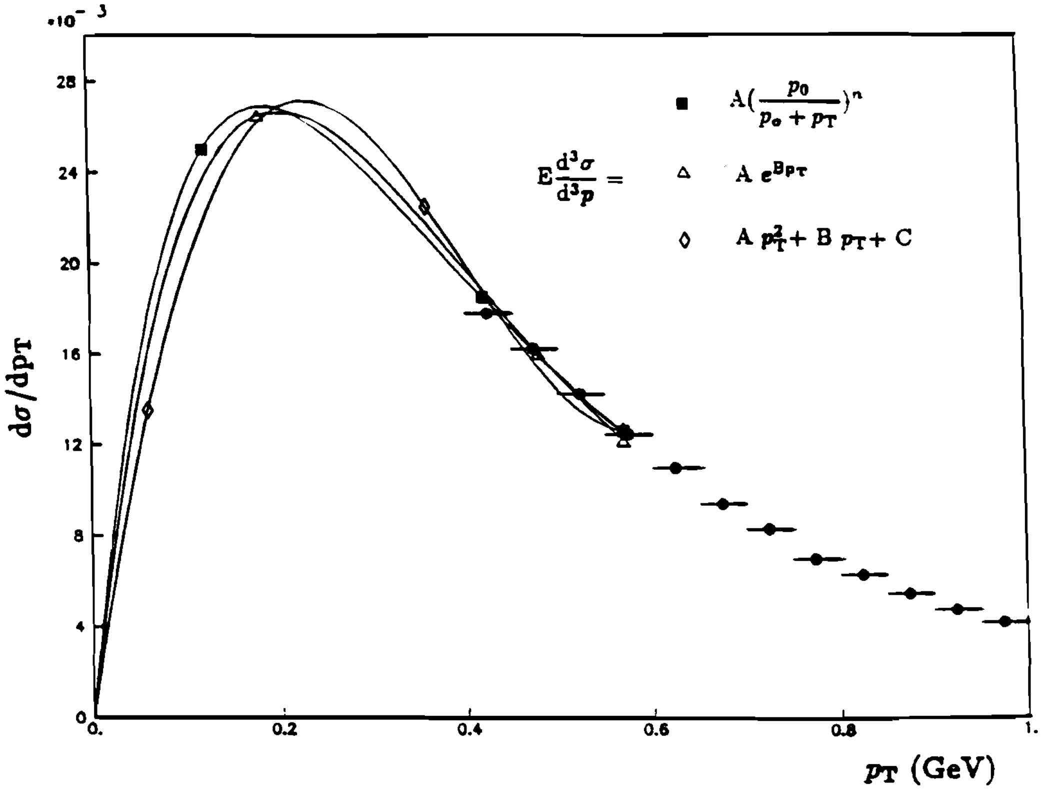

Figure 5.5 The extrapolated $d\sigma/dp_T$ by different functional forms.

value of $dN/d\eta$ at 630 GeV gives an additional error of 20 MeV/c common to both values of $< p_T >$. The fit parameters of the invariant cross section at $p_T < 400$ MeV/c and values of $< p_T >$ from the different functional forms are listed in Table 5.5 - 5.7.

log(s) dependence of $< p_T >$

The calculated $< p_T >$ values were compared with values from other measurements [16,18,22]. The value of $< p_T >$ grows significantly as a function of $\sqrt{s}$ (Figure 5.6), in agreement with the trend observed in cosmic ray interactions [74].

Although the rise with log(s) of the high p_T tail of the particle spectrum is striking, the value of $< p_T >$ is largely determined by particles with 1 GeV/c $< p_T <$ 3 GeV/c. This can be seen from the measured (for $p_T \geq 400$ MeV/c) and estimated (for $p_T < 400$ MeV/c) invariant cross sections. The contributions of particles in the higher p_T range to the value of $< p_T >$ were compared for $\sqrt{s} = 1800$ and 630 GeV in Figure 5.7. The average transverse momentum excluding the particles above a certain p_T cut-off (x-axis) and the ratio between 1800 and 630 GeV are shown where the difference in $< p_T >$ values between 630 and 1800 GeV is mostly coming from charged particles with $p_T < 2$ GeV/c.

$< p_T >^*$ dependence on Multiplicity

In Figure 5.8 the charged p_T spectrum is shown seperately for three bands of charged particle multiplicity in the rapidity range $|y| < 1.0$. The three spectra are normalised at $p_T = 0$ GeV/c. The p_T spectrum becomes flatter as the multiplicity increases, and this trend occurs even at low values of p_T.

Due to the large uncertainty in the multiplicity measurement for finer multiplicity bins, the method which was used to calculate $< p_T >$ for the total invariant cross section was not applicable for calculating $< p_T >$ as a function

Table 5.5 Functional forms used for $< p_T >$ calculation.

functional forms ($f_n = E\frac{d^3\sigma}{d^3p}$)	parameters				fit interval p_T (MeV/c)
	p1	p2	p3	p4	
f_1	A	p_o	n		400-800
f_2	A	B			400-600
f_3	A	B	C		400-600
f_4	A	B	C	n	400-600

$$
\begin{aligned}
f_1 &= A\frac{p_o^n}{(p_T + p_o)^n} \\
f_2 &= A\ e^{-B\ p_T} \\
f_3 &= A\ e^{(-B\ p_T^2 + C\ p_T)} \\
f_4 &= A\ (p_T^{n+1} + B\ p_T^n + C)
\end{aligned}
$$

Table 5.6 Fit parameters and $< p_T >$ values at $\sqrt{s} = 1800$ GeV.

$dN/d\eta = 4.2$

f_n	p1	p2	p3	p4	χ^2/DOF	$< p_T >$ (MeV/c)
f_1	0.44	1.37	8.6		60.3/38	494
f_2	0.37	4.99			99.0/19	496
f_3	0.36	0.10	-4.9		105.7/18	496
f_4	0.28	-12.4	11.5	0.063	41.0/17	492

$dN/d\eta = 4.3$

f_n	p1	p2	p3	p4	χ^2/DOF	$< p_T >$ (MeV/c)
f_1	0.52	0.98	6.9		71.9/38	483
f_2	0.41	5.19			154.8/19	487
f_3	0.40	0.10	-5.1		166.2/18	487
f_4	0.33	-11.2	10.3	0.067	54.2/17	482

$dN/d\eta = 4.1$

f_n	p1	p2	p3	p4	χ^2/DOF	$< p_T >$ (MeV/c)
f_1	0.37	2.16	12.1		50.0/38	505
f_2	0.34	4.81			59.6/19	506
f_3	0.33	0.0002	-4.8		58.5/18	506
f_4	0.24	-11.9	11.0	0.070	32.1/17	503

Table 5.7 Fit parameters and $< p_T >$ values at $\sqrt{s} = 630$ GeV.

$dN/d\eta = 3.3$

f_n	p1	p2	p3	p4	χ^2/DOF	$< p_T >$ (MeV/c)
f_1	0.39	0.86	6.7		37.7/38	429
f_2	0.29	5.61			28.0/19	434
f_3	0.29	0.10	-5.5		28.6/18	434
f_4	0.25	-10.7	9.8	0.067	17.0/17	429

$dN/d\eta = 3.3\times1.05$

f_n	p1	p2	p3	p4	χ^2/DOF	$< p_T >$ (MeV/c)
f_1	0.52	0.58	5.4		38.6/38	412
f_2	0.35	5.94			36.4/19	418
f_3	0.35	0.04	-5.9		36.4/18	418
f_4	0.31	-11.2	10.3	0.060	17.4/17	413

$dN/d\eta = 3.3\times0.95$

f_n	p1	p2	p3	p4	χ^2/DOF	$< p_T >$ (MeV/c)
f_1	0.29	1.61	10.3		36.7/38	449
f_2	0.25	5.24			21.8/19	451
f_3	0.24	0.10	-5.2		22.2/18	451
f_4	0.19	-10.6	9.7	0.073	17.4/17	447

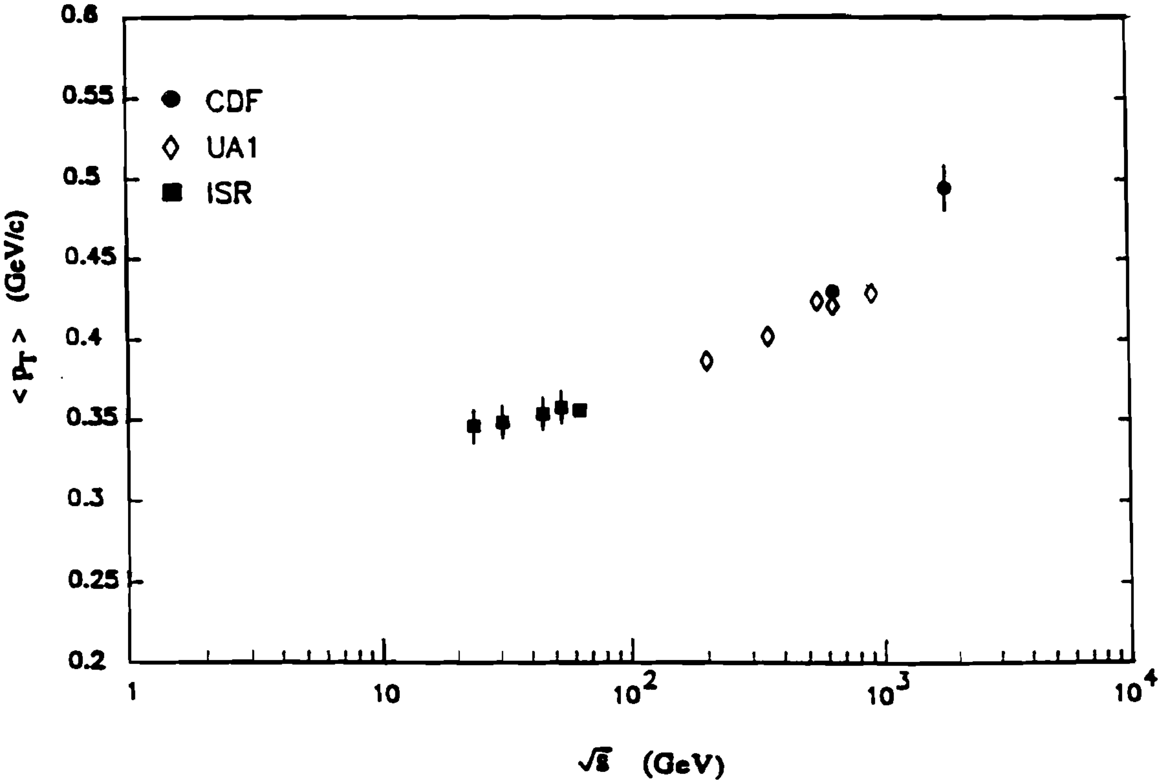

Figure 5.6 $< p_T >$ versus $\sqrt{s}$.

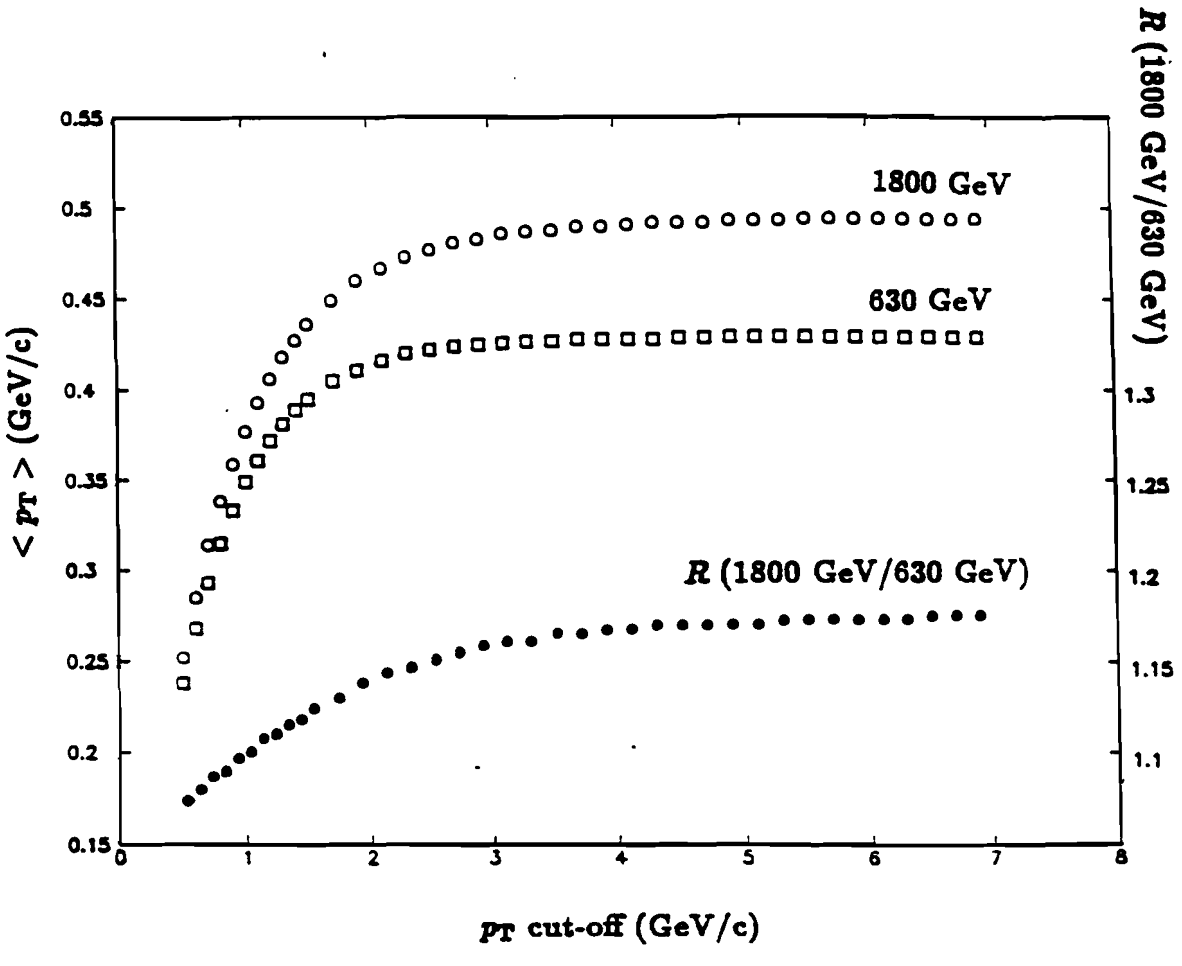

Figure 5.7 $< p_T >$ below p_T cut-off.

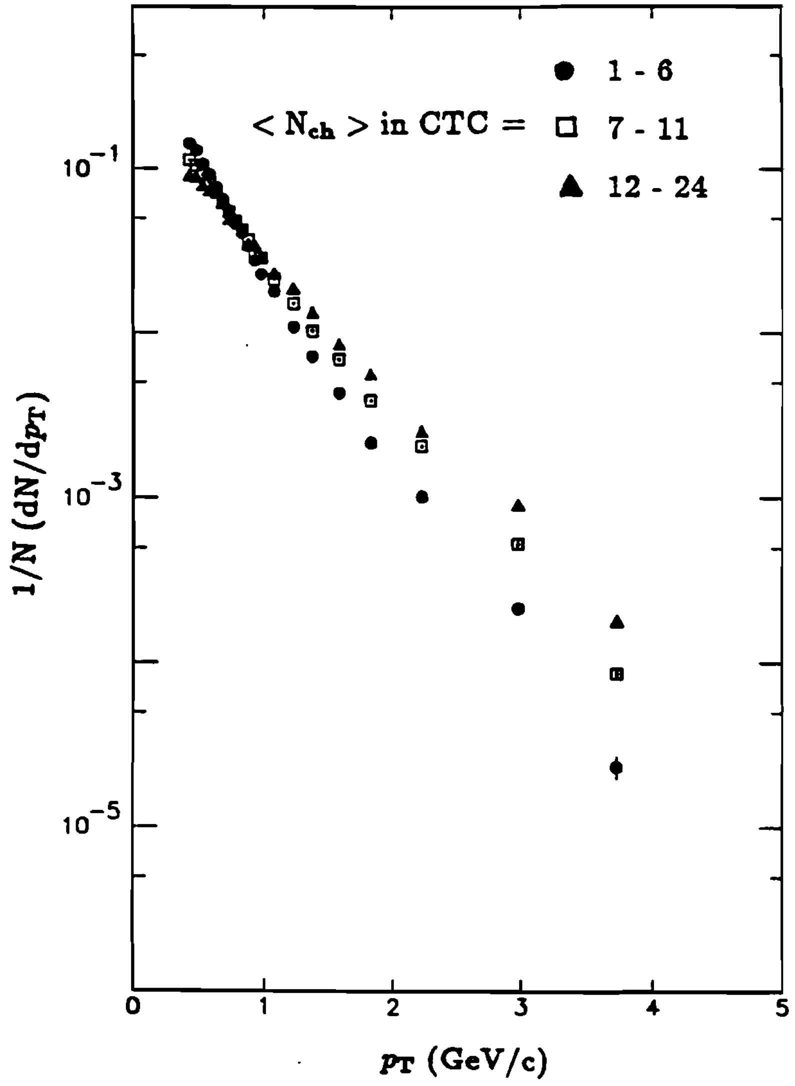

Figure 5.8 The p_T spectra in different multiplicity bins.

of multiplicity.

The multiplicity dependence of the average momentum was studied for tracks with $p_T \geq 400$ MeV/c. By defining $< p_T >^*$:

$$< p_T >^* = \frac{\int_{p_T^*}^{\infty} \frac{d\sigma}{dp_T} p_T \, dp_T}{\int_{p_T^*}^{\infty} \frac{d\sigma}{dp_T} dp_T}, \tag{22}$$

the observed dependence of $< p_T >^*$ on the charged particle multiplicity, N_{ch}^*, for $p_T \geq 400$ MeV/c in $|\eta| \leq 1.0$ is shown in Figure 5.9. The increase in $< p_T >^*$ with increasing charged multiplicity was observed at both 630 and 1800 GeV, but it was more pronounced at the higher energy.

This strong multiplicity dependence of the $< p_T >^*$ was also observed by the E735 (C0) collaboration at FNAL [75] for $\sqrt{s} = 1800$ GeV. For a comparison, the following cuts were applied on the data from each experiment.
(1) CDF data : the multiplicity was measured by the VTPC in $|\eta| \leq 2.5$ for charged particles with $p_T > 50$ MeV/c, and $< p_T >^*$ was calculated by using momentum measurements for $p_T \geq 400$ MeV/c from the CTC.
(2) E735 data : the multiplicity measurement from the central hodoscope in $|\eta| \leq 2.5$ and the momentum measurement from the straw chamber for charged particles with p_T cut-off at ≥ 400 MeV/c to match the CTC p_T cut-off.
The distributions of multiplicity verse $< p_T >^*$ from CDF and E735 were shown in Figure 5.10, where both measurements agree well.

5.5 <u>dN*/dη and Scaling Behavior in the CTC.</u>

For charged particles with $p_T \geq 400$ MeV/c, the multiplicity distributions (dN*/dη), distributions of KNO and Feynman scaling were measured in $|\eta| \leq 1.0$.

<u>dN*/dη distribution</u>

The distributions of average charged particle multiplicity per unit pseudorapidity in the region $|\eta| \leq 1.0$ and $p_T \geq 400$ MeV/c are shown in Figure 5.11

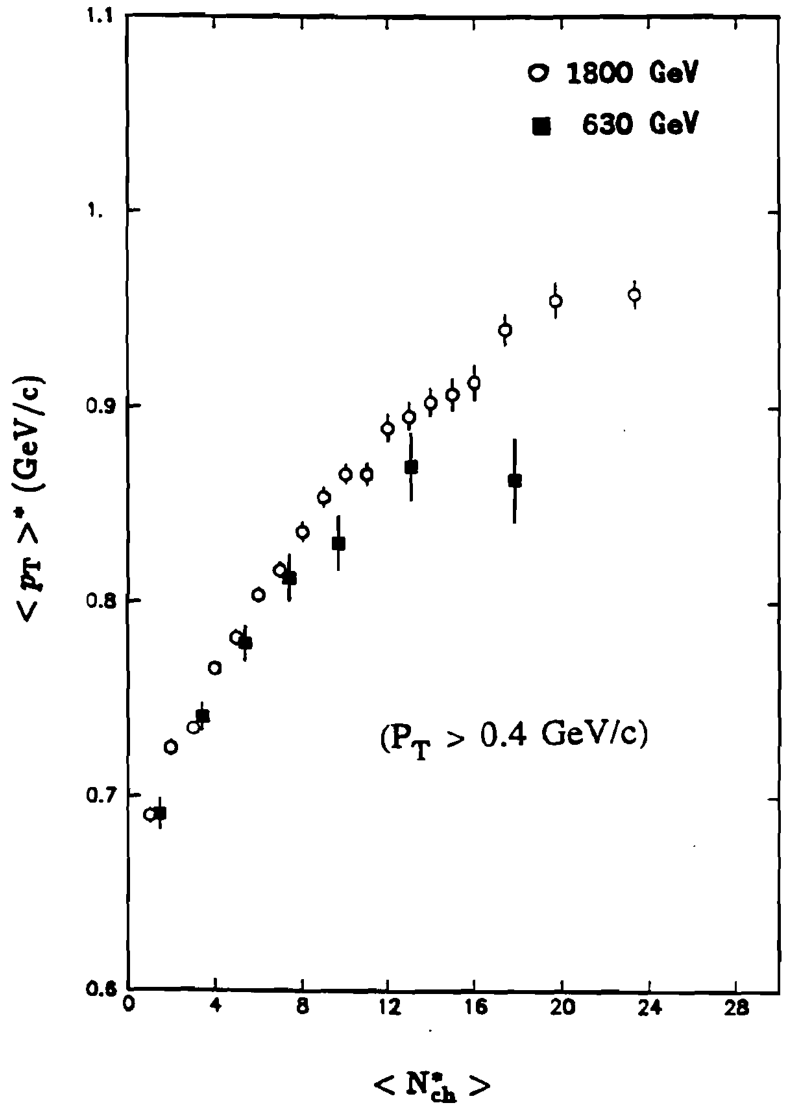

Figure 5.9 $< p_T >^*$ **versus** $< N^*_{ch} >$.

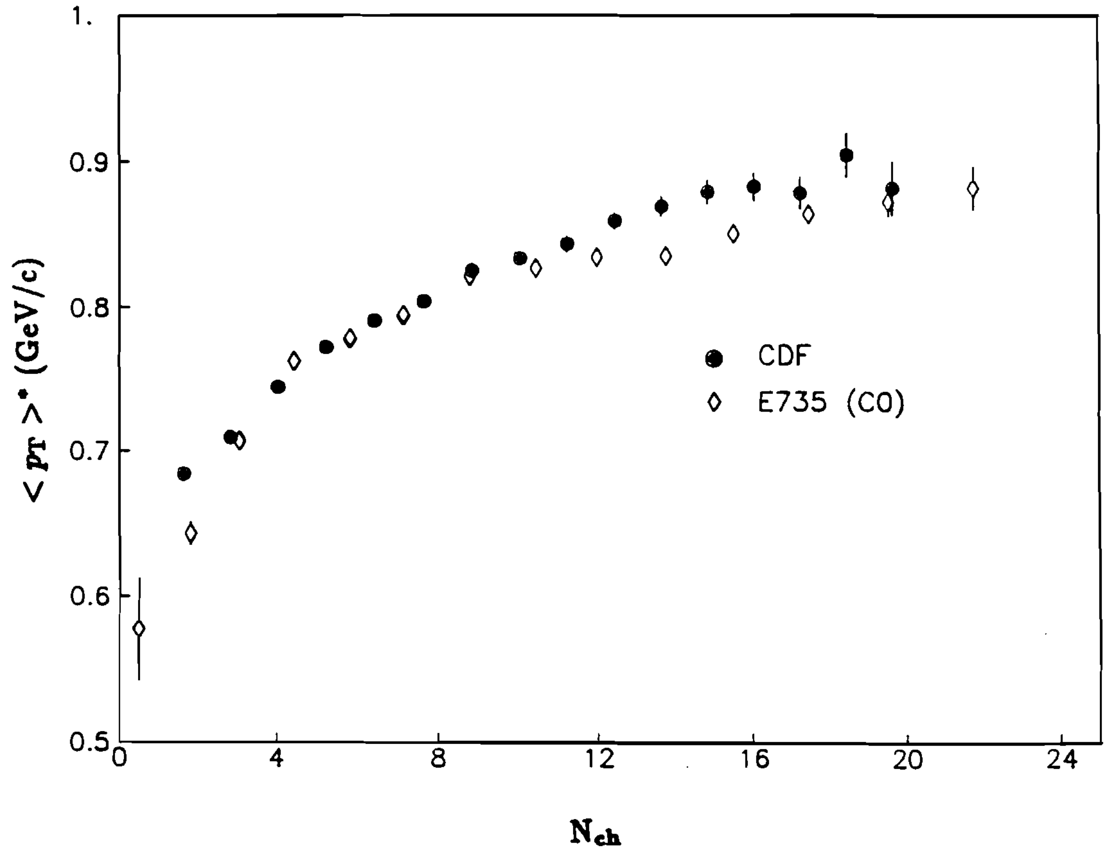

Figure 5.10 $< p_T >^*$ versus multiplicity from CDF and E735.

for the both $\sqrt{s}$ = 630 and 1800 GeV data. The values of $< dN^*/d\eta >$ are 2.1±0.1 for 1800 GeV and 1.5±0.1 for 630 GeV. The average multiplicity per unit pseudorapidity interval is shown as a function of η in Figure 5.12 for for positive and negative particles separately. The shapes of the distributions are consistent with being identical and no η dependence is observed. Figure 5.13 shows the average charged multiplicity per unit pseudorapidity in the region $|\eta| \leq 1.0$ and $p_T \geq p_T$ cut-off for 1800 and 630 GeV. The dotted lines are extrapolations down to p_T cut-off = 0 MeV/c using the estimated values of $dN/d\eta$ from Section 5.4.

KNO Scaling

The KNO scaling [11] in the CTC was obtained by plotting the probability (Ψ) for a particular produced particle multiplicity as a function of the multiplicity normalized to the mean multiplicity ($N^*_{ch}/ < N^*_{ch} >$) (Figure 5.14). The violation of KNO scaling from $\sqrt{s}$ = 630 GeV to 1800 GeV does not seem to be obvious.

Feynman Scaling

One of scaling rules which were valid at lower energy range was Feynman scaling [1]. At higher center of mass energy, even though $\sqrt{s}$ varies by factor of 3 from 630 to 1800 GeV, unlike the KNO scaling, the violation of Feynman scaling was clearly observed (Figure 5.15).

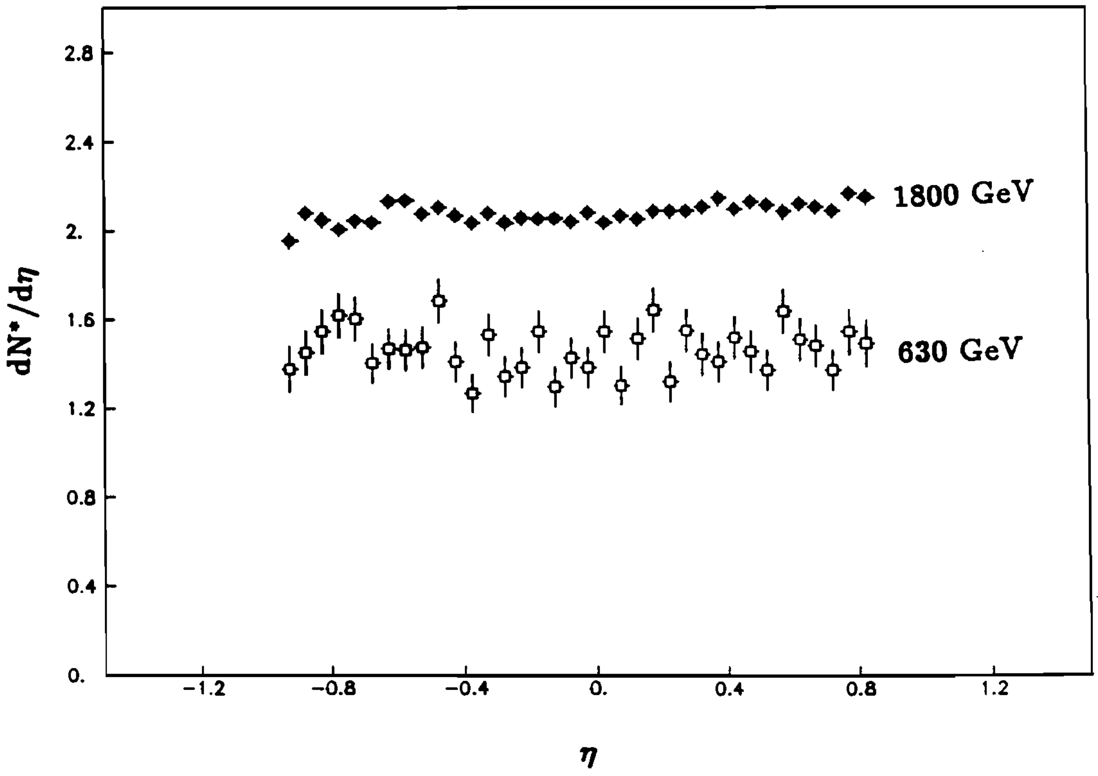

Figure 5.11 dN*/dη measured in the CTC.

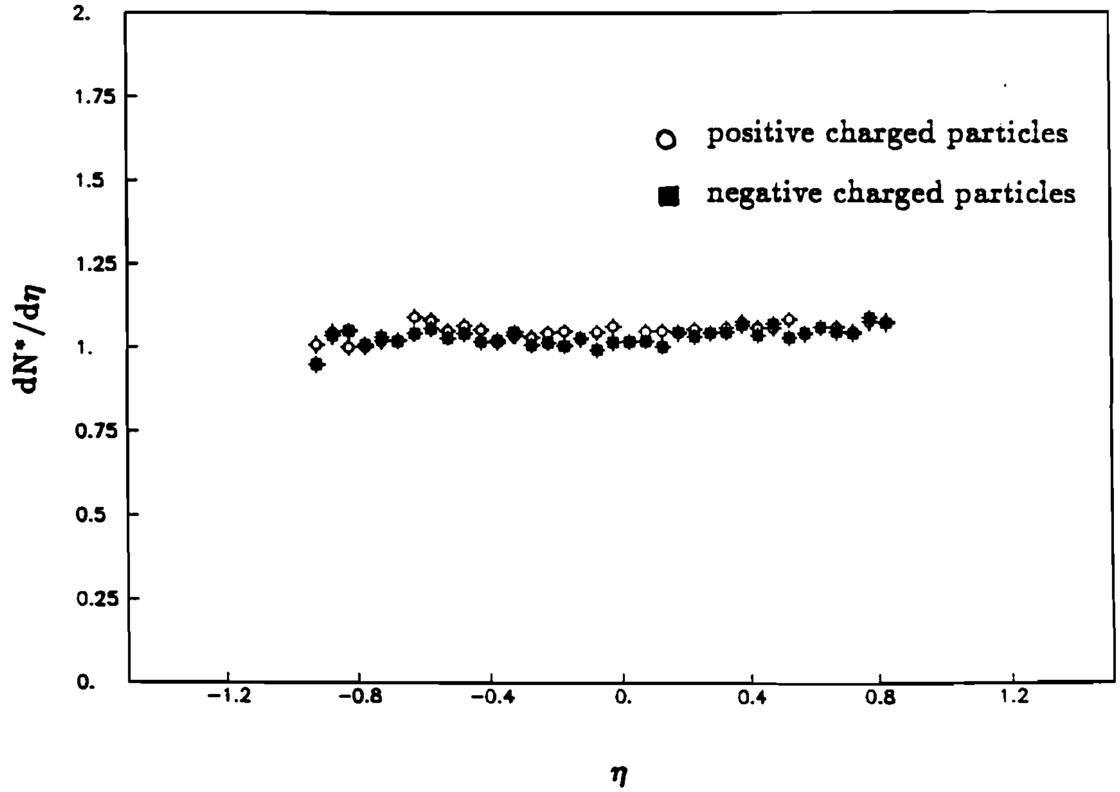

Figure 5.12 $dN^*/d\eta$ for positive and negative particles.

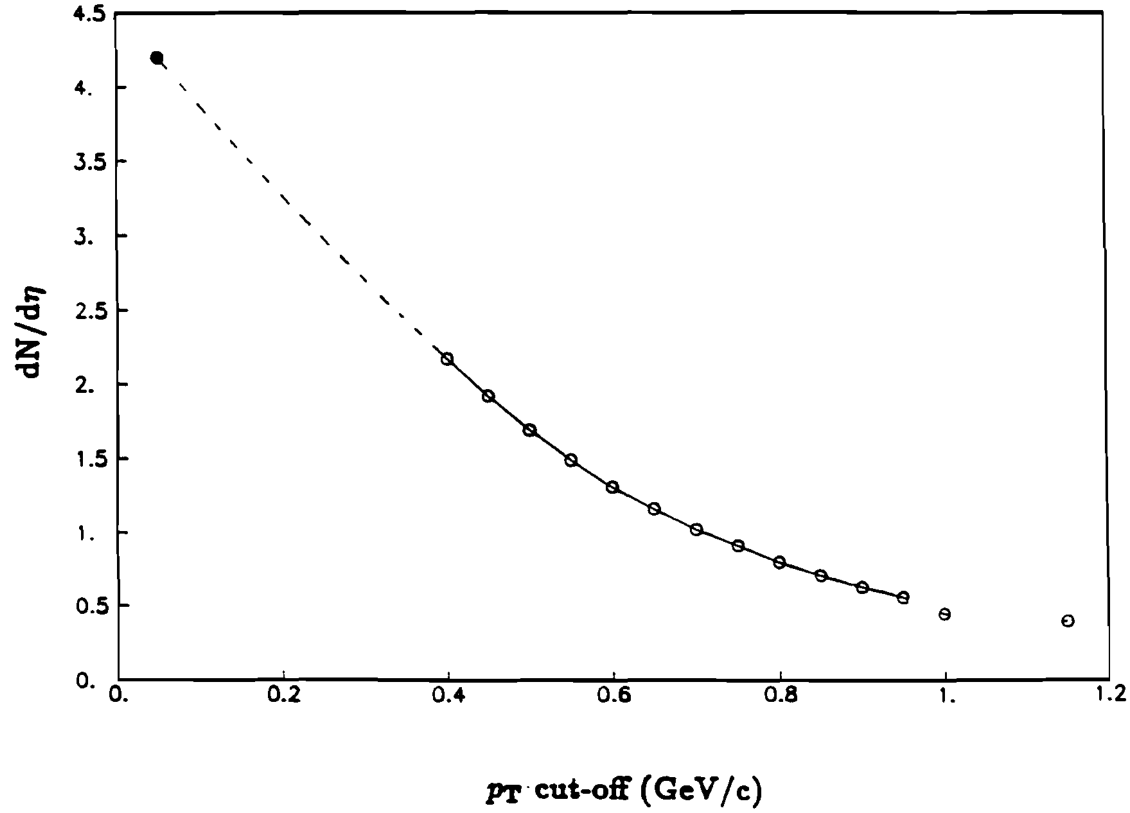

Figure 5.13 dN/dη for $p_T \geq p_T$ cut-off.

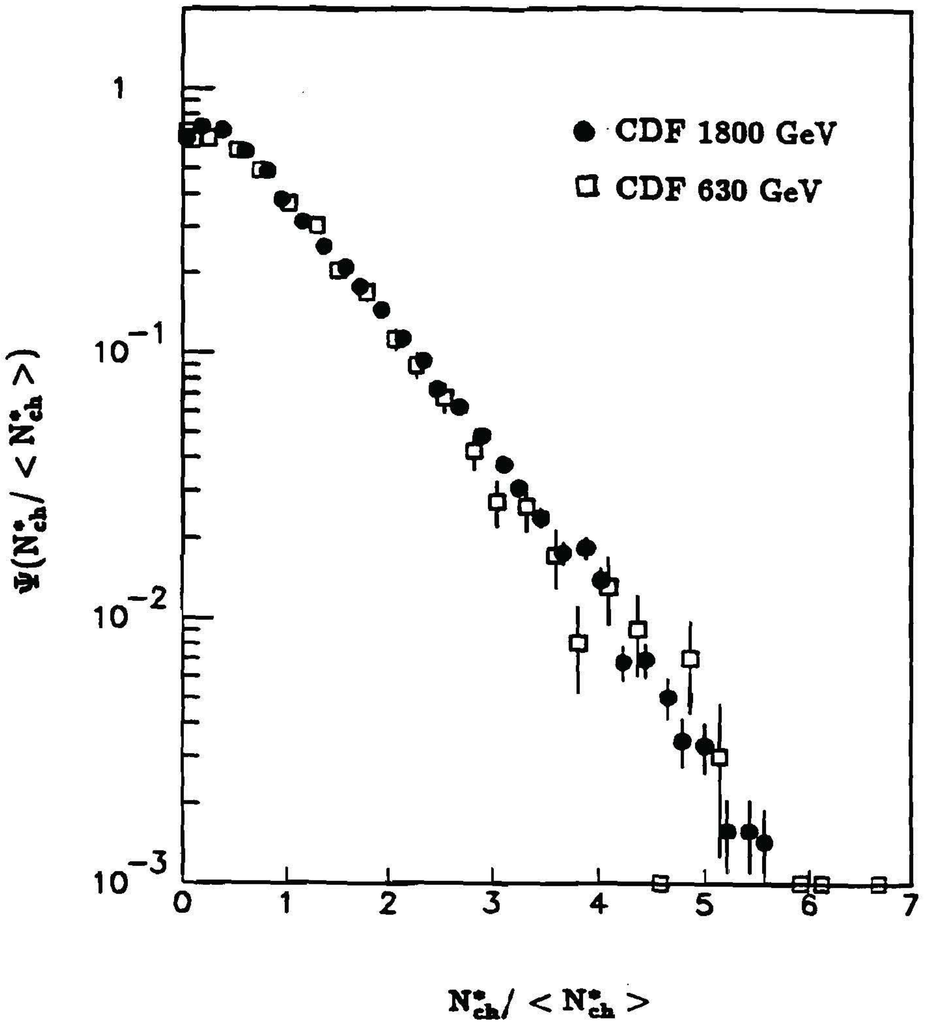

Figure 5.14 KNO distribution for $p_T \geq 400$ MeV/c.

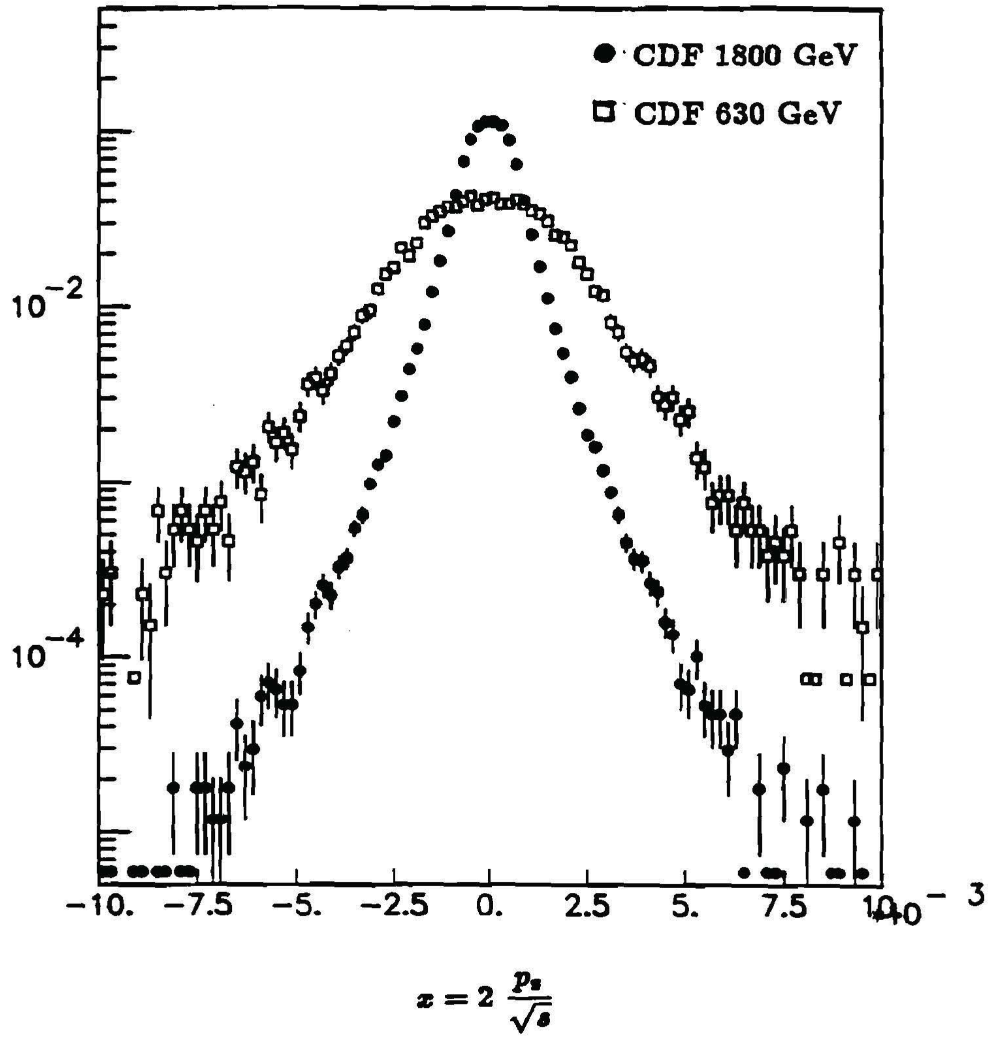

Figure 5.15 Feynman scaling for $p_T \geq 400$ MeV/c.

CHAPTER 6 - CORRELATION OF CHARGED PARTICLES

Strong correlations between particles in minimum bias events with the presence of a high momentum particle were observed at ISR and SPS energies [28,76-78]. These correlations were usually interpreted as a sign of hard scattering and subsequent fragmentation of partons into hadrons. In this Chapter, the correlations and momentum densities in pseudorapidity and azimuthal angle between charged particles are studied at $\sqrt{s} = 1800$ GeV. It has been observed that charged tracks tend to cluster around high p_T tracks. With the presence of a high p_T particle, the correlations become more pronounced as the transverse momentum of the "trigger" particle increases and are much stronger than the general two particle correlations in minimum bias events.

6.1 Correlations in $\phi - \eta$

Without referring to a particular model, the overall event structure can be observed qualitatively. One method which is very frequently used is the study of $\phi - \eta$ correlations between two particles. Using techniques similar to that used at lower energies [28,76], a software "trigger" particle was defined as a track having p_T in a required interval. Because the geometrical acceptance and track finding efficiency of the CTC drops rapidly for $|\eta| > 1.0$, the trigger particle was required to be within $-0.5 \leq \eta \leq 0.5$ to give a reasonable efficiency of measuring the "secondaries". The secondary particles are defined as all other tracks measured in the same event.

The azimuthal plane was divided into two semicircles as the "towards" direction (the azimuthal semicircle centered on the trigger particle) and the "away" direction (the semicircle opposite to the trigger particle). In the $\phi - \eta$

correlation studies, the trigger particle was not included in the correlation histograms.

Minimum bias data

Figure 6.1 shows the multiplicity density of all secondary particles with respect to a randomly chosen trigger particle (any value of p_T and $|\eta| \leq 0.5$) in unselected minimum bias events. The pseudorapidity distributions are also given separately for the towards and away ϕ semicircles. There is a weak structure in both ϕ and η which is similar to the short range correlations seen by the UA1 collaboration for a random trigger particle [28].

On the contrary, stronger correlations in both ϕ and η are observed by requiring higher p_T ($p_T \geq 1$ GeV/c, $p_T \geq 2$ GeV/c) for the secondary particles (Figures 6.2 - 6.3) or higher p_T (≥ 4 GeV/c) trigger particle (Figures 6.4 and 6.5). To see the energy flow of the event, the entries were also weighted by their momenta (second rows of Figures 6.1 - 6.5) and it is observed that high p_T secondaries tend to cluster around the trigger particle in both ϕ and η.

For towards secondaries, a clear correlation is seen in both ϕ and η. For away secondaries, the relative rapidity distribution remains broad. However, an azimuthal correlation emerges around 180° with respect to the trigger. This indicates that high p_T away secondaries are preferentially coplanar with the trigger and the beam.

Jet data

The correlations in minimum bias events were qualitatively compared with those in hard scattering (jet) events. From the 1987 run, a fraction of jet events were selected using a central calorimeter jet trigger and clustering algorithm [79] by demanding ΣE_T of jets in the events should be ≥ 70 GeV, which were clearly dominated by two jet events. Even though the track finding efficiency in jet events was lower than that in minimum bias events due to the dense environment, it was ≥ 70 %.

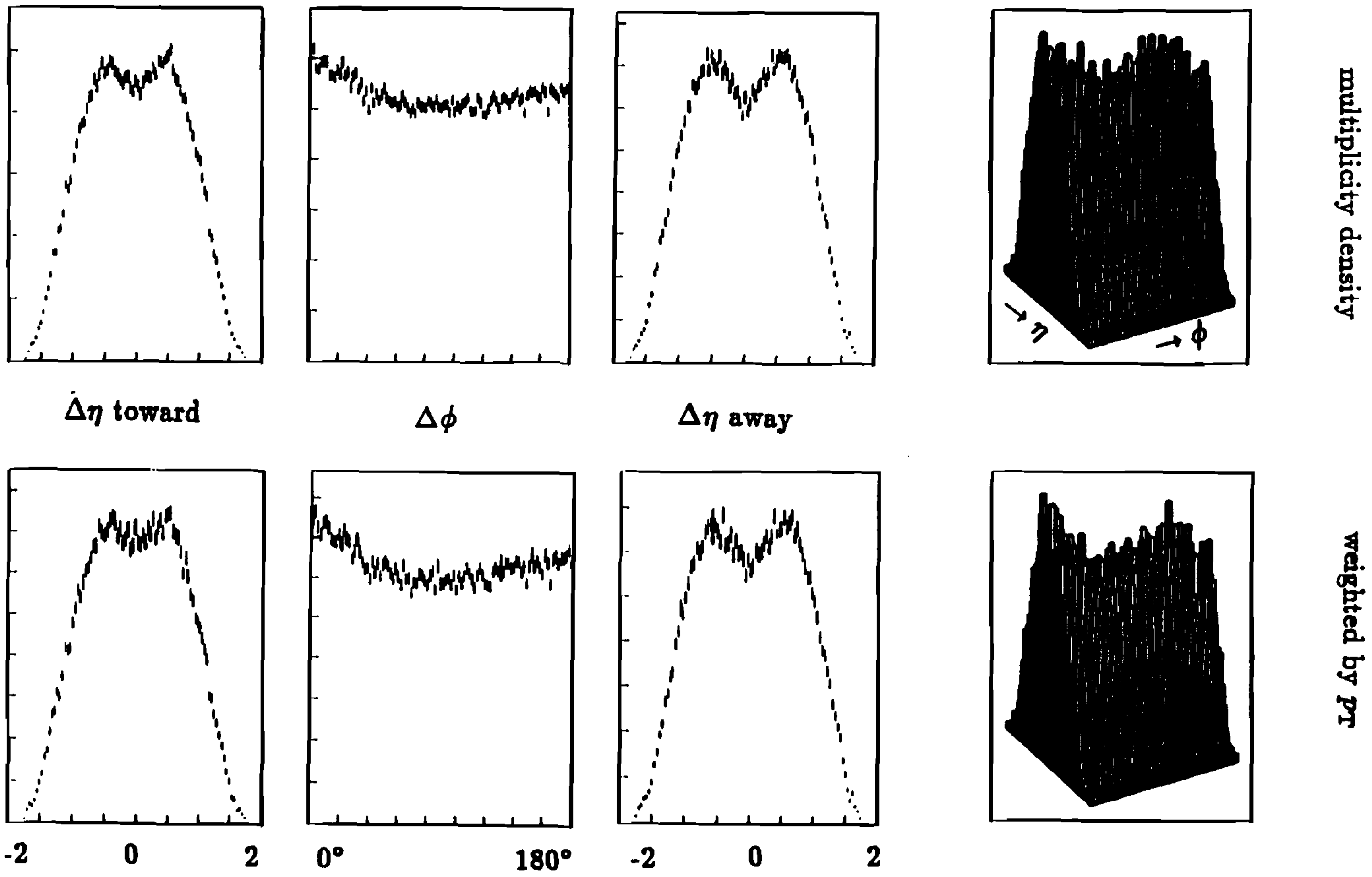

Figure 6.1 $\Delta\phi - \Delta\eta$ with a random trigger and all secondaries.

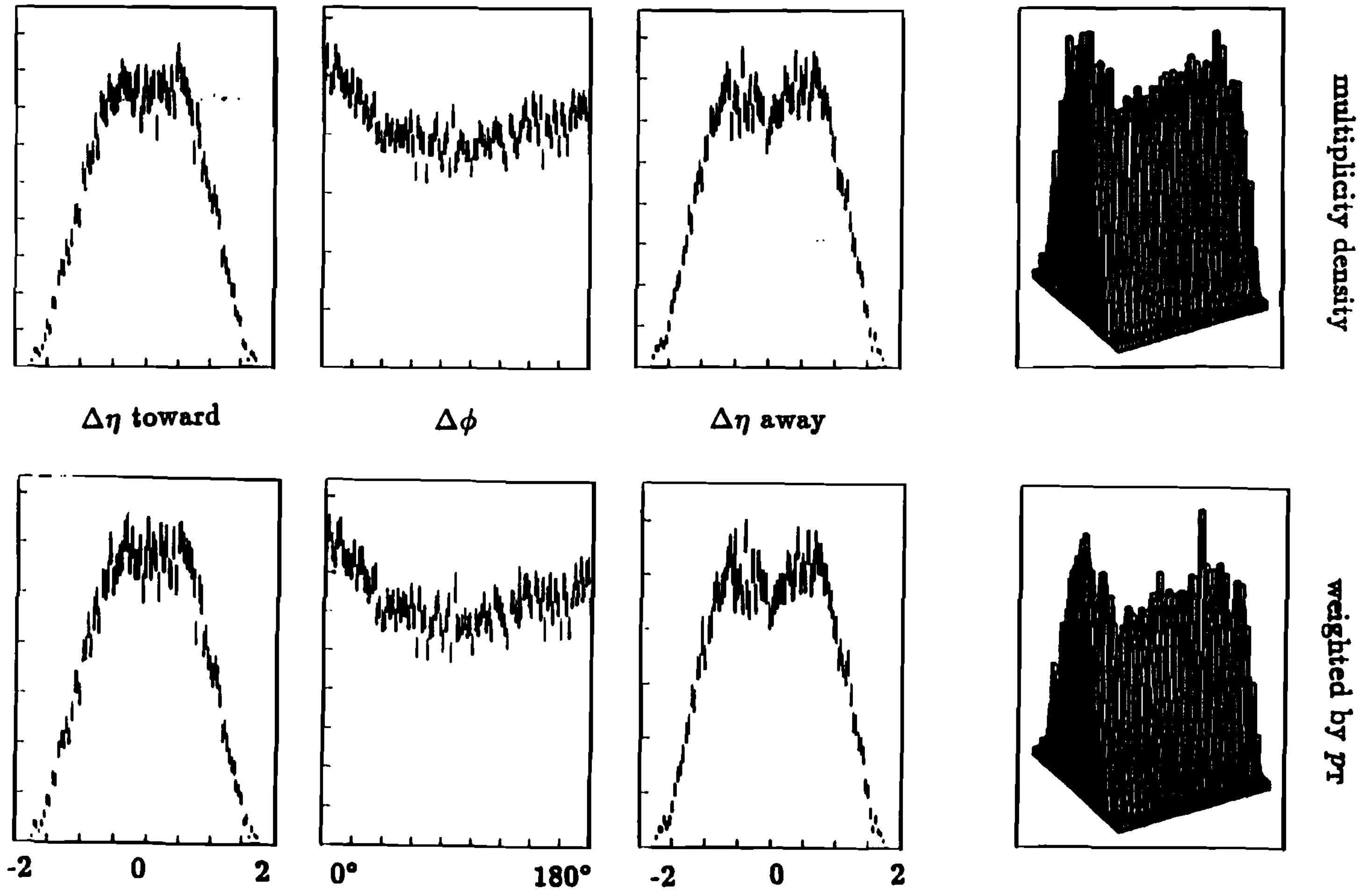

Figure 6.2 $\Delta\phi - \Delta\eta$ with a random trigger and secondary $p_T \geq 1$ GeV/c.

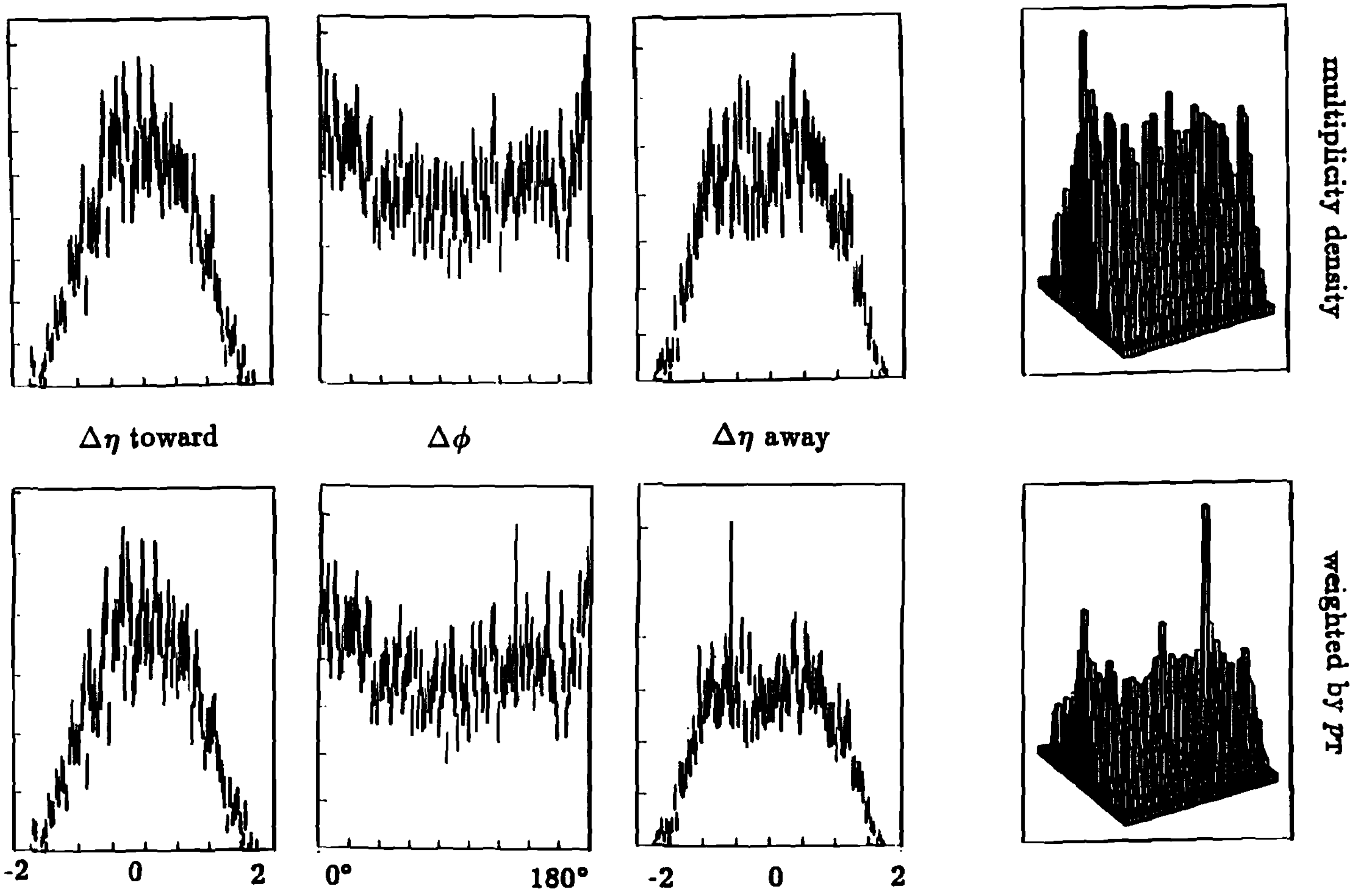

Figure 6.3 $\Delta\phi - \Delta\eta$ with a random trigger and secondary $p_T \geq 2$ GeV/c.

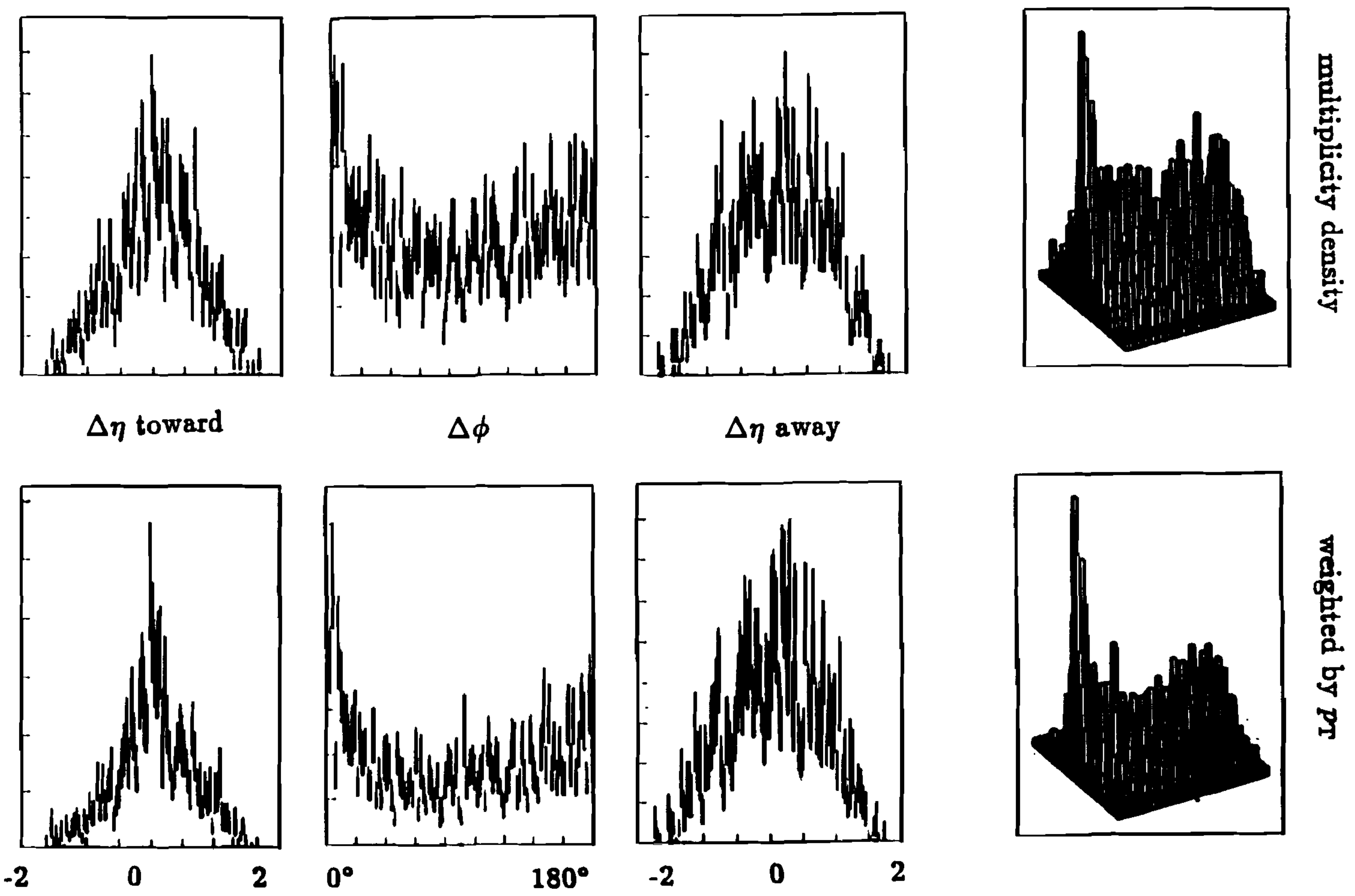

Figure 6.4 $\Delta\phi - \Delta\eta$ with a trigger $p_T \geq 4$ GeV/c and all secondaries.

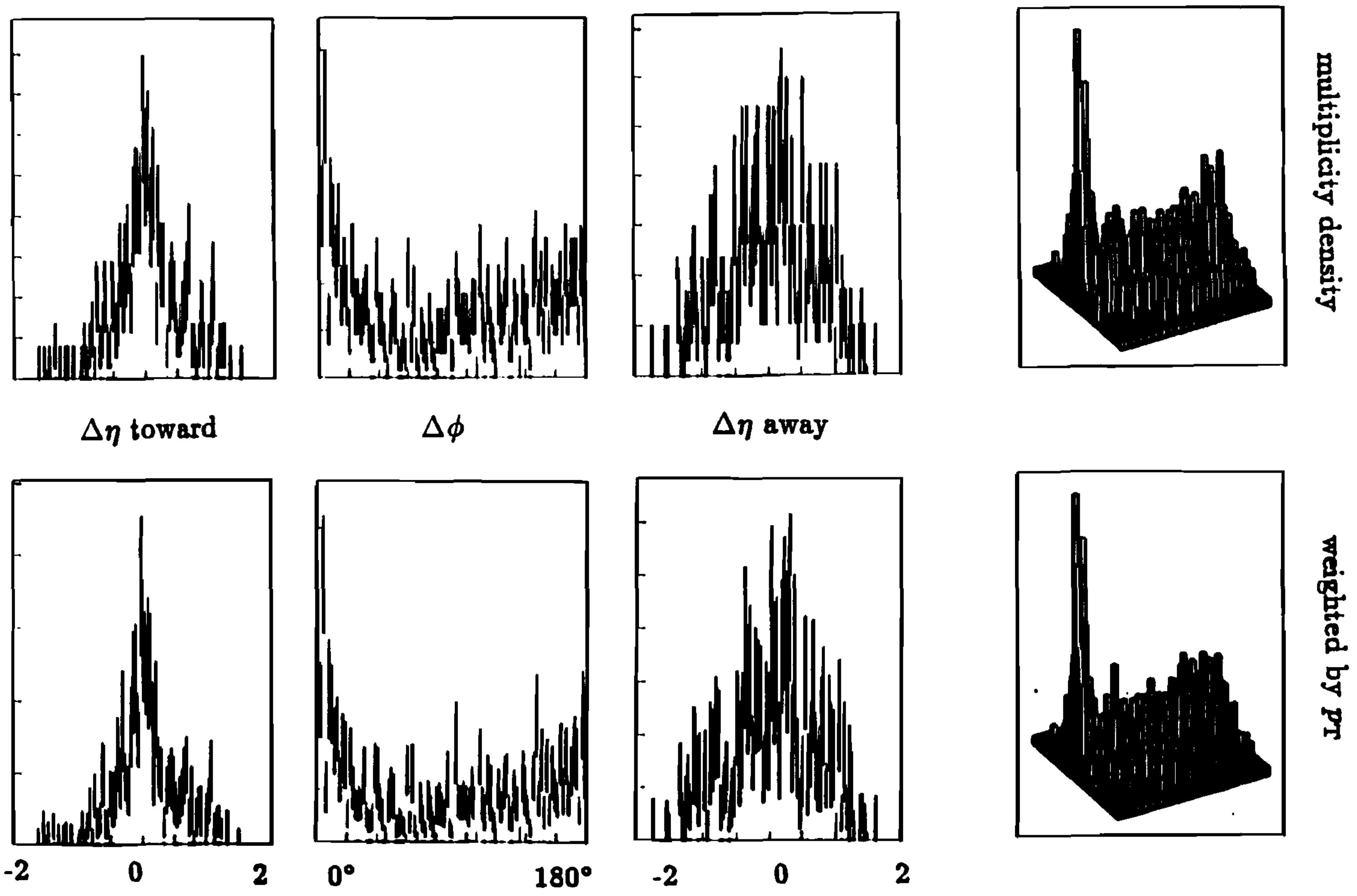

Figure 6.5 $\Delta\phi - \Delta\eta$ with a trigger $p_T \geq 4$ GeV/c and secondary $p_T \geq 1$ GeV/c.

Figure 6.6 shows the distributions of ϕ and η for secondaries in each event plotted relative to the randomly chosen trigger particle in 70 GeV jet events. In Figure 6.7, the trigger particle was demanded to have $p_T \geq 4$ GeV/c for the same sample. In both cases, very similar patterns of strong correlations were observed, regardless of the momentum of trigger particle.

Even though the same patterns of $\phi - \eta$ correlations are seen both in minimum bias events with the presence of a high p_T particle and in jet events, the correlations are much more pronounced in the jet events.

The correlations in the presence of a high momentum particle exhibit features which are consistent with the widely adapted framework of parton scattering. It seems that a particle with high transverse momentum defines reasonably well the direction of the scattering parton, since it takes a large fraction of the parton momentum due to the steep fall of the inclusive p_T spectrum. In those cases where additional high p_T particles exist on the towards side, they tend to cluster around the trigger particle because of their limited transverse momentum with respect to the parton axis in the fragmentation process. On the away side, the direction of the scattered parton is unknown and this results in a smearing of high p_T particles over a wide range in rapidity.

6.2 Momentum Flow Around the Trigger

As a next step from the qualitative correlation studies for the charged particles, quantitative energy densities of charged particles around the trigger were measured. Since the η distribution of charged particles is symmetric around $\eta = 0$, the larger remaining acceptance side in pseudorapidity was kept after the selection of the trigger particle, and the difference in pseudorapidity between the trigger and secondary particles ($\Delta\eta$) was folded in η to extend the η phase space.

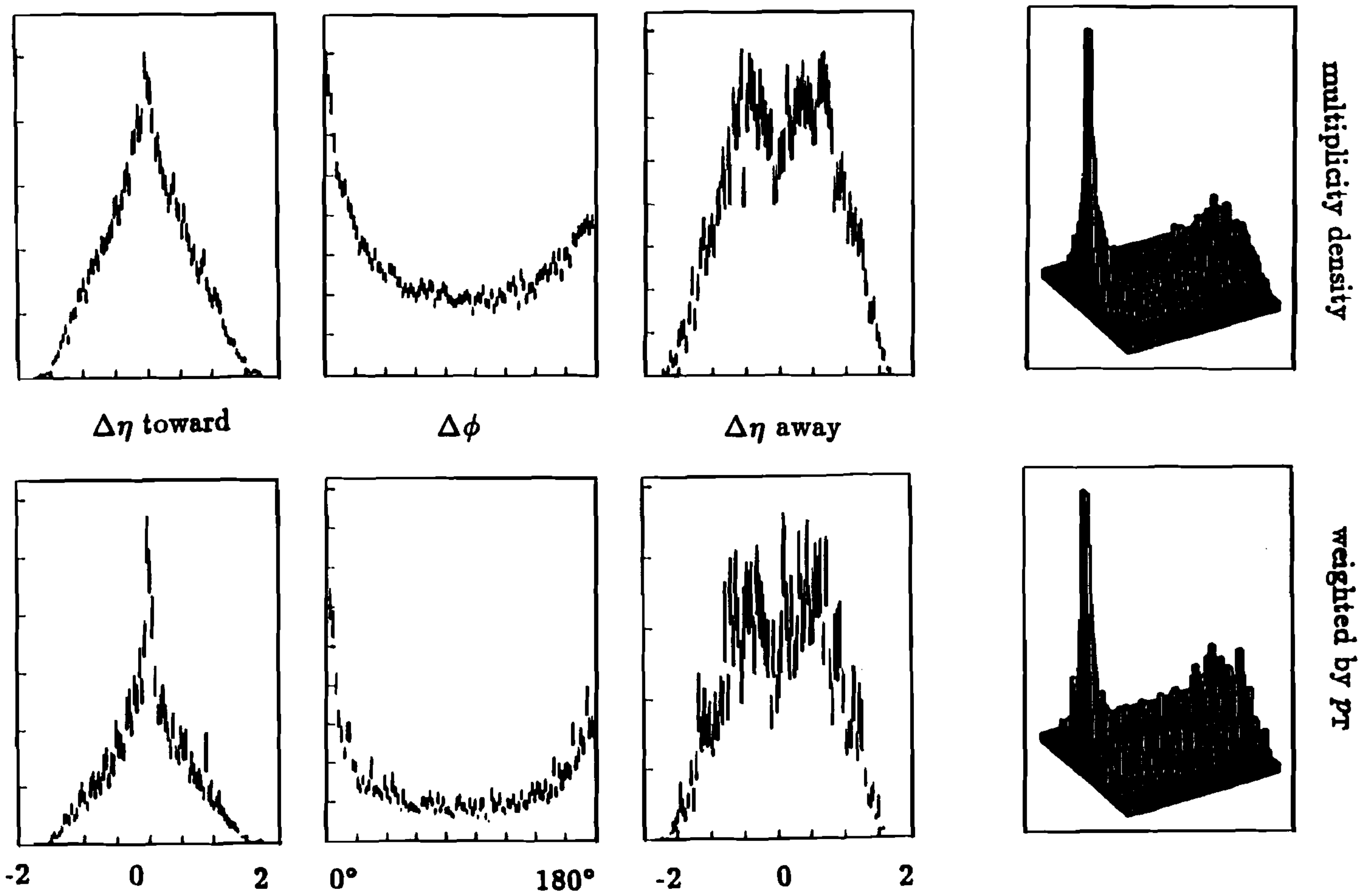

Figure 6.6 $\Delta\phi - \Delta\eta$ in jet data with a random trigger.

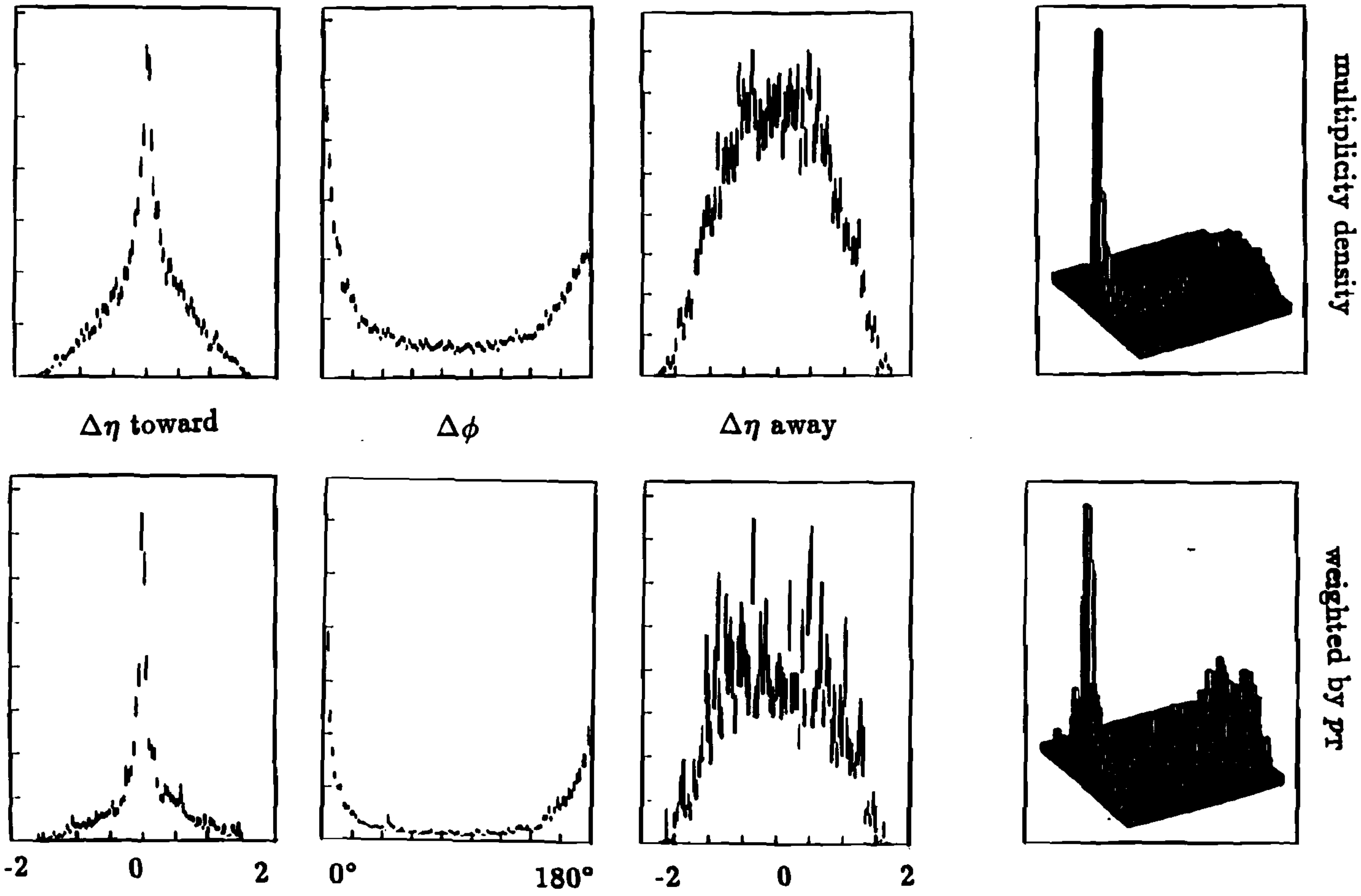

Figure 6.7 $\Delta\phi - \Delta\eta$ in jet data with p_T of trigger ≥ 4 GeV/c.

Energy flow in $\phi - \eta$ space

Using the same geometrical definition as in section 6.1, the momentum density around the trigger particle in unit η and ϕ was measured as a function of p_T of the trigger particle for both minimum bias events and the jet data sample.

In Figure 6.8, the momentum densities, $\mathrm{d}\Sigma p_T/(\mathrm{d}\Delta\phi \mathrm{d}\Delta\eta)$, as a function of distance in pseudorapdity and azimuthal angle from the trigger particle in minimum bias events were plotted (the trigger particle was not included in the plot). The momentum density in the towards ϕ-semicircle shows a very strong correlation with the distance in η from the trigger particle. In particular, a very strong correlation is observed on the towards side for $\Delta\eta \leq 0.6$, and its strength increases with the p_T of the trigger. Whereas, no correlation with the pseudorapidity of the trigger is observed on the away side. An increase of the transverse momentum in the away side with the increasing p_T of the trigger can be interpreted as local momentum conservation in limited phase space ($|\eta| \leq 1$). The momentum density as a function of ϕ with respect to the trigger particle (Figure 6.8) also shows a very strong correlation for $\Delta\phi \leq 0.6$ from the trigger and peaks both in the direction of the trigger particle and at $\Delta\phi = 180°$ opposite to the trigger particle. From Figure 6.8, the σ width of the clustering of particles can be deduced as a cone in $\phi - \eta$ space with radius ≤ 0.6 around the trigger, which is in agreement with a previous measurement [76,78] of $= 30° \pm 5°$.

The distributions of momentum densities in jet events (Figure 6.9) show strong correlations with both η and ϕ in the towards ϕ-semicircle. For the away ϕ-semicircle, the distributions show strong correlations only with ϕ. However, unlike those in minimum bias events, these correlations seem to be identical regardless of the momentum of trigger particle.

It should also be noted that in minimum bias events, the momentum density at $\Delta\eta = 1.0$ in the towards ϕ-direction is the same as the average value

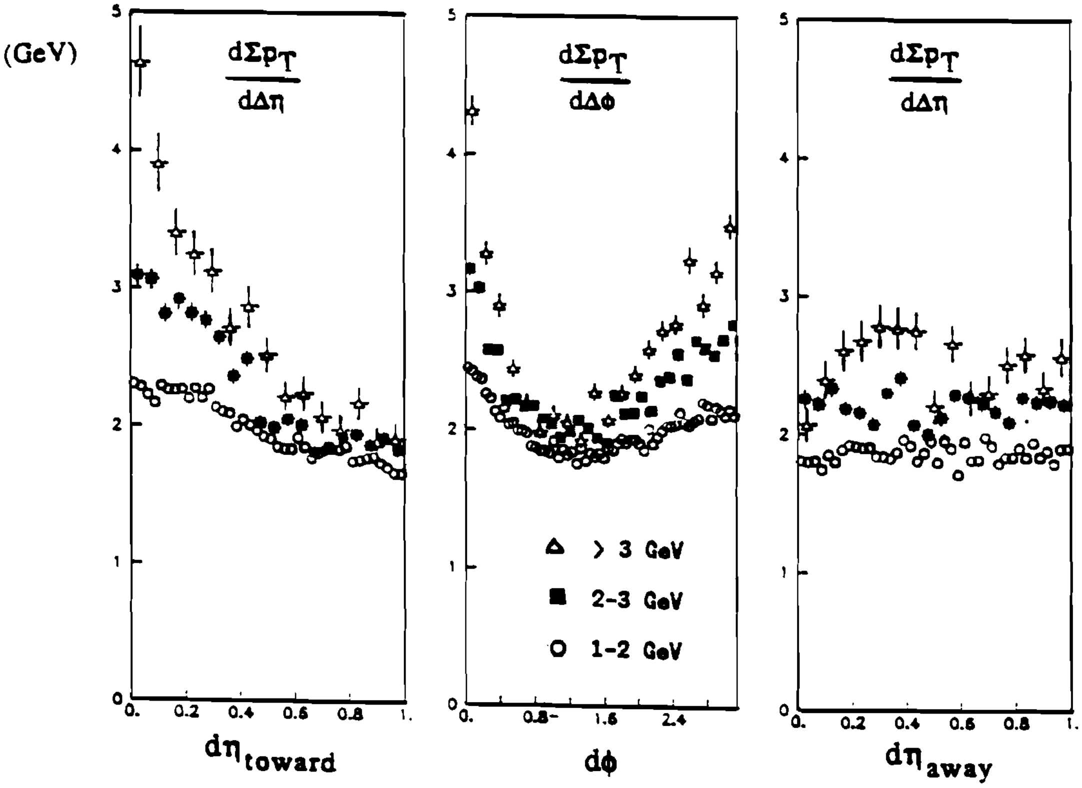

Figure 6.8 The momentum densities in minimum bias data.

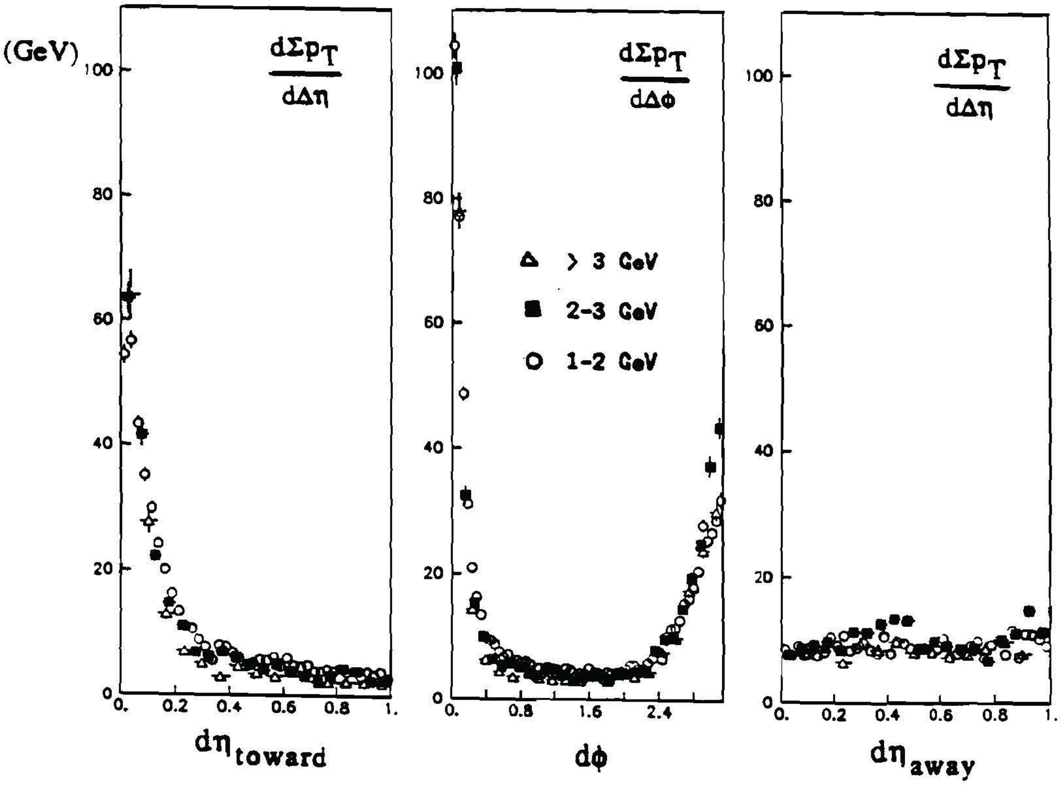

Figure 6.9 The momentum densities in jet data.

in the away side for trigger p_T of 1 to 2 GeV/c and the momentum density in the away ϕ-semicircle increases with the increasing p_T of the trigger. However, in jet events, the patterns seen are roughly consistant with local transverse momentum conservation where the away side momentum density is not correlated in η but instead is seen to be uniformly spread in η.

Pedestal effects

From the direction of the trigger particle in the minimum bias events, ϕ space was divided into four 90° wedges as "same" (centered on the trigger particle), "opposite" (opposite to the trigger particle) and two "sides" (perpendicular to the trigger particle). The momentum density (per unit area in ϕ, η plane) emitted in the 90° azimuthal wedges was measured as a function of increasing transverse momentum of the trigger particle. The amount of momentum emitted into all four wedges increases with increasing transverse momentum of the trigger particle (see Figure 6.10).

The increase in momentum density with increasing p_T of the trigger, both on the same and on the opposite side, was observed in a previous measurement [77]. The small difference between the momentum densities observed on the opposite side and the same side in Figure 6.10 could result partly from trigger bias. Since the constituents lie on a steeply falling p_T spectrum, a small amount of transverse momentum in the initial hadrons can boost the observed p_T of final particles [80]. After fragmentation, the momentum density on the trigger side is increased by this factor while on the opposite side, it is reduced.

The momentum density of tracks at 90° (side) also increases with increasing trigger p_T, which is in disagreement with the previous measurement [77] which observed a constant value. As the p_T of the trigger particle changes from 0.75 GeV/c to 2.5 GeV/c, the amount of momentum emitted at 90° with respect to the trigger particle increases by a factor of two (so called "pedestal effect" [81]) and starts to saturate. It is possible that this effect is due to a

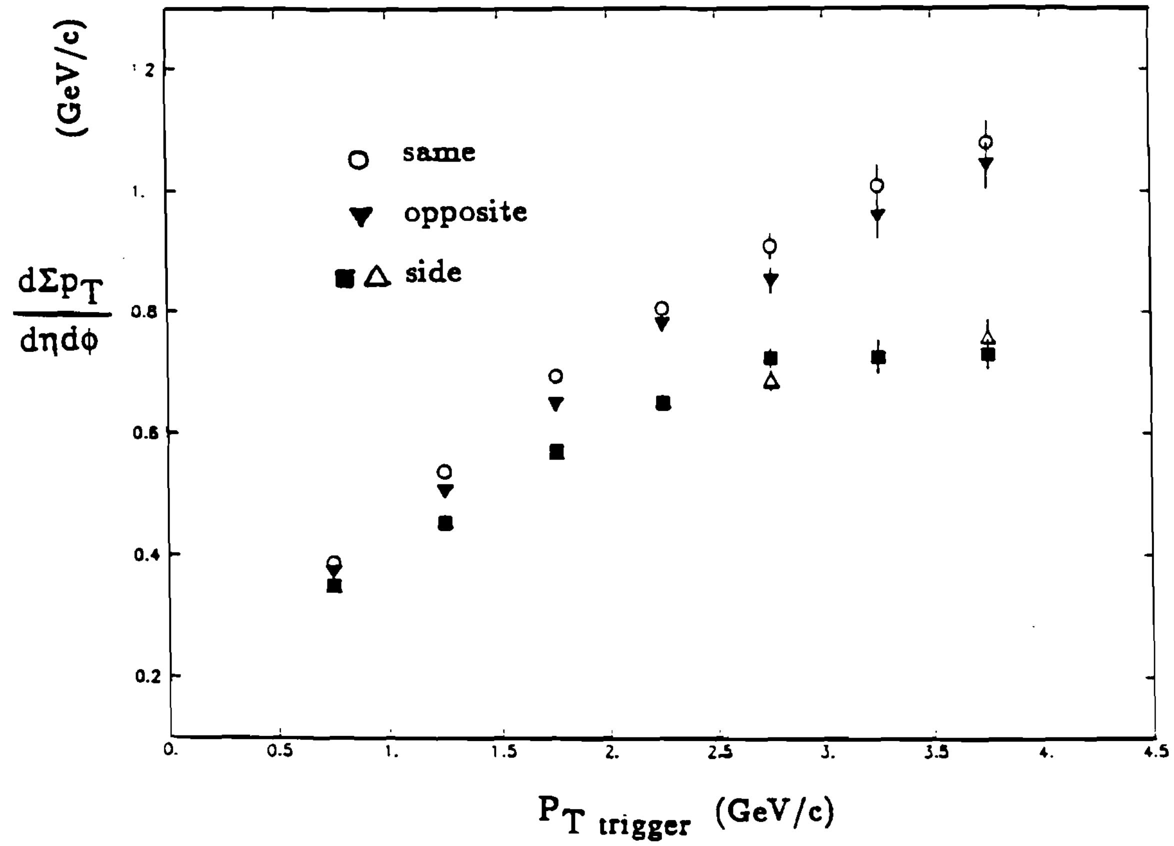

Figure 6.10 The p_T densities emitted into four ϕ wedges.

contribution from software trigger bias acting on the soft underlying event in addition to 2 → 2 parton parton scattering, as will be discussed further in Chapter 7.

CHAPTER 7 - PARTICLE CLUSTERS

As shown in Chapter 5, transverse momentum spectra harden as the center of mass energy increases, a QCD-inspired parton model gives a qualitative agreement with the data over a very wide range of $\sqrt{s}$ and p_T, and the mean transverse momentum of charged particles increases faster than linearly with $\log(s)$. In Chapter 6, strong correlations are shown between particles in the presence of high p_T particles which are often interpreted as a sign of parton-parton scattering. Also, other anomalies, such as KNO and Feynman scaling violations [7-9,27], the $\log(s)$ dependence of the K/π ratio [19,35], and an increase in σ_{inel} have been observed as $\sqrt{s}$ increases [33,34]. Using a track clustering algorithm, more quantitative studies were done to answer the question of whether these are due to low E_T jets from a hard scattering component or are possibly just fluctuations at the tail of minimum bias events. More understanding of event topologies in soft and hard scatterings is needed along with reasonable theoretical predictions.

7.1 Clustering Algorithm

Jets have been defined in e^+e^- collisions down to very low transverse energies ($E_T \sim$ a few GeV) [82]. Since high energy e^+e^- collisions have the simplicity of the parton level processes which are dominated by quark fragmentation into quark jets, the jet events are selected with low background and even the spin of the quark can be determined from the jet axis angular distribution at low center of mass energy [83].

In hadron collisions, however, since the constituents (quarks and gluons) are surrounded by a cloud of gluons and virtual $q\bar{q}$ pairs, where the interactions between the different constituent quarks and gluons are treated as separate subprocesses, the picture of the interactions is not simple and the background in jet events is much higher. In addition, at lower transverse momenta in hadron collider jets, gluons are thought to predominate [84], and very little experimental information is available on gluon fragmentation. It is expected that gluon jets will be fatter, softer, and of higher multiplicity than quark jets because of the higher color charge of the gluon [85].

Study of low E_T clusters at $\bar{p}p$ collider

The interpretation of the event topology in hadron collider jets of low E_T becomes more difficult due to:

(1) possible multiple parton-parton interactions [86],

(2) an increase in relative contribution from gluon radiation to the transverse energy, as the momentum transfer (Q^2) decreases [87],

(3) difficulties in describing parton-parton collisions at low values of E_T by QCD perturbative calculations,

(4) the experimental definition of a jet becoming less reliable when the E_T of the scattered parton is not large with respect to the contribution from the "underlying events" (the contribution from hadronization of the beam spectators and initial state bremsstrahlung),

(5) an increase in the fraction of events with high multiplicity, without evident jet production, which can produce large ΣE_T, and

(6) a large uncertaintity in energy measurement by the calorimetry [88] at low energy (E_T of cluster $<$ 20 GeV), which leads to possible doubt about the measured production rates and the energy scale of clusters.

At the center of mass energies of 200 to 900 GeV, the UA1 collaboration showed evidences for the production of a non-negligible fraction of events containing low transverse energy (E_T) jets, called "mini-jets", in minimum bias events [22,30,89]. The mini-jets are defined with the UA1 jet finding algorithm [81] based on E_T clustering in $\eta - \phi$ space using information from the calorimeters. The E_T distribution was measured within the pseudorapidity window $|\eta_{\mathbf{axis}}| < 1.5$ ($\eta_{\mathbf{axis}} = \eta$ acceptance for cluster axis). For the signal of a low E_T jet, it was required that the minimum amount of E_T observed in a small moving window around a seed tower with $E_T > 1.5$ GeV should be more than 5 GeV within a "cone" size of $\Delta R = \sqrt{\Delta\eta^2 + \Delta\phi^2} = 1$ [30]. The fraction of mini-jet events was non-negligible (6 % at 200 GeV and 17 % at 900 GeV of the inelastic cross section) and increased with $\sqrt{s}$ over 200 to 900 GeV [89]. The UA1 collaboration concluded that the jet cross section increases like log(s) and gives a large fractional contribution to the inelastic non single diffractive cross section as $\sqrt{s}$ increases [89]. In addition, the average multiplicity of these jet events was observed to be twice as large as the "no-jet" events, and the $< p_T >$ dependence on multiplicity had different behaviors in jet and no-jet events [22,89]. It was also shown that the mini-jets with $E_T \geq 5$ GeV exhibit properties in agreement with QCD expectations for parton scattering, supporting the interpretation in terms of jet production [30].

During the past few years, many studies [90] investigated how low in transverse momentum perturbative QCD could be used to describe the dynamics of hadron collisions (based on measurements from the UA1 collaboration) and made predictions of jet cross sections at the higher center of mass energies. However, the interpretation of clusters at such low E_T is hard to understand since the applicability of perturbative QCD is not clear.

The UA2 collaboration suggests that the emergence of hard scattering occurs at much larger values of jet E_T than 5 GeV [31,91]. In their studies, a phenomenological parameterization for the soft and hard cross sections was made directly from the data. From the parameterizations of the total transverse energy (ΣE_T), the sum of transverse energies of the two highest E_T clusters ($\hat{E}_T$), and the ratios of the E_T of the clusters to ΣE_T or to $\hat{E}_T$, it was shown that the hard cross section does not prevail over the soft cross section for ΣE_T up to 60 GeV and $\hat{E}_T \approx 25$ GeV in $|\eta_{\rm axis}| \leq 1$. It was also indicated that the clusters with $E_T < 15$ GeV are mostly due to fluctuation of the soft component. Other studies using statistical methods also have shown that some properties of the observed mini-jet events are due to statistical effects resulting from the experimental cuts [32].

Clustering algorithm with calorimetry

Using energy measurements by the calorimetry to study low E_T clusters has a few problems:

(1) a large uncertainty in the measurement due to the poor resolution at small E_T, in particular, from the hadron calorimeter [88]: for CDF, the energy resolution of the CEM is $\sim 17/\sqrt{E}\%$ and of the CHA is $\sim 67/\sqrt{E}\%$;

(2) a nonlinearity of the hadron calorimeter response at low E_T [88]; and

(3) an incorrect azimuthal direction of low momentum charged particles at the calorimeter by the sweeping of the magnetic field.

In minimum bias events at $\sqrt{s} = 1800$ GeV, the rates of clusters defined by the standard CDF jet finding algorithm [79] based on calorimeter transverse energy depositions in $\eta - \phi$ space ($|\eta| \leq 1.0, \phi = 2\pi$) with a cone size of $\Delta R = 0.7$ were < 2 % for the E_T of the clusters above 5 GeV and < 0.1 % for $E_T \geq 15$ GeV [92].

Clustering algorithm of particles

As a solution to the possible problems in measurement of low E_T clusters using calorimetry, a new "track clustering algorithm" was developed to find low E_T clusters. It uses a momentum measurement of charged particles from the CTC and an energy measurement of neutral particles from the EM calorimeter. The track clustering algorithm is similar to the standard calorimetry E_T clustering algorithms which were used to find high E_T jets [79,81,91]. However, in the low E_T region, the track clustering has a number of advantages over the calorimeter clustering, such as: much better energy resolution in the measurement of charged particles due to good track momentum resolution, an absence of non-linearity or poor resolution from the hadron calorimeter, and measuring correct directions of the outgoing particles from the primary vertex.

A particle cluster in this algorithm is defined as a set of tracks having rapidity $y > y_{min}$ along a common axis. The clustering algorithm is as follows:

(1) A particle with the highest p_T in an event becomes a seed of a cluster.

(2) All other particles are ordered according to their transverse momenta.

(3) If a particle has a relative rapidity $(\Delta y) > y_{min}$ from a cluster axis, it is merged to the cluster, and a new cluster axis is computed.

(4) If a particle has a relative rapidity $(\Delta y) \leq y_{min}$ from any existing cluster axes, it becomes a seed of a new cluster.

(5) Steps (3) and (4) are repeated until all the particles in the event are used.

In this analysis, the value used for the cluster size was $y_{min} = 1.0$ which is roughly equivalent to within a cone of half angle $\sim 40°$ or within a radius (ΔR) of 0.7 in $\eta - \phi$ space from the cluster axis. After the merging is done, the transverse energy of a cluster was calculated as

$$E_T = \sqrt{(\sum_i E_i)^2 - (\sum_i p_{z_i})^2},$$

where the energy of particle (E_i) was evaluated assuming the pion mass.

7.2 Calorimetry Data

The characteristics of calorimetry data in minimum bias events were examined. First, the energy measurements from the calorimeters in minimum bias events were studied and compared with previous measurements from the lower $\sqrt{s}$ experiments. The method used to extract neutral particle momenta from the EM calorimeters is then described.

Data from the central calorimeters

For the data from the 1987 run, a number of towers in the Plug and

Forward calorimeters showed noise levels that were high compared to the value of the average energy expected in minimum bias events. Therefore, only data from the central calorimeters were studied.

The selected triggers discribed in Chapter 3 were further cleaned by checking the noise level, pedestal shift, and errors in the calibration of each tower. The average ΣE_T per event, average E_T in each tower, and mean occupancy of each tower were histogramed on a run by run basis. The runs with noise or hot towers were removed from the data sample. The remaining events after the clean-up were about 36,000 events at 1800 GeV and 3,800 events at 630 GeV.

In the following studies, none of the corrections for longitudinal leakage, dead areas (cracks), and other possible inefficiencies were made. The corrections for the non-linearity of the hadron calorimeter at low energies and for the missing energy carried by low p_T charged particles which spiral inside the calorimeter were ignored. These effects will give an underestimation of the measured energy from the true energy by a factor of (true energy/measured energy) $\leq 1.35 \pm 0.20$ [93].

The ΣE_T distribution

The total transverse calorimeter energy of an event (ΣE_T) was calculated as a scalar sum of all towers in $|\eta| \leq 1.0$ and $0 \leq \phi < 2\pi$ with $E_T \geq 100$ MeV/c^2. In Figure 7.1, the distributions of the total transverse energy at $\sqrt{s}$ = 1800 and 630 GeV are compared with the measurements by the AFS Collaboration [94] at the ISR energies. The distributions from both experiments show an exponential fall off at large ΣE_T and a flattening of the spectrum with an increase of $\sqrt{s}$.

The transverse momentum distributions of charged particles as a function of ΣE_T are shown in Figure 7.2 for $\sqrt{s} = 1800$ and 630 GeV. A hardening of the p_T distribution with increasing ΣE_T is observed. At fixed ΣE_T, the shape

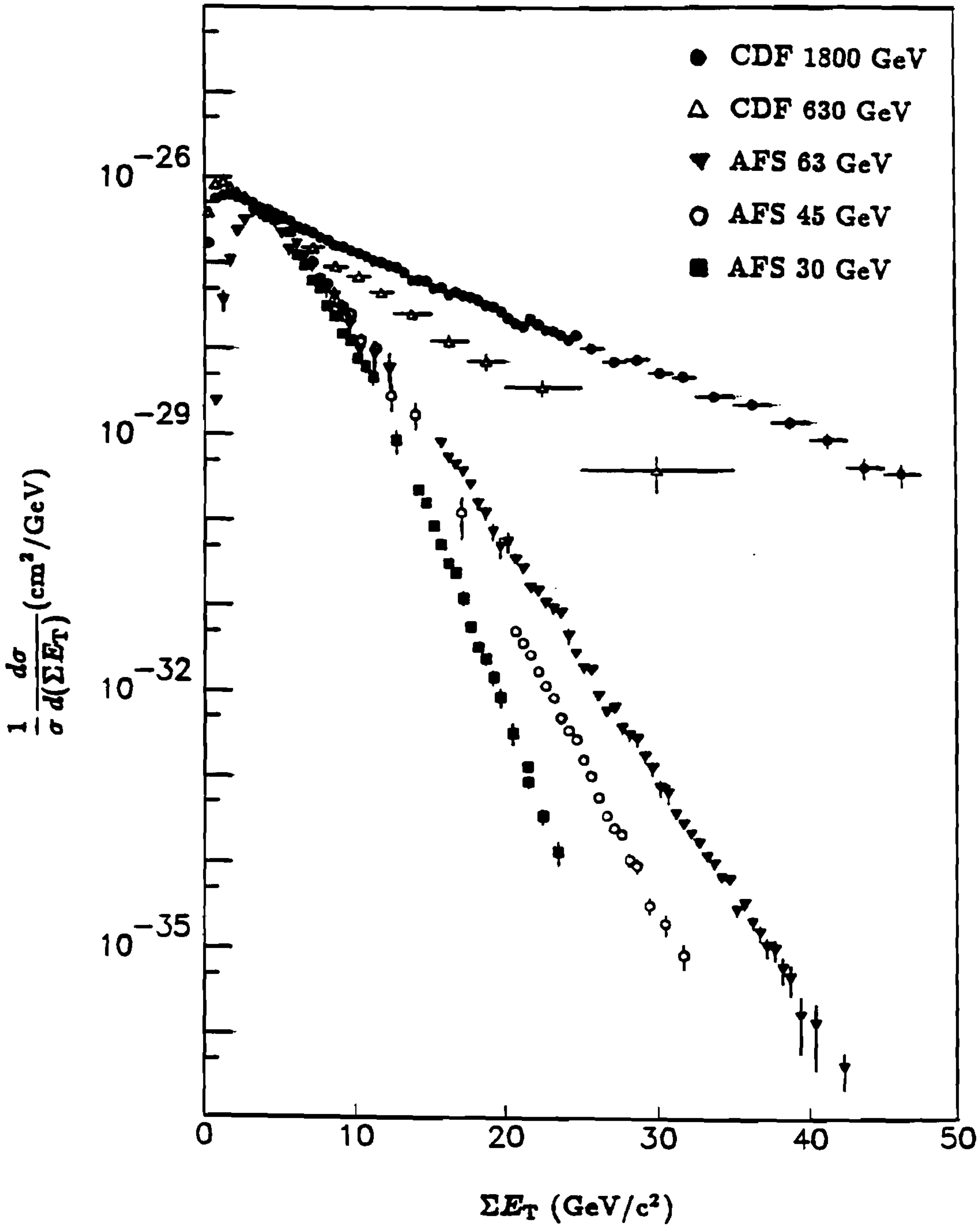

Figure 7.1 The ΣE_T distributions in minimum bias data.

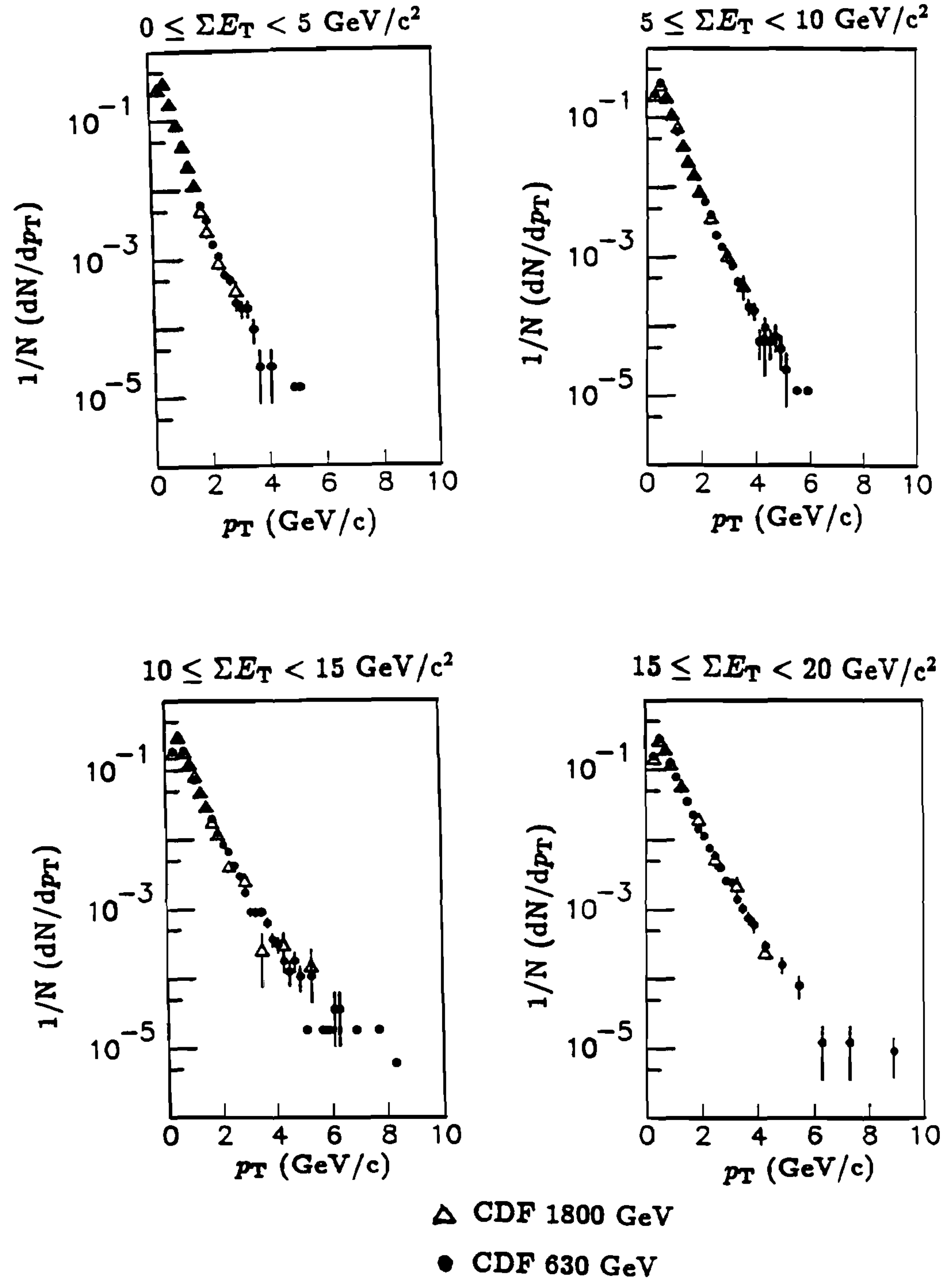

Figure 7.2 p_T spectra as a function of ΣE_T.

of the p_T spectrum is almost identical at both energies. The flattening of the overall p_T distribution at higher $\sqrt{s}$ is therefore coming from the higher production rate of events with higher ΣE_T.

Transverse energy and charged particle multiplicity

Figure 7.3 shows the plot of E_T density in the central calorimeter as a function of η. The distribution is fairly flat which is kinematically consistent with a uniform rapidity distribution of the charged particle multiplicity.

In order to explore the relationship between the transverse energy and the multiplicity, the dependence of ΣE_T on the observed charged particle multiplicity was studied within $|\eta| \leq 1$ using reconstructed tracks in the CTC. Figure 7.4 shows the mean total transverse energy ($< \Sigma E_T >$) as a function of the average multiplcity of charged particles with $p_T \geq 400$ MeV/c ($< N^*_{ch} >$). The charged particle multiplicity rises rapidly with increasing total transverse energy which agrees with a previous measurement at the ISR [94]. The rate of increase in $< \Sigma E_T >$ with multiplicity seems to be a constant in all ranges of ΣE_T. In Figure 7.4, $< \Sigma E_T >$ in the CEM only is also separately plotted as a fuction of charged paticle multiplicity in the CTC. Assuming that the ratios of charged to neutral multiplicity and $< \Sigma E_T >$ are 2 to 1 (which would not depend on the total multiplicity), it can be concluded that the energy measured in the CEM has a large contribution from charged particles, since the ΣE_T actually seen in the CEM is greater than 1/3 of the total ΣE_T in the CEM + CHA.

Deduction of neutral energies from the CEM

Charged particle momenta were measured precisely in the CTC, but neutral particles were measured in the fine-grained electromagnetic calorimeters and included in the track clustering algorithm. Since most of the test beam calibration for the central calorimeter modules involved incident beam momenta, p, of ≥ 50 GeV/c and there were no calibration data taken for $p < 10$ GeV/c,

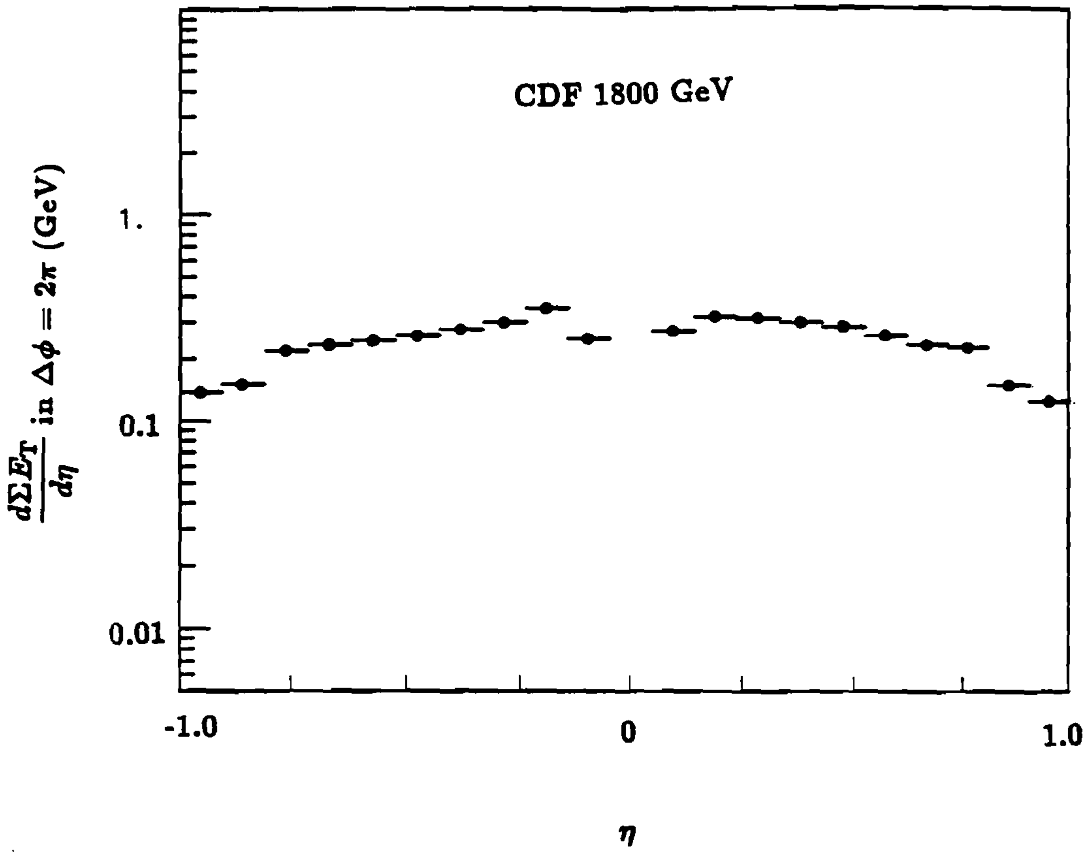

Figure 7.3 E_T density as a function of η.

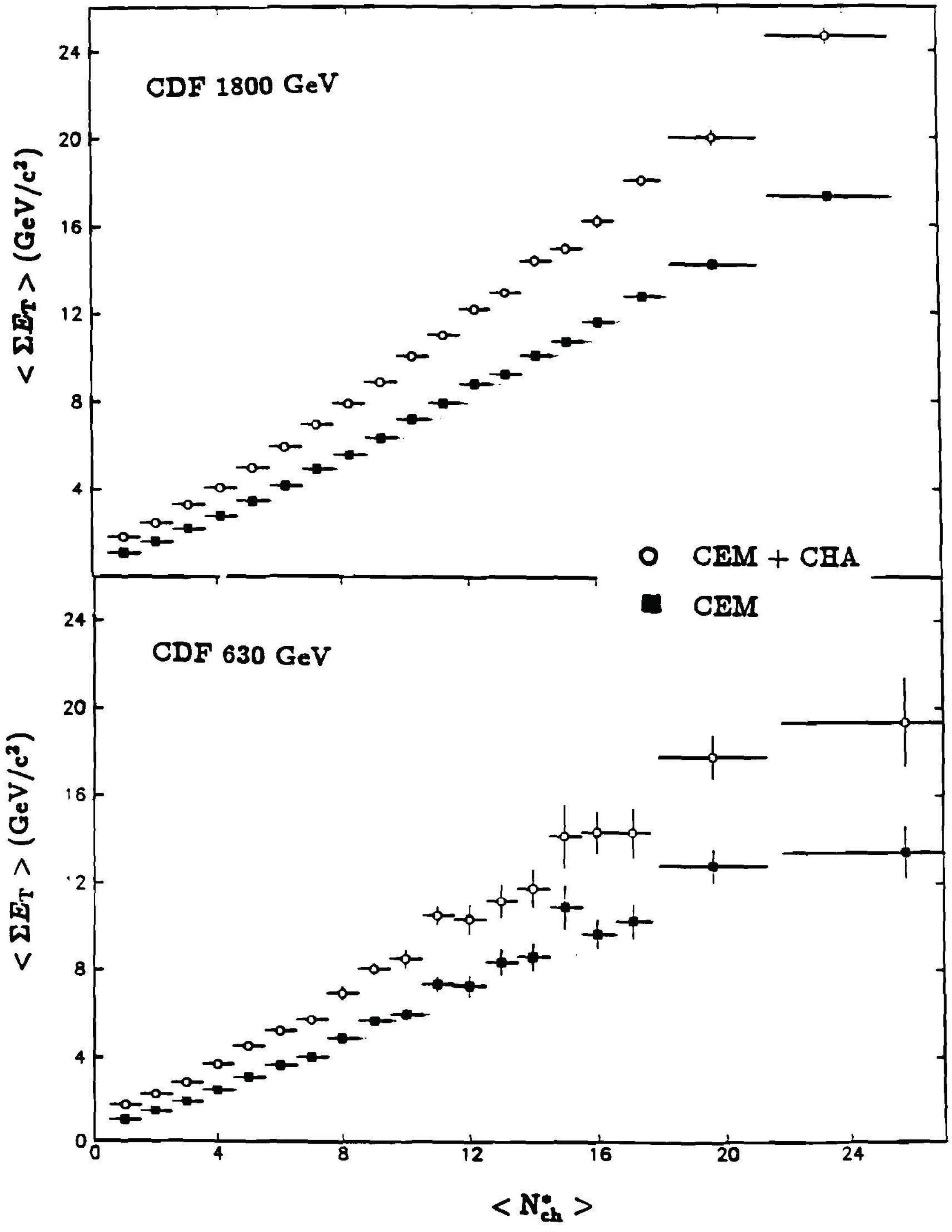

Figure 7.4 $< \Sigma E_T >$ as a function of $< N^*_{ch} >$.

the study of calorimeter response to low energy hadrons was done by using low energy charged particles measured in the CTC [95]. The best estimate of the CEM calorimeter response as a function of incident momentum was used to correct the energy measured in the CEM for the contamination from charged particles. The most probable fraction of their energy deposited by charged hadrons in the CEM varies between 50 % at $p_T = 400$ MeV/c to 30 % at 3 GeV/c (see Figure 7.5). The deduced energy of neutral particles was introduced as "pseudo-neutral particles" to the particle clustering algorithm in the following way:

(1) Each tower with raw energy deposition in the CEM ≥ 50 MeV was sorted in descending order of energy. This improves the chance of correctly identifying the interaction location of particles in the CEM for both charged and neutral particles without spreading the correction out over several towers, or leaving a hole in the peak tower of energy deposition.

(2) Correction for the energy deposition by charged particles in the CEM was done. For each charged track, a prediction was made for which tower it hit, then a most probable deposition of the track energy to the CEM counter (Figure 7.5) was subtracted from that tower. Towers were allowed to have negative energies after the subtraction.

(3) Using the sorted list from (1), towers were merged in a 3×3 tower matrix. Starting with the highest energy tower in the list, the corrected energy from its eight neighbors was added to the corrected seed tower energy and the energies in these eight neighboring towers were set to zero.

(4) The direction and transverse momentum of each merged tower (ie. each pseudo-neutral) was calculated assuming the pion mass. The pseudo-neutral tracks with $p_T \geq 400$ MeV/c were entered in the track clustering.

Since there are strong correlations between high p_T charged particles as shown in Chapter 6, the probability of two charged particles entering into the same window in phase space is a function of p_T. In minimum bias data, the

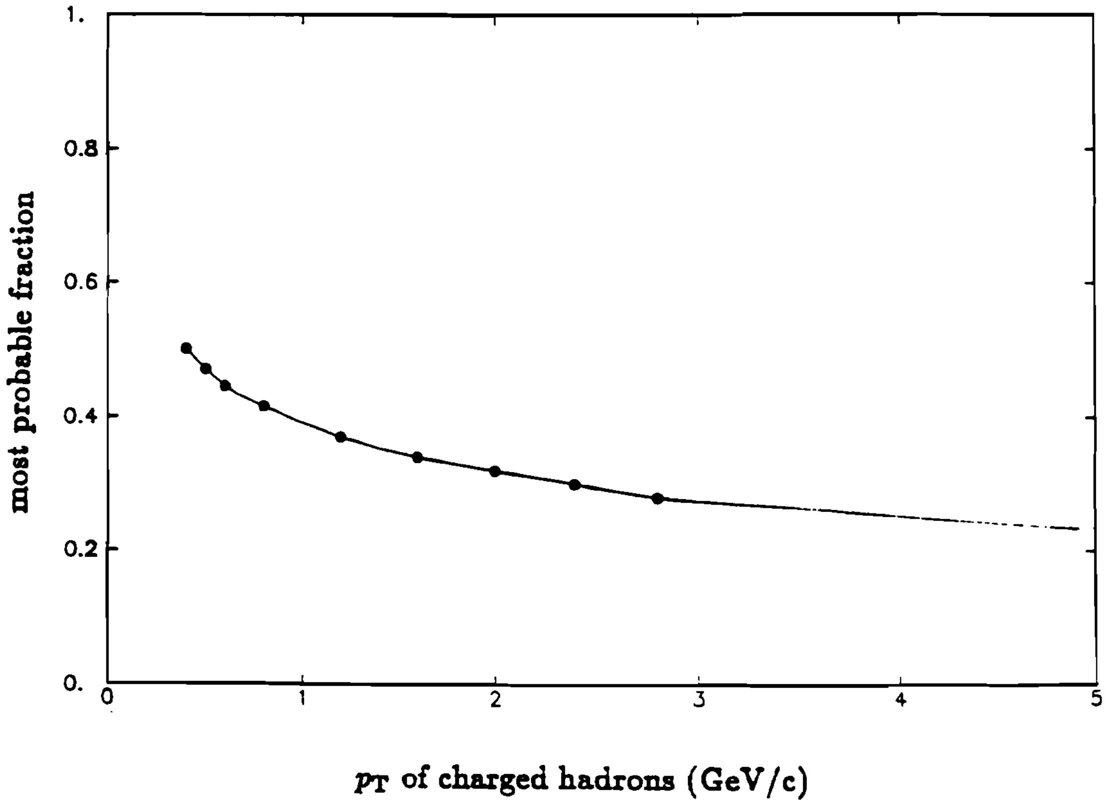

Figure 7.5 Most probable fraction of energy deposited by charged hadrons in CEM.

average probability of two charged particles with $p_T \geq 400$ MeV/c entering the same calorimetry tower was less than 0.5 %. For the window size of 3×3 calorimetry towers, the average probability for tracks with $p_T \geq 400$ MeV/c was < 5 %, but for particles with $p_T \geq 3$ GeV/c, this probability became 32 %.

The deduced multiplicity distribution of the pseudo-neutral tracks for $p_T \geq 400$ MeV/c and $|\eta| \leq 1$ is shown in Figure 7.6 and compared with the distribution of charged particles. The average multiplicity of pseudo-neutral particles agrees suprisingly well with the expected value, assuming a charged to neutral particle ratio of 2 to 1 and given the difference seen at low multiplicity, which may in part be an artifact of the 3×3 merging used to create the pseudo-neutrals. Figure 7.7 shows the distribution of the ratio of charged particles multiplicity to "all" (charged and pseudo-neutral) particles ($< \mathrm{N_{ch}/N_{all}} >$) in an interaction. The distribution has a mean value of 0.65 and a width (σ) of 0.11.

The p_T distributions of the pseudo-neutral and charged particles are shown in Figure 7.8. Due to the merging of 3×3 towers in the CEM and the possible strong correlations between high p_T neutral particles, the p_T spectrum of pseudo-neutral particles seems to be flatter than the charged particles in the high p_T tail. However, the overall shapes of the distributions and $< p_T >^*$ values agree well.

The error in deducing neutral energies due to the correction of the contribution from charged particles in the CEM was estimated by varying the correction between 0 and 200 % of the nominal value. The average value and width of the p_T, multiplicity, and $< \mathrm{N_{ch}/N_{all}} >$ distributions are listed in Table 7.1. None of quantities are very sensitive to the amplitude of the correction function. The error due to this correction was considered to be small enough to be neglected.

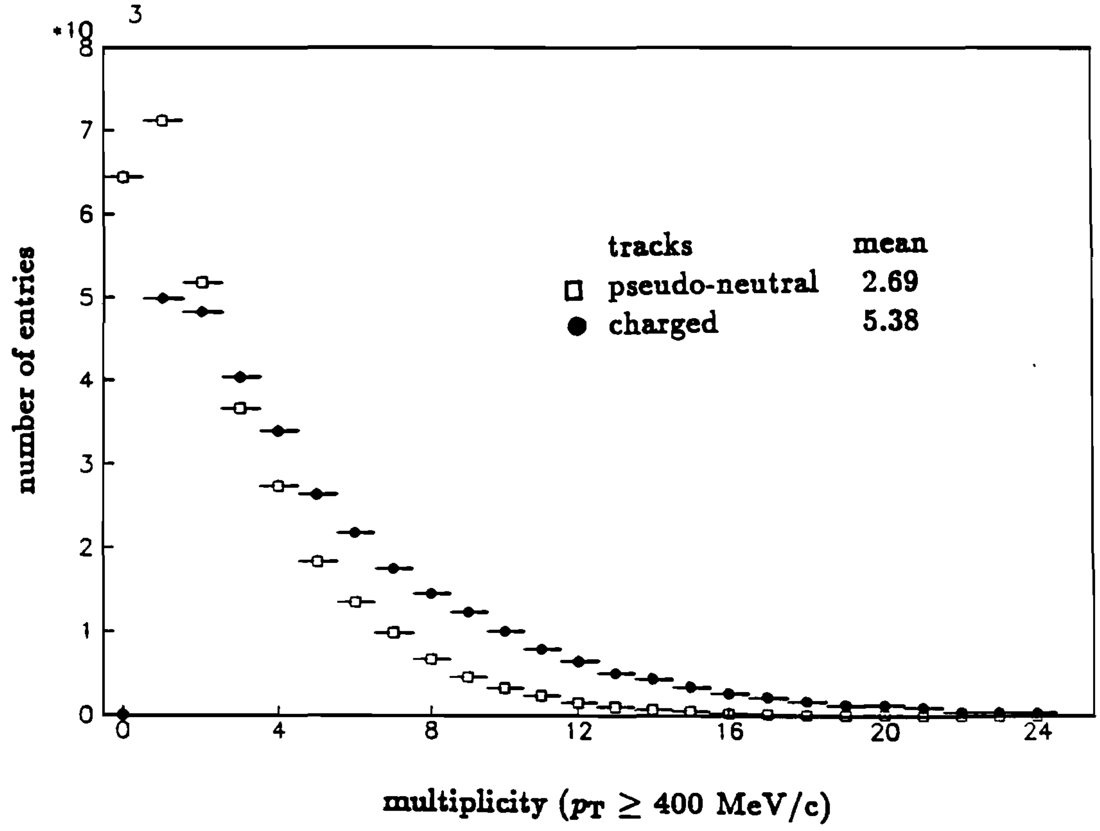

Figure 7.6 Multiplicity distribution of pseudo-neutral tracks.

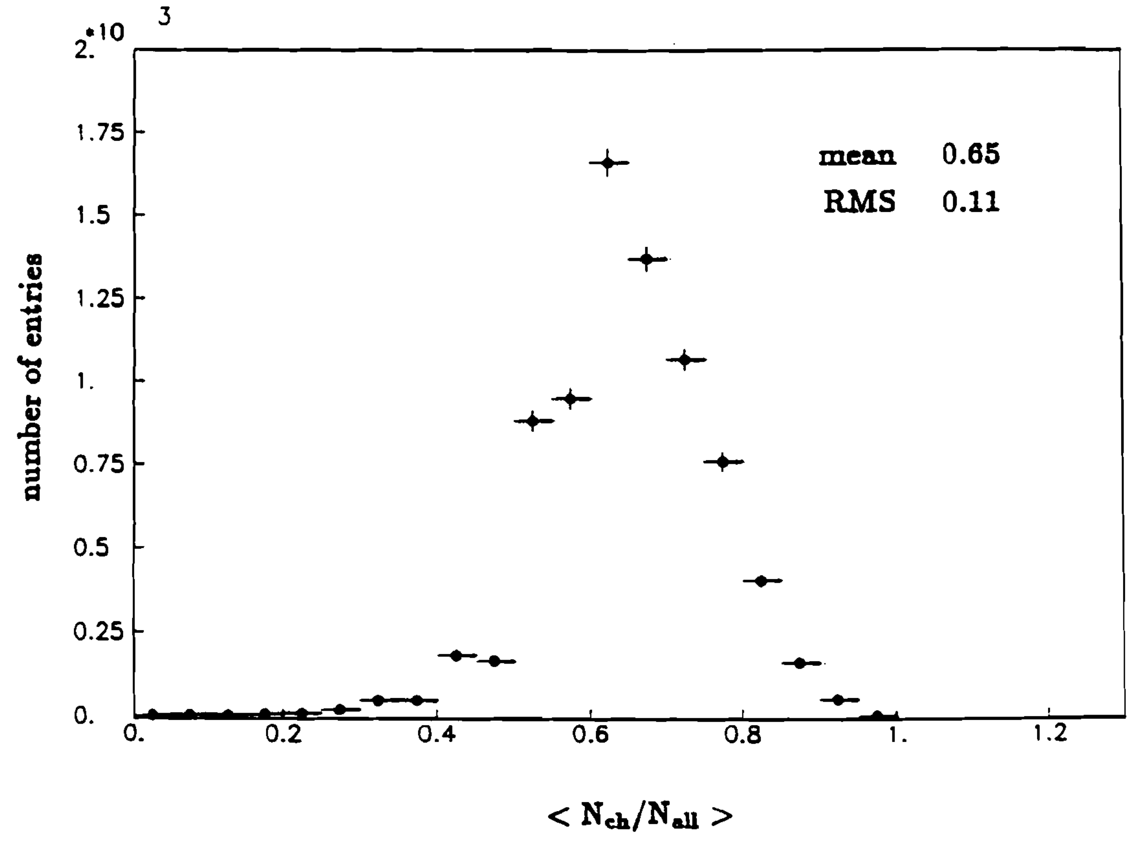

Figure 7.7 Ratio of charged particle multiplicity to all particles.

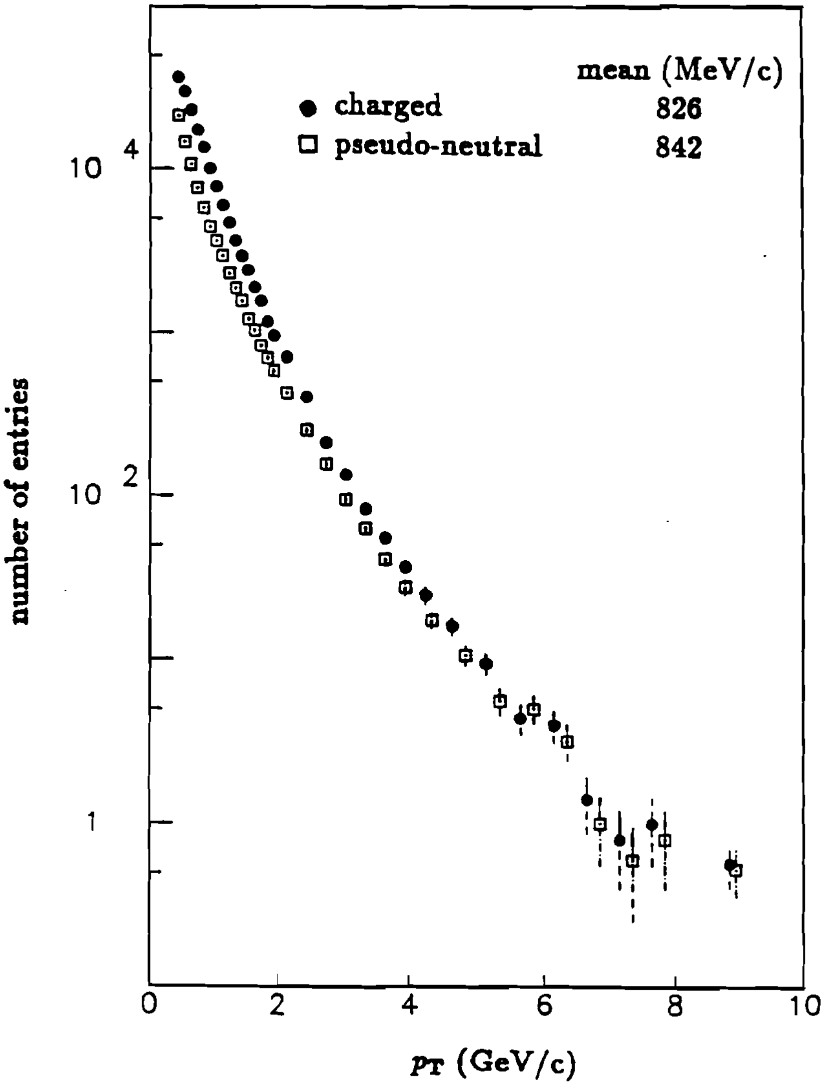

Figure 7.8 p_T spectra of pseudo-neutral and charged particles.

Table 7.1 Estimated error due to correction of charged hadrons in CEM.

pseudo-neutral tracks					
correction function	p_T (MeV/c)		multiplicity		N_{ch}/N_{all} in a event
	mean	RMS	mean	RMS	
× 0.0	843	545	2.97	3.11	0.63 ±0.11
× 0.5	843	546	2.80	2.91	0.64 ±0.11
× 1.0	842	545	2.69	2.77	0.66 ±0.11
× 1.5	840	543	2.63	2.68	0.66 ±0.11
× 2.0	839	542	2.58	2.62	0.66 ±0.11

charged tracks					
	827	481	5.38	4.46	

7.3 Clusters in Minimum Bias Events

The clusters found by the particle clustering algorithm were studied for $|\eta_{\mathrm{axis}}| \leq 0.5$. In these studies, no corrections for calorimetry cracks, decays or conversions were made for any measured quantities such as E_{T}, multiplicity or p_{T}. Properties of clusters observed by CDF, UA1 and UA2 are compared, even though different calorimeters, cluster algorithms, and acceptance regions were used in the measurements.

Geometrical acceptance of clusters

Since the full η acceptances for both charged and pseudo-neutral particles are confined to $|\eta| \leq 1.0$, the geometrical acceptance in η of the clusters (η_{axis}) is even smaller. For $y_{min} = 1$ (a cone of half angle $\sim 40°$), the geometrical full acceptance for the clusters is roughly $|\eta_{\mathrm{axis}}| \leq 0.1$. To see if the acceptance in η_{axis} could be extended, the multiplicity and energy density distributions in $\Delta\eta$ (difference in η between tracks in the cluster and cluster axis) were plotted in Figure 7.9 for clusters with $E_{\mathrm{T}} \geq 5$ GeV and $|\eta_{\mathrm{axis}}| \leq 0.1$. The average contribution from particles at $\Delta\eta > 0.5$ to the cluster energies was less than ~ 2 %. Therefore the full acceptance of the cluster axis was extended out to $|\eta_{\mathrm{axis}}| \leq 0.5$.

Probability of particle clusters

The inclusive E_{T} spectra for clusters with $|\eta_{\mathrm{axis}}| \leq 0.5$ are shown in Figure 7.10 and listed in Table 7.2, for $\sqrt{s}$ of 1800 and 630 GeV minimum bias events. The distributions were normalized to give the probability per unit of η of clusters in a minimum bias event as a function of E_{T}. The spectrum hardens as the center of mass energy increases: the production rate of clusters with E_{T} between 3 and 10 GeV increases by a factor of two with an increase in

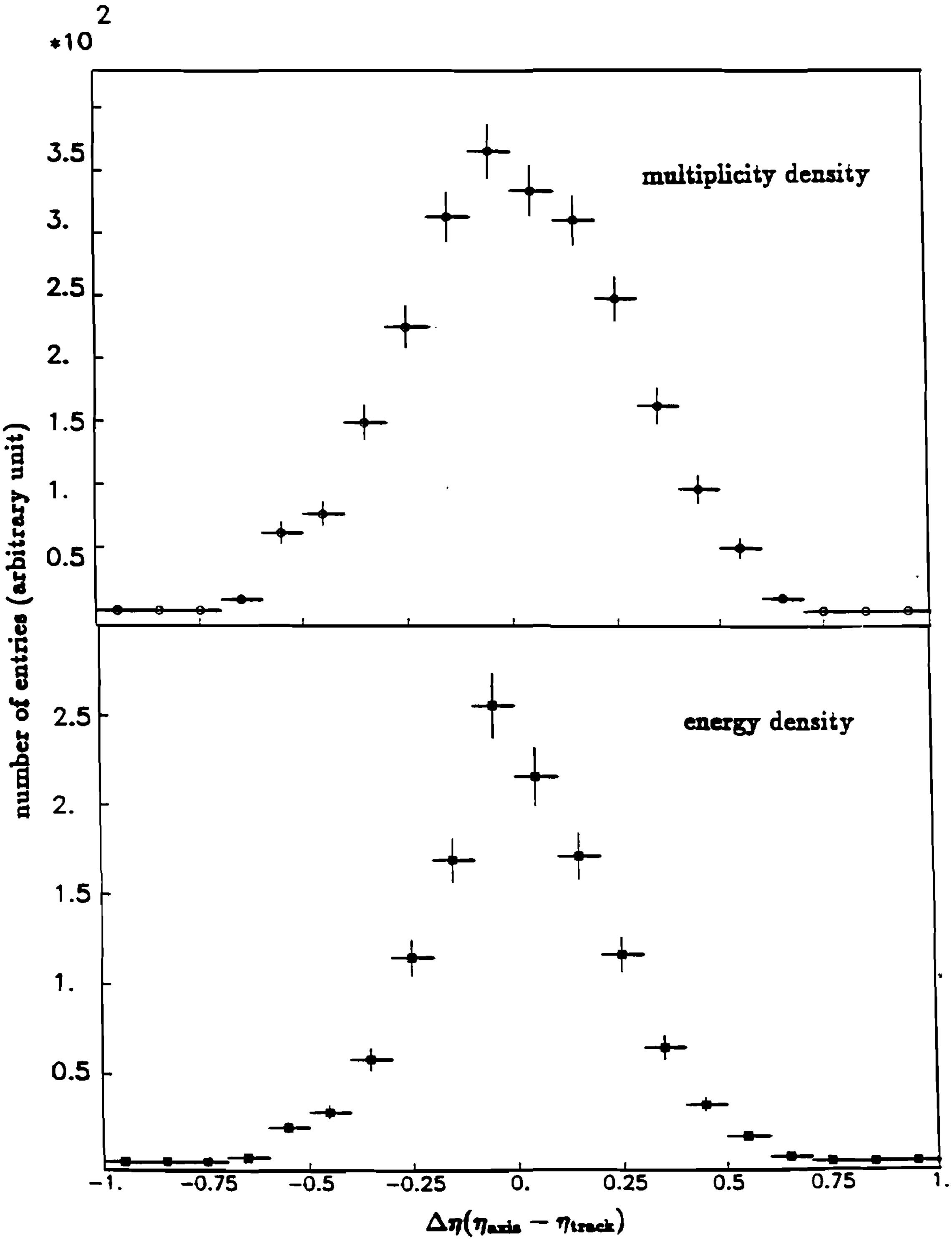

Figure 7.9 Multiplicity and energy density distributions in clusters.

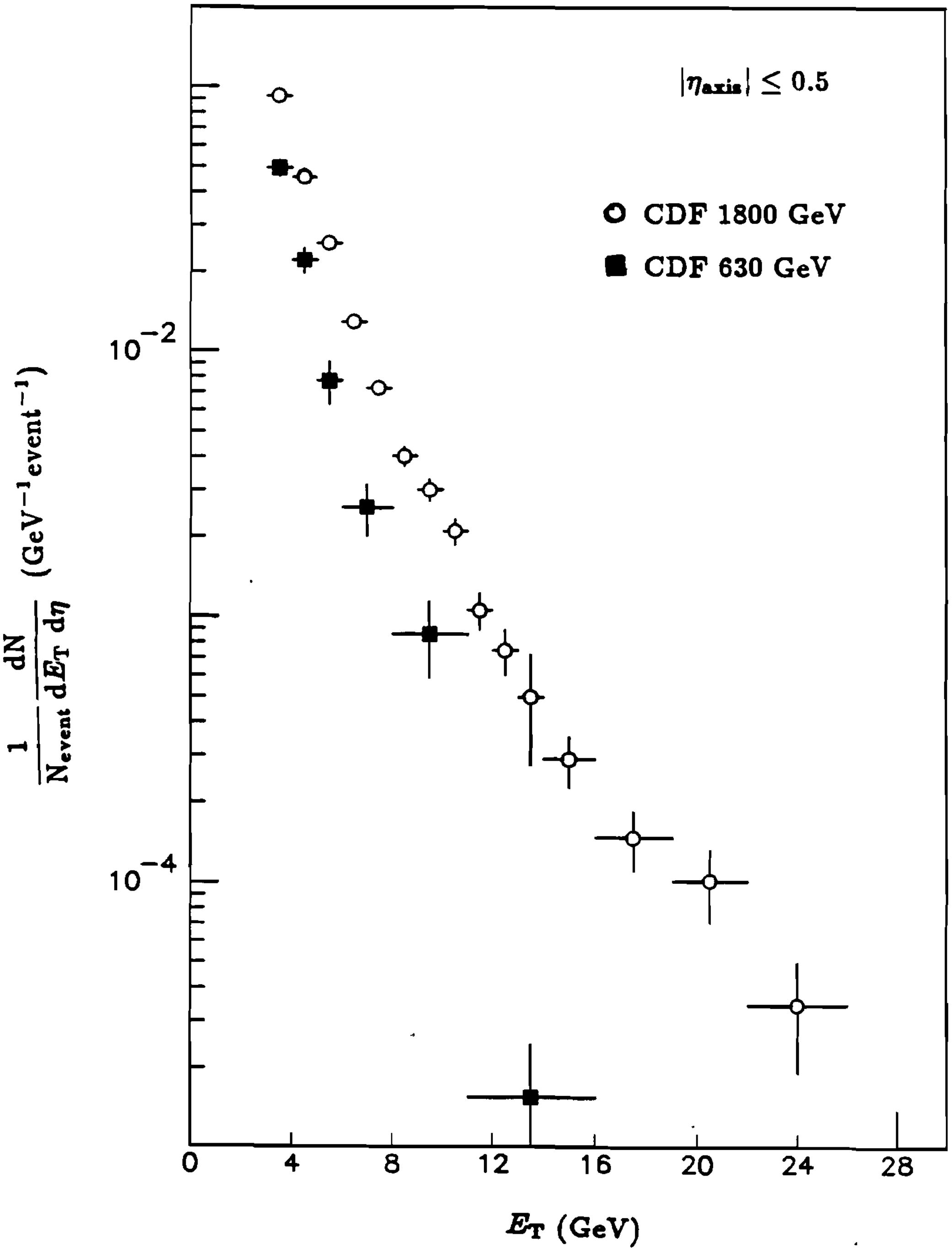

Figure 7.10 Probability of clusters in minimum bias data.

Table 7.2 Probability of clusters in minimum bias events.

$\sqrt{s} = 1800$ GeV		$\sqrt{s} = 630$ GeV	
E_T (GeV)	$1/N_{event}\ dN/(dE_T d\eta)$ (GeV^{-1})	E_T (GeV)	$1/N_{event}\ dN/(dE_T d\eta)$ (GeV^{-1})
3.0-4.0	$(9.24 \pm 0.16) \times 10^{-2}$	3.0-4.0	$(4.94 \pm 0.36) \times 10^{-2}$
4.0-5.0	$(4.57 \pm 0.11) \times 10^{-2}$	4.0-5.0	$(2.22 \pm 0.24) \times 10^{-2}$
5.0-6.0	$(2.57 \pm 0.08) \times 10^{-2}$	5.0-6.0	$(7.76 \pm 1.42) \times 10^{-3}$
6.0-7.0	$(1.30 \pm 0.06) \times 10^{-2}$	6.0-8.0	$(2.59 \pm 0.58) \times 10^{-3}$
7.0-8.0	$(7.31 \pm 0.45) \times 10^{-3}$	8.0-11.0	$(8.63 \pm 2.73) \times 10^{-4}$
8.0-9.0	$(4.06 \pm 0.34) \times 10^{-3}$	11.0-16.0	$(1.55 \pm 0.90) \times 10^{-4}$
9.0-10.0	$(3.03 \pm 0.29) \times 10^{-3}$		
10.0-11.0	$(2.11 \pm 0.24) \times 10^{-3}$		
11.0-12.0	$(1.06 \pm 0.17) \times 10^{-3}$		
12.0-13.0	$(7.51 \pm 1.44) \times 10^{-4}$		
13.0-14.0	$(5.00 \pm 2.24) \times 10^{-4}$		
14.0-16.0	$(2.92 \pm 0.64) \times 10^{-4}$		
16.0-19.0	$(1.48 \pm 0.37) \times 10^{-4}$		
19.0-22.0	$(1.02 \pm 0.31) \times 10^{-4}$		
22.0-26.0	$(3.48 \pm 1.55) \times 10^{-5}$		
26.0-30.0	$(6.95 \pm 6.95) \times 10^{-6}$		

Averaged over the bin size.
Statistical errors only.

$\sqrt{s}$ from 630 GeV to 1800 GeV. The fraction of events containing at least one cluster of $E_{\rm T} \geq 5$ GeV in $|\eta_{\rm axis}| \leq 0.5$ also increases with the center of mass energy. At 1800 GeV, it is 8 % of the total number of analysed events and at $\sqrt{s} = 630$ GeV, it is 4 % of the events (see Table 7.2). This cannot be directly compared with the UA1 measurements since the $\eta_{\rm axis}$ acceptances for the cluster axis in the two experiments are not same. The ratio of the fraction of events at 1800 GeV with at least one cluster to that at 630 GeV is ~ 2.0, which is approximately the same as the ratio of UA1 mini-jet events at 900 GeV to 350 GeV [30].

A back to back azimuthal correlation, which is one of the distinct features of hard scattering, could not be observed in the present analysis due to statistical limitations. In $|\eta_{\rm axis}| \leq 0.5$, only ~ 0.06 % of the total 36,000 events ($\approx$ 22 events) at 1800 GeV have more than one cluster with $E_{\rm T} \geq 5$ GeV and the sum of transverse energies of the first and second highest $E_{\rm T}$ clusters being $\geq$ 70 % of $\Sigma E_{\rm T}$ of the event (This latter requirement is intended to ensure that $2 \rightarrow 2$ parton scattering will be within the full acceptance range.).

Properties of particle clusters

The increase in the mean charged particle multiplicity of jets produced in e^+e^- annihilation was observed as a function of the jet $E_{\rm T}$ [96]. The data from e^+e^- collisions are dominated by $e^+e^- \rightarrow q\bar{q}$ and thus gives the mean multiplicity for quark fragmentation averaged over all flavors. Conversely, low $E_{\rm T}$ jets in $\bar{\rm p}$p collision should be predominately gluon jets. The mean multiplicity of charged particles with $p_{\rm T} \geq 400$ MeV/c for clusters in minimum bias events is shown in Figure 7.11 as a function of cluster $E_{\rm T}$. These clusters also show an increase in charged particle multiplicity at higher $E_{\rm T}$. The mean multiplicity values for all (both charged and pseudo-neutral) particles are also shown in Figure 7.11. The ratio of the charged to pseudo-neutral multiplicity seems to agree well with the expected value of 2 to 1 for all $E_{\rm T}$ values. For

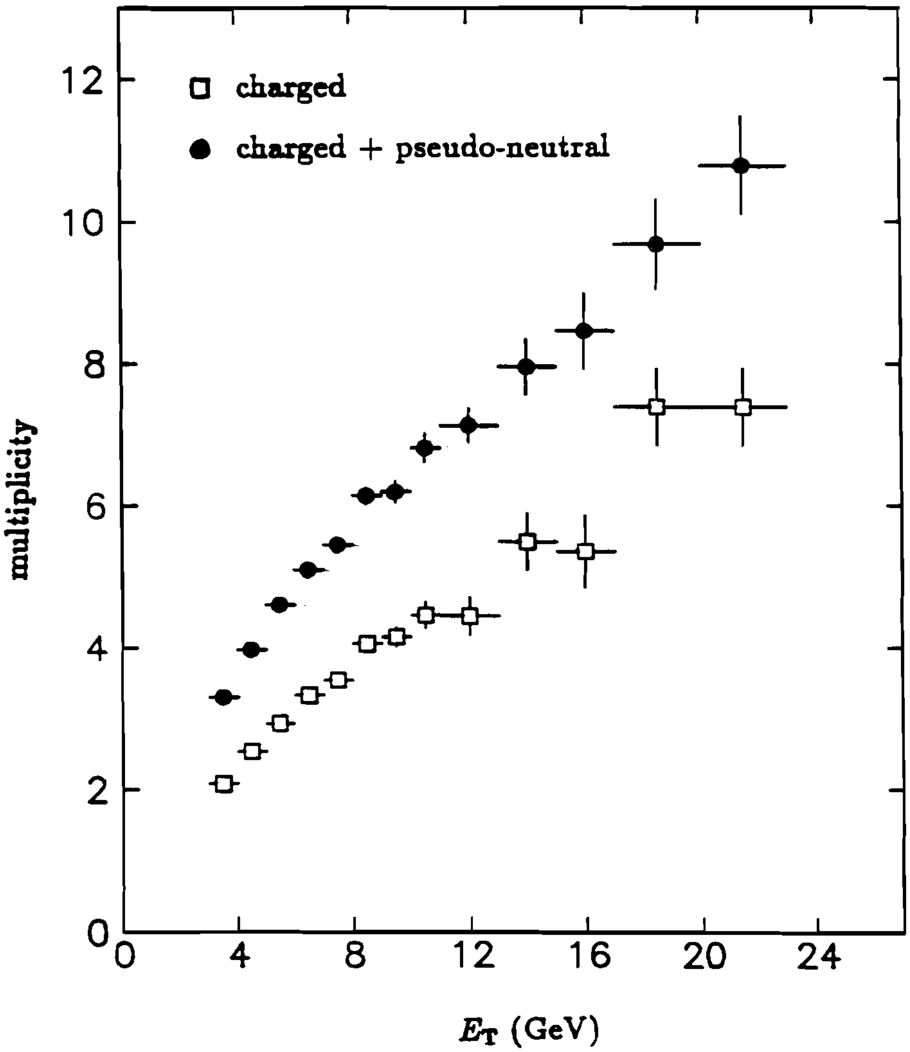

Figure 7.11 Mean mulitplicity of particles in low E_T clusters.

clusters in small E_T intervals:

$$\begin{array}{ll} \text{I} & 3 \leq E_T < 5 \text{ GeV} \\ \text{II} & 5 \leq E_T < 8 \text{ GeV} \\ \text{III} & 10 \leq E_T \text{ GeV}, \end{array} \tag{1}$$

the distribution of charged particle multiplicities ($p_T \geq 400$ MeV/c) are shown in Figure 7.12. The distributions in the three E_T intervals all show peaks near the average value.

Figure 7.13 shows the fractional E_T contribution of the charged particles (E_{Tch}) to the E_T of the cluster as a function of E_T. The mean value of the ratio, $< E_{Tch}/E_T >$, agrees well with the expected ~ 65 % in all E_T ranges. The distributions of $< E_{Tch}/E_T >$ in the three E_T intervals are shown in Figure 7.14 where at lower E_T, the distribution is much broader.

At low E_T, the experimental definition of a jet can lose its significance because clusters can be generated by a single high p_T particle plus fluctuations of the transverse energy density within a defined window around the initiator. The width of the jet cone for $E_T > 20$ GeV is known to be roughly independent of the jet E_T due to the limited transverse momentum of the fragments around the jet axis [81]. The width of low E_T clusters was studied to possibly determine the minimum value of E_T for a cluster to be a "jet" and to find the fraction of reconstructed clusters which can be attributed to QCD jets rather than to transverse energy fluctuations in soft collisions. A quantity F is defined as the ratio between the E_T contained in a cone of radius $\Delta R = \sqrt{\Delta\eta^2 + \Delta\phi^2} = 0.2$ around the cluster axis and the E_T of the cluster:

$$F = \frac{\Sigma E_T(\Delta R = 0.2)}{\Sigma E_T(\Delta R = 0.7)}.$$

Figure 7.15 shows the distribution of the average value of F as a function of E_T of the clusters in minimum bias data. As the E_T of the cluster increases, $< F >$ shows a fast decrease then starts to increase slowly above $E_T \sim 6$ GeV. A similar measurement by the UA1 collaboration [30] shows a good agreement

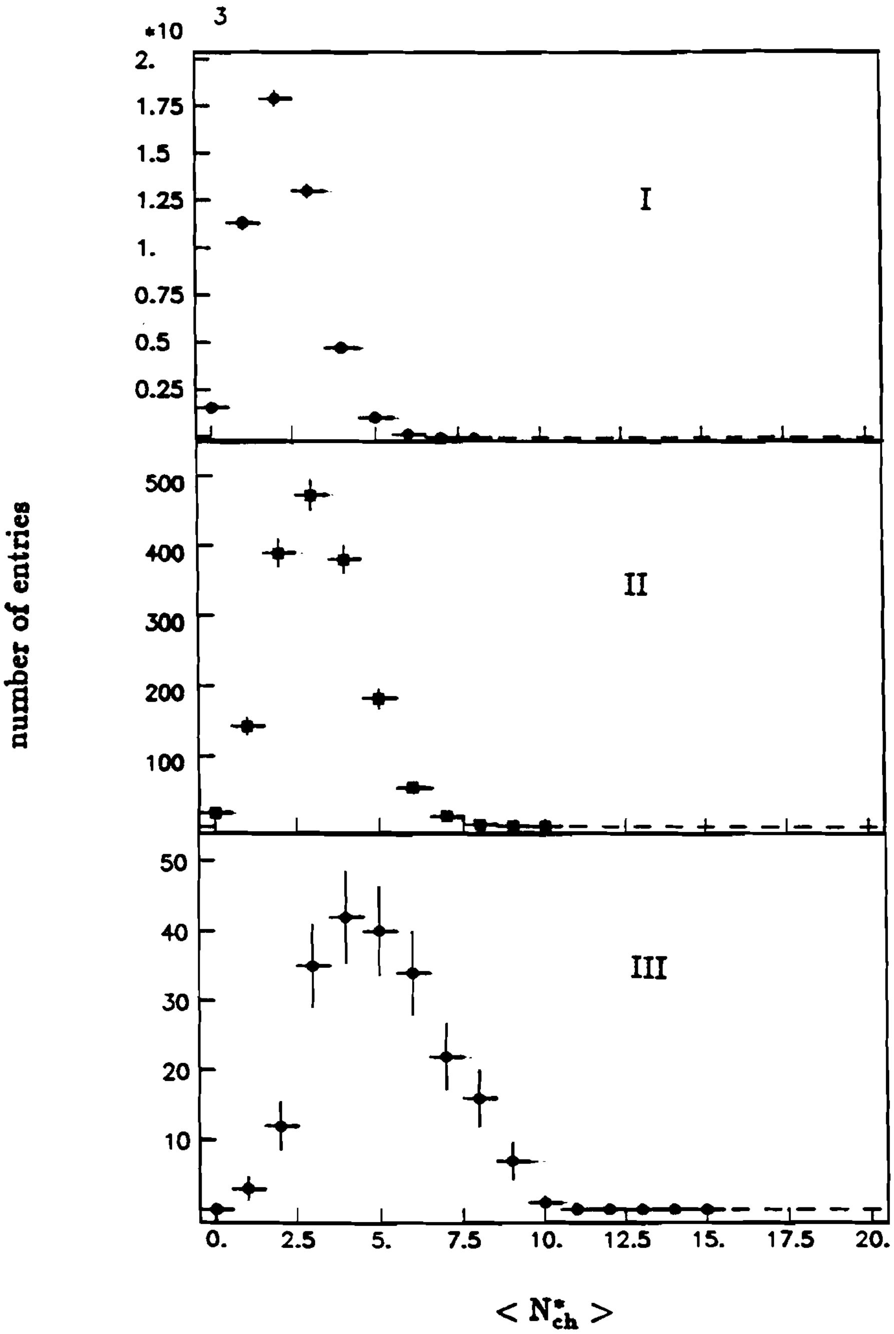

Figure 7.12 Multiplicity distribution of charged particles in low E_T clusters.

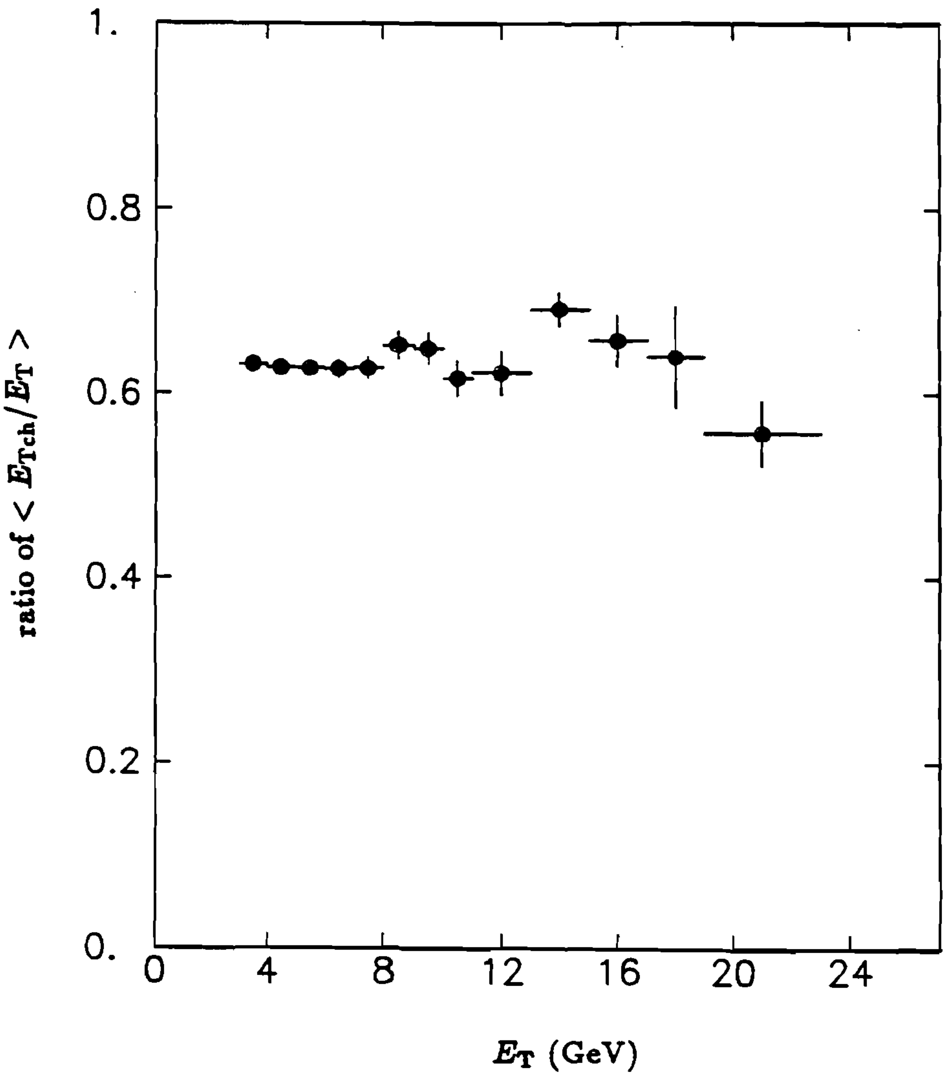

Figure 7.13 $< E_{\mathrm{Tch}}/E_{\mathrm{T}} >$ of low E_{T} clusters.

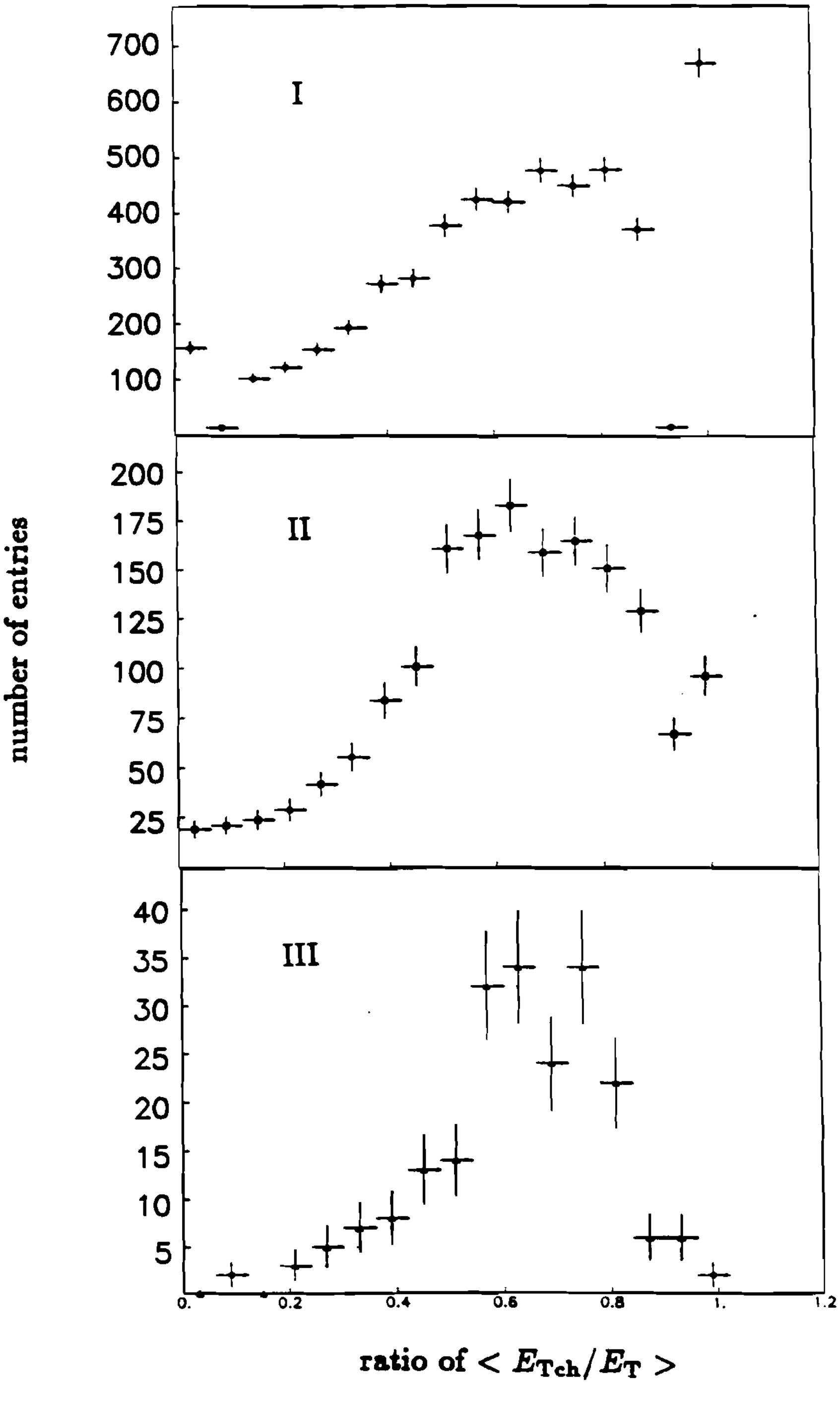

Figure 7.14 $< E_{\mathrm{Tch}}/E_{\mathrm{T}} >$ **distributions in the three** E_{T} **intervals.**

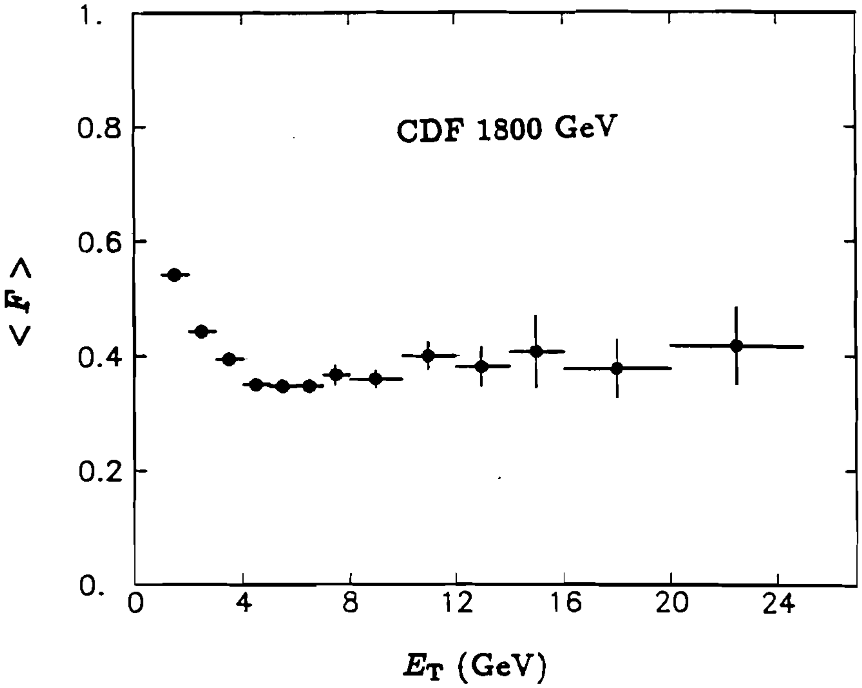

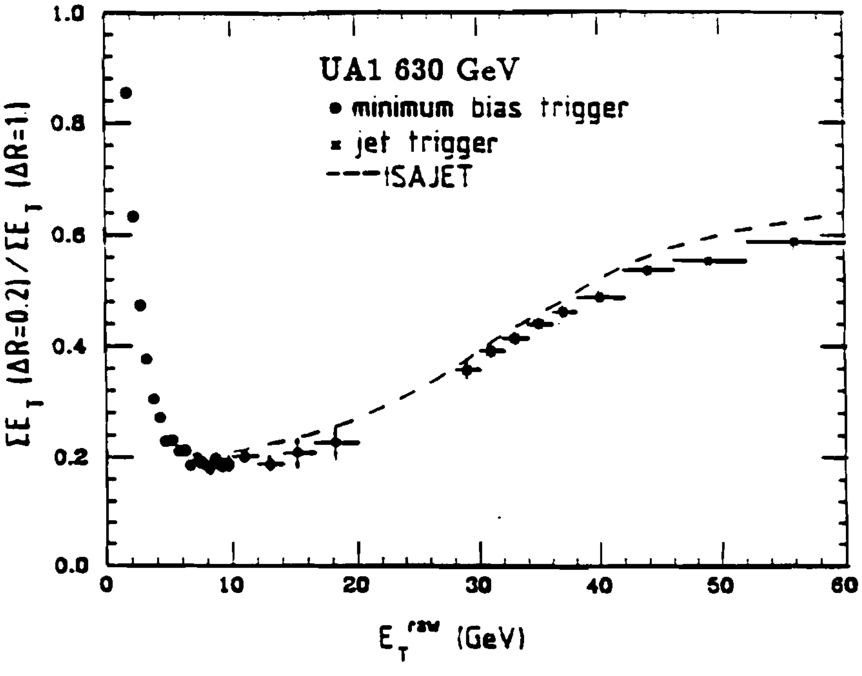

Figure 7.15 Average value of F as a function of E_T.

(see Figure 7.15). As shown in Figure 7.15, UA1 compared their result to the ISAJET prediction and concluded that $< F >$ increases slowly up to the high E_{T} region and the jet profile does not change down to $E_{\mathrm{T}} > 5$ GeV [30]. However, when the CDF distributions of F are examined in the three E_{T} intervals (Figure 7.16), it is seen that the average values of F for the two low E_{T} intervals are not the most probable values and the distributions give an indication of a large contribution to clusters with $E_{\mathrm{T}} < 10$ GeV from fluctuations of the transverse energy density both with (in case of $F \sim 1$) and without ($F \sim 0$) the presence of single high p_{T} particle. The spikes at $F \sim 0$ and $F \sim 1$ seen for $E_{\mathrm{T}} < 10$ GeV are absent or much less pronounced both in region III and the real jet data to be shown in Figure 7.30.

The average p_{T} of the 'leading (seed)' track in clusters seems to increase linearly as a function of E_{T} (Figure 7.17). In Figure 7.18, the energy contribution from the leading track to E_{T} of clusters is shown as a function of E_{T}. The ratio between p_{T} of leading particle and E_{T} of cluster decreases as E_{T} increases, and then tends to flatten off for $E_{\mathrm{T}} > 10$ GeV. The distributions of $< p_{\mathrm{T\,seed}}/E_{\mathrm{T}} >$ in the three E_{T} intervals (Figure 7.19) show peaks near the mean value. At higher E_{T}, the distribution is somewhat narrower.

Global event variables with clusters

For jet $E_{\mathrm{T}} > 20$ GeV, the transverse energy density outside the jet cone (underlying event) has been known to be roughly independent of the jet E_{T} [81]. Figure 7.20 shows the behavior of the transverse momentum density, $d\Sigma p_{\mathrm{T}}/d\eta$, of particles in $\pi/4 \leq |\Delta\phi| \leq 3\pi/4$ from the cluster axis as a function of E_{T} in minimum bias data. The p_{T} density shows an increase in the average value by ~ 2 GeV/$(\Delta\eta\Delta\phi)$ from a cluster E_{T} of 3 GeV to 8 GeV and a tendency to flatten off for $E_{\mathrm{T}} > 8$ GeV. A comparision with UA1 minimum bias and jet trigger data at $\sqrt{s} = 630$ GeV was made by rescaling the UA1 data [30] of $dE_{\mathrm{T}}/d\eta$ measured in $\Delta\phi = \pm\pi/2$ around the cluster axis and at $\Delta\eta = 1.5$ from

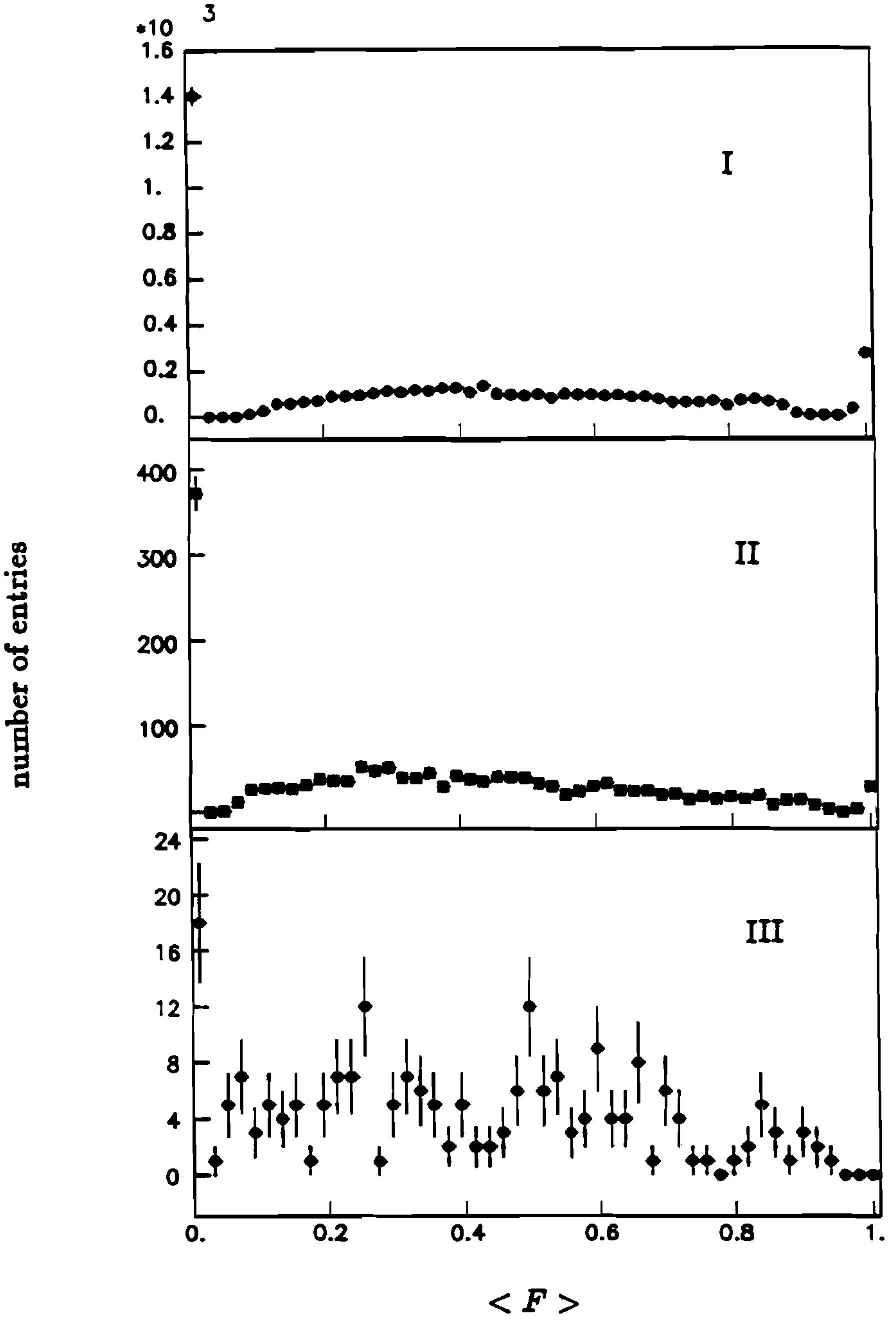

Figure 7.16 Distributions of F in the three E_T intervals.

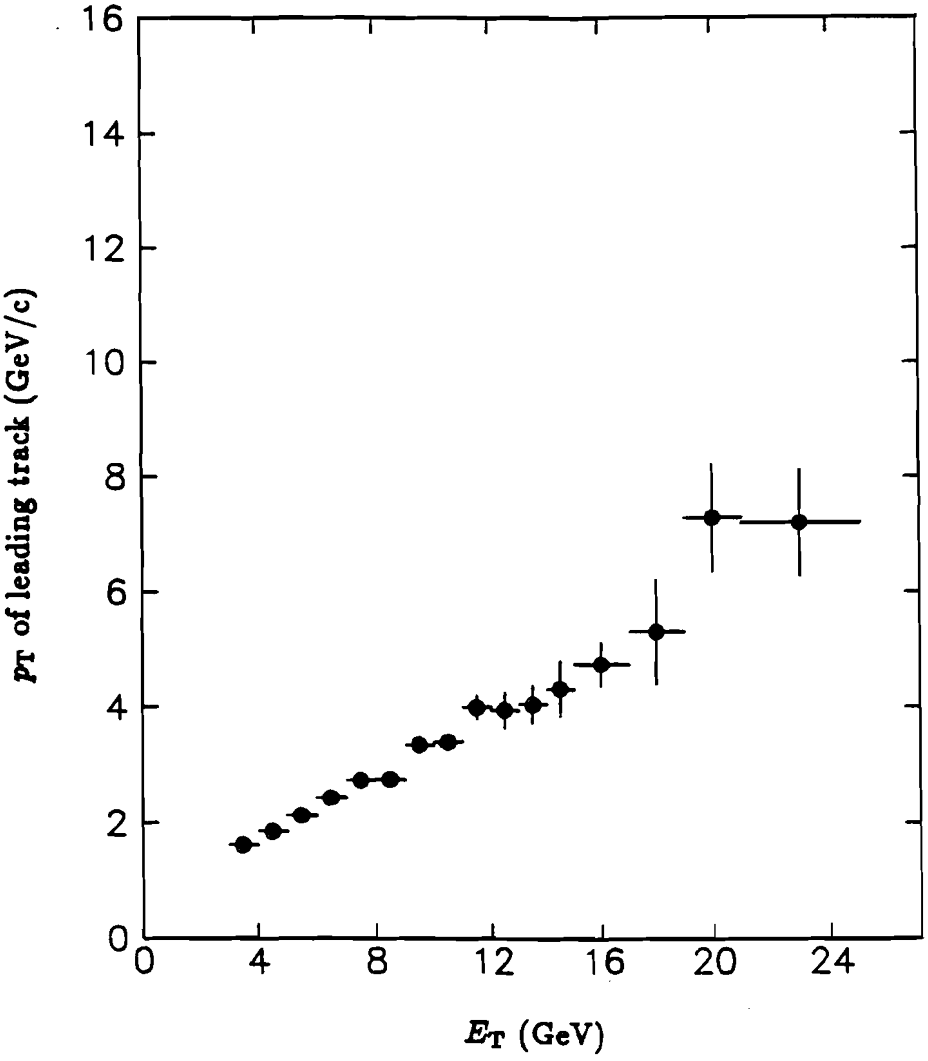

Figure 7.17 Average p_T of leading track in clusters.

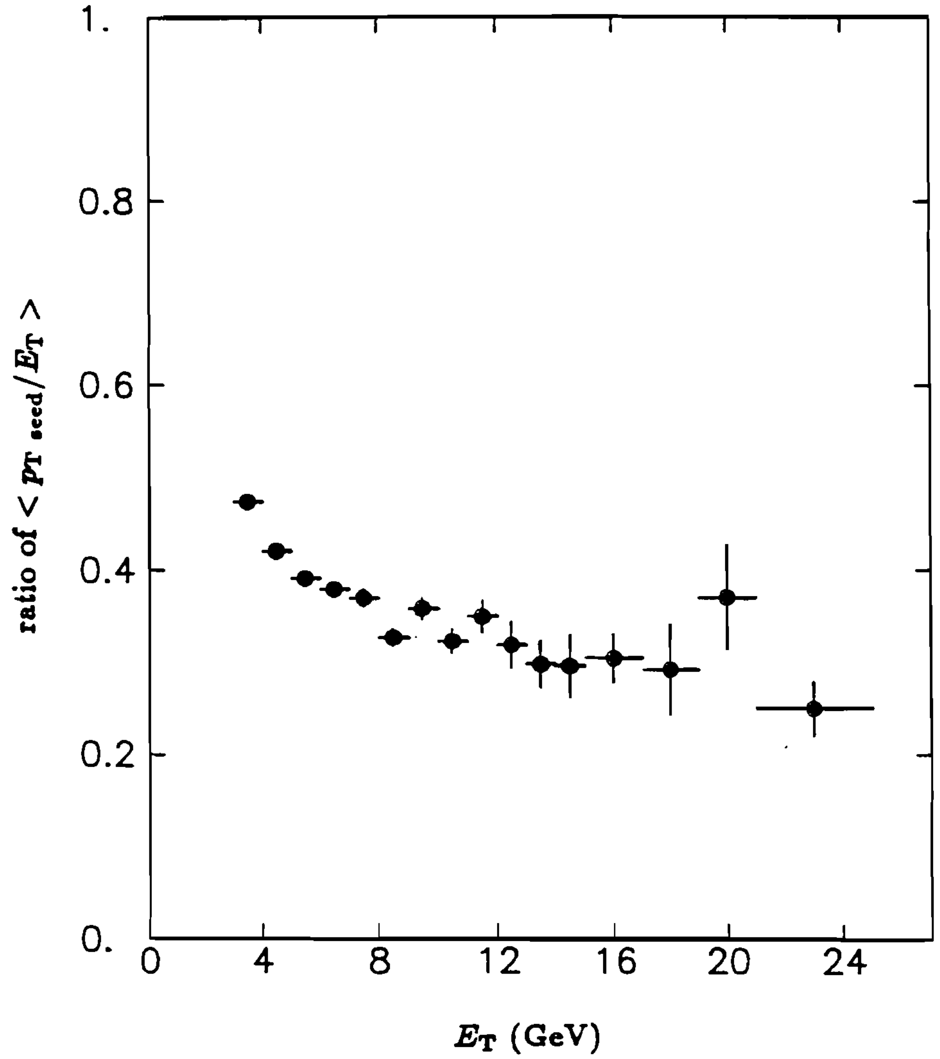

Figure 7.18 Ratio between p_T of leading track and E_T of cluster.

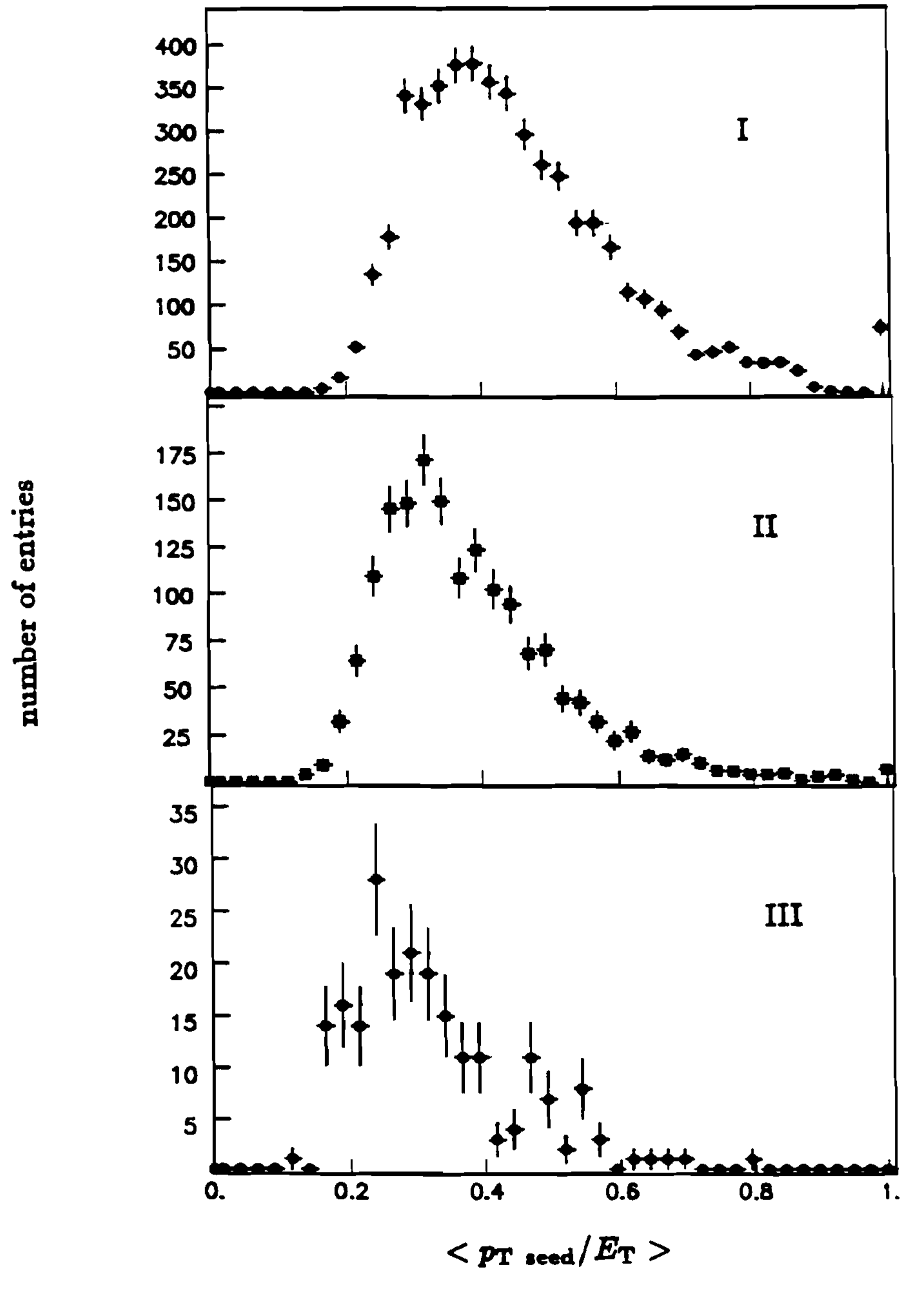

Figure 7.19 Distributions of $< p_{T\ \mathrm{seed}}/E_T >$ in the three E_T intervals.

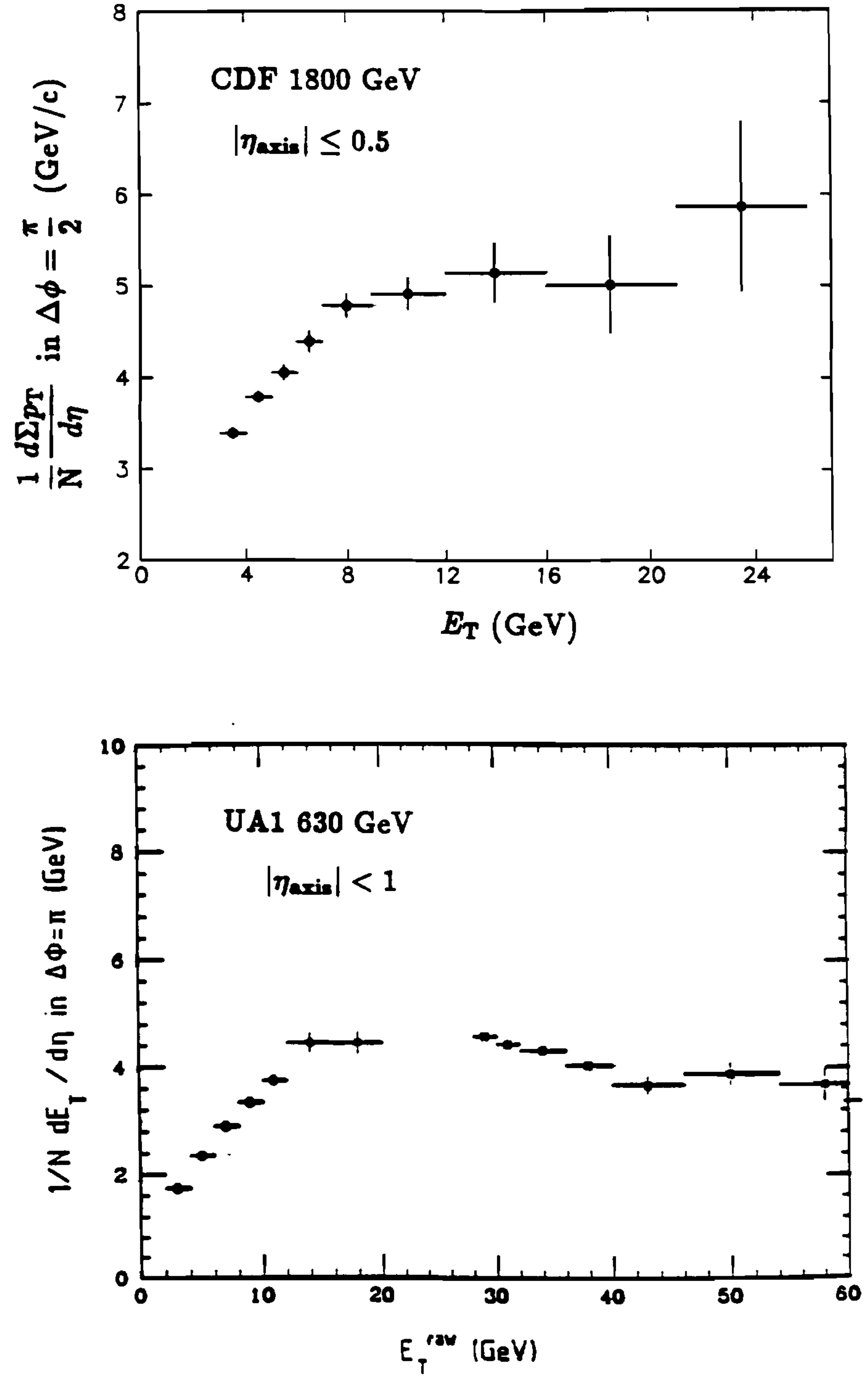

Figure 7.20 The p_T density at $\pi/4 \leq |\Delta\phi| \leq 3\pi/4$ from cluster axis.

the cluster axis. As seen in Figure 7.20, the shape of the distribution shows a good agreement between the two measurements.

The correlation between clusters and the event which contains the clusters were studied using UA2 parametrizations [31]. The ratios h_1 and h_2 are defined as

$$h_1 = \frac{E_{T1}}{\Sigma E_T}$$

$$h_2 = \frac{(E_{T1} + E_{T2})}{\Sigma E_T} = \frac{\hat{E}_T}{\Sigma E_T}$$

where E_{T1} and E_{T2} are the transverse energies of the first and second highest E_T clusters produced in $|\eta_{\mathrm{axis}}| < 0.5$. In Figure 7.21, h_1 and h_2 are plotted as a function of $\hat{E}_T$ at $\sqrt{s} = 1800$ GeV. Similar measurements were made by the UA1 [30] and UA2 [31] collaborations in $|\eta_{\mathrm{axis}}| < 1$ (Figure 7.22). Although different calorimeters and clustering algorithms were used, all three sets of data show a reasonable agreement in the behaviors of h_1 and h_2.

7.4 Properties of Cluster/Non-cluster Events

The minimum bias events can be divided into two groups: events containing at least one cluster ('cluster events') and events without any clusters ('non-cluster events'), with a cluster defined as having $E_T \geq 3$ GeV. In this study, to minimize the residual contamination of cluster events in the sample of non-cluster events, the acceptance of the cluster axis was extended out to $|\eta_{\mathrm{axis}}| < 1$.

Multiplicity distributions

The multiplicity distributions, using the measurement from the VTPC in $|\eta| < 3.0$ for the events with/without clusters, are shown in Figure 7.23 for $\sqrt{s} = 630$ and 1800 GeV. The cluster events exhibit a factor of 2 higher mean charged multiplicity ($< N_{ch} > = 56$ at 1800 GeV) with respect to the non-cluster events ($< N_{ch} > = 26$ at 1800 GeV).

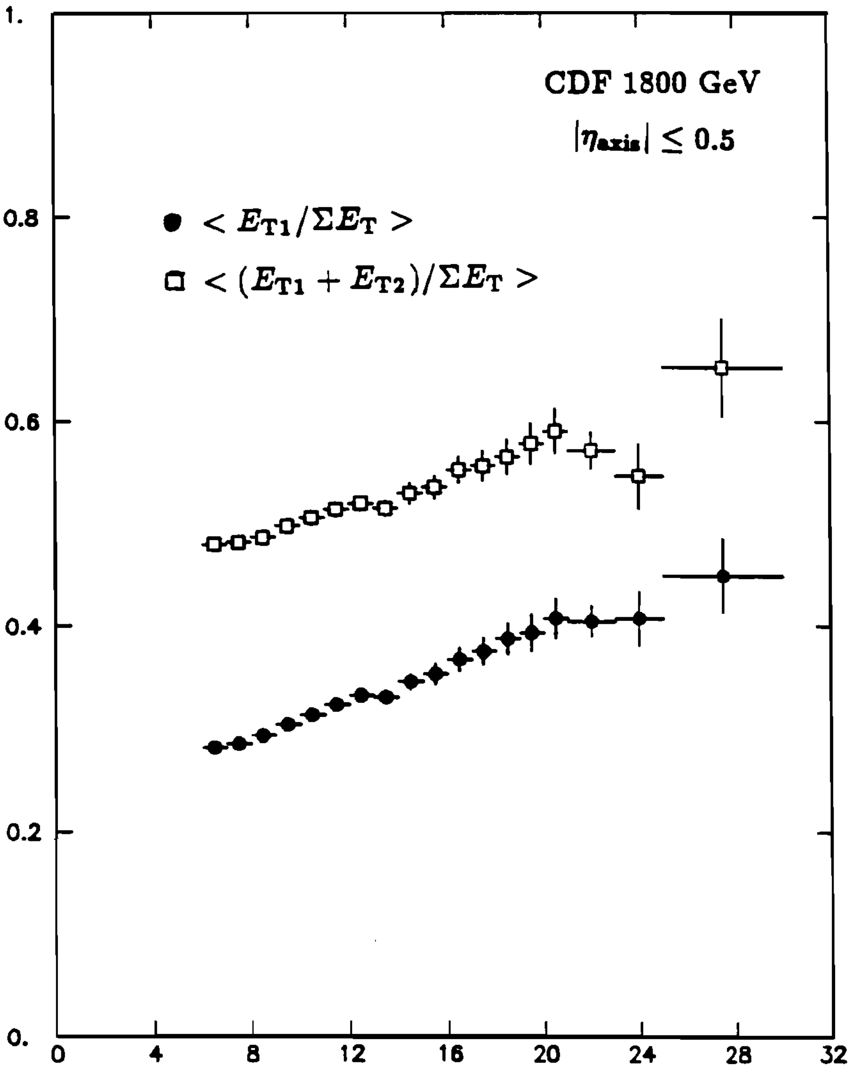

Figure 7.21 Mean value of h_1 and h_2 as a function of $\hat{E}_T$.

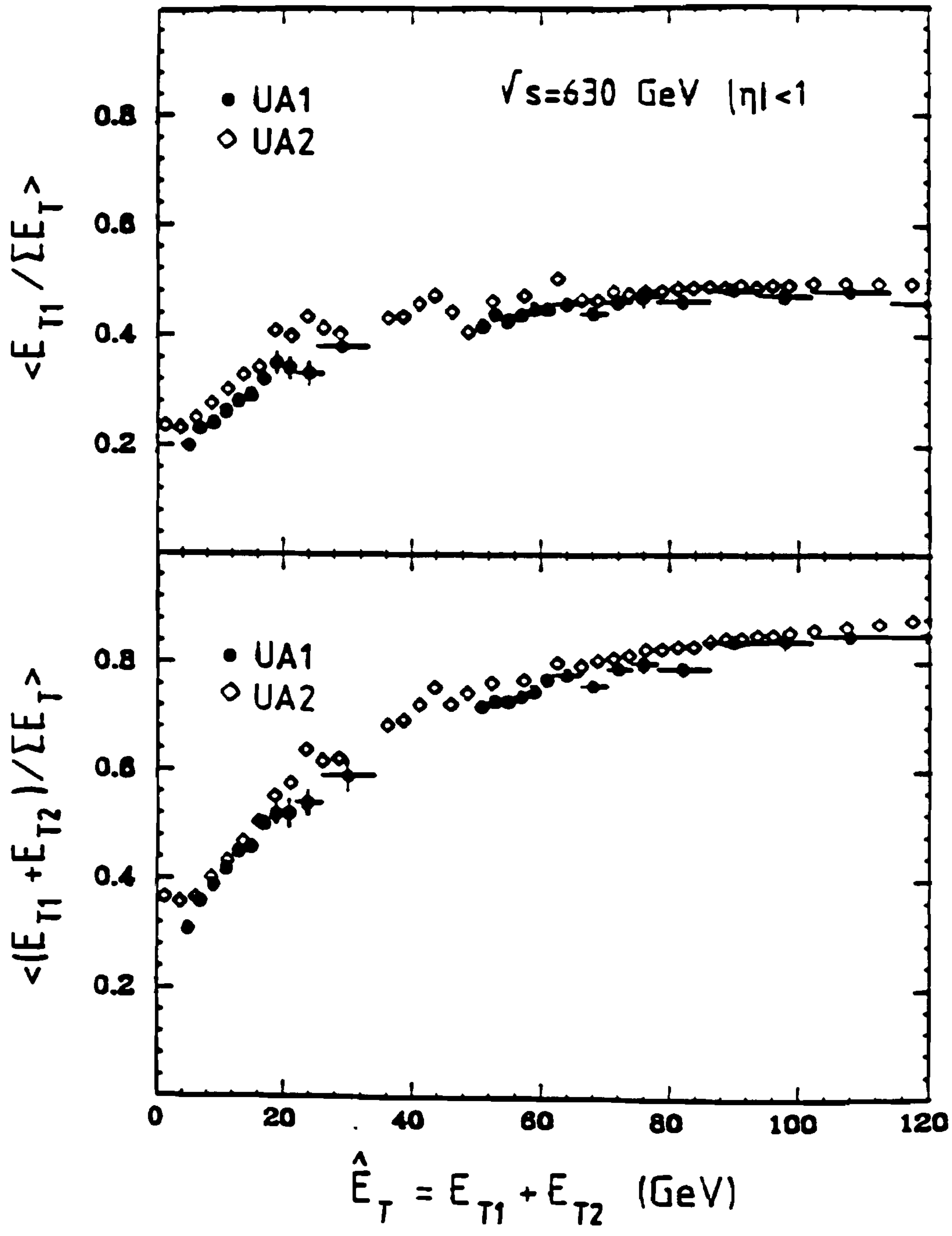

Figure 7.22 Mean value of h_1 and h_2 by UA1 and UA2.

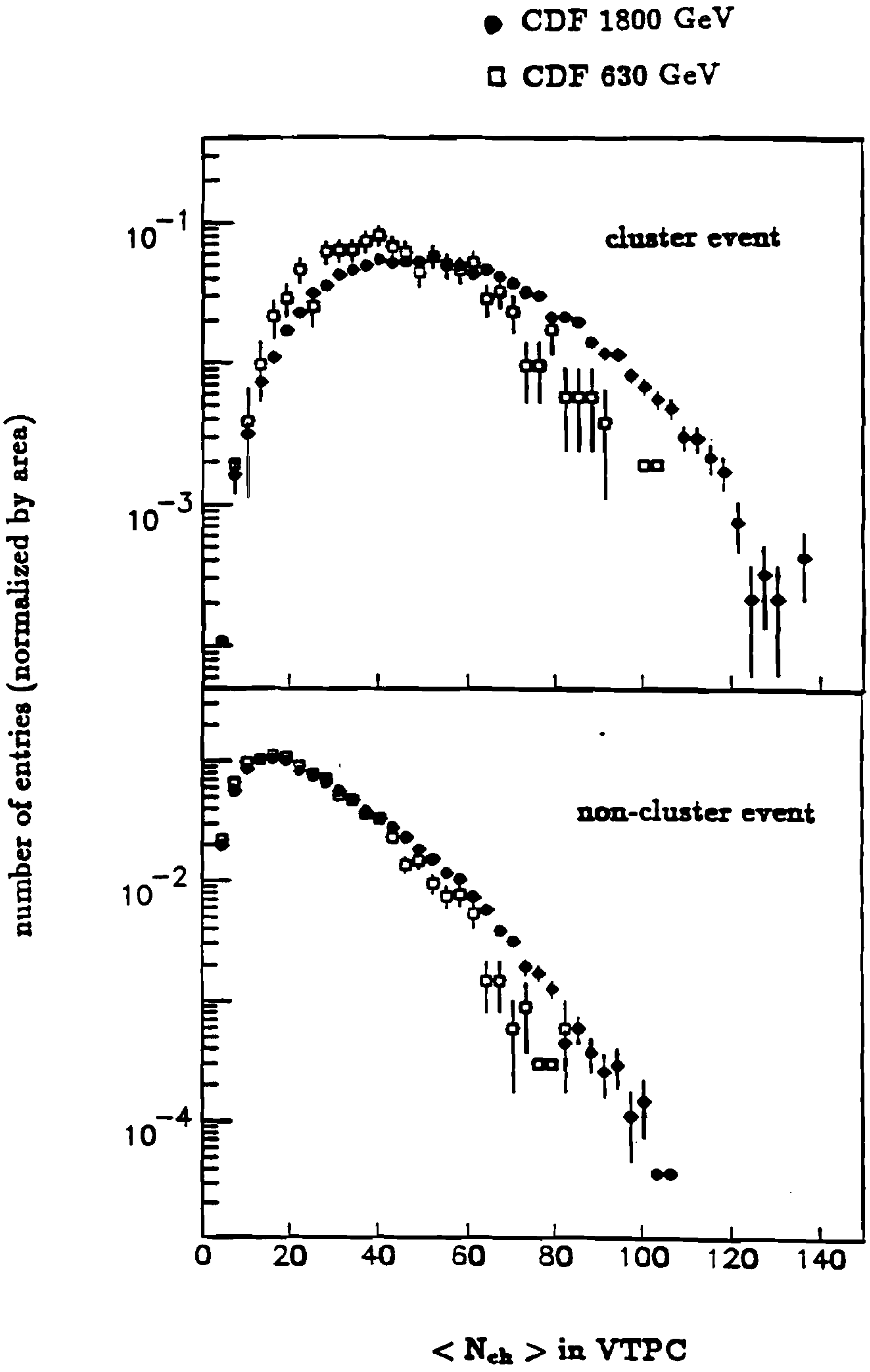

Figure 7.23 N_{ch} of VTPC in cluster/non-cluster events.

Figure 7.24 shows the multiplicity distribution in terms of the KNO variables. The measurements from the UA1 collaboration [30] show a similar behavior that the KNO distribution for the cluster events is much narrower compared to the non-cluster events. The shape of KNO distributions for both cluster and non-cluster events seems to be independent of the center of mass energy.

p_T distributions

The p_T distributions of tracks in the cluster and non-cluster events are shown in Figure 7.25 for $\sqrt{s} = 1800$ and 630 GeV. The shape of the distributions for both cluster and non-cluster events also seems to be independent of $\sqrt{s}$. The distributions for the non-cluster events have an exponential fall-off as was observed in minimum bias events in lower $\sqrt{s}$ experiments [14-17]. The 3 GeV/c cut-off is due to the $E_T \geq 3$ GeV definition of a cluster; and the shape of distributions is presumably also in part an artifact of the cluster definition.

Multiplicity versus $< p_T >$

Figure 7.26 shows the distribution of average transverse momentum ($< p_T >^*$) as a function of the mean multiplicity ($< N^*_{ch} >$) of charged particles with $p_T \geq 400$ MeV/c in the cluster and non-cluster events at $\sqrt{s} = 630$ and 1800 GeV. Above $< N^*_{ch} > \sim 6$, the cluster events show a $< p_T >^*$ depending weakly on $< N^*_{ch} >$, which has been seen in the distribution of the underlying events for high E_T jet data [81]. Below $< N^*_{ch} > \sim 6$, the requirement E_T of cluster ≥ 3 GeV forces the average p_T of charged particles in the cluster event to be higher. The correlation between the average transverse momentum and the multiplicity for the non-cluster events looks very similar to the observations made in minimum bias events at lower $\sqrt{s}$ [17,20]. Again, the distributions for both cluster and non-cluster events seem to be independent of the center of mass energy. What is changing is the increasing proportion of cluster events as $\sqrt{s}$ rises, which seems to be the source of the rise in $< p_T >$ as a function

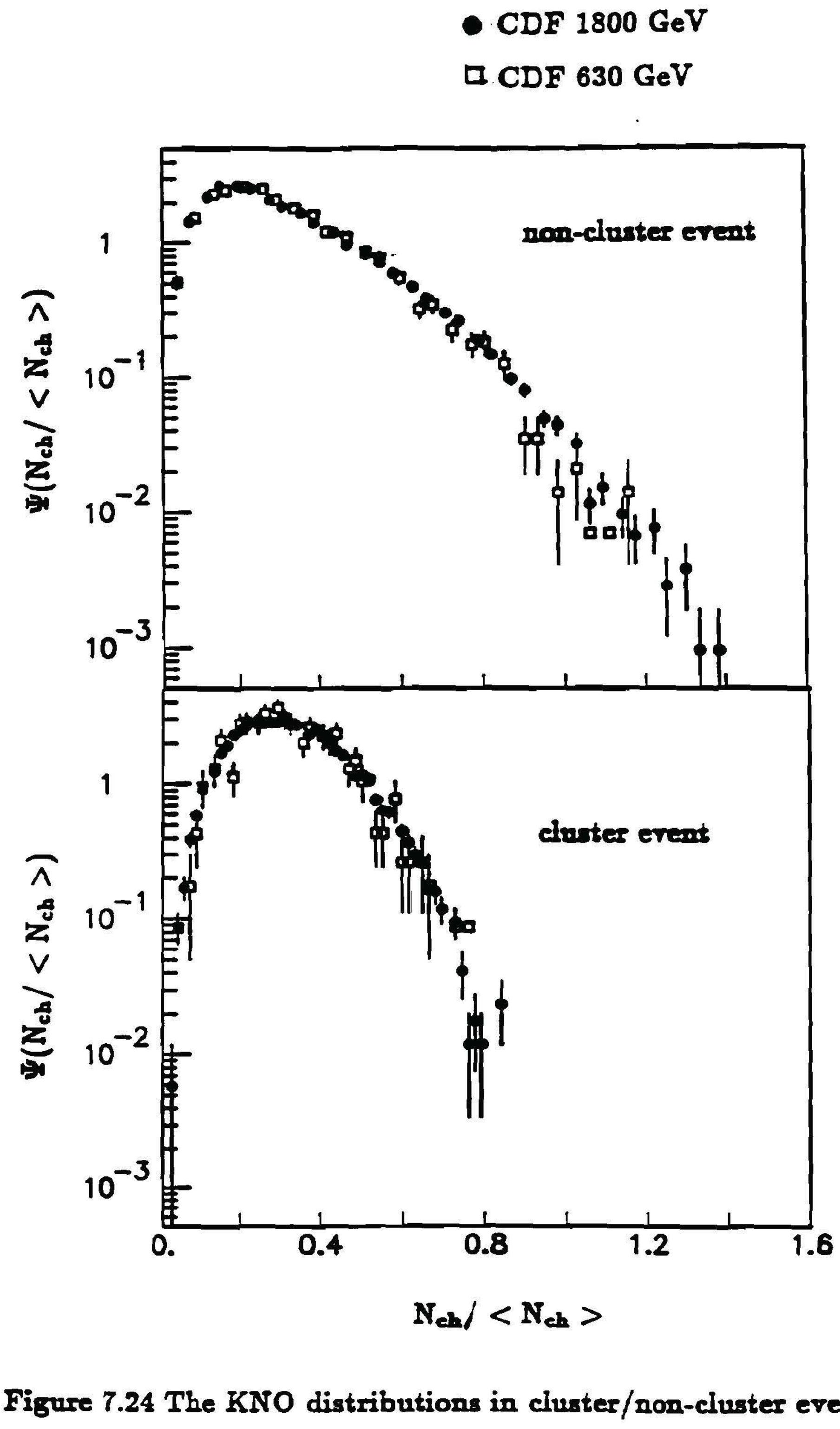

Figure 7.24 The KNO distributions in cluster/non-cluster events.

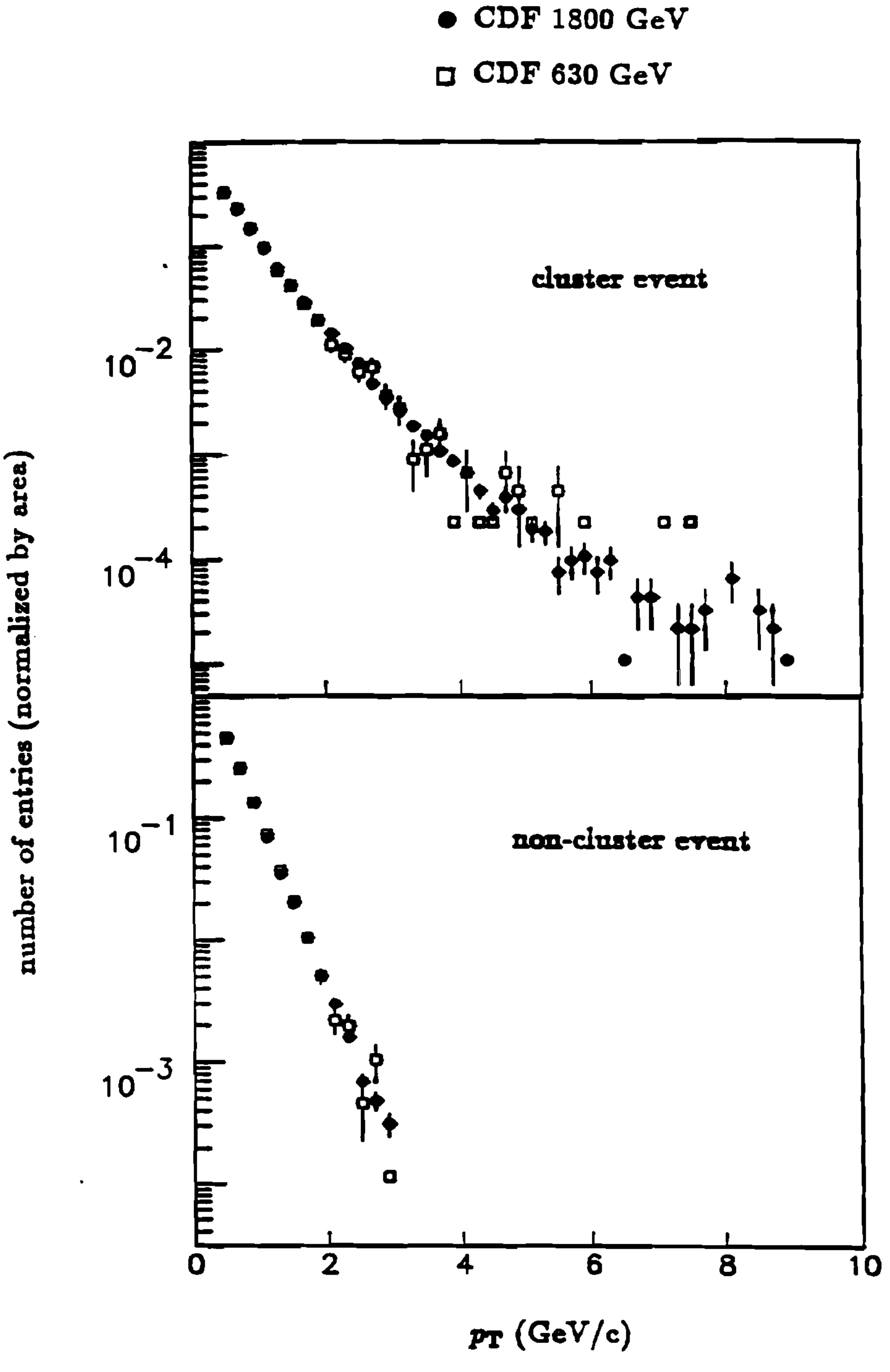

Figure 7.25 The p_T distributions in cluster/non-cluster events.

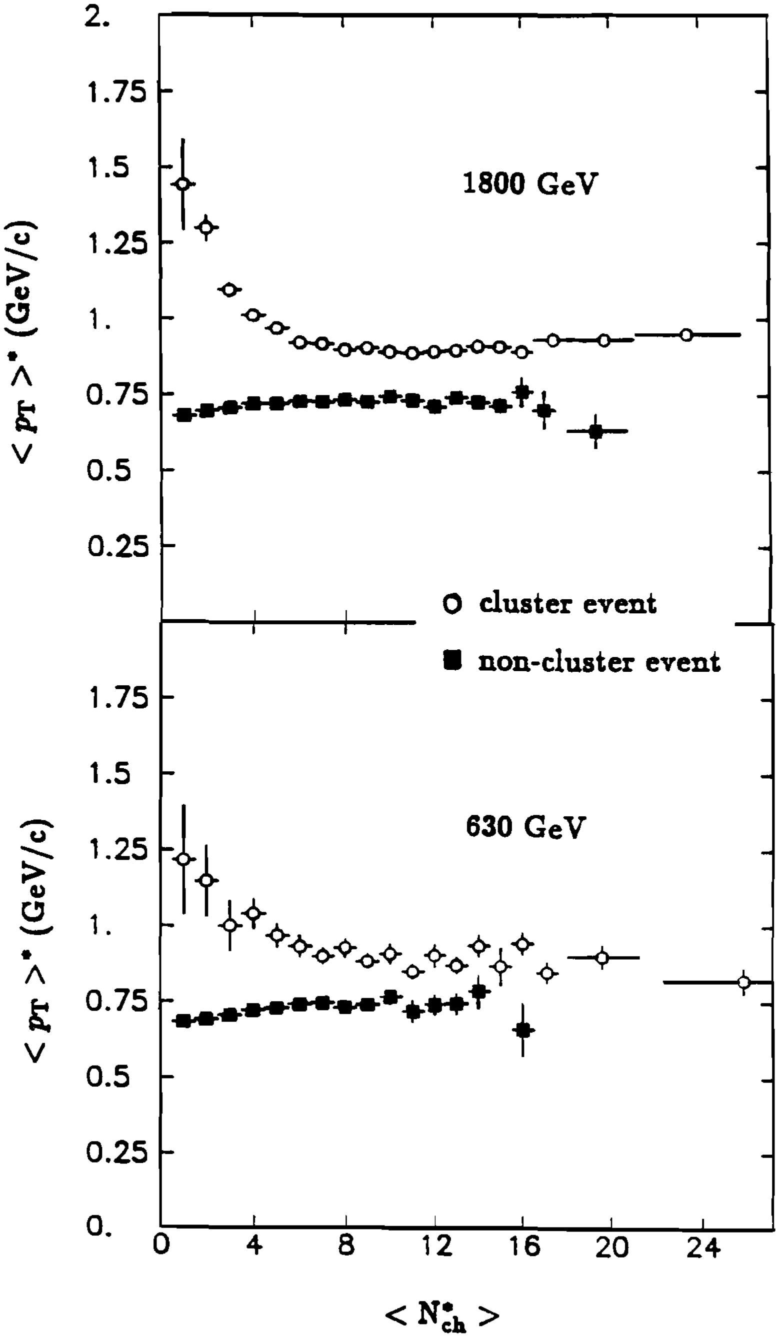

Figure 7.26 $< p_T >^*$ verse N^*_{ch} in cluster/non-cluster events.

of $\sqrt{s}$.

Distribution of ΣE_T

The mean total transverse energy, $< \Sigma E_T >$, of cluster and non-cluster events is plotted in Figure 7.27 for both 1800 and 630 GeV data. The distributions for non-cluster events show an exponential fall off and seem to be independent of $\sqrt{s}$.

Summary of properities of cluster and non-cluster events

The event characteristics such as the average multiplicity, multiplicity distribution (KNO scaling), transverse momentum distribution, correlation between $< p_T >$ and multiplicity and ΣE_T distribution were compared for the two types of events at both $\sqrt{s} = 1800$ and 630 GeV. The cluster events have very different properties from the events which do not contain any clusters. The characteristics of cluster and non-cluster events are largely independent of $\sqrt{s}$, with the exception of the $< \mathrm{N_{ch}} >$ and $< \Sigma E_T >$ distributions for cluster events. The overall changes (flattening of the p_T spectrum, increase in $< p_T >$, and other scaling behaviors) in the total cross sections seem to be coming mainly from the different proportions of these two types of events at different $\sqrt{s}$. The analogous studies done by the UA1 collaboration [30] for their jet ($E_T > 5$ GeV) and non-jet events show good agreements in all the characteristics.

7.5 Comparison with Randomized and Monte Carlo Events

The properties of clusters and the characteristics in the cluster/non-cluster events show good agreement with the measurements by both UA1 and UA2 collaborations. All of these measurements describe the events and clusters in a phenomenological way and the interpretation of QCD perturbative calculations at such low E_T is doubtful and hard to understand since the applicability of perturbative QCD is not clear. A back to back azimuthal correlation could

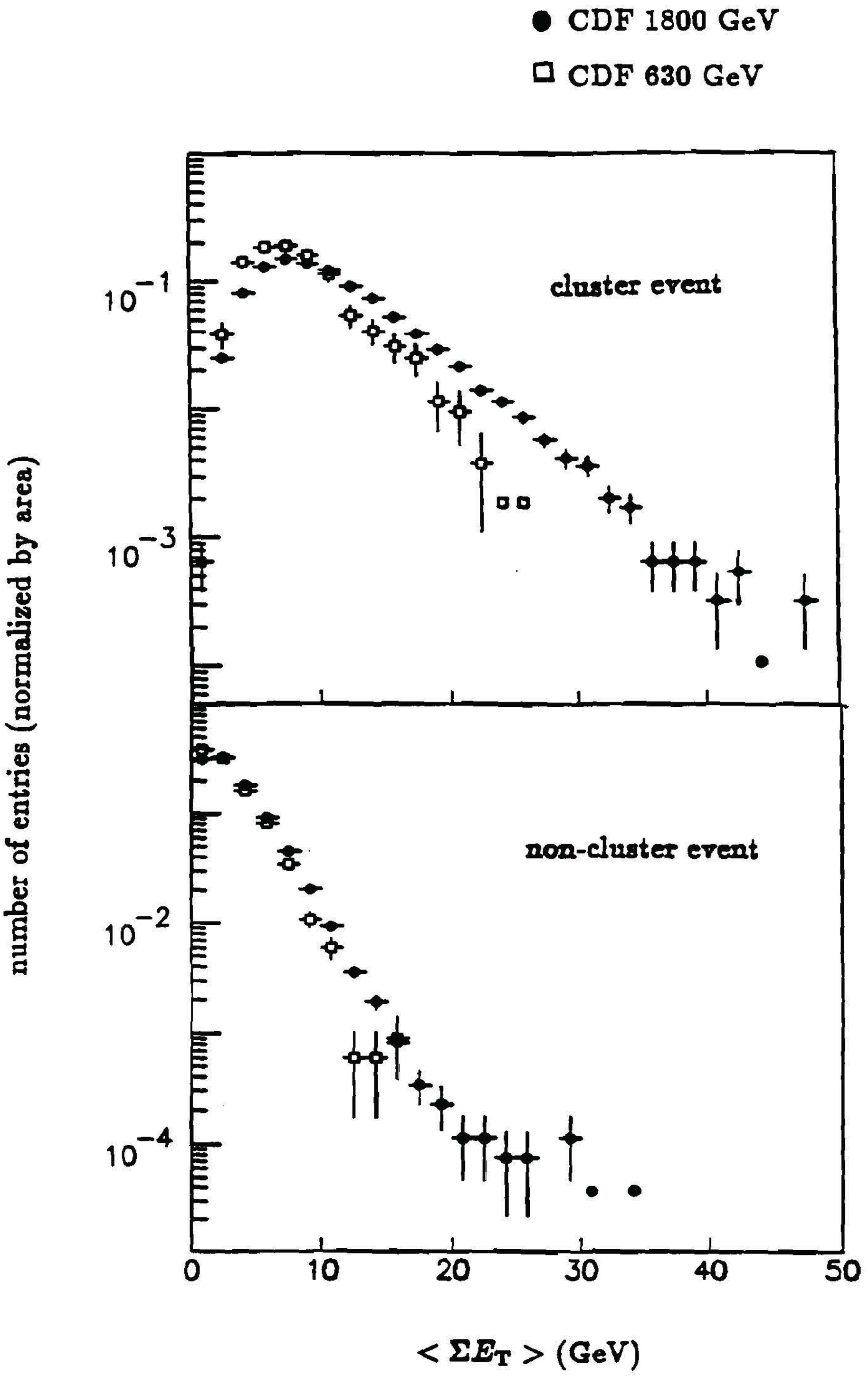

Figure 7.27 $< \Sigma E_T >$ distributions in cluster/non-cluster evnets.

not be seen in this analysis due to a very small η_{axis} acceptance range for the cluster axis, and there were some evidences for the possible inclusion of underlying event energy in the clusters. As a test of whether the clusters which were found in minimum bias events are low E_{T} jets from a hard scattering, are just due to fluctuations, or are some combination, the randomization method discussed below was used.

Randomized events

The tracks in minimum bias events were randomized and the clusters in the randomized events were compared to the real data, with an assumption that if an interaction was from a hard scattering process, it should be 'calculable' by perturbative QCD and have a structure which is distinguishable from random fluctuations. The multiplcity of the event and the p_{T} of each particle were kept, and the directions of each particle were randomized in the limited $\eta - \phi$ space. There was no effort to balance transverse momentum in the randomization.

In Figure 7.28, the E_{T} distribution of clusters from the randomized events was compared with the real events. The probability of clusters as a function of E_{T} is quite similar between the real and randomized events for $E_{\mathrm{T}} < 10$ GeV. One finds 20 % more (3 % less) clusters in real versus randomized events at $E_{\mathrm{T}} = 5$ GeV ($E_{\mathrm{T}} = 3$ GeV). Other properties of low E_{T} clusters which were discussed in Section 7.3 were also studied. The distributions show no significant differences from the real data and the comparision between the real and randomized events is summarized in Table 7.3 in terms of mean values of the various distributions.

To verify the assumption concerning hard scattering and the randomization method, the high E_{T} jet data sample from CDF was studied using the same method. The results are listed in Table 7.4. The probability and the properties of the clusters were completely different between the real events and events after the randomization. For example, ~ 40 % more clusters are

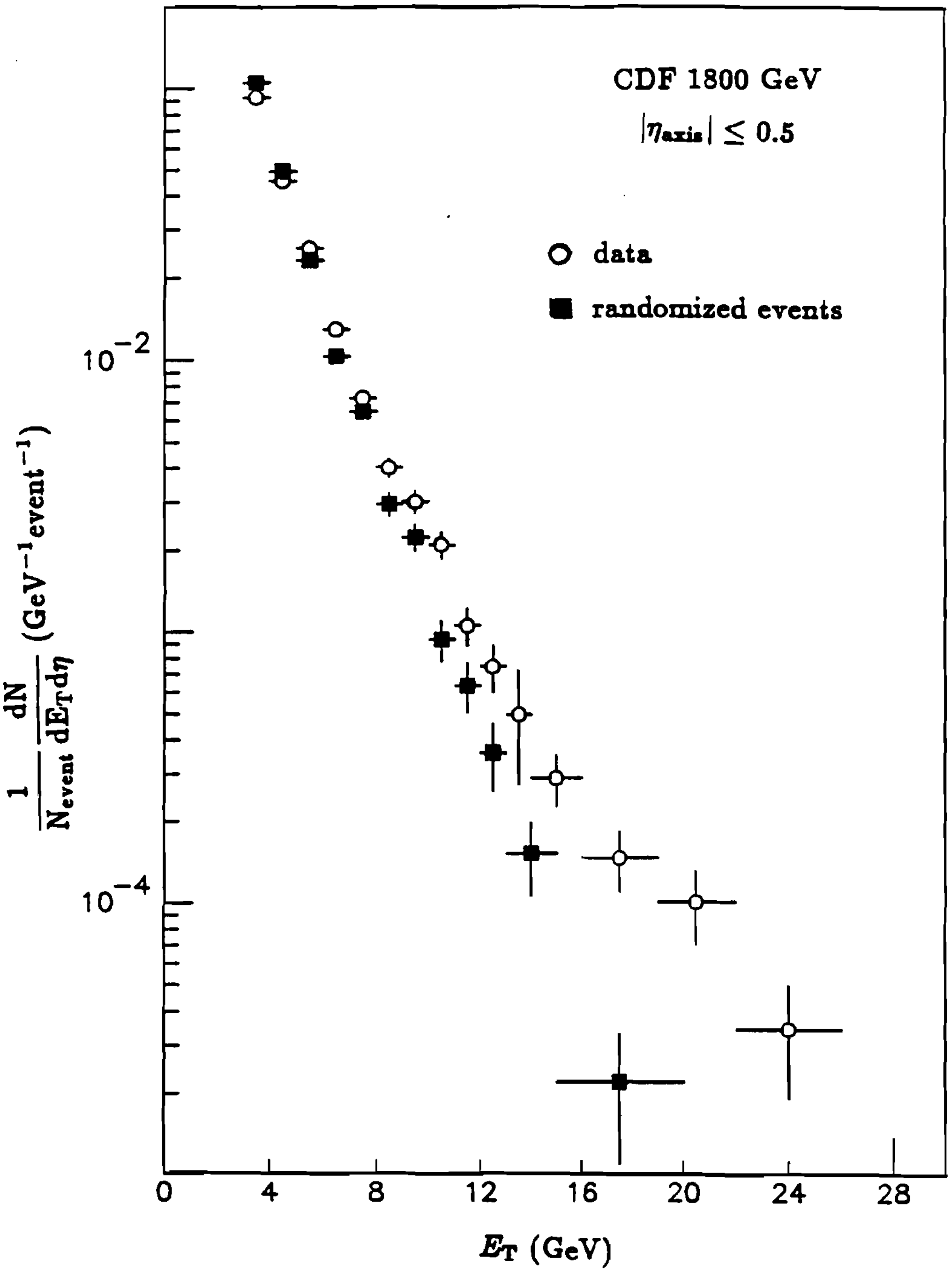

Figure 7.28 E_T of clusters in randomized minimum bias events.

Table 7.3 Clusters in minimum bias events.

$E_T \geq$		data	random	MBR
3 GeV	# events with cluster	5400	5141	5967
	# of clusters per event	1.31	1.42	1.16
	total # of clusters	7092	7282	6932
	$< E_T >$ (GeV)	4.82	4.50	4.03
	$< N_{all} >$	4.06	3.83	3.43
	$< N_{ch} >$	2.60	2.53	2.33
	$< E_{Tch}/E_T >$	0.63	0.66	0.68
	$< F >$	0.37	0.37	0.40
	p_T of seed track (GeV/c)	1.97	1.99	1.96
	$< p_{T\ seed}/E_T >$	0.43	0.46	0.50
	$< E_T$ away$>$ (GeV)	3.77	4.25	2.96
	# events with > 1 cluster	111	29	80
5 GeV	# events with cluster	1835	1403	1618
	# of clusters per event	1.16	1.23	1.03
	total # of clusters	2122	1720	1662
	$< E_T >$ (GeV)	7.13	6.69	6.04
	$< N_{all} >$	5.31	4.92	4.33
	$< N_{ch} >$	3.45	3.21	2.93
	$< E_{Tch}/E_T >$	0.63	0.65	0.68
	$< F >$	0.36	0.33	0.38
	p_T of seed track (GeV/c)	2.58	2.71	2.78
	$< p_{T\ seed}/E_T >$	0.37	0.41	0.47
	$< E_T$ away$>$ (GeV)	4.39	5.11	3.37
	# events with > 1 cluster	22	3	7

from total 36,000 events

$|\eta_{axis}| \leq 0.5$

Table 7.4 Clusters in real and randomized jet events.

$E_T \geq$		data	random
10 GeV	$< E_T >$ (GeV)	34.43	21.12
	$< N_{ch} >$	6.77	3.76
	$< E_{Tch}/E_T >$	0.55	0.57
	$< F >$	0.55	0.51
	$< p_{T\ seed}/E_T >$	0.38	0.56
	# events with > 1 cluster	174	32
20 GeV	# events with cluster	952	691
	$< E_T >$ (GeV)	41.16	31.61
	$< N_{ch} >$	7.40	3.75
	$< E_{Tch}/E_T >$	0.54	0.43
	$< F >$	0.59	0.58
	$< p_{T\ seed}/E_T >$	0.39	0.62
	# events with > 1 cluster	148	17

from total 1,200 events

$|\eta_{axis}| \leq 0.5$

found in real versus randomized events for $E_T \geq 20$ GeV. In Figure 7.29 - 7.31, some of the distributions which have very distinct differences between real and randomized events are shown. The distributions of $< E_{Tch}/E_T >$ and $< F >$ for real jet data are similar to those for $E_T \geq 10$ GeV (interval III) in minimum bias data (see Figure 7.14 and 7.16) whereas the distributions for the randomized jet data show the same behaviors as seen in the distributions of $E_T < 10$ GeV (interval I and II) minimum bias data. In Figure 7.31, the back to back azimuthal correlation between the first and second highest E_T (≥ 20 GeV) clusters is plotted for the events with the sum of E_{T1} and $E_{T2} \geq 70$ % of ΣE_T. The $\Delta\phi$ distribition for the real jet data shows a clear back to back behavior. In the randomized jet events, this back to back behavior can not be seen because there was no attempt to balence p_T in the randomization.

Monte Carlo events

The randomization of events in such a limited acceptance range in η ($|\eta| < 1.0$) is questionable in its effect, in particular, considering the size of clusters in the phase space. The phase space of $\eta \times \phi = 2 \times 2\pi$ can hold only ~ 10 clusters with cones of half angle $\sim 40°$ without allowing any overlaps.

Monte Carlo studies using a complete random event generator in full phase space which can reproduce all the behaviors (p_T spectrum, multiplicity and their correlations, etc.) of the real data would be the perfect solution to test whether the observed clusters are from real hard scattering or merely from random fluctuations. However, most available Monte Carlo programs do not give a proper description of the real data. Table 7.5 shows the summary of average values found in 4 minimum bias Monte Carlo generators for the multiplicity and p_T distributions at $\sqrt{s}$ of 1800 and 630 GeV using default parameters.

Since it is extremely difficult to tune any of these programs, a study has been done with a simple Monte Carlo model which generates the correct p_T spectrum and the average multiplcity of events. The CDF minimum bias Monte

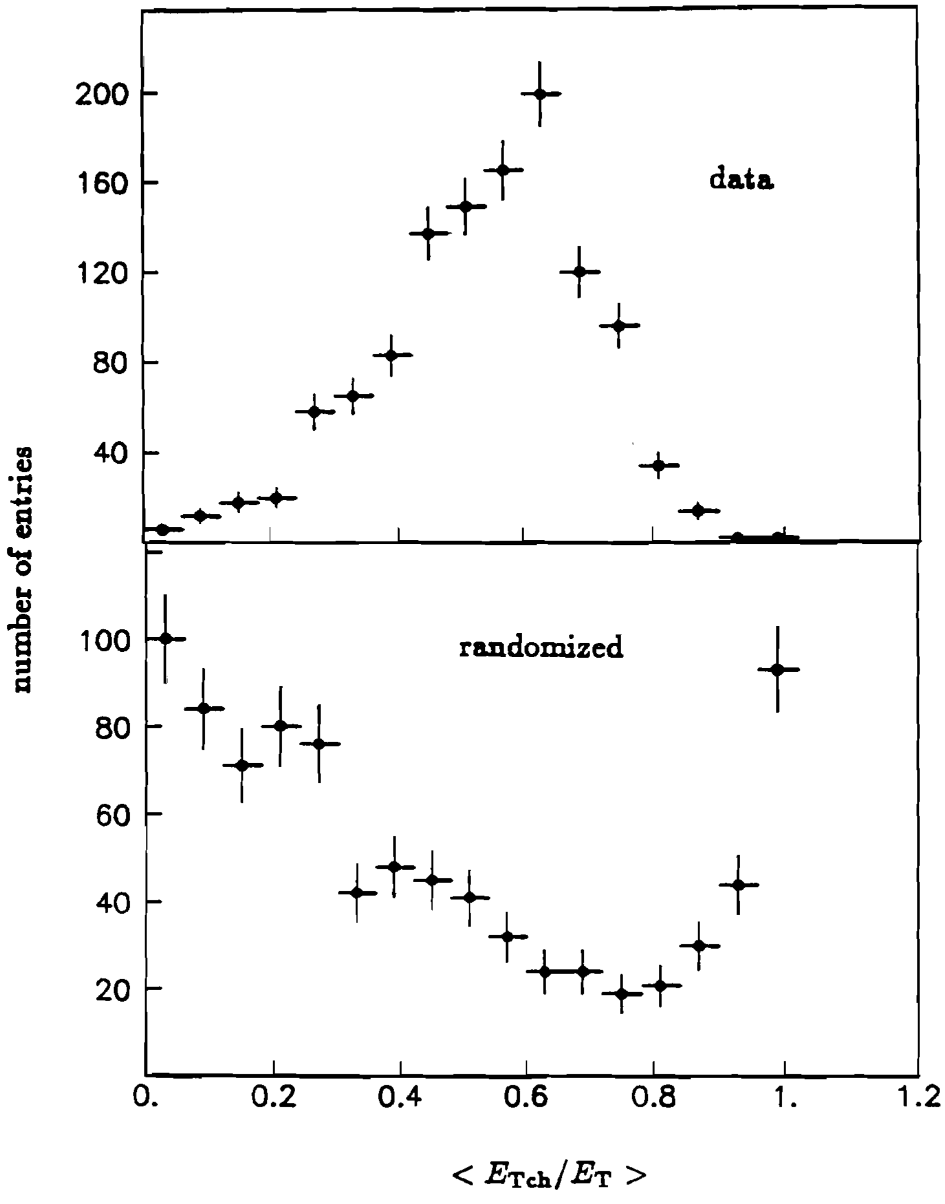

Figure 7.29 $< E_{\mathrm{Tch}}/E_{\mathrm{T}} >$ in real and randomized jet events.

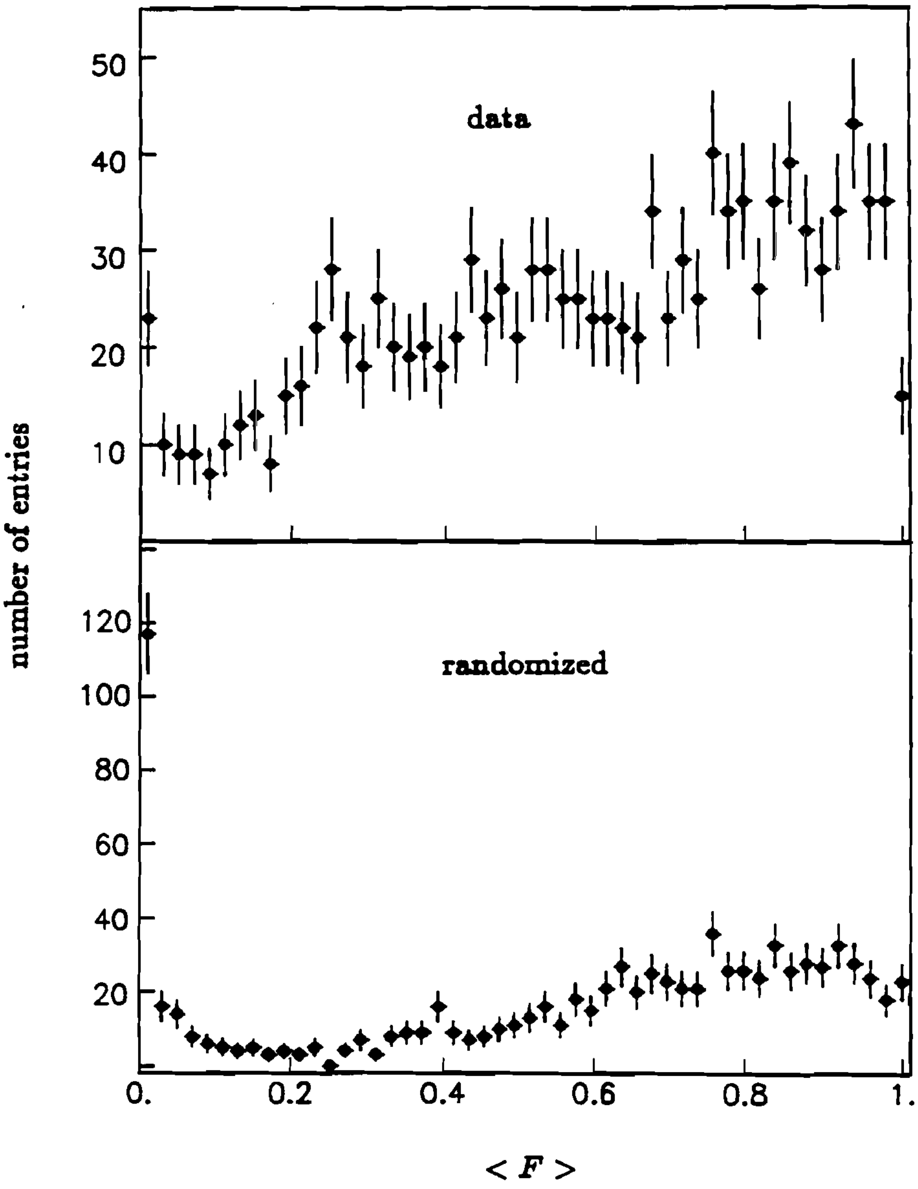

Figure 7.30 $< F >$ in real and randomized jet events.

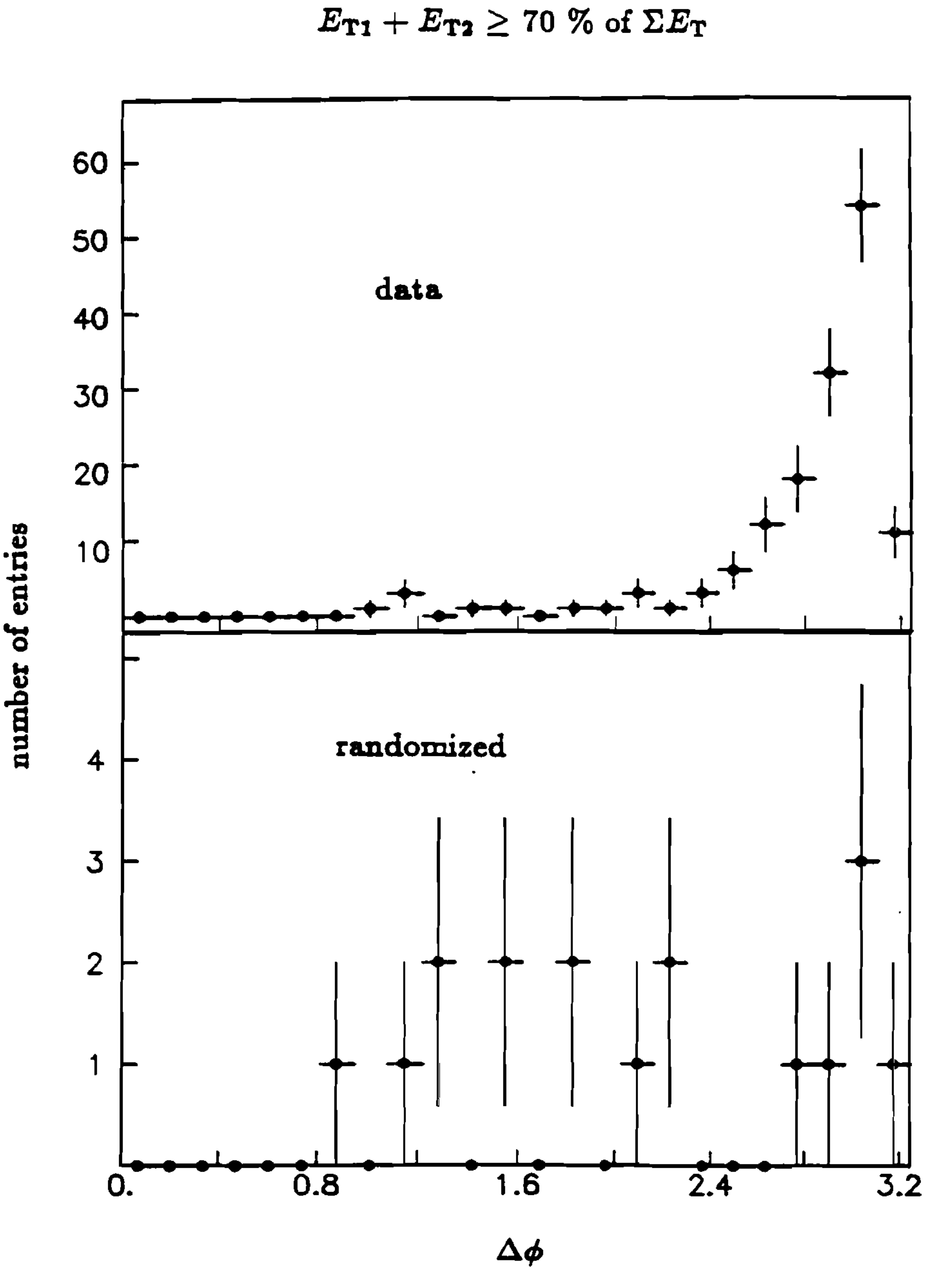

Figure 7.31 $\Delta\phi$ in real and randomized jet events.

Table 7.5 Mean of kinematic variables in Monte Carlo event generators.

$p_T > 0$ MeV/c

Monte Carlo	MBR	MB1	ISAJET	LUND	data
p_T (MeV/c)	476 (436)	587 (469)	295 (247)	607 (618)	495
N_{ch}	12.0 (6.3)	13.2 (8.0)	15.7 (11.0)	25.3 (11.5)	12
N_{ch}/N_{all}	0.68 (0.18)	0.63 (0.17)	0.50 (0.16)	0.46 (0.12)	

$p_T \geq 400$ MeV/c

Monte Carlo	MBR	MB1	ISAJET	LUND	data
p_T (MeV/c)	810 (458)	832 (488)	631 (255)	909 (698)	828
N_{ch}	5.3 (3.3)	7.6 (4.8)	4.1 (3.4)	14.0 (7.4)	5.4
N_{ch}/N_{all}	0.68 (0.25)	0.63 (0.23)	0.51 (0.30)	0.43 (0.16)	0.65

The values in ( ) are RMS.

tuned MBR ($p_T \geq 400$ MeV/c)

p_T (MeV/c)	825
N_{ch}	5.45
N_{ch}/N_{all}	0.68

Carlo (MBR) [97] was tuned to give the correct p_T distribution and average multiplicity for $p_T \geq 400$ MeV/c and in $|\eta| \leq 1$. Even though the multiplicity distribution from the MBR has the same mean value, the generated events do not reproduce the real data well for the high multiplicity tail. Also, the correlation between p_T and multiplicity was not observed in the generated data. The effect of fluctuations in the real data would be hard to deduce with such a disagreement.

The value of the average multiplicity in the MBR was varied to test the sensitivity of the production rate of low E_T clusters to the change in multiplicity. The probability of clusters as a function of E_T changed rapidly with this variation. For the events generated by the MBR with a 20 % lower average multiplicity, the production rate of clusters with $E_T \geq 5$ GeV was lower by 15 %. With tuned parameters in the MBR generator, some of properties for low E_T clusters were also checked and the comparision in terms of mean values of the distrbutions is summarized in Table 7.3. The average values of $< E_T >, < \mathrm{N_{all}} >$ and the number of events with more than 1 cluster in the MBR generated events are lower probably due to the missing high multiplicity tail. Therefore, these disagreements between data and MBR events are not necessarily due to hard scattering.

7.6 Charged Particle Clusters in Extended η

Using an improved tracking algorithm, clusters of charged particles were studied in an extended η range, $|\eta_{\mathrm{axis}}| \leq 1.5$. Because of the increased statistics due to the larger acceptance, it was now possible to study correlations in ϕ between the two highest E_T clusters. The production rate and other properties of clusters were also examined for real and randomized data.

Improvements in track finding algorithm

Improvements were made in the track finding algorithm to increase the efficiency in the region of $1 < |\eta| \leq 2$. The track finding efficiency in $1 < |\eta| \leq 2$ was checked using two independent methods. First, the multiplicity, η and p_T distributions of tracks found in $|\eta| \leq 1$ (with a known efficiency of 99 ± 1 %) were compared with the distributions of the tracks in $1 < |\eta| \leq 2$. Assuming a uniform rapidity distribution of particle production in the central region [4], a rough estimation can be drawn for the track finding efficiency as a function of η from Figure 7.32, which indicates that the efficiency varies between 80 $\sim$ 95 % in $1 < |\eta| \leq 2$. This can also be observed from the multiplicity distributions from the two η regions (Figure 7.33) where the mean value in $1 < |\eta| \leq 2$ is $\sim$ 15 % lower than that from $|\eta| \leq 1$. The p_T distributions from the two η regions are shown in Figure 7.34. The overall mean values from two distributions agree within 2 % ($< p_T >^* = 863$ MeV/c in $|\eta| \leq 1, < p_T >^* = 881$ MeV/c for $1 < |\eta| \leq 2$). However, the distribution for $1 < |\eta| \leq 2$ may indicate a possible double counting or misreconstruction of tracks, especially in the high p_T tail. As a second method of checking the track finding efficiency in $1 < |\eta| \leq 2$, a search for the decay electrons from electro-weak Z Boson candidates in $1 < |\eta| \leq 2$ was done. It was shown that the efficiency of finding the electrons using the CTC and the VTPC was ≥ 90 % in the region $1 < |\eta| \leq 2$.

Charged particle clusters

With the extended η coverage for the charged particles, the properties of charged particle clustering were studied. The geometrical acceptance of the cluster axis was extended to $|\eta_{\mathbf{axis}}| \leq 1.5$. Figure 7.35 shows the probability of charged particle clusters as a function of E_T for $\sqrt{s} = 1800$ GeV.

The most interesting property to be checked is the back to back behavior ($\Delta\phi$ between the first and second highest E_T clusters). About 0.7 % of the total 36,000 events ($\approx$ 240 events) have more than one cluster with $E_T \geq 3$ GeV (With the missing energy contribution from the neutral particles, the

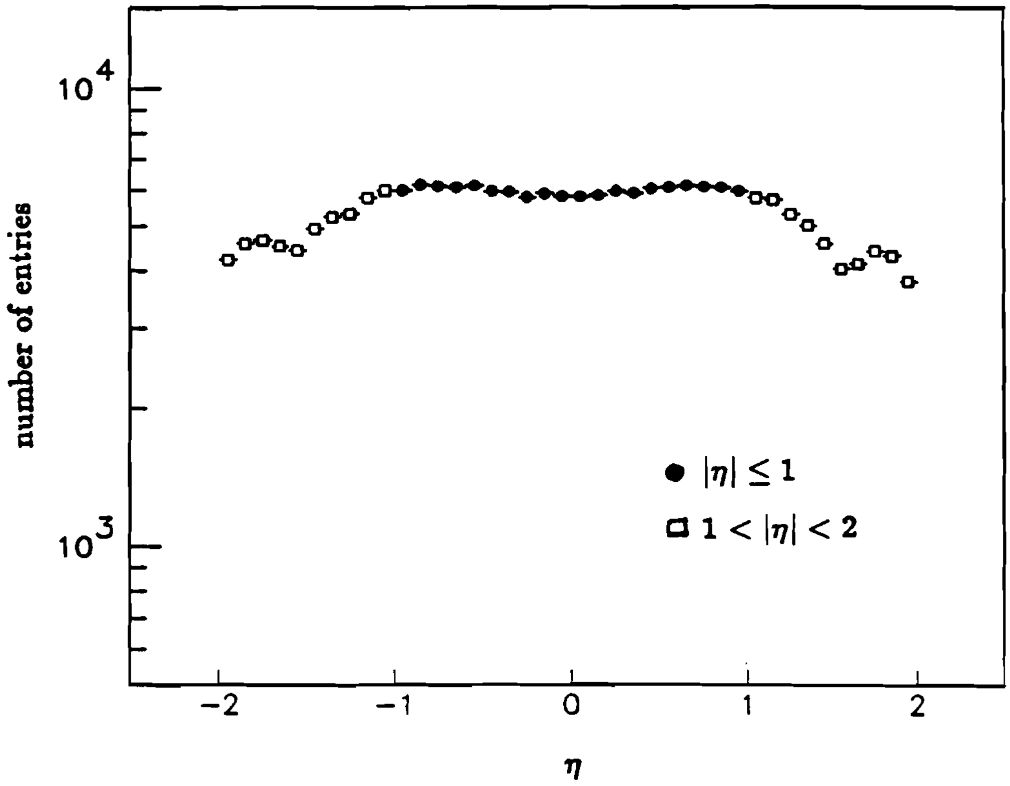

Figure 7.32 η distribition of charged particles in $|\eta| \leq 1$ and $1 < |\eta| \leq 2$.

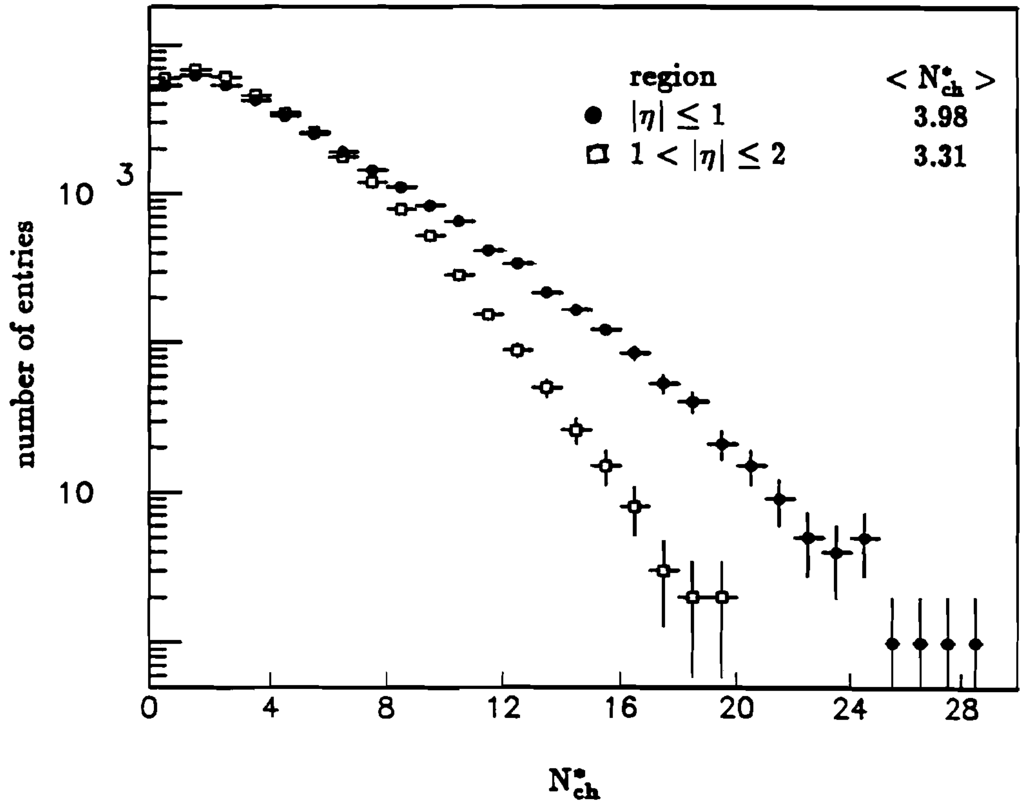

Figure 7.33 N^*_{ch} in $|\eta| \leq 1$ and $1 < |\eta| \leq 2$.

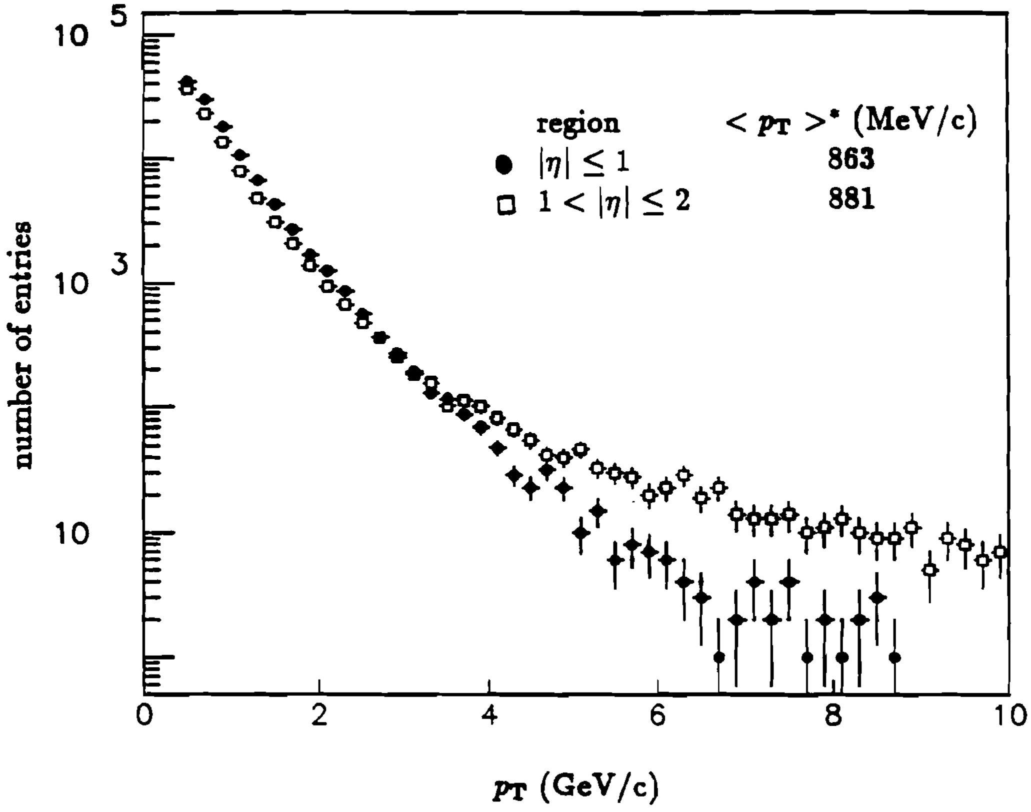

Figure 7.34 p_T distribution of charged particles in $|\eta| \leq 1$ and $1 < |\eta| \leq 2$.

threshold for the charged particle cluster was lowered to $E_T = 3$ GeV.) in $|\eta_{axis}| \leq 1.5$ and the sum of E_{T1} and $E_{T2} \geq 70$ % of ΣE_T. In Figure 7.36, the distribution of $\Delta\phi$ shows a clear back to back behavior.

Randomized events

The probability of randomized charged particle clusters in $|\eta_{axis}| \leq 1.5$ is shown in Figure 7.35 compared with the distribution from the real data. The distribution changes little between the real and randomized events. Other properties of low E_T clusters were also checked and the distributions show no significant difference from the real data as listed in Table 7.6, except the back to back behavior. In Figure 7.36, the randomized distribution of $\Delta\phi$ shows very little back to back behavior. Since there was no attempt made to balance p_T in the randomization, this may be due to the breaking of local momentum conservation.

7.7 Summary and Conclusions

Using a track clustering algorithm, low transverse energy clusters in minimum bias data were studied at the TeV region. They exhibit the properties of clusters and also the event characteristics similar to those measured by both UA1 and UA2 collaborations. The two cluster correlation in $\Delta\phi$ for charged particles also shows a back to back behavior which one would expect to observe in the hard parton scattering. However, in the distributions of $< F >$ and $< E_{Tch}/E_T >$ at low $E_T (< 10$ GeV), there were some evidences for the possible contamination of clusters from the fluctuation of underlying event.

Since the measured properties and characteristics describe the clusters and events in a phenomenological way, it is not obvious to answer whether the clusters found are low E_T jets from a hard scattering, are due to fluctuations, or are some combination. With a lack of Monte Carlo programs which can give a proper description of real data, and a question of the applicability of

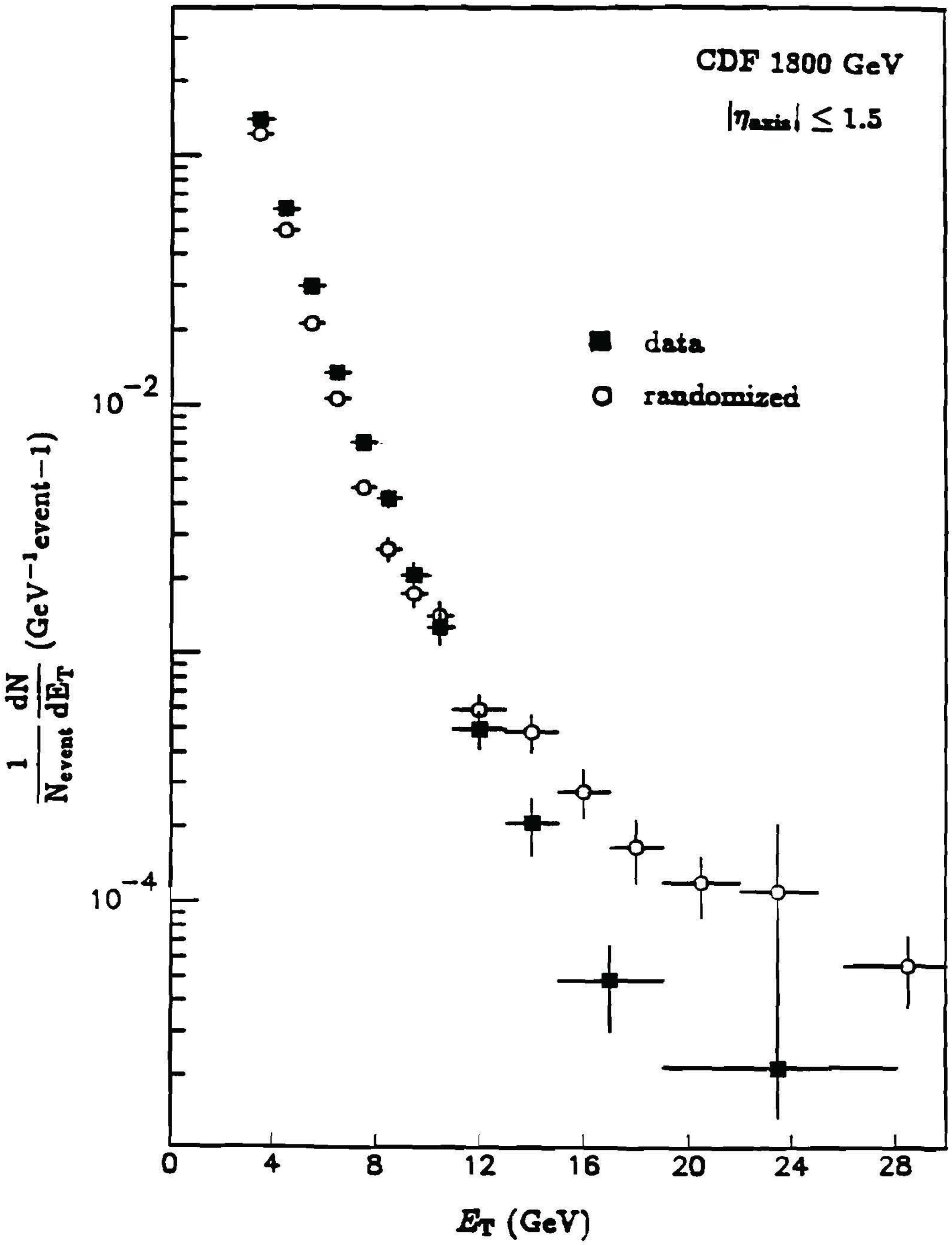

Figure 7.35 E_T of charged particle clusters in $|\eta_{axis}| \leq 1.5$.

$E_{T1} + E_{T2} \geq 70\ \%$ of ΣE_T

$|\eta_{axis}| \leq 1.5$

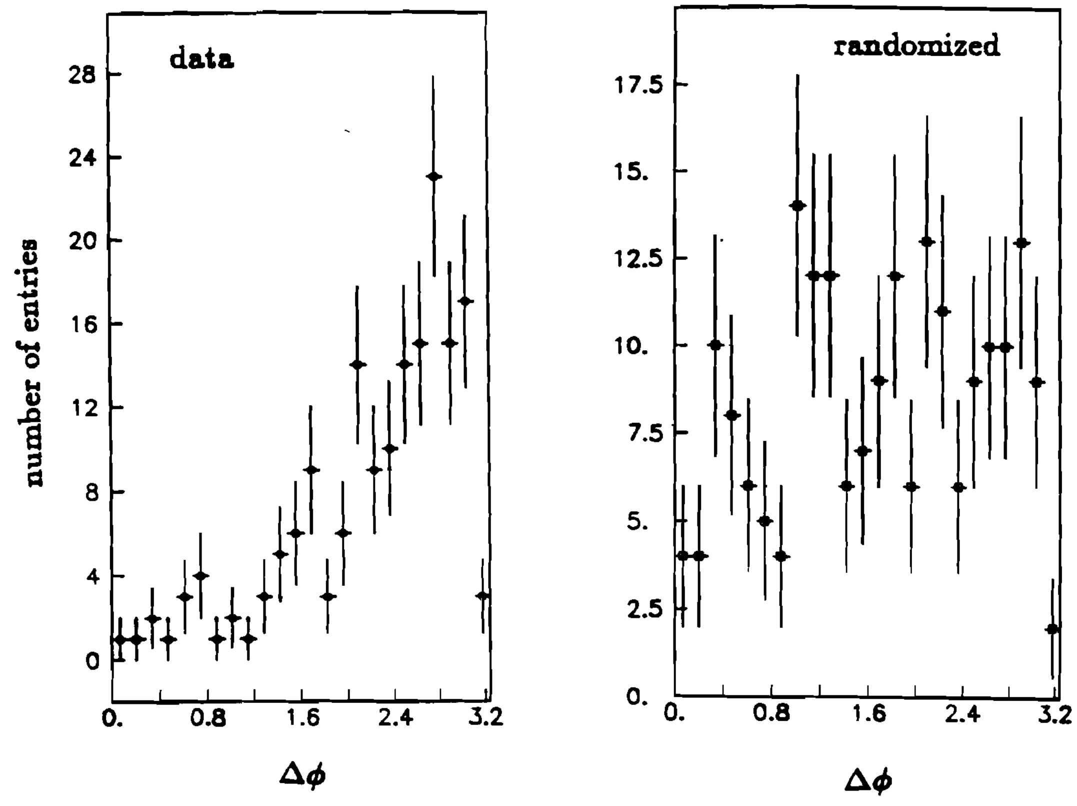

Figure 7.36 $\Delta\phi$ of charged particle clusters in $|\eta_{axis}| \leq 1.5$.

Table 7.6 Charged particle clusters in minimum bias events.

$E_T \geq$		data	random
3 GeV	# events with cluster	6652	5819
	# of clusters per event	1.41	1.37
	total # of clusters	9401	8056
	$< E_T >$ (GeV)	4.46	4.54
	$< N_{ch} >$	3.72	3.37
	$< F >$	0.33	0.35
	p_T of seed track (GeV/c)	2.10	2.47
	$< p_{T\ seed}/E_T >$	0.49	0.56
	$< E_T$ away$>$ (GeV)	3.39	3.34
	# events with $>$ 1 cluster	243	152
5 GeV	# events with cluster	1870	1599
	# of clusters per event	1.16	1.10
	total # of clusters	2166	1854
	$< E_T >$ (GeV)	6.69	7.35
	$< N_{ch} >$	4.68	3.75
	$< F >$	0.33	0.46
	p_T of seed track (GeV/c)	2.94	4.18
	$< p_{T\ seed}/E_T >$	0.45	0.62
	$< E_T$ away$>$ (GeV)	3.86	3.60
	# events with $>$ 1 cluster	44	23

from 36,000 events

$|\eta_{axis}| \leq 1.5$

perturbative QCD at such a low values of E_T, the randomization method was used and the inclusive cluster yield in real data shows no significant difference from the randomized events in particular for $E_T < 10$ GeV.

From the comparison between real and randomized minimum bias and jet data, it can be concluded that the majority of clusters in minimum bias events with $E_T < 10$ GeV are coming as a result of fluctuation from a soft scattering interaction and the transition between the soft and hard regime occurs at $10 < E_T < 20$ GeV where the contamination of soft events decreases and the purity of hard scattering increases as a function of E_T. The quantitative level of contamination (or purity) requires a further study of the selection criteria for the hard scattering clusters.

Also, until the selection criteria for the hard scattering clusters are established, the non-scaling features of minimum bias events (rise of rapidity plateau in the central region, increase of $< p_T >$, KNO scaling breaking, and the correlation between multiplicity and transverse momentum) can not be totally related to hard scattering components since the energy density in the underlying event also rises as a function of E_T for low E_T clusters, as seen in the distribution of p_T density away from the cluster axis (Figure 7.20); and since the p_T densities emitted into four ϕ wedges (Figure 6.10) also are seen to rise as a function of p_T of the trigger particle.

BIBLIOGRAPHY

BIBLIOGRAPHY

1. R. P. Feynman, Phys. Rev. Lett. 23 (1969) 1415

2. M. Gell-Mann, Phys. Lett. 8 (1964) 214
   M. Gell-Mann, Phys. Rev. 125 (1962) 1067

3. C. H. Llewellyn, Phys. Rep. 3C (1974) 261 and references therein.

4. K. Tesima, Phys. Lett. 133B (1983) 115
   J. Dias de Deus, Phys. Lett. 194B (1987) 297

5. W. M. Morse et al., Phys. Rev. D15 (1977) 66
   C. Bromberg et al., Phys. Rev. Lett. 31 (1973) 1563
   S. Barish et al., Phys. Rev. D9 (1974) 2689
   M. Adamus et al., Z. Phys, C32 (1986) 475
   A. Firestone et al., Phys. Rev. D10 (1974) 2080
   F. T. Dao et al., Phys. Lett. 45B (1973) 513
   J. L. Bailly et al., Z. Phys. C23 (1984) 205
   R. D. Kass et al., Phys. Rev. D20 (1979) 6050
   R. Ammar et al., Phys. Lett. 178B (1986) 124

6. A. Breakstone et al., Phys. Rev. D30 (1984) 528

7. K. Alpgrad et al., Phys. Lett. 107B (1981) 310 & 315
   K. Alpgrad et al., Phys. Lett. 121B (1983) 209
   G. Arnison et al., Phys. Lett. 123B (1983) 108
   G. J. Alner et al., Phys. Lett. 138B (1984) 304
   G. J. Alner et al., Phys. Lett. 160B (1985) 193 & 199

8. G. J. Alner et al., Phys. Lett. 167B (1986) 476
   G. J. Alner et al., Z. Phys. C33 (1986) 1

9. G. Ekspong, Nucl. Phys. A461(1987) 145
   G. J. Alner et al., Phys. Rep. 154 (1987) 247

10. CDF Col., presented by A. Para, Proc. of the 7th Topical Workshop on p̄p Collider Physics, Batavia, Illinois USA (1988) 131
CDF Col., presented by V. Barnes, Nucl. Phys. A498 (1989) 193
11. Z. Koba, H. B. Nielsen, P. Olesen, Nucl. Phys. B40 (1972) 317

12. J. Bjorken and J. Kogut, Phys. Rev. D8 (1973) 1341

13. J. Vandermeulen, Nuovo Cimento 32A (1976) 55
and references therein.

14. Angelis et al., Phys. Lett. 79B (1978) 505
F. W. Busser et al., Nucl. Phys. B106 (1976) 1
W. Thone et al., Nucl. Phys. B129 (1977) 365
A. Breakstone et al., Phys. Lett. 132B (1983) 458
K. Guettler et al., Phys. Lett. 64B (1976) 111

15. D. Antreasyan et al., Phys. Rev. D19 (1979) 764

16. A. Rossi et al., Nucl. Phys. B84 (1975) 269 and
references therein

17. B. Alper et al., Nucl. Phys. B100 (1975) 237

18. G. Arnison et al., Phys. Lett. 118B (1982) 167

19. M. Banner et al., Phys. Lett. 122B (1983) 322
M. Banner et al., Z. Phys. C27 (1985) 329

20. A. Breakstone et al., Phys. Lett. 132B (1983) 463
A. Breakstone et al., Z. Phys. C33 (1987) 333
A. Breakstone et al., Europhys. Lett. 7 (1988) 131

21. L. Van Hove, Phys. Lett. 118B (1982) 138

22. UA1 Col., Proc. of the International Europhysics Conference on High-Energy Physics, Bari, Italy (1985) 363

23. T. Alexopulos et al., Phys. Rev. Lett. 60 (1988) 1622

24. G. Pancheri and C. Rubbia, Nucl. Phys. A418 (1984) 117
G. Pancheri and Y. Srivastava, Phys. Lett. 159B (1985) 69
F. W. Bopp, P. Aurenche and J. Ranft, Phys. Rev. D33 (1986) 1867

25. S. Barshay Phys. Lett. 127B (1983) 129

26. H. Boggild and T. Ferbel, Ann. Rev. Nucl. Part. Sci., 24 (1974) 451

27. J. Rushbrooke, Proc. Eur. Phys. Soc. (1985) 837

28. G. Arnison et al., Phys. Lett. 118B (1982) 173

29. R. P. Feynman, Photon-Hadron Interactions,
W. A. Benjamin Inc. (1972)
J. Bjorken, Phys. Rev. 179 (1969) 1547
J. Bjorken and E. A. Paschos, Phys. Rev. 185 (1969) 1975

30. C. Albajar et al., Nucl. Phys. B309 (1988) 405

31. J. A. Appel et al., Phys. Lett. 165B (1985) 441
R. Ansari et al., Z. Phys. C36 (1987) 175

32. Chao Wei-gin, Meng Ta-chung and Pan Ji-cai, Phys. Rev. Lett. 58 (1987) 1399

33. M. Bozzo et al., Phys. Lett. 147B (1984) 392
D. Bernard et al., Phys. Lett. 166B (1986) 459
D. Bernard et al., Phys. Lett. 186B (1987) 227

34. G. J. Alner et al., Z. Phys. C32 (1986) 153

35. R. Ansorge et al., Phys. Lett. B149 (1987) 311

36. G. J. Alner et al., Phys. Rep. 154 (1987) 247 and references therein.

37. A. Capella, LPTHE-ORSAY-87/66, Oct. 1987
G. Gustafson, LU-TP-88-18, Oct. 1988

38. C. Fuglesang, CERN-EP/88-143, Oct. 1988

39. T. Sjostrand and M. van Zijl, Phys. Rev. D36 (1987) 2019
H. U. Bengtsson and T. Sjostrand, Comput. Phys. Com. 46 (1987) 43

40. B. Andersson, G. Gustafson and B. Nilsson-Almquist, Nucl. Phys. B281 (1987) 289

41. A. Capella, J. Tran Thanh Van and J. Kwiecinski, Phys. Rev. Lett. 58 (1987) 2015
A. Capella, A. Staar and J. Tran Thanh Van, Phys. Rev. D32 (1985) 2
A. Capella and J. Tran Thanh Van, Phys. Lett. 93B (1980) 146
A. Capella and J. Tran Thanh Van, Z. Phys. C10 (1981) 249
A. Capella et al., Phys. Lett. 81B (1979) 68

42. Chan Hong-Mo et al., Nucl. Phys. B86 (1975) 470
G. F. Chew and C. Rosenzweig, Phys. Rep. 41C (1978) 263

43. R. Baltrus Aitas et al,. Phys. Rev. Lett. 52 (1984) 1380

44. S. Berman, J. Bjorken and J. Kogut, Phys. Rev. D4 (1971) 3388

45. J. Kwiecinski, Inst. of Nucl. Phys., Cracow, Report 1338/PH (1986)

46. F. Abe et al., Nucl. Instrum. Methods A271 (1988) 387
and references therein.

47. Design Report for the Tevatron I Project, FNAL, Sept. 1984 (unpublished)

48. S. Bhadra et al., Nucl. Instrum. Methods A268 (1988) 92

49. M. Atac et al., Nucl. Instrum. Methods A269 (1988) 40

50. H. Minemura et al., Nucl. Instrum. Methods A238 (1985) 18

51. L. Balka et al., Nucl. Instrum. Methods A267 (1988) 272

52. S. Bertolucci et al., Nucl. Instrum. Methods A267 (1988) 301

53. Y. Fukui et al., Nucl. Instrum. Methods A267 (1988) 280
G. Brandenburg et al., Nucl. Instrum. Methods A267 (1988) 257
S. Cihangir et al., Nucl. Instrum. Methods A267 (1988) 249

54. G. Ascoli et al., Nucl. Instrum. Methods A268 (1988) 33
K. Byrum et al., Nucl. Instrum. Methods A268 (1988) 46

55. L. Van Hove, Phys. Rep. 1 (1971) 347

56. D. Amidei et al., Nucl. Instrum. Methods A269 (1988) 51

57. F. Snider et al., Nucl. Instrum. Methods A268 (1988) 75

58. F. Bedeschi et al., Nucl. Instrum. Methods A268 (1988) 50

59. H. Brafman et al., IEEE Trans. NS32 (1985) 336

60. E. Barsotti et al., Nucl. Instrum. Methods A269 (1988) 82

61. K. Yasuoka et al., Nucl. Instrum. Methods A267 (1988) 315

62. R. G. Wagner et al., Nucl. Instrum. Methods A267 (1988) 330

63. S. Hahn et al., Nucl. Instrum. Methods A267 (1988) 351

64. G. Giacomelli, Phys. Rep. 23 (1976) 123
U. Amaldi et al., Annual Rev. of Nucl. Science 26 (1976) 385

65. M. M. Block and R. N. Cahn, Phys. Lett. 118B (1987) 143

66. M. Sekiguchi, "Multiplicity and Transverse Momentum Distributions of Charged Particles in $\bar{p}p$ Collisions at $\sqrt{s} = 630$ and 1800 GeV", PhD Thesis, University of Tsukuba, June 1988

67. M. Schub, "Strange Particle Production in $\bar{p}p$ Collisions at $\sqrt{s}$ $= 630$ and 1800 GeV", PhD Thesis, Purdue University, August 1989

68. R. P. Feynman, R. D. Field and G. C. Fox, Phys. Rev. D18 (1978) 3320
R. Horgan and M. Jakob, Nucl. Phys. B179 (1981)

69. Program written by S. Ellis and J. Stirling

70. J. F. Owens and E. Reya, Phys. Rev. D17 (1978) 3003

71. H. Abramovicz et al., Z. Phys. C12 (1982) 289

72. R. Baier, J. Engels and B. Petersson, Z. Phys. C2 (1979) 265

73. N. Bali et al., Phys. Rev. Lett. 25 (1970) 557
R. Hagedorn, Rev. Nuovo Cimento 6 (1983) 10

74. C. Lattes et al., Phys. Rep. 65 (1980) 151

75. E735 Col., Proc. of the 7th Topical Workshop on p̄p Collider Physics, Batavia, Illinois USA (1988) 157

76. J. H. Cobb et al., Phys. Rev. Lett. 40 (1978) 1420

77. T. Akesson et al., Phys. Lett. 118B (1982) 193

78. T. Akesson et al., Phys. Lett. 121B (1983) 439

79. F. Abe et al., Fermilab-Pub-88/213-E, Dec 1988.

80. M. Jacob and P. V. Landshoff, Nucl. Phys. B133 (1976) 395

81. G. Arnison et al., Phys. Lett. 132B (1983) 214

82. M. Althoff et al., Phys. Lett. 135B (1984) 243
M. Sakuda et al., Phys. Lett. 152B (1985) 399
P. Kesten et al., Phys. Lett. 161B (1985) 412

83. J. G. Korner et al., Nucl. Phys. B185 (1981) 365

84. P. Bagnaia et al., Phys. Lett. 144B (1984) 291

85. S. J. Brodsky and J. F. Gunion, Phys. Rev. Lett. 37 (1976) 402

86. F. Halzen, P. Hoyer, and W. Stirling, Phys. Lett. 188B (1987) 375
N. Paver and D. treleani, Z. Phys, C28 (1985) 187

87. F. A. Berends and W. T. Giele, Nucl. Phys. B313 (1989) 595
M. Danos and J. Rafelski, Phys. Rev. D27 (1983) 671

88. M. J. Corden et al., Phys. Scripta. Vlo. 25 (1982) 11
M. J. Corden et al., Phys. Scripta. Vlo. 25 (1982) 5
A. Berr et al., Nucl. Instrum. Methods 224 (1984) 360

89. UA1 Col., Proc. of the Topical Workshop on p̄p Collider Physics Saint-Vincent, Aosta Valley, Italy (1985) 488

90. I. Sarcevic, S. D. Ellis and P. Carruthers, DOE-ER-40423-13-P8, Sep 1988
A. H. Mueller and H. Navelet, Nucl. Phys. B282 (1987) 727

91. J. A. Appel et al., Phys. Lett. 160B (1985) 441

P. Bagnaia et al., Phys. Lett. 144B (1984) 283

92. B. Flaugher and S. Kuhlmann, CDF note 685

93. H. Jensen, CDF note 532

94. C. De Marzo et al., Phys. Lett. 112B (1982) 173

95. S. Behrends et al., CDF note 583

96. W. Bartel et al., Z. Phys. C21 (1983) 37
H. Aihara et al., Z. Phys. C28 (1985) 31
M. Derrick et al., Phys. Lett. 165B (1985) 449

97. S. Belforte and K. Gouliano, CDF note 256
K. Gouliano and J. Grunhaus, CDF note 675

VITA

VITA

NAME	Aesook Byon
PERSONAL	
Place of Birth:	Seoul, Korea.
ACADEMIC	
Degrees:	B.S., Physics, 1984 Southern Illinois University at Carbondale
	M.S., Physics, 1986 Purdue University
	Ph.D., Physics, 1989 Purdue University
EMPLOYMENT EXPERIENCE	
1986-Present	Research Assistant, Experimental High Energy Physics, Purdue University. Faculty advisor, Virgil E. Barnes. Thesis topic: "Central Production of Charged Particles at CDF "
1984-1985	Teaching Assistant, Physics Department Purdue University